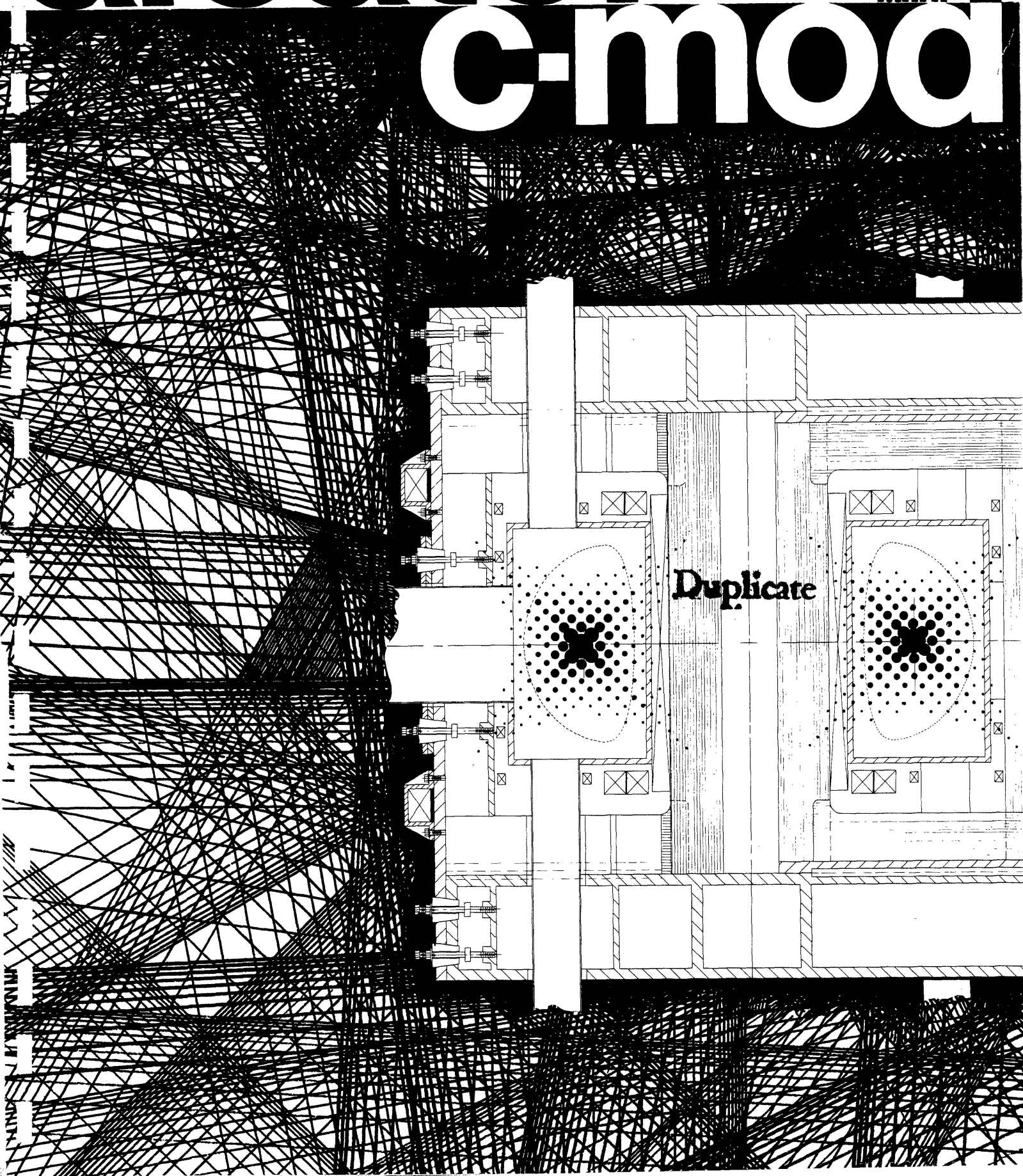


alcatraz

PROPOSAL
BY PLASMA
FUSION
CENTER
M.I.T.

c-mod



Duplicate

MASSACHUSETTS INSTITUTE OF TECHNOLOGY

PLASMA FUSION CENTER

ALCATOR C-MOD PROPOSAL

October 1985

Submitted to

OFFICE OF FUSION ENERGY

U.S. DEPARTMENT OF ENERGY

WASHINGTON, D. C. 20545

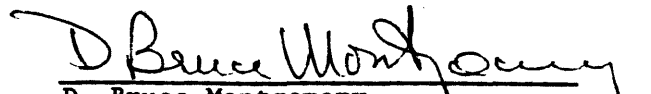


Ronald C. Davidson, Director
Plasma Fusion Center

George H. Dummer, Director
Office of Sponsored Programs



Ronald R. Parker
PFC Associate Director for
Confinement Experiments



D. Bruce Montgomery
PFC Associate Director for
Engineering Systems

PFC/RR-85-18

DOE/ET-51013-158

ALCATOR C-MOD PROPOSAL

J. Freidberg, M. Greenwald, D. Gwinn, I. Hutchinson,
B. Lipschultz, E. Marmor, D. B. Montgomery,
R. R. Parker, M. Porkolab, J. Schultz, D. Sigmar,
R. Thome, S. M. Wolfe, T. Yang

Plasma Fusion Center
Massachusetts Institute of Technology
Cambridge, MA 02139

October 1985

This work was supported by the U.S. Department of Energy Contract No. DE-AC02-78ET51013. Reproduction, translation, publication, use and disposal, in whole or in part by or for the United States government is permitted.

TABLE OF CONTENTS

1.	INTRODUCTION	
1.1	Introduction	1-1
1.1.1	Background	1-1
1.1.2	Alcator C-MOD Objectives	1-2
1.2	Alcator C-MOD Description	1-5
1.2.1	General Description	1-5
1.2.2	Physics Performance	1-12
1.2.3	Magnet Design	1-15
1.2.4	RF Heating	1-16
1.2.5	First Wall Protection	1-17
1.2.6	Device Flexibility	1-18
1.3	Baseline and Extended Performance Options	1-18
2.	PLASMA PHYSICS CONSIDERATIONS	
2.1	Introduction	2-1
2.2	Plasma Parameters - Transport Calculations	2-6
2.2.1	O-D Modeling	2-6
2.2.2	1-D Simulations	2-17
2.3	MHD Configuration	2-30
2.3.1	Design Scenario	2-30
2.3.2	Basic D-Shaped Configuration	2-31
2.3.3	β -Dependence	2-39
2.3.4	Start-up Scenario	2-39
2.3.5	Advanced Configurations	2-43
2.4	Impurity Control	2-48
2.4.1	Introduction	2-48

2.4.2	Limiter and Divertor Configurations	2-49
2.4.3	High Recycling Regime	2-54
2.4.4	Reduction of Evaporation	2-55
2.5	ICRF Heating of Alcator C-MOD	2-62
2.5.1	Background and Choice of Frequencies	2-62
2.5.2	Absorption Efficiencies	2-67
	a. Fast Wave Harmonic Resonance ($\omega = 2\omega_H$)	2-67
	b. Minority Fast Wave Absorption	2-77
	c. Ion Bernstein Wave Heating	2-83
2.5.3	The Alcator C-MOD ICRF System	2-85
	a. Fast Wave Antenna	2-85
	b. Bernstein Wave Antenna	2-88
	c. Tuning and Matching	2-93
	d. The FPS-17 ICRF 6 MW System	2-93
	e. The FMIT 10 MW ICRF System	2-96
3.	ALCATOR C-MOD POINT DESIGN	
3.0	Introduction	3-1
3.1	TF Magnet System	3-6
3.1.1	General Description of the TF Coil System	3-6
3.1.2	Structural Behavior of the TF Coil System	3-8
	3.1.2.1 Coil Structure Behavior with Slip Joints ...	3-9
	3.1.2.2 Coil Structural Behavior with Fixed Joints	3-14
	3.1.2.3 Comparison of Applied Stresses with Allowables	3-15

3.1.	TF Coil Joint Behavior	3-26
3.1.4	TF Power and Energy Requirements	3-31
3.2	PF Magnet System	3-38
3.2.1	PF Current Requirements	3-38
3.2.2	PF Power and Energy Requirements	3-42
3.2.3	Electromagnetic Considerations	3-48
3.3	Vacuum Vessel	3-53
3.3.0	Introduction	3-53
3.3.1	Disruption Structural Response	3-55
3.3.2	Wall Protection and Divertor Collector Plates ...	3-59
3.4	Cryogenic Considerations	3-62
3.4.0	Introduction	3-62
3.4.1	Recool Following a Pulse	3-62
3.4.2	Cooldown from Room Temperature	3-69
3.4.3	Nitrogen Consumption	3-70
4.	ALCATOR C-MOD DIAGNOSTICS	
4.1	Introduction	4-1
4.2	Fully Developed Diagnostic Systems	4-1
4.2.1	Multi-point Ruby Thomson Scattering	4-1
4.2.2	Infrared Density Interferometer	4-2
4.2.3	Electron Cyclotron Emission	4-2
4.2.4	Neutral Particle Energy Analysis	4-2
4.2.5	Neutron Diagnostics	4-3
4.2.6	Visible and UV Spectroscopy	4-4
4.2.6.1	Survey of Intrinsic Impurity Levels	4-4
4.2.6.2	Doppler Broadening and Shifts	4-4
4.2.7	X-ray Diagnostics	4-5

4.2.7.1	Spectroscopic	4-5
4.2.7.2	Broad Band Diode Arrays	4-6
4.2.8	Bolometry	4-7
4.2.9	CO ₂ Scattering	4-8
4.2.10	Edge Plasma and Wall Diagnostics	4-8
4.3	Diagnostic Systems In Development	4-9
4.3.1	Nd:YAG Thomson Scattering	4-9
4.3.2	CO ₂ Dual Wavelength Interferometer	4-9
4.3.3	Neutral Particle Analyzer	4-10
4.3.4	Diagnostic Neutral Beam	4-10
4.3.5	Time of Flight Low Energy Neutral Spectrometer ..	4-10
4.3.6	Charged Fusion Product Measurements	4-11
4.3.7	Infrared Surface Temperature Measurements	4-12
4.4	Summary	4-12
5.	DATA ACQUISITION and CONTROL	
5.1	Data Handling	5-1
5.1.1	System Description	5-1
5.1.2	Data Acquisition Hardware - CAMAC	5-4
5.1.3	Computers	5-4
5.1.4	Back-End Network	5-5
5.1.5	Local Area Network	5-6
5.1.6	Data Display System	5-7
5.1.7	Data System Software	5-8
5.2	Automated Control System	5-9
6.	FACILITIES	
6.1	Siting and Building Layout	6-1
6.1.1	Overall Site Description	6-1

6.1.2	Experimental Cell and Power Equipment Area Description	6-1
6.1.3	Support Areas	6-3
6.2	Power Systems	6-3
6.2.1	Prime Power	6-3
7.	COST AND SCHEDULE	
7.0	Introduction	7-1
7.1	Cost Basis	7-1
7.1.1	TF Coil Costing Basis	7-5
7.1.2	TF Structure Cost Basis	7-7
7.1.3	PF Coil Costing Basis	7-9
7.1.4	Vacuum Vessel Costing Basis	7-11
7.1.5	Wall Protection Costing Basis	7-13
7.1.6	Thermal Shield Cost Basis	7-15
7.1.7	Cryosystem Cost Basis	7-16
7.1.8	Site Modification Cost Basis	7-17
7.1.9	Power Systems Modification Cost Basis	7-18
7.1.10	Control Modification Cost Basis	7-20
7.1.11	RF Modification	7-20
7.1.12	ANSALDO Preliminary Cost Estimate	7-24
7.1.13	Cost Basis for Future Reconfiguration Options ...	7-24
7.1.14	Relationship of C-MOD Costing to Cost Projections for Ignition Scale Devices	7-27
7.2	Schedule	7-31
7.2.1	Relationship of ISP and C-MOD Schedules	7-35
7.3	Cost Profiles	7-37
7.4	Contingency and Cost Escalation	7-41

7.5	Manpower Levels	7-43
7.6	Project Management	7-48
7.6.1	Management Plan	7-48
7.6.2	Project Organization	7-50
7.6.3	Program Management Software	7-52

8. PROGRAM PLAN

APPENDICES

A. COST ESTIMATE FOR INSTALLATION OF ADDITIONAL ENERGY

B. THEORETICAL CONSIDERATIONS FOR ALCATOR C-MOD AS A TOKAMAK

CONCEPT IMPROVEMENT EXPERIMENT

I.	Introduction	B-2
II.	Shaping Options	B-2
II.1	Higher Beta	B-2
II.2	Confinement Improvement	B-13
II.3	New Regimes of Other Parameters	B-15
III.	Advanced Impurity Control	B-16
IV.	Lower Hybrid Current Drive and MHD Stabilization Experiments	B-20
IV.1	Current Drive Experiments	B-20
IV.2	MHD Stabilization Experiments	B-22

CHAPTER 1

INTRODUCTION

1.1 Introduction

1.1.1 Background

The success of Alcator C in achieving a Lawson parameter in excess of that required for breakeven at higher temperatures has underscored the value of the high-field, high-density tokamak. Present plans for a near-term ignition experiment focus on this approach as the most promising and economical means of exploring fundamental issues associated with the physics of burning plasmas, as called for in the Magnetic Fusion Program Plan. The Alcator C-MOD facility is proposed as an upgrade to Alcator C aimed at investigating the characteristics of high-temperature, ICRF-heated plasmas, with the goal of understanding and optimizing confinement and stability of such plasmas, and exploring methods of heating, controlling impurities, fueling, and shaping in high performance tokamaks. The information obtained on Alcator C-MOD will be helpful to the implementation and operation of a high-field ignition device, including the gathering of experience with advanced magnet designs.

Concept improvement is a second major thrust of the Magnetic Fusion Program Plan. The C-MOD modification will address issues related to the ultimate goal of an attractive tokamak reactor on two fronts: i) motivated by recent theoretical progress towards high beta in the readily accessible first stability region through large elongation combined with triangularity and indentation, or very small aspect ratio, such design modifications of the base version of C-MOD are being developed, basically within the same magnet system and overall machine size. These modifications will

allow elongations $1 < \kappa < 3$ and/or aspect ratios $1.67 < A < 4$, i.e., an extraordinary range of MHD-scaling parameters in one installation. ii) By operating at reduced fields, C-MOD can operate for 10 second pulses, and with its combination of improved RF access advanced launchers and an expanded boundary divertor will provide key elements in seeking more efficient methods of impurity control and non-inductive current drive.

1.1.2 Alcator C-MOD Objectives

There are two major goals of the Alcator C-MOD experiment: the first is to extend the plasma regimes attainable in state-of-the-art devices such as Alcator C to temperatures and nT values characteristic of plasmas near ignition; the second is to improve the tokamak concept for reactor application through exploration of advanced shapes and methods of impurity control and current drive.

Associated with these goals are the following specific objectives:

1. Determine the confinement properties of plasmas with temperatures and confinement parameters close to those required for ignition. Optimize confinement by use of edge control, fueling, shaping and other plasma handling techniques.
2. Develop methods of RF heating appropriate to high-field, high-density, compact tokamaks. These methods must be compatible with shaped (i.e., non-circular) and diverted plasmas.
3. Explore highly shaped MHD equilibria and other special geometrical configurations together with profile optimization to improve confinement, beta and stability.

4. Control plasma heat fluxes and edge conditions in order to maintain acceptable plasma impurity levels using limiters (pumped or non-pumped) and expanded boundary divertors. Explore new concepts in impurity control.
5. Develop novel methods of RF current drive for use in extending the tokamak pulse length and improving tokamak stability.
6. Develop new copper magnet technology permitting easy access and maintenance of the tokamak load assembly.

Achievement of the first four objectives will substantially improve the data base relevant to operation of high-field, RF-heated tokamaks, and the information obtained will be invaluable to a compact tokamak ignition experiment. For example, a key issue for an ignition experiment is confinement under conditions of intense ICRF and α -particle heating. Profile averaged 0-D transport models reveal that confinement in the ignition device must be significantly better (at least a factor of 2) than "L-Mode" confinement characteristic of most NBI heating experiments. Clearly, it is desirable to investigate the transport mechanisms appropriate to the regime of an ignition device. It is even more important, and in fact crucial to the success of the venture to develop the operational techniques such as edge control, fueling, shaping, etc., necessary to optimize confinement at the relevant plasma parameters (density, field, current, q_ψ , κ , δ , . . .). Alcator C-MOD is designed both to extend the transport data base at ignition-relevant parameters and to develop methods of confinement optimization.

We note that the advanced shaping options envisioned for Alcator C-MOD are in close harmony with the goal of reaching near-ignition parameters in a compact tokamak. For example, the strong dependence of current on elongation, $\sim \kappa^2$ for $\kappa^2 \gg 1$ coupled with the observed sensitivity to current in the auxiliary heating scaling laws suggests that highly-elongated (or for that matter ultra-low aspect ratio) plasmas are likely to have excellent confinement properties. Furthermore, since for fixed $q(0)$, the central current density is proportional to $(\kappa + \kappa^{-1})/2$, strong ohmic heating performance is obtained in high field, highly elongated plasmas as well, thus enhancing the prospects for reaching ignition without additional RF or NB heating. For this reason, we are incorporating elongations κ of at least 2.5 in the baseline design.

The information obtained in the first few years of operation of Alcator C-MOD will be especially useful and supportive to the Ignition Project. For example, the RF heating method will be directly prototypical of that which will be used in the ignition device. Key design information pertaining to the antenna configuration, heating efficiency and quality of confinement will be made available in timely fashion for design of the RF systems. Similarly, the operational experience gained on C-MOD can be used to guide the detailed design of the plasma boundary control system. In this sense, Alcator C-MOD would serve as a plasma systems simulator for an ignition experiment and the data from C-MOD will greatly increase the probability of a successful ignition project.

The last two objectives reflect a longer range interest in improving the tokamak reactor concept. We plan to continue our work on extending the tokamak pulse length by exploring more efficient methods of current

drive, for example by use of the fast wave branch of the lower hybrid wave. Current drive will also be used to modify and control the current density profile, thereby optimizing beta and overall stability. Finally, if sufficiently high beta can be achieved (possibly by entry into the second stability regime) the prospect of a copper reactor may become viable. In this case, the advanced magnet design developed for C-MOD offers the possibility of easy maintainability of the nuclear island.

1.2 Alcator C-MOD Description

1.2.1 General Description

The Alcator C-MOD load assembly will feature a major radius of about 75 cm, slightly larger than Alcator C, with an aspect ratio of approximately 3. The maximum capability at the toroidal field magnet is 10 Tesla, less than the design field of Alcator C but permitting plasma currents of more than 4 MA and densities above $5 \times 10^{14} \text{ cm}^{-3}$. The present 225 MVA alternator which supplies prime power to Alcator C is capable of producing 7.5 T operation in Alcator C-MOD. We refer to this as the baseline mode. By adding additional prime power capability, operation at $B_T = 10 \text{ T}$ can be achieved. This is referred to as the extended performance option. (See also Section 1.3 and Appendix A.)

The design concept is illustrated in Fig. 1-1. The major part of the poloidal field system, including the OH transformer is located inside the TF coil. The latter is of rectangular construction and uses sliding joints at each of the four corners. This design largely eliminates tensile loads in each leg of the TF coil, and permits rapid disassembly, allowing relatively easy access to the pf system and the vacuum chamber. The poloidal field system design is not yet fully optimized; at this

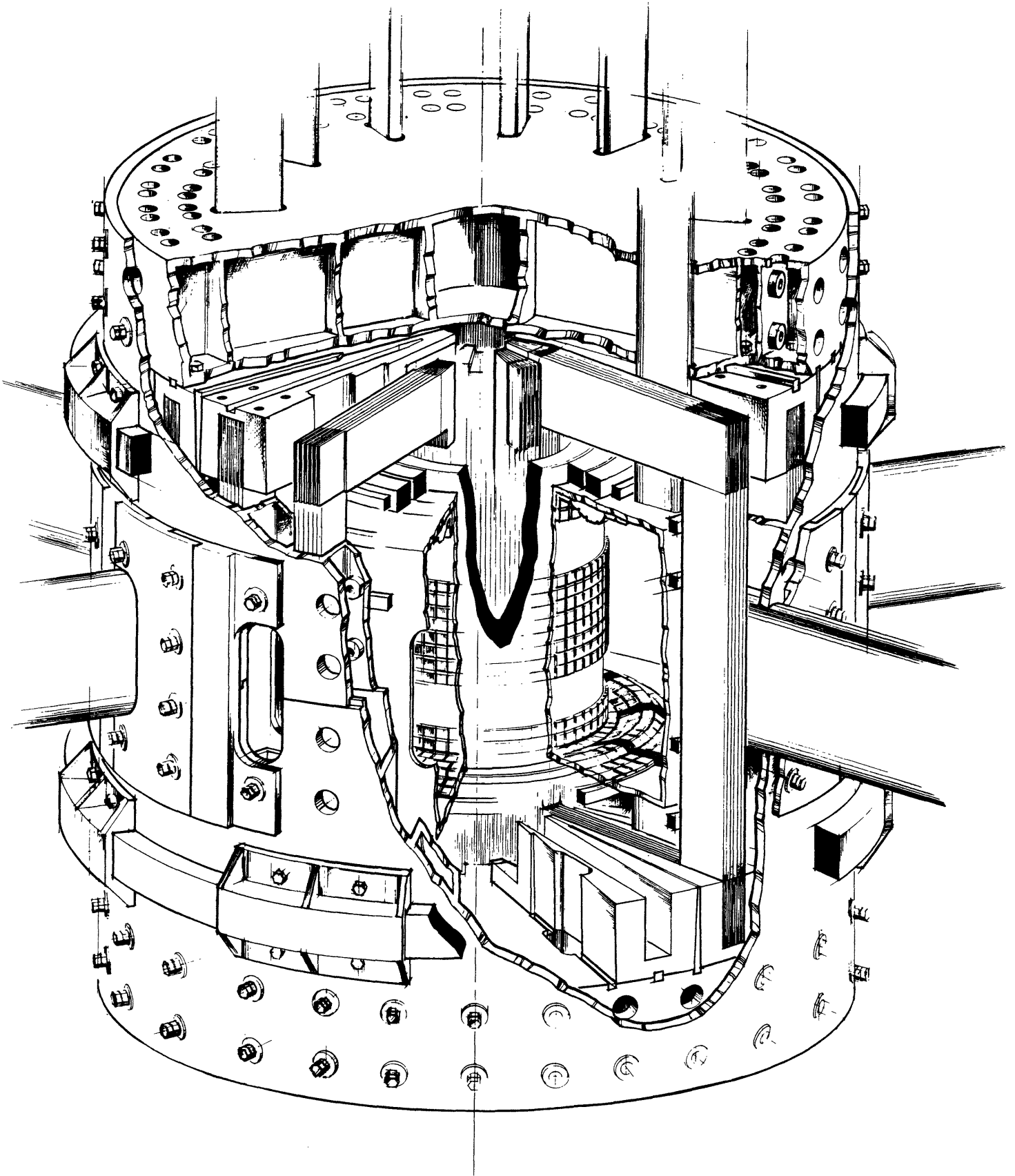


FIG. 1-1a The Alcator C-MOD Design Concept: Isometric View

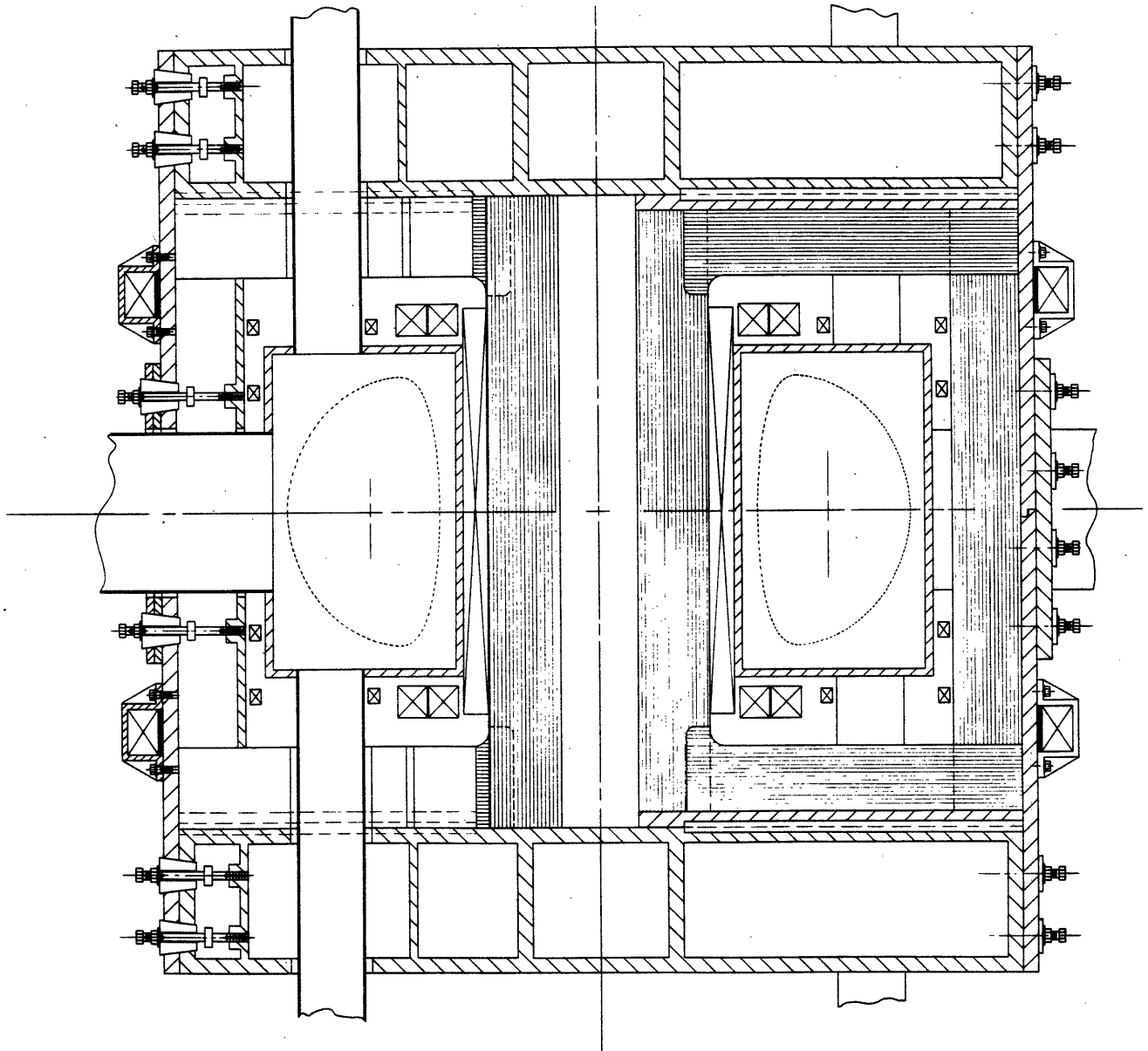


FIG. 1-1b The Alcator C-MOD Design Concept: Cross-sectional View

point we only illustrate what we expect will be representative of the ultimate capability. Figure 1-2 shows a diverted plasma ($I_p = 4$ MA, $B_T = 8$ T, $q_\psi = 2.6$, $\kappa \sim 2$) in which the distance between separatrix and a divertor target plate can be made larger than the neutral mean path. In this case, high-recycling divertor action is expected to occur.

With modification of the coil currents and relatively minor modification of the PF coil set, highly elongated ($\kappa > 2.5$), moderate aspect ratio ($A \approx 3$) plasmas can be produced. (See Section 2.3 for examples.) Our intention is to capitalize on the significant increase in current at fixed q_ψ due to strong elongation ($q_\psi I \sim 1 + \kappa^2$), thereby permitting optimization of confinement and overall performance.

Further optimization of the pf design should allow plasmas with high triangularity and modest indentation to be created. Such plasmas are expected to be close to the shapes required for optimum stability against ballooning modes at high β . (See Appendix B and Ref. [II-1c] cited therein.) While high β studies would require additional RF heating power compatible with lower field operation, the baseline design can be used to study axisymmetric stability and confinement optimization of these advanced shapes at low to moderate β .

The substantial qualitative improvements over Alcator C are the capability for elongated, highly-shaped equilibria; greatly increased access for RF heating, power removal, and diagnostics; and an expanded boundary-divertor configuration for impurity control and confinement enhancement (H-mode). The baseline design provides for approximately 6 MW of RF heating in the ion cyclotron range, using the Shemya equipment acquired several years ago for the Alcator C program. The extended performance

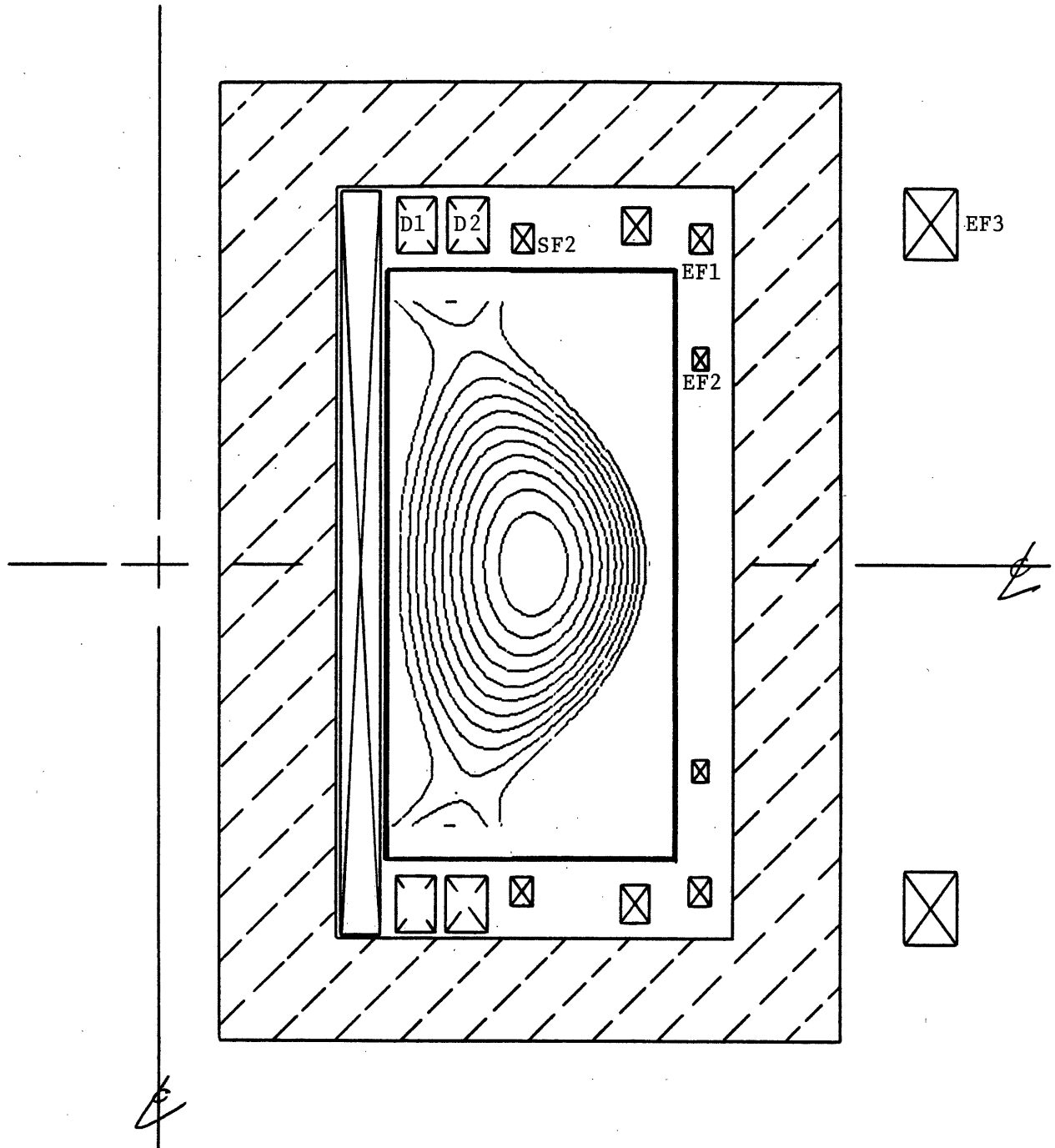


FIG. 1-2 A diverted plasma equilibrium in Alcator C-MOD. $B_T = 8$ T, $I_p = 4$ MA, $q_\psi = 2.6$, $\kappa \approx 1.9$. The coil currents in MA are: D1:1, D2:1, SF2:-0.3, EF1:-0.3, EF2:-0.26, EF3:2.6.

mode utilizes 10 MW of ICRF power. This power may be supplied in whole or in part by FMIT transmitters. In either case, a collaborative effort with RF heating specialists from PPPL is anticipated. The details of this collaborative arrangement await a successful C-MOD review and definition of a national ICRF program.

The basic C-MOD engineering and expected plasma parameters are shown in Tables 1-1 and 1-2 respectively, compared with two representative compact ignition experiment designs. The machine is an approximate full-field, half-scale version of ISP, the compact ignition device under current study at PPPL. It is actually closer in size to Ignitor but the design field is somewhat lower (10 T vs 13 T). Nevertheless, the projected maximum density ($\sim 10^{21} \text{ m}^{-3}$) is close to that anticipated in an Ignitor-like device. Note that the wall loading is comparable to that under ignited, high- β conditions in the ISP; it is also typical of that expected for moderate- β ($\sim 3\%$) ignition in Ignitor.

TABLE 1-1

PROPOSED ENGINEERING PARAMETERS

	C-MOD (7.5 T)	C-MOD (10 T)	ISP (PPPL)	IGNITOR
Major Radius (m)	0.75	0.75	1.6	1.0
Minor Radius (m)	0.25	0.25	0.53	0.4
Magnetic Field (T)	7.5	10	8.9	13
Elongation (Nominal)	1.8	1.8	1.6	1.6
Triangularity	0.3	0.3	0.4	0.2
Plasma Current (MA)	3	4	7.8	10
Flat-Top Pulse (s)	1	1	5	0.5
Flat-Top Pulse @ 5 T (s)	10	20	-	-
Volt-Seconds (Webers)	12	12	26	20
RF Heating (MW)	6	10	30	0-10
Average Heat Flux (MW/m ²)	0.6	1	0.8 ¹⁾	3.6 ¹⁾
Plasma Surface Area (m ²)	9.6	9.6	43.5	20.5
Stored Energy Required (MJ)	350	640	-	-

1) Assumes an ignition point at $T_0 = 30$ keV, $n_0 = 0.7$ B/R.

TABLE 1-2

EXPECTED PLASMA PARAMETERS

	C-MOD (7.5 T)	C-MOD (10 T)	ISP (PPPL)	IGNITOR
Peak Density ¹ ($\times 10^{20} \text{ m}^{-3}$)	7	9.3	3.9	9.1
Peak Temperature (keV)	4-8	6-12	20-30	20-30
Beta (%)	1.6-3.1	1.7-3.5	3.1-4.7	3.4-5.1
Troyon Beta Limit (%)	4.8	4.8	5	5.8
Maximum Average Pressure (atm)	7	12.4	15	34

¹ Assumes Murakami limit, $n_0 = 0.7 \text{ B/R}$

Comparing the magnet design of C-MOD to that in the ignition devices one finds that the TF current density is about two times higher than in ISP. Consequently, the flat-top magnet pulse length is limited to being one quarter as long (1s vs 4s). Assuming a NeoAlcator-type of energy confinement law, the ratio of pulse length to confinement time would be about the same. It is interesting to note that the ratio of pulse time to skin time in C-MOD will actually be longer relative to ISP since C-MOD would operate at lower temperature.

1.2.2 Physics Performance

The expected physics performance of C-MOD operating at 7.5 T and 10 T is summarized in a $T-n\tau_E$ plane in Figs 1-3a and 1-3b. The anticipated locus of operation of an ignition device ($Q > 50$) is shown for comparison. These results were obtained from a simple 0-D power balance in which appropriate averaging was performed using profiles of the form

Alcator C-Mod Performance
 $B=7.5\text{ T}, I=3\text{ MA}$

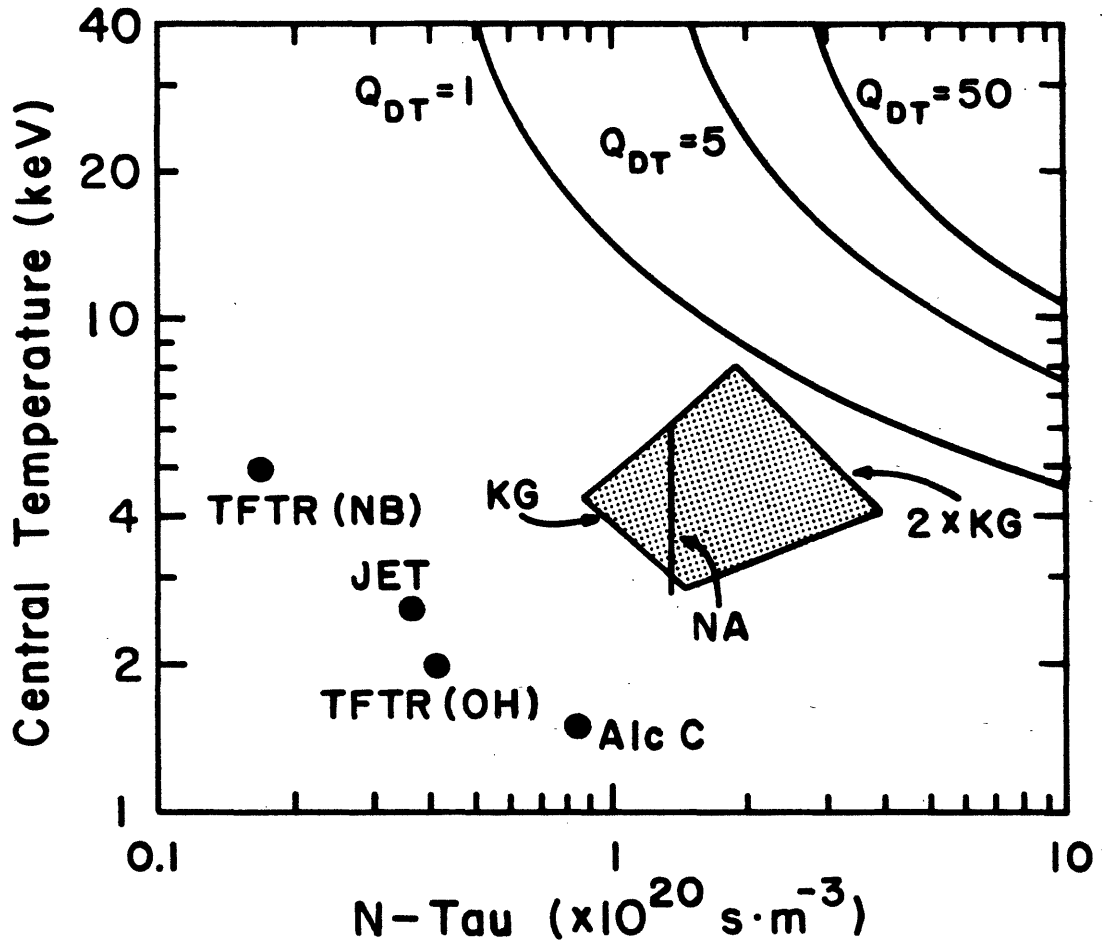


FIG. 1-3a Expected performance of Alcator C-MOD at 7.5 T. The solid lines labeled KG, $2 \times \text{KG}$ and NA correspond to use of Kaye-Goldston, 2 times Kaye-Goldston and NeoAlcator scaling laws, and the auxiliary power varies from 0 to 6 MW along these trajectories.

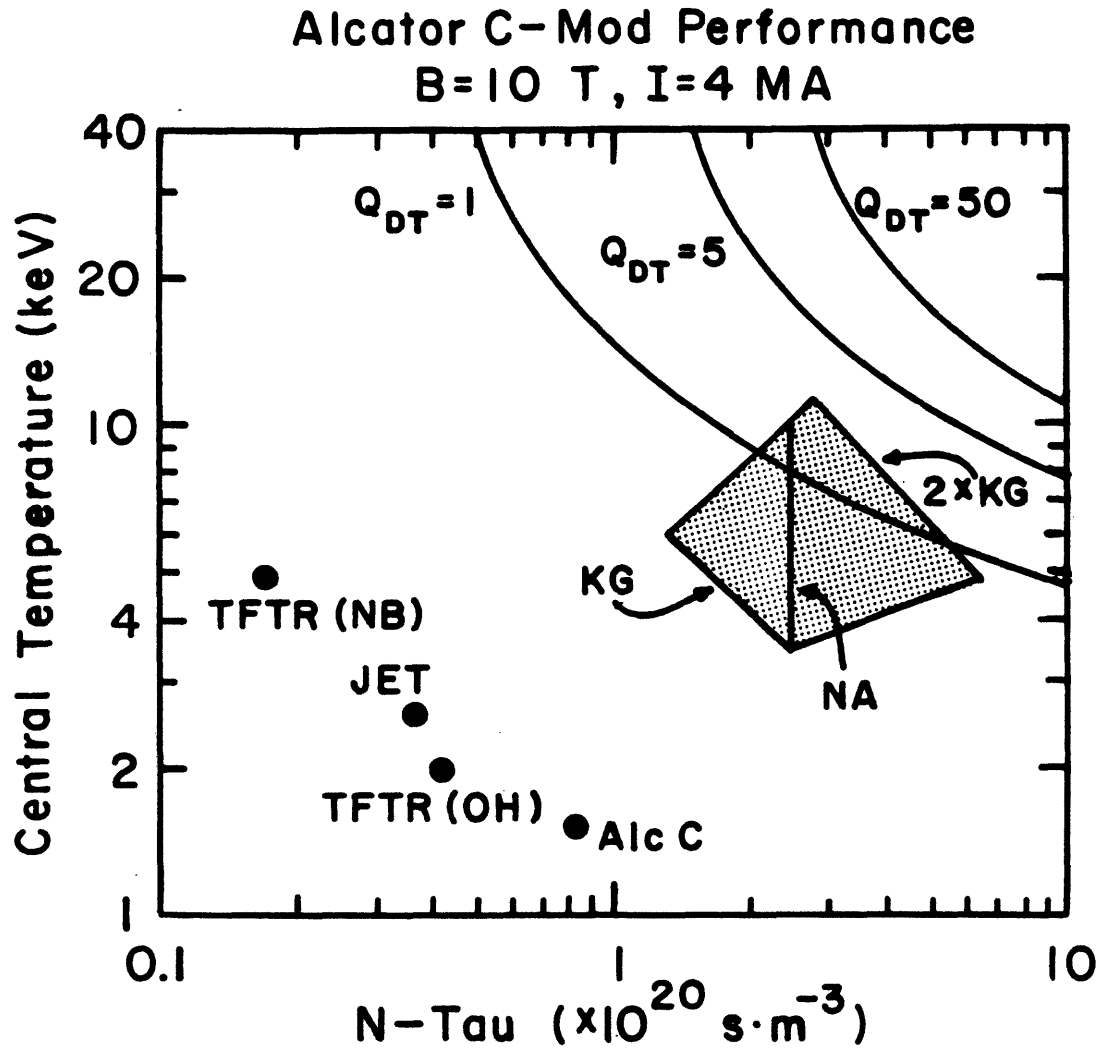


FIG. 1-3b Expected performance of Alcator C-MOD at 10 T. The labels have the same meaning as in Fig. 1-3a, and a maximum auxiliary power of 10 MW (absorbed) is assumed.

$T(r) = T_0(1-(r/a)^2)^{m_t}$ and $n(r) = n_0(1-(r/a)^2)^{m_n}$. The profile indices $m_t = 1$ and $m_n = 0.5$ have been used in Fig. 1-3 and the peak density has been set at the Murakami limit, $n_0 = 0.7$ B/R. The available auxiliary power was assumed to be 6 MW at 7.5 T and 10 MW at 10 T. The performance has been evaluated using NeoAlcator, Kaye-Goldston and twice Kaye-Goldston energy confinement laws. For each model, the lowest temperature corresponds to ohmic heating and the highest to full auxiliary power, i.e., 6 MW @ 7.5 T and 10 MW @ 10 T. The last two confinement laws typify results which may be expected from auxiliary-heated tokamaks and the factor of 2 variation incorporates the anticipated variation arising from the L-mode to H-mode transition. In the absence of the bremsstrahlung loss, a confinement scaling of the form $\tau_E \sim P^{-\gamma}$ where P is the total power results in the $T-n\tau_E$ trajectory - $T\tau_E^\nu = \text{const}$ where $\nu = (1-\gamma)/\gamma$. The high current (4 MA at 10 T) ensures that even L-mode confinement as determined from NBI experiments will lead to plasma regimes comparable to those predicted by the NeoAlcator model.

1.2.3 Magnet Design

The compact ignition devices currently under study require magnet systems which represent an advance in the state-of-the-art beyond the high power density devices represented by the current generation Alcator C and Frascati tokamaks. One of the major goals for the C-MOD device is to model a representative set of the required advanced concepts.

A conceptual design for the C-MOD device has been developed, and is based on the "jointed rectangular coil" concept under study at PPPL for the compact ignition device. This concept uses an external frame to

reduce the tension loads on the TF magnet. When the external frame is combined with sliding joints in the TF coil, it is potentially possible to remove all the tension loads, hence only the radial compression loads remain to limit the magnet design. This offers the possibility of achieving ignition conditions in devices of the 1.5 meter major radius class.

The inclusion of joints in the TF coils opens up another major advantage, namely the ability to remove internal components in a relatively straightforward manner. The vacuum chamber can be made in one piece, and PF coils internal to the TF coil can be used to provide a controllable divertor configuration, and to provide adequate volt seconds. (The same comments apply to the large elongation or small aspect ratio versions of the machine.) The use of these design concepts in Alcator C-MOD will result in a flexible, easily serviced configuration, prototypical of ISP, as well as instrumental to advanced shaping experiments.

1.2.4 RF Heating

The C-MOD will greatly extend the limited RF access available in Alcator C. The device will have 12 horizontal ports of approximately 15 cm width. This access will allow a major physics program to be carried forward on high density RF heating and advanced concepts experiments and facilitate development of antennas for the ignition experiment. Since the C-MOD field will be the same range as in the ignition device, the same frequencies and heating scenarios can be used, for example, minority H with a transition to second harmonic D in the frequency range 120-150 MHz. Ion Bernstein wave heating, e.g. at $3/2 \omega_{CH}$, can also be investigated.

It is proposed to use either the FMIT sources, with the PPPL RF Group carrying a major responsibility for the RF systems in collaboration with MIT, or to use the available FPS-17 radar sources obtained from the U.S. Air Force site at Shemya several years ago. The development of the FMIT sources for use on Alcator C-MOD has the additional advantage that these systems could be transferred to ISP when that device becomes operational. The MIT FPS-17 radar transmitters, with some modification, would be employed to investigate alternative heating schemes, such as ion Bernstein waves at $3/2 \omega_{CH}$, and fast waves at $2 \omega_{CH}$.

1.2.5 First Wall Protection

The high-power-density plasma operation in C-MOD will require development of first wall protection and collectors which will in turn be prototypical of the ignition experiment. Heat fluxes will be comparable with the ignition experiment under the sub-ignited conditions.

The baseline design for Alcator C-MOD employs an expanded-boundary poloidal divertor for controlling plasma edge conditions since present experience world wide indicates impurity control to be a major need in RF-driven plasmas, and the divertor provides the most promising solution. Additional advantage is gained by use of the divertor, as evidenced by the transition to H-mode in NBI-heated discharges. Operation will be compared with pumped limiter operation in order to determine whether or not it will be necessary to install a poloidal divertor in the compact ignition experiment.

1.2.6 Device Flexibility

The use of a fully jointed TF magnet concept in C-MOD can add a great deal to the future flexibility of the device. After removal of the upper support structure, the upper TF legs can be removed, allowing the central TF core to be removed. Different PF coil sets and TF cores could then be installed to allow alternate magnetic configurations. For example, replacement of the inner TF leg would allow an elongation of $\kappa = 3$ but at lower aspect ratio, $A < 3$. Installation of a strong bean-shaping coil is also easily accomplished. (Mild indentations are already permitted in the baseline load assembly.) By substitution of an alternate central TF leg, a very low aspect ratio ($A = 1.7$) plasma with a central field of 1.5 T could be generated. Thus, after the major mission of support to the ignition experiment has been fulfilled, the flexibility of Alcator C-MOD permits rapid reorientation toward the tokamak concept improvement area.

1.3 Baseline and Extended Performance Options

Two basic design options are presently under consideration for Alcator C-MOD. In the first, the 225 MVA alternator donated to the Plasma Fusion Center for use in Alcator C, remains as the primary energy source. Some overspeeding, either by means of a gear box or inverter variable-speed drive system, will be added so that a total energy of about 350 MJ can be extracted. This results in a maximum field capability of 7.5 T and would yield, for example, the performance shown in the shaded region in Fig. 1-3a. The RF heating required for this option would be supplied by the Shemya sources, acquired from the Air Force several years ago, and presently being used for ICRF experiments on Alcator C. This baseline option will cost \$17 M in materials, engineering, fabrication and installation

costs and, as will be shown in Chapter 7, can be accommodated on a fixed Alcator C program budget over the next three fiscal years, FY '86-FY '88. Operation of the baseline device would commence at the beginning of FY '89.

In the second option, a new rotating machine would be added to the PFC resources, and a maximum energy approaching 1 GJ could be extracted for use in Alcator C-MOD. The maximum field capability could then be 10 T and the improved performance shown in Fig. 1-3b would be expected. Significantly longer pulses would also be permitted at the 7.5 T maximum field of the baseline option. The Shemya sources may no longer be useful for heating at 10 T (depending on the success of the Bernstein wave technique at $1.5 \omega_{ch}$) and consequently additional ICRF power would need to be deployed. At present, we are considering use of several FMIT transmitters which would be modified for this purpose under a collaboration with PPPL. The cost of this extended performance option would be approximately \$22 M not including RF power. It is impractical to attempt to bear this cost on a flat Alcator program budget.

At the present time, negotiations are underway with the U.S. Air Force which has expressed interest in installing a new rotating machine at MIT with stored energy well-matched to the extended performance needs of Alcator C-MOD. Should these negotiations prove successful, it will become possible to build a device with extended performance capability within the constraint of a flat Alcator operating budget. The construction timetable in this case is still expected to be three years.

CHAPTER 2

PLASMA PHYSICS CONSIDERATIONS

2.1 Introduction

As an upgrade to the highly successful Alcator C device, Alcator C-MOD provides improved access and impurity control as well as advanced shaping capabilities which permit higher currents than are attainable on the present device. These enhancements are expected to lead to improved plasma performance in terms of absolute parameters, such as total pressure, confinement time, and $n\tau T$ and to permit study of relevant phenomena in novel regimes of tokamak operation.

The physics program on Alcator C-MOD is aimed at extending the tokamak database in the areas of transport, RF heating, MHD stability and impurity control. The operating regimes in which these studies will be carried out are close to those characteristic of ignited plasmas and represent an appreciable advance over present experiments. The full-field parameters selected for Alcator C-MOD ($B^2 a\kappa^{1/2} > 30$) offer the potential of ohmic confinement times in excess of 200 msec and $n\tau_E > 10^{20} \text{ sec-m}^{-3}$. The relatively small aspect ratio and large elongation permit high current operation ($I_p > 4 \text{ MA}$) and consequently good confinement is expected even for strongly auxiliary heated plasmas. Standard L-mode scalings, e.g. Kaye-Goldston, predict confinement times similar to the ohmic values, while H-mode scalings correspond to larger than neo-Alcator confinement times. The initial RF heating system (baseline case) provides up to 6 MW of ICRF, which, even for L-mode confinement, is sufficient to produce plasma pressures above 3 atmospheres (stored energy of order 1 MJ) with central temperatures in the range of 5 to 10 keV and density $\bar{n}_e \sim 5 \times 10^{20} \text{ m}^{-3}$.

Tokamak transport in this parameter regime, characterized by high pressure at rather low β_p , is essentially unexplored experimentally, and extrapolations from the present empirical scalings are highly uncertain. The database for transport in auxiliary heated plasmas is drawn primarily from neutral beam injection experiments in which the confinement degrades significantly from the ohmic level. The confinement time is generally found to decrease with increasing heating power, so that the stored energy increases approximately as the square root of the power, rather than linearly. Similar effects have been observed in RF heated plasmas. In the present case, the standard scalings derived from this database (e.g. Kaye-Goldston) predict confinement times larger than the neo-Alcator ohmic value; roughly speaking this is due to the relatively high ratio of current to plasma density characteristic of C-MOD operation. In present experiments this condition holds only for somewhat downgraded operating parameters, for example with Murakami parameters well below the density limit.

The actual behavior of confinement, and therefore the plasma parameters obtained in Alcator C-MOD, will depend on the physics underlying the presently observed behavior, i.e., the mechanism through which transport appears to depend on input power. One possibility is that transport in auxiliary heated discharges is driven by resistive MHD turbulence, so that the relevant parameter is not power as such but β_p or the normalized pressure gradient. It has also been suggested, by Ohkawa, that the power density drives turbulence through distortions of the velocity space distribution function, leading to enhanced transport. In this case the parameter of interest is of the form (P^*/nT_{ve}) , where P^* is the effective power density contributing to distortion of the electron distribution

function. Recently, considerable attention has been focused on the interpretation of the observation that temperature profiles tend to retain a canonical shape, independent of the auxiliary power deposition profile. This "Principal of Profile Consistency" may be related to the current density profile, for example as a manifestation of the stability criterion for tearing modes, or it may arise from a dependence of the thermal diffusivity on temperature or pressure gradients. The Alcator C-MOD experimental program will have as a principal focus the clarification of these physics questions.

The principal heating technique to be employed on Alcator C-MOD will be RF in the ion cyclotron range. This technique is also presently favored for near term ignition experiments and will be employed on several existing experiments, including ASDEX, JET and JT-60. The unique features of the ICRF heating experiments on Alcator C-MOD arise from the high target plasma density ($\bar{n}_e > 5 \times 10^{20} \text{ m}^{-3}$), toroidal field ($7 < B_T < 10 \text{ T}$), and average power density (3-5 MW/m³). While our understanding of the physics of ICRF heating has grown significantly over the past decade, the experimental database is, with the exception of low power experiments on Alcator C, restricted to much lower fields and densities. The coupling to the plasma and the evolution of non-thermal distribution functions may be expected to differ markedly from lower density experiments.

ICRF heating on Alcator C-MOD will be carried out using both the fast wave, interacting at either the majority species second harmonic or at the fundamental resonance of a minority ion component, and the ion Bernstein wave. In the case of fast wave heating, the antenna must be designed to launch the waves with k_z sufficiently large to avoid mode

conversion losses, but small enough not to reduce k_{\perp} , since the damping mechanism for the fast wave is a finite Larmor radius effect. The port width in Alcator C-MOD has been designed to accommodate either loop or coupled cavity type antennas which satisfy this requirement. Ion tail formation may occur in the majority species in the case of second harmonic heating or in the minority for fundamental damping. While the presence of a high-energy tail leads to increased damping for the wave, it may also be detrimental in terms of increased losses, transport degradation, and impurity generation. The wide range of power density and collisionality accessible in Alcator C-MOD will enable us to investigate these effects in detail.

In the case of Ion Bernstein Wave heating, short wavelength electrostatic waves with a frequency corresponding to an odd half-harmonic of the gyrofrequency of the majority species are absorbed by either linear or non-linear cyclotron harmonic damping near the plasma center. Since $\omega/k_{\perp} \sim v_{T1}$, the bulk of the distribution is heated and no ion tail formation is expected. Since the desired wave polarization at the launcher is $E \parallel B$, as in the case of lower hybrid heating, waveguide launchers may be employed. A limited amount of experimental work with this technique has been carried out at low power and density on PLT and JIPP-T-II-U, and higher density experiments are in progress on Alcator C. In the former cases, the results support the interpretation that non-linear effects are responsible for the absorption. High power density experiments on Alcator C-MOD will increase the understanding of the physics and determine the suitability of this attractive technique for advanced experiments.

As has been mentioned, a major advance in Alcator C-MOD relative to Alcator C is the incorporation of elongated D-shaped plasmas. This feature, together with the reduction in aspect ratio from 3.9 to 3, allows C-MOD to operate with much higher currents and I/aB values than its predecessor while retaining comparable values of B/R . In addition, the design incorporates a poloidal divertor capability for impurity control and as a tool for influencing the edge parameters and transport. The role of elongation and shaping on plasma stability and transport remains an important issue in the understanding and optimization of tokamak performance. The Alcator C-MOD design provides sufficient flexibility to investigate these effects systematically. One aspect of these studies will involve the relative importance of elongation and aspect ratio in both confinement and stability, which will lead to improved configurations for advanced tokamak experiments.

Despite the demonstration of very high $n_0\tau_E$ values on Alcator C, the limits of ohmic tokamak plasma performance are still unclear. In the case of Alcator C, neoclassical ion thermal transport limits confinement at the highest accessible densities and currents. This limit turns out to be similar to that which might be predicted for H-mode scaling, taking the total power equal to the ohmic power. In the case of Alcator C-MOD, on the other hand, the higher poloidal field and reduced collisionality results in relatively larger values of the neoclassical ion confinement time. Moreover, for full-field operation the central current density, which scales as $(B/R)(\kappa + \kappa^{-1})$, is similar to the highest values in Alcator C and essentially equal to those of proposed high field ohmic ignition experiments. Results on Alcator C-MOD should therefore be highly relevant

to the question of ohmic tokamak performance limits and the prospects for pure ohmic ignition.

In the remainder of this chapter we present more detailed discussions of anticipated plasma parameters, RF heating physics, MHD equilibria and stability, and divertor and limiter design for the baseline configuration. In addition we present some results of calculations pertaining to full-field (10 Tesla) operation and alternate geometries related to the concept improvement aspects of the Alcator C-MOD program.

2.2 Plasma Parameters - Transport Calculations

2.2.1 0-D Modeling

We have carried out 0-D confinement modeling in order to obtain a first approximation estimate of the parameter range of the Alcator C-MOD plasmas. In this section we present results for both ohmic (neo-Alcator) scaling and H- and L-mode auxiliary heating scalings, for both baseline and extended full-field operation.

The form of the neo-Alcator scaling employed in these calculations is

$$\tau_E^{NA} = 1.9 \times 10^{-21} n_R^{2.04} a^{1.04} \kappa^{0.5}$$

which is identical to the original formulation [2.2-1] with the exception of the dependence on elongation κ . The favorable linear dependence on q reported by TFTR [2.2-2] and JET [2.2-3] is not included, consistent with experimental results on Alcator C for $q > 3$. It may be expected that actual confinement will be somewhat reduced at lower q values due to sawtooth effects.

To estimate the possible degradation in confinement at elevated power density (or $\epsilon\beta_p$), we have adopted the Kaye-Goldston expression [2.2-4]

$$\tau_E^{KG} = 0.55 I_p^{1.24} (MA) B^{-0.09} (T) \bar{n}^{-0.26} (10^{20} m^{-3}) R^{1.65} a^{-0.49} \kappa^{0.28} P_{tot}^{-0.58} (MW)$$

The above regression fit was derived from L-mode neutral beam discharges and has been observed to be consistent with ICRF results on several machines. For possible H-mode operation we have taken the rather crude estimate $\tau_E^H = 2\tau_E^{KG}$.

In these 0-D scalings we have not taken account of ion heat conduction losses, which are in fact found to be important in high density Alcator C discharges. However in the present case this omission may be justified a posteriori from the observation that, for typical operating conditions, e.g. $\bar{n} = 5 \times 10^{20} m^{-3}$, $I_p = 2$ MA, $B = 7.5$ T, the neoclassical ion confinement time is a factor of order five or more greater than τ_E^{NA} and exhibits a scaling with current similar to that of Kaye-Goldston. On the other hand, anomalous ion transport with a scaling different from neoclassical, as suggested by the Alcator C experiments, could significantly impact the global confinement. Ion transport is, of course, explicitly considered in the 1-D simulations described in the following section.

The operating space for Alcator C-MOD, in terms of the $(1/q)$ vs (nR/B) (Hugill) diagram is estimated on the basis of Alcator C experiments. Thus, we take the density limit to be given by

$$nR/B \leq \min[0.6, 1.6/q_c]$$

where the value 0.6 corresponds approximately to the maximum Murakami

parameter obtained on Alcator C with pellet injection. For our baseline parameters the density limit is then approximately $6 \times 10^{20} \text{ m}^{-3}$. Based on experience on Alcator C and other devices we may conservatively estimate the current limit to be given by $q_\psi > 2.5$ for limiter discharges and $q_\psi > 3$ for divertor or expanded boundary operation. For the baseline configuration these limits correspond to approximately 4 MA and 3.3 MA respectively.

In Figs 2.2-1 and 2.2-2 we depict the scaling of global energy confinement time for the baseline configuration as a function of total density and current for neo-Alcator and Kaye-Goldston scaling laws. We note that the H-mode scaling, as defined above, always exceeds the neo-Alcator value by a significant factor. If we assume that the total confinement will be given by some combination of the empirical scalings, the stored energy should vary roughly as indicated by the lower dashed line in Fig. 2.2-3, if L-mode scaling is appropriate, and be essentially equal to the neo-Alcator prediction if H-mode obtains. The total power available in the baseline configuration

$$P_{\text{tot}} = \eta P_{\text{RF}} + P_{\text{OH}} \approx 6 \text{ MW}$$

where the source power from the FPS-17 transmitters is $P_{\text{RF}} \approx 6 \text{ MW}$, the transmission and coupling efficiency $\eta \approx 0.7$, and P_{OH} for the parameters shown is of the order of 2 MW.

If we assume a Gaussian profile for the electron and ion temperatures we can estimate

$$\langle n(T_e + T_i) \rangle \approx \bar{n} \langle T_e + T_i \rangle \approx \alpha \bar{n} (T_{e0} + T_{i0})$$

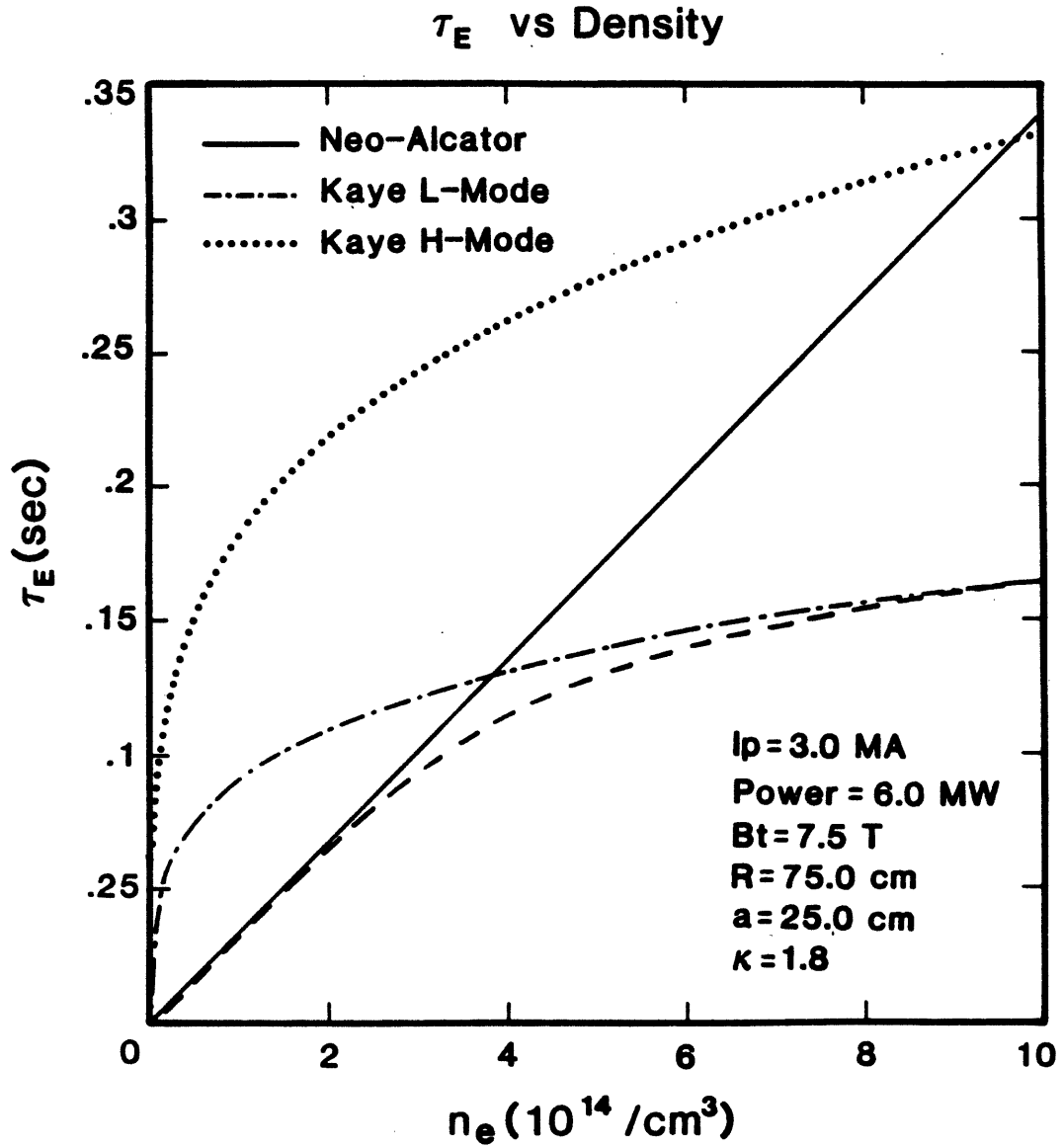


FIG. 2.2-1 Global confinement time as a function of density for baseline configuration of Alcator C-MOD. For L-mode scaling the effective confinement may be expected to follow the lower dashed curve.

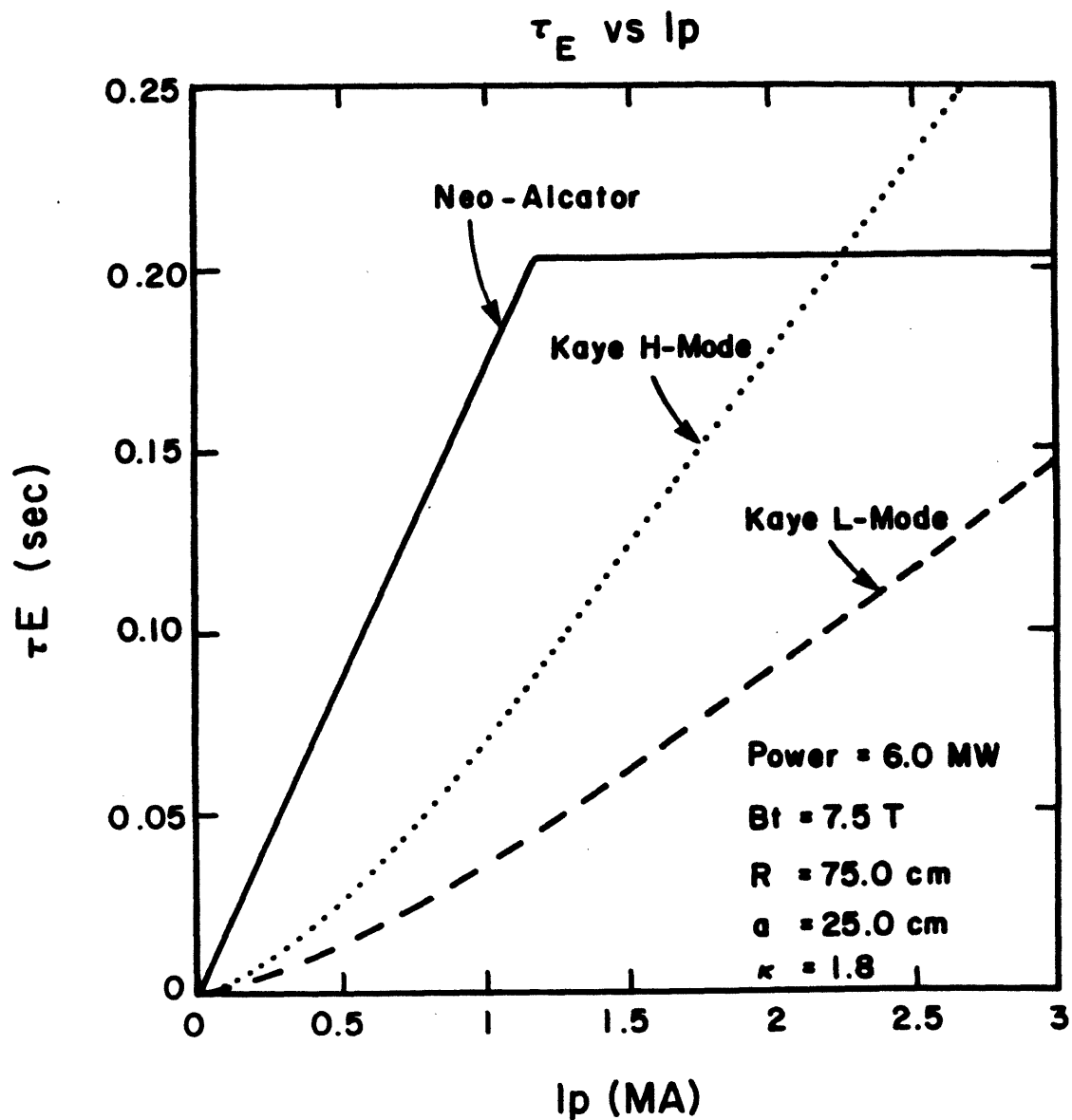


FIG. 2.2-2 Global confinement time as a function of plasma current for the baseline configuration, with density limited by the constraint on the Murakami parameter.

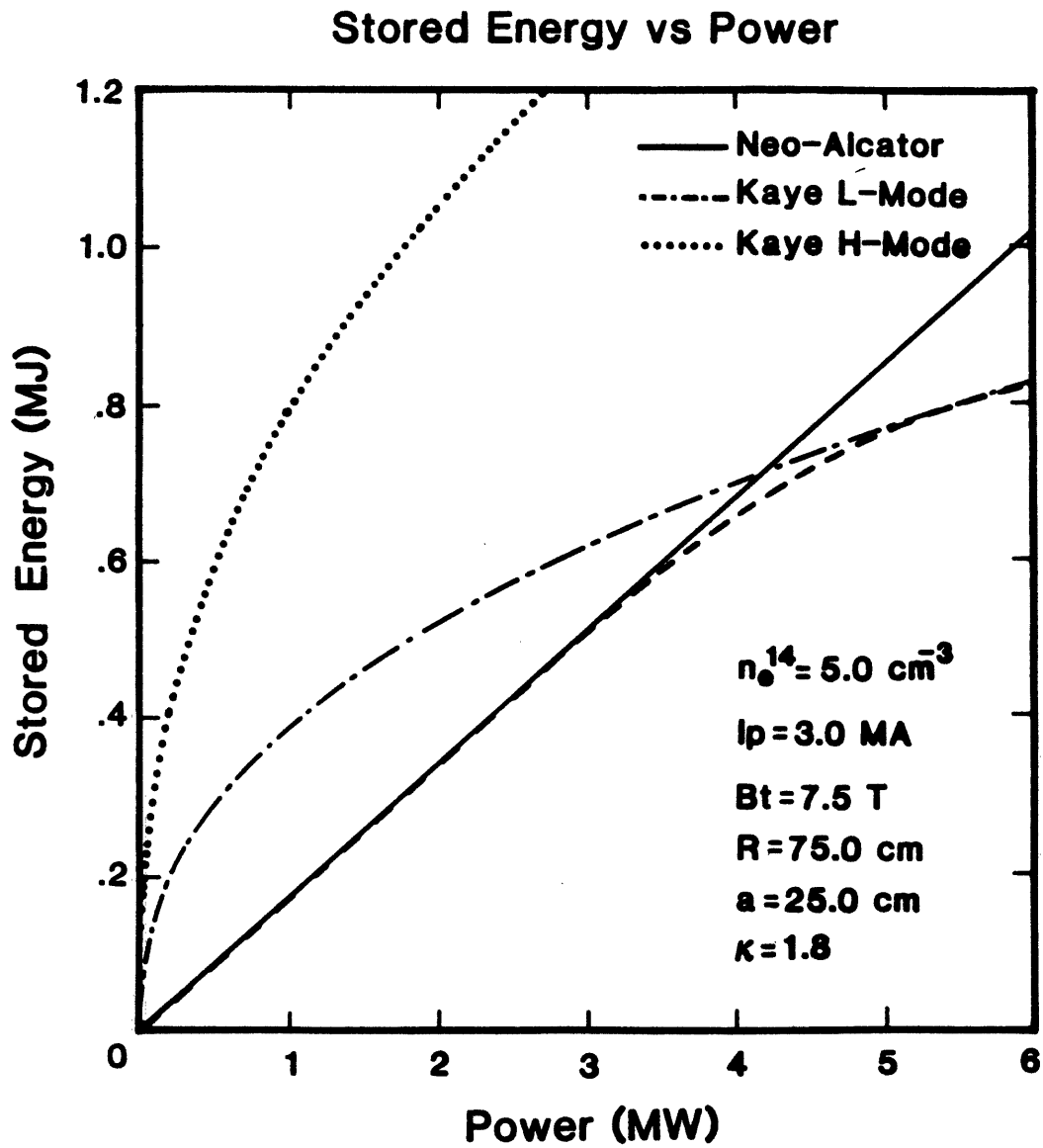


FIG. 2.2-3 Plasma stored energy as a function of total input power for typical Alcator C-MOD parameters, with different transport assumptions.

where

$$\alpha = \frac{\langle T_e + T_i \rangle}{T_{e0} + T_{i0}} \approx \left(\frac{a_T}{a} \right)^2 \approx 1.5 \frac{q_0}{q_a}$$

and a_T is the gaussian width of the temperature profile and q_a is the edge safety factor. We may then estimate the operating temperature from the stored energy as

$$kT_0 \approx \frac{1}{3\alpha} \frac{1}{\pi} \frac{W}{V}$$

where $W = P_{TE}$ is the plasma stored energy and $V \approx 2\pi^2 R a^2 \kappa$ is the plasma volume and we assume $T_{e0} = T_{i0} = T_0$. For the conditions of Fig. 2.2-3, we predict central ion temperatures between 5 and 7 keV with line average density of $5 \times 10^{20} \text{ m}^{-3}$ and 6 MW total input power.

Enhanced performance can be achieved in Alcator C-MOD by installation of a new alternator, permitting the toroidal field to be increased to 10 Tesla, and by use of the FMIT RF sources, with a total power of 10 MW. The 10 Tesla option is discussed in Appendix A, and the FMIT sources are described in Section 2.5 of this chapter. Here we present the predictions of the 0-D scaling models for this operating scenario. Again taking approximately 70% coupling and transmission efficiency for the RF and of the order of 1 MW residual ohmic power, we find that L-mode scaling would begin to dominate at a density of $\bar{n}_e \approx 5 \times 10^{20} \text{ m}^{-3}$. As can be seen from Figs 2.2-4 and 2.2-5, the stored energy under these conditions should exceed 1.3 MJ, corresponding to a plasma pressure of approximately 5 atmospheres at a confinement parameter $\bar{n}_e \tau_E \approx 10^{20} \text{ m}^{-3} \text{ sec}$. These values lie above the thermalized breakeven curve on the Lawson diagram,

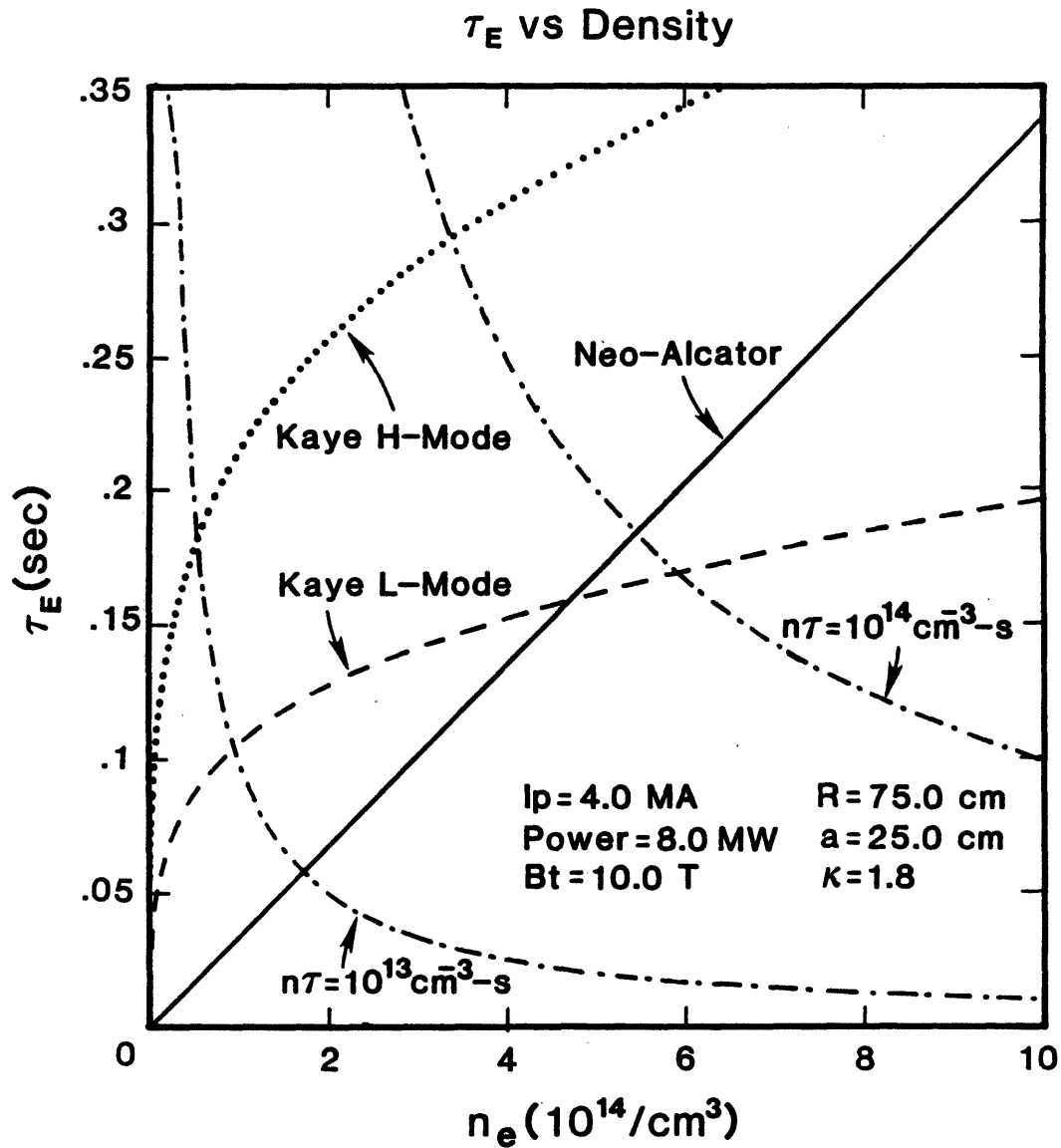


FIG. 2.2-4 Global confinement time as a function of density for full-field operation of Alcator C-MOD. Contours of constant Lawson parameter are shown by the double dashed lines.

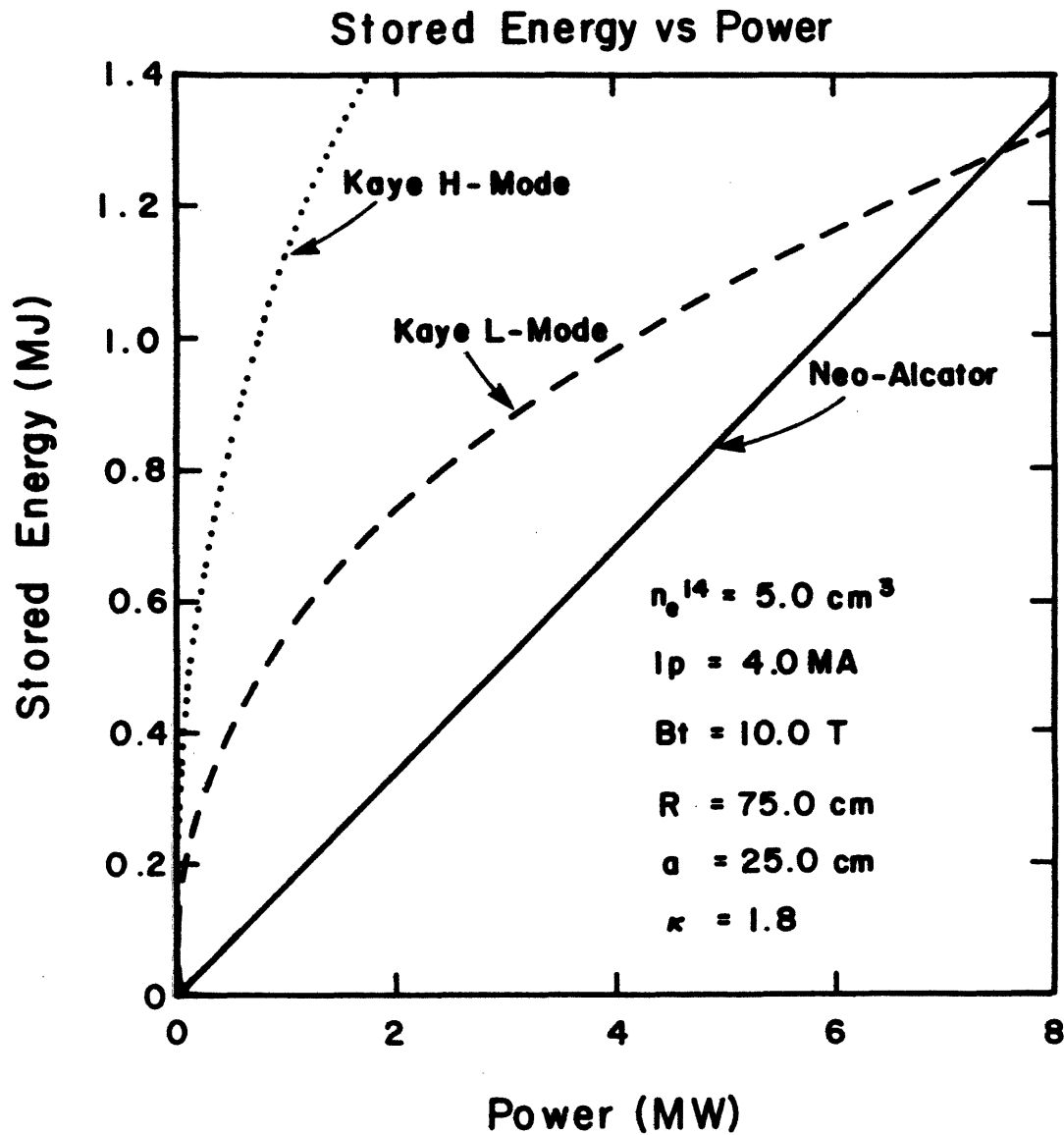


FIG. 2.2-5 Stored energy as a function of input power for parameters typical of full-field operation of Alcator C-MOD. For these parameters, the L-mode and neo-Alcator predictions coincide at the highest power.

with equivalent Q values near 2, in excess of the performance predicted, by the same models, for JET, JT-60, or TFTR. If H-mode scaling is obtained, still higher parameters may be expected as we increase the density to the Murakami limit. At a line-averaged density of $8 \times 10^{20} \text{ m}^{-3}$, neo-Alcator scaling predicts a pressure of 8 atmospheres and $\bar{n}_e \tau_E > 2 \times 10^{20} \text{ m}^{-3} \text{ sec}$.

It is worthwhile to note that there are large uncertainties in projections based on these empirical scaling formulas. The ohmic confinement scaling employed here is consistent with experimental results from Alcator C at similar fields and densities, and the geometric scaling appears to be well founded, with the possible exception of the κ -dependence. Nevertheless, there remain some discrepancies with other experiments, notably the strong dependence on safety factor observed on the large tokamaks TFTR and JET. In the case of the L and H-mode scalings, the extrapolation to our parameters is greater and the level of confidence consequently reduced. We may for example, compare the predictions of the earlier Goldston L-mode scaling [2.2-5], based on a similar but more restricted database and employing slightly different methodology:

$$\tau^G = 0.037 I_p(\text{MA}) \kappa^{0.5} R^{1.75} a^{-0.37} P_{\text{tot}}^{-0.5}.$$

While the two L-mode scalings agree quite well in the regimes for which they were derived, they differ by more than a factor of two when extrapolated to typical C-MOD operating parameters. The major discrepancies between the two expressions involve the dependence on density and current density, which are the quantities requiring the largest extrapolation from the original auxiliary heating database.

An additional uncertainty arises from the method by which we combine the scaling laws in the "transition" region, assuming that L-mode scaling (or Goldston H-mode) holds. Goldston has suggested, on purely empirical grounds, that the transition is best fit by a quadrature sum

$$\left(\frac{1}{\tau_E}\right)^2 = \left(\frac{1}{\tau_E^{NA}}\right)^2 + \left(\frac{1}{\tau_E^{AUX}}\right)^2$$

while a straightforward interpretation in terms of independent diffusion coefficients would imply

$$\frac{1}{\tau_E} = \frac{1}{\tau_E^{NA}} + \frac{1}{\tau_E^{AUX}}$$

and a model based on most efficient removal of free energy might suggest

$$\tau_E = \min[\tau_E^{NA}, \tau_E^{AUX}]$$

In sketching the dashed curves in the transition regions of the preceding figures, we have essentially taken the latter interpretation, which also produces the most optimistic prediction. The purely diffusive assumption would lead to maximum confinement times which were lower by about a factor of two. However such an assumption severely underestimates the maximum confinement times observed in ohmic discharges in Alcator C, as in fact does the Goldston prescription if neoclassical ion losses are also taken into account. The actual experimental results will provide a good experimental test of this issue, and therefore yield information about the linearity of the transport mechanism.

2.2.2 1-D Simulations

While the steady-state 0-D modeling described above serves to estimate the parameter range to be expected, 1-D modeling has been also been employed to investigate profile and time-dependent effects, and to more clearly delineate the effects of different transport assumptions and engineering constraints. Simulations were carried out using the ONETWO code [2.2-6]; all the results reported here have been obtained using the purely 1-D section of the code with elliptical flux surfaces.

There is at present no consensus on the appropriate form for local transport coefficients in tokamak plasmas. As indicated above, the fundamental mechanisms responsible for anomalous transport are unknown. Further, theoretical treatments of the different possibilities (e.g. drift mode turbulence, resistive MHD activity, etc.) are in general unable to predict absolute magnitudes for the diffusivities arising from various instabilities, but can indicate scalings with experimental parameters. Alternatively, purely empirical values of the transport coefficients may be extracted from analyses of experimental data, and then examined for consistency with fundamental theoretical constraints. In applying any of these transport coefficients in a predictive manner, it is important to recognize that the results may have even less relevance to the real world than those of global 0-D scaling laws. Our principal purpose in carrying out such 1-D simulations is to investigate phenomena which are explicitly time and/or space dependent, and as far as possible to compare the implications of different assumptions regarding unknown physics. We may therefore evaluate, on the one hand, the extent to which our design is optimized to be insensitive to the physics uncertainties, and on the other, our

ability to conduct experiments which may help distinguish between different mechanisms and thereby remove the uncertainties.

Our basic transport model assumes an ohmic transport contribution of the neo-Alcator form

$$\kappa_e^{NA} = n_e \chi_e^{NA} = 5.0 \times 10^{20} r/R^2 + n_e \chi_e^{NC} \quad (1)$$

where χ_e^{NC} is the neoclassical electron thermal diffusivity, which is negligible compared with the anomalous contribution except near the axis, where sawtooth activity is typically dominant. This expression is purely empirical, and has been found to be consistent with experimental results on Alcator C and other tokamaks during the ohmic heating phase. The time-averaged effect of sawteeth on electron and ion transport have been modelled by addition of an effective thermal diffusivity in the $q < 1$ region of the form

$$\chi_e^{Saw} = D_b \left(1 - \frac{1}{1 + (1/q - 1)^2} \right).$$

Alternatively the sawteeth are modelled explicitly, with an internal disruption triggered either by the decrease of q_0 below some value, typically .95, or by the calculated width of the $m=1$ island. The resistivity is taken to be neoclassical, as suggested by recent JET results [2.2-7].

As one model of the degraded transport observed in auxiliary heated discharges, we have taken an anomalous thermal conductivity of the form

$$\kappa_e^{Aux} = 5.0 p^{1.0} n_e^{0.8} r^{0.4} B_T^{-2} q^{2.2} \epsilon (|\lambda_p|) (|\lambda_q|)^{-1} \quad (2)$$

where $p = n_e T_e + n_i T_i$ is the local pressure in units of keV/cm³, ϵ is the

inverse aspect ratio, $\lambda_p = (r/p)(dp/dr)$, and λ_q is the shear parameter $\lambda_q = (r/q)(dq/dr)$. This expression is consistent with transport associated with pressure gradient driven, shear stabilized MHD activity and is identical to that suggested by Singer, et al. [2.2-8], except for a weaker dependence on shear. While the scalings are based on theoretical considerations, this expression is also empirical. The dependence on pressure and current are such as to at least qualitatively mimic the Goldston or Kaye-Goldston scalings, and the magnitude is essentially that used by Singer to model PDX and ASDEX neutral beam discharges. In applying this model, the total electron thermal conductivity is taken to be the sum

$$\kappa_e^{eff} = \kappa_e^{NA} + \kappa_e^{Aux} \quad (3)$$

Since the additional transport is assumed to be driven by plasma pressure, rather than by differences in the heat source, this expression is applied during both the ohmic and RF heating stages of the discharge.

An alternative model for the anomalous electron transport, based on drift wave turbulence rather than resistive MHD, is that suggested by Perkins [2.2-9]. The turbulence is assumed to be responsible for transport in the region between $q=1$ and $q=2$. Expressions for the thermal diffusivity in the collisional and collisionless regimes are given by

$$\chi_1 = C_1 \frac{3T_e^{3.5} c^2 m_e^{0.5}}{4(2\pi)^{0.5} e^6 B^2 n(Z \ln \Lambda)} \left(\frac{r}{R} \right)^{1.5} \left(\frac{1}{n} \frac{dn}{dr} \right)^2$$

and

$$\chi_2 = C_2 \frac{3T_e^{1.5} M_i^{0.5} c^2}{e^{2B^2}} \left(\frac{r}{R} \right)^{0.5} \left| \frac{1}{n} \frac{dn}{dr} \right|$$

which are combined in the form

$$\chi_e^{\text{Perkins}} = (\chi_1^{-2} + \chi_2^{-2})^{-1/2} \quad (4)$$

Here the forms for the two terms are derived from theory, but the coefficients $C_1 = 3$ and $C_2 = 0.5$ have been obtained by normalizing to experimental results, principally from PLT and TFTR. The transport inside the $q=1$ surface is given by our usual sawtooth models, while the region outside $q=2$ is taken to have enhanced transport. In this model, the same physics is assumed to be responsible for transport in both the ohmic and auxiliary heated regimes, with the observed differences in scaling being explained by the transition from the collisional to the collisionless regime. In applying this model we therefore use only the single expression for χ_e^{Perkins} given above, with additional terms for $q < 1$ and $q > 2$ serving to constrain the overall shape of the profile.

In our basic model, we assume an ion transport given by 3 times the Chang-Hinton neoclassical value, plus additional terms due to toroidal field ripple. For the low ripple in Alcator C-MOD we find that these terms make no significant contribution to transport. In addition we can compare results with one times neoclassical ion thermal diffusivity, as demonstrated on Alcator C with pellet fueling.

In Fig. 2.2-6 we show results of several 1-D simulations for confinement as a function of density in the baseline configuration. The RF power is assumed to be deposited uniformly within the 60% radius, with

Global Confinement Time

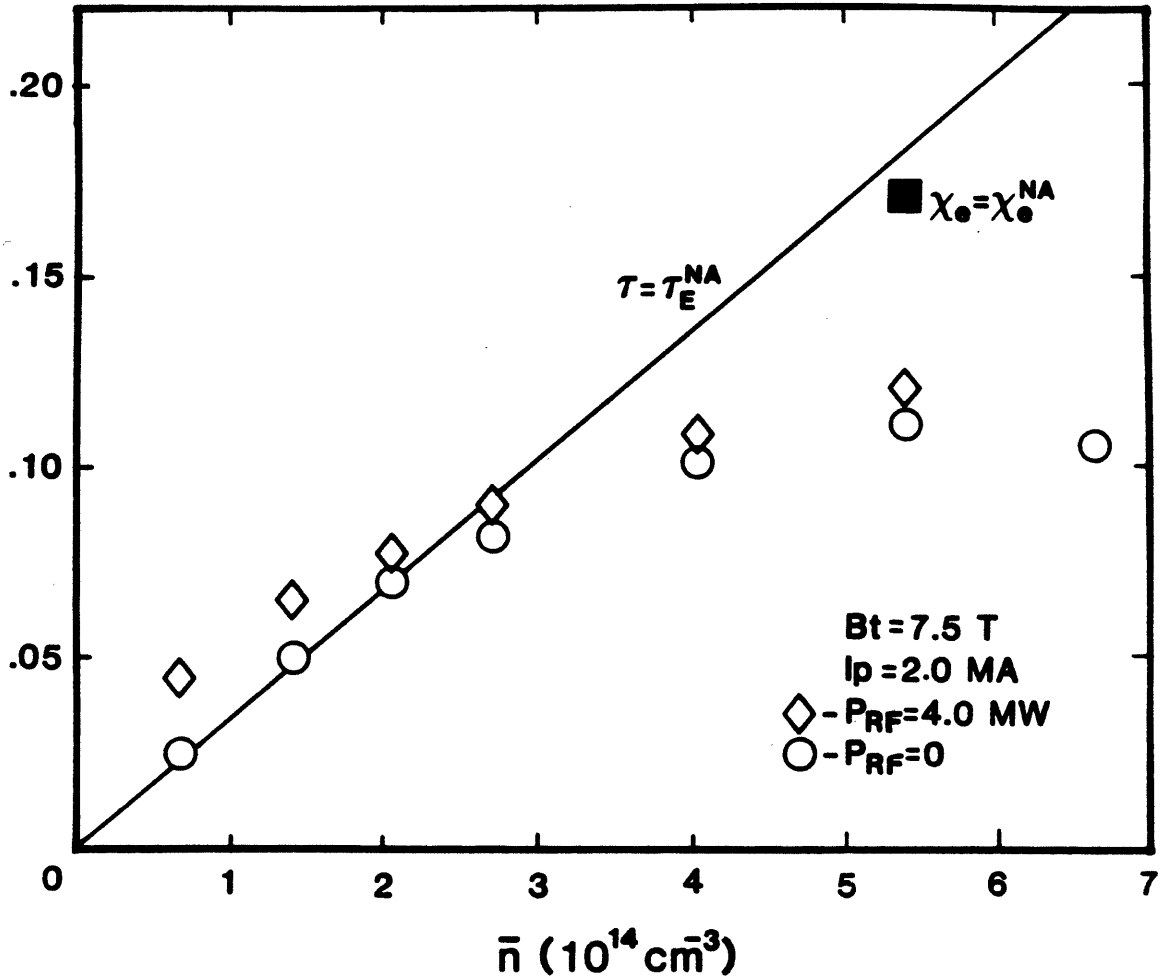


FIG. 2.2-6 Global confinement times derived from 1-D simulations including a pressure dependent χ_e and 3 times neoclassical ion thermal conduction. Open circles correspond to ohmic operation and diamonds to 4 MW of ICRF. The straight line is the prediction of the 0-D neo-Alcator scaling, with no correction for finite ion losses. The box represents a calculation with neoclassical ions and χ_e given only by the neo-Alcator expression (Eq.(1)).

90% going to ions and the remainder to electrons. Results from the model of Eq. (3) described above are fairly consistent with the 0-D modeling of the last section. At the higher density the ohmic discharge is in fact somewhat limited by our assumption of 3 times neoclassical ion losses and more importantly by the finite pressure driven term, while in the RF cases the pressure dependent χ_e^{Aux} becomes dominant over much of the profile. However, because of the assumed power deposition profile, the global confinement times actually improve slightly in the RF phase relative to the ohmic target, although the local electron thermal conductivity at the half-radius increases. This result emphasizes the difficulty of comparing the scaling of global confinement with that of the local transport coefficients. Calculated profiles of κ_e and κ_i for a typical case are shown in Fig. 2.2-7. For comparison a high density point calculated with the pressure dependent term χ_e^{Aux} removed and with ion losses reduced to 1 times neoclassical is also shown in Fig. 2.2-6. In this case, the confinement approximates the 0-D neo-Alcator result, as expected. Ion and electron temperatures for the standard assumptions and 4 MW of RF are shown in Fig. 2.2-8. At the lower densities the ion temperature significantly exceeds that of the electrons, accounting for the increased global confinement time in these cases.

Due to the short pulse length available on Alcator C-MOD, it is important to consider the poloidal field diffusion during the current rise phase, in order to assure that a quasi-steady state equilibrium is attained during the heating pulse. In Fig. 2.2-9, we show the evolution of the temperature and current density during a 1.5 second magnet flat-top for the baseline configuration ($B_T = 7.5$ T, $I_p = 2.5$ MA). For this simulation, the sawteeth are explicitly modelled, with an internal disruption

Electron and Ion Thermal Conductivities

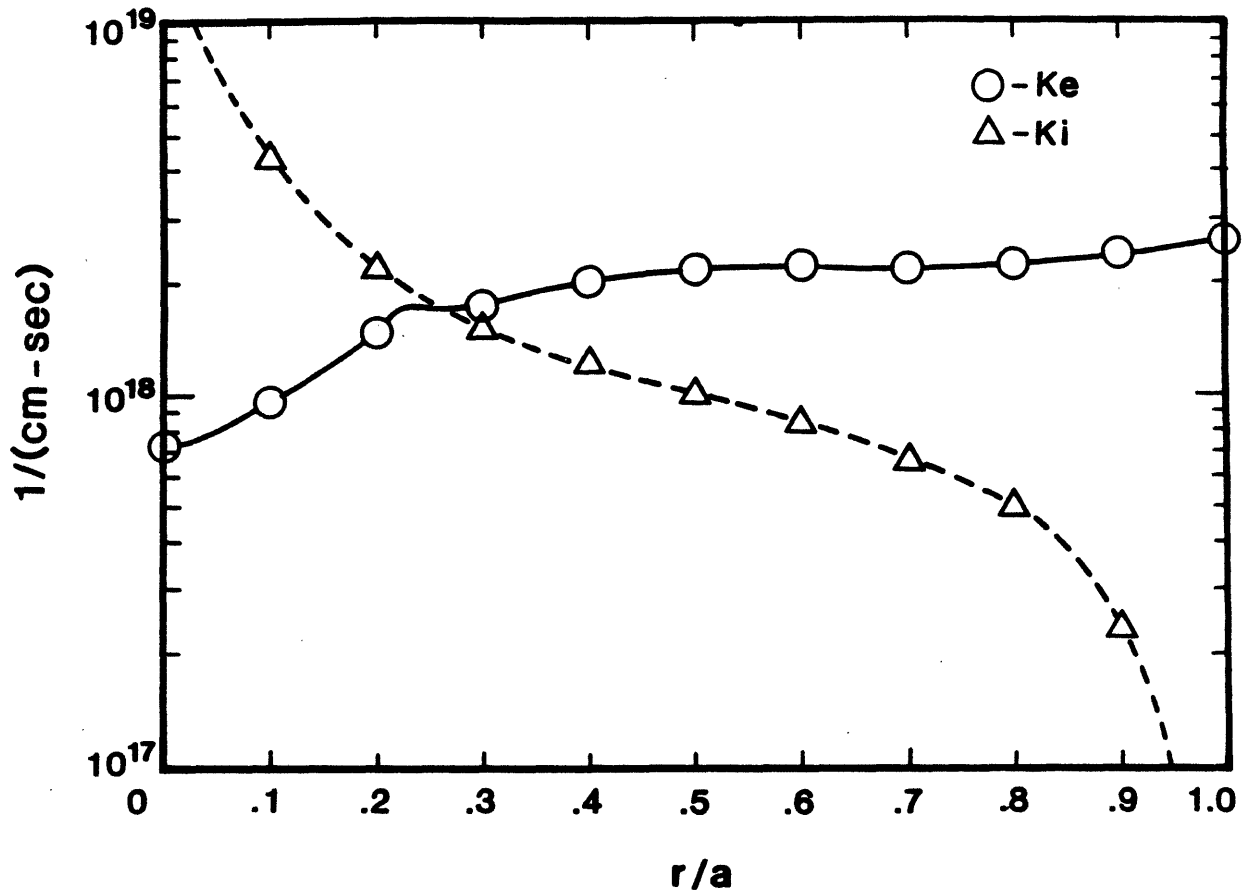


FIG. 2.2-7 Electron and ion thermal conductivities as a function of radius for $\bar{n}_e = 5.4 \times 10^{14} \text{ cm}^{-3}$, $I_p = 2 \text{ MA}$, $B_T = 7.5 \text{ T}$, $P_{RF} = 4.0 \text{ MW}$ as given by the model of Fig. 2.2-6.

Central Electron and Ion Temperatures

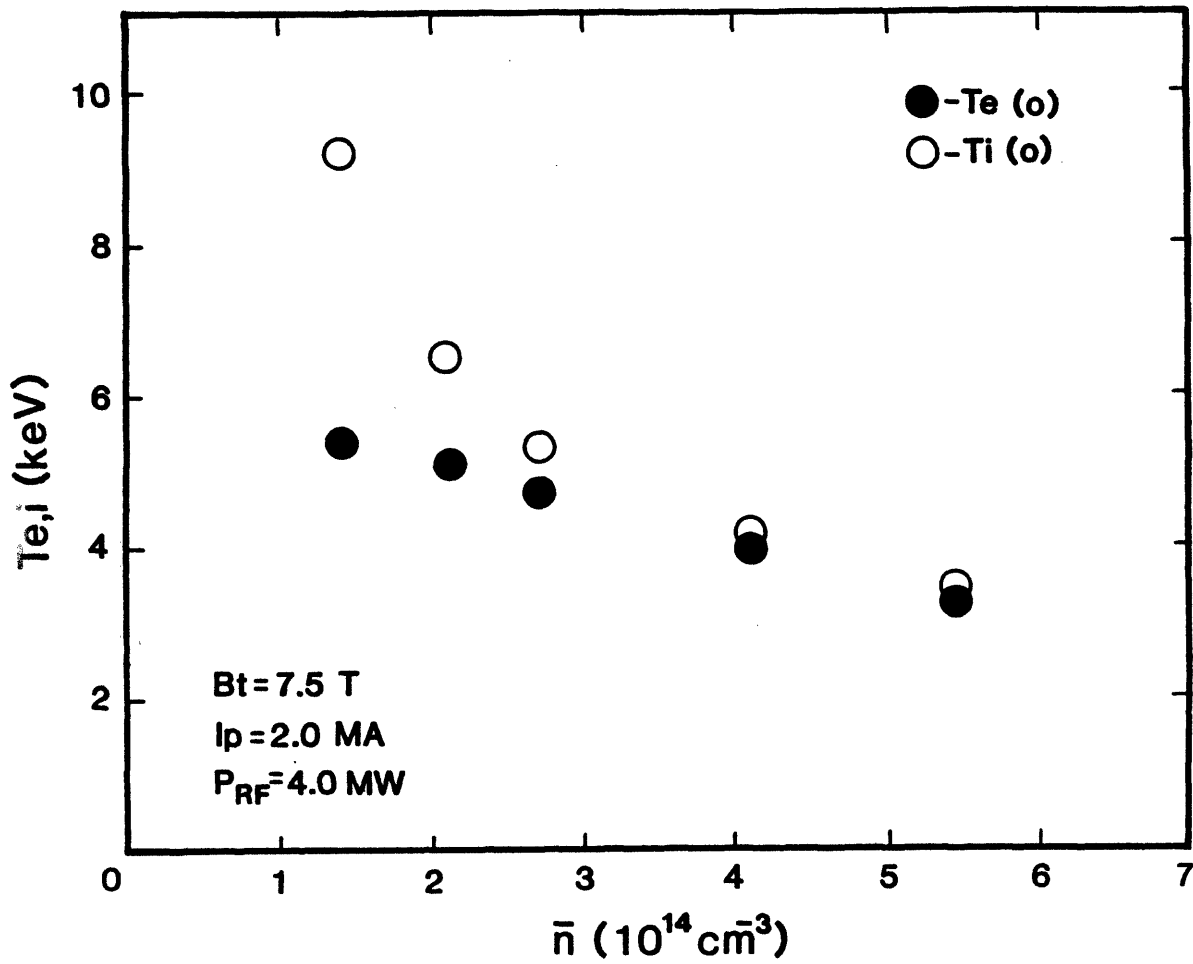
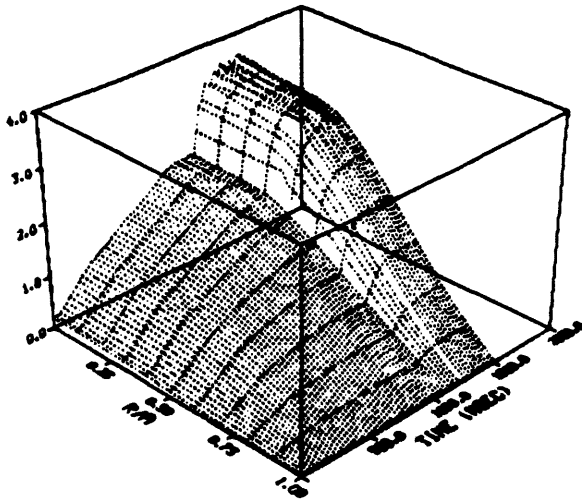
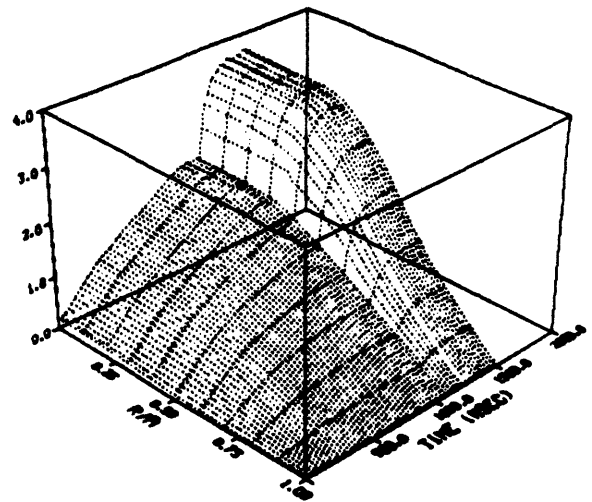


FIG. 2.2-8 Central electron and ion temperatures as a function of line-averaged density assuming κ_e^{eff} (Eq. (3)), and $\chi_i = 3\chi_i^{Neo}$, for $I_p = 2 \text{ MA}$, $B_T = 7.5 \text{ T}$, $P_{RF} = 4 \text{ MW}$.

ELECTRON TEMPERATURE (KEV)



ION TEMPERATURE (KEV)

CURRENT DENSITY (AMPS/CM²)

CENTRAL ELECTRON AND ION TEMPERATURES

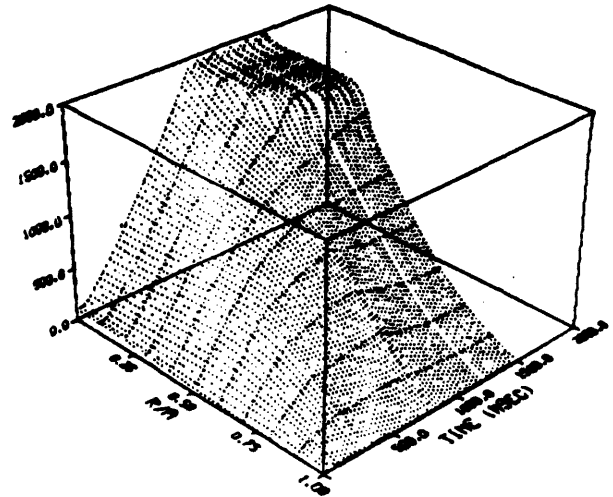
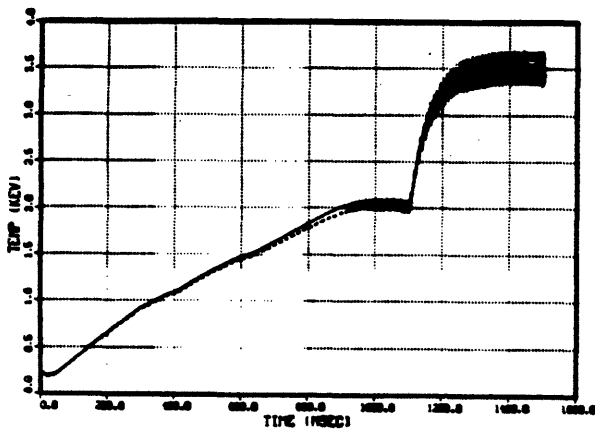


FIG. 2.2-9 Evolution of the temperature and current density profiles, and central electron and ion temperatures during start-up and heating for a 1.5 sec. magnet pulse. RF heating is turned on at 1.1 seconds.

triggered when q_0 drops to 0.95, resulting in a helical flux conserving reconnection, as suggested by Kadomtsev. As can be seen from the figure in this case, a quasi-steady sawtooth discharge is established before the initiation of the 4.0 MW heating pulse at 1.1 sec. For full-field operation, however, the maximum flat-top pulse time will be limited by heating of the magnet to about 1 second; in this case it will be necessary to break down and begin the current rise during the toroidal field ramp, such that q is approximately constant, if disruptive MHD activity due to tearing modes [2.2-10] during the rise is to be suppressed.

The higher currents and densities accessible for full-field (10 Tesla) operation should permit even larger pressures and higher temperatures using RF heating. In addition, this mode of operation will permit investigation of high performance ohmic discharges, including the effects of elongation. As noted above, for the high poloidal field values characteristic of full-performance C-MOD operation, neoclassical ion transport should not impose a practical limit on confinement. In Fig. 2.2-10, we show the temperature evolution for a $8 \times 10^{20} \text{ m}^{-3}$, 10 Tesla, 4 MA deuterium discharge with 7 MW of ICRF heating at a frequency of 140 MHz, ($\omega \approx 2\omega_{cD}$). The different cases shown correspond to three different transport assumptions, namely neo-Alcator electron thermal conduction, drift wave thermal diffusivity as given by the Perkins formulation, and the pressure driven MHD model of Eq. (3). The ion thermal conductivity has been taken to be neoclassical, and the density profile is approximately proportional to a parabola-squared, typical of pellet fueled high density discharges in Alcator C. The RF power deposition for the fast wave is calculated, neglecting mode conversion effects, and for this case the ion heating peaks inside the $q=1$ surface. In the case of neo-Alcator χ_e alone (Fig.

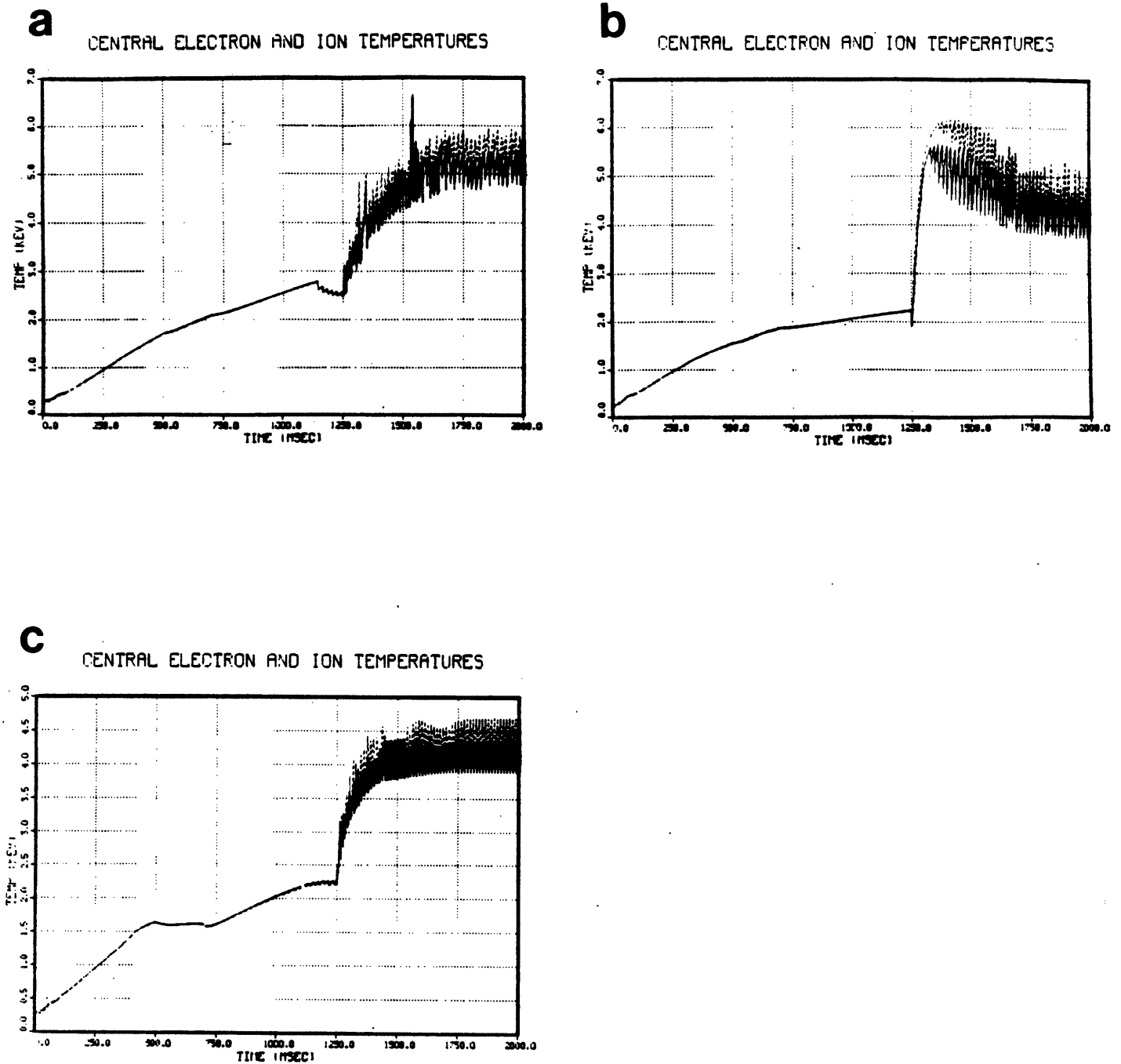


FIG. 2.2-10 Evolution of the central electron and ion temperatures for a discharge with $B_T = 10$ T, $I_p = 4$ MA, $\bar{n}_e = 8 \times 10^{14} \text{ cm}^{-3}$, $P_{RF} = 7$ MW, assuming a) only neo-Alcator χ_e ; b) drift wave transport given by $\chi_e = \chi_e^{\text{Perkins}}$; c) pressure driven transport in addition to the neo-Alcator conductivity.

2.2-10a), the value of $n_0\tau_E$ for these parameters is $2.8 \times 10^{20} \text{ m}^{-3} \text{ sec}$ while the central ion temperature reaches 5.5 keV. The plasma pressure exceeds 7 atmospheres. The ohmic power is still about 2 MW and radiation losses ($Z_{\text{eff}} = 1.2$ due to O_2) account for 1.2 MW. In the pre-RF phase radiation accounts for more than half of the central power balance, as might be expected for operation close to the Murakami limit. The different behavior with the other transport assumptions is shown in Fig. 2.2-10b,c. In the case of Perkins' drift wave model, the strong temperature dependence of the thermal diffusivity results in a drop in confinement after the RF is turned on. Nevertheless, the plasma parameters are only slightly degraded, and $n_0\tau_E$ still exceeds $2 \times 10^{20} \text{ m}^{-3}$. This is also true for the case of the MHD model (Fig. 2.2-10c).

References

- [2.2-1] Alcator Group, MIT Report PFC/IR-82-3, (December, 1982); R. R. Parker, et al., "Progress in Tokamak Research at MIT," MIT Report PFC/JA-85-14 (April, 1985). To be published in Nucl. Fus. 25, No.9.
- [2.2-2] R. J. Hawryluk, et al., "Recent Results from TFTR," Proceedings of the Conference on Heating in Toroidal Geometry, Rome 1984.
- [2.2-3] J. G. Cordey, et al. "Particle and Energy Confinement in Ohmically Heated JET Plasmas," 10th International Conference on Plasma Physics and Controlled Nuclear Fusion Research, London 1984.
- [2.2-4] S. M. Kaye and R. G. Goldston, Nucl. Fus. (To be published, 1985).
- [2.2-5] R. Goldston, Plasma Physics and Controlled Nuclear Fusion 26, 87 (1984).
- [2.2-6] W. W. Pfeiffer, R. H. Davidson, R. L. Miller, and R. E. Waltz,

- "ONETWO: A Computer Code for Modelling Plasma Transport in Tokamaks" GA-A16178, (1980).
- [2.2-7] J. P. Christiansen, et al., "Resistivity and Field Diffusion in JET," Proceedings of the European Physical Society Meeting on Plasma Physics and Controlled Fusion, Budapest (1985).
- [2.2-8] C. E. Singer, et al., "Semi-Empirical Models of Hmode Discharges," PPPL-2103 Princeton Plasma Physics Laboratory (May, 1985).
- [2.2-9] F. W. Perkins, "Confinement Scaling in Tokamaks: Consequences of Drift Wave Turbulence" Proc. 4th Intl. Symp. on Heating in Toroidal Plasmas, Vol. 2, 977, (Rome, 1984); F. W. Perkins and Y. C. Sun, "On Confinement Scaling and Ignition in Tokamaks" Intl. School of Plasma Physics Workshop and School on Basic Physical Processes in Toroidal Fusion Plasmas, (Varenna, Italy, August 1985), to be published.
- [2.2-10] R. S. Granetz, I. H. Hutchinson, D. O. Overskei, Nucl. Fusion 19 1587 (1979).

2.3 MHD CONFIGURATION

2.3.1 Design Scenario

An extensive MHD equilibrium and stability study has been carried out for a wide range of plasma β and shapes. Three types of configurations have been obtained: (1) a limiter plasma configuration, (2) a divertor plasma, and (3) advanced shapes, indicating that the design is very versatile, and can be used to investigate not only standard plasma shapes, but advanced shaping concepts as well.

This device is approximately half the scale of the Compact Ignition Device, ISP, currently under investigation. The basic parameters critical to the MHD equilibrium design are $R_0 = 0.75$, $a = 0.25$ m, $A = 3$, $B_0 = 8$ T, $I_p = 4$ MA, $I_{OH} = 12$ MA, and elongation $\kappa > 1.6$. To keep the device compact, the half width of the vacuum chamber is chosen to be 0.30 m. For plasma elongation $\kappa = 1.6$, the height has to be at least 0.48 m. During the MHD calculations it was found that a vessel elongation of 1.8 was needed to obtain enough plasma cross sectional area to accommodate 4 MA of plasma at $q_\psi = 2.5$, and the height of the chamber was then chosen to be 0.53 m. To maintain compactness, all the computations, except the tall divertor case with 4 MA plasma current, were done within these physical constraints.

The TF coil magnet has a unique design feature, demountable joints at the corners. This allows one to locate the OH coils, divertor coils, shaping coils, and most of the EF coils linking the TF coil. To provide engineering design flexibility, two coil system designs will be presented for each equilibrium discussed: (1) a fully internal PF coil system, and (2) a partial external PF coil system. The selection will be made based on coil size, ohmic power loss, structural requirement and accessibility.

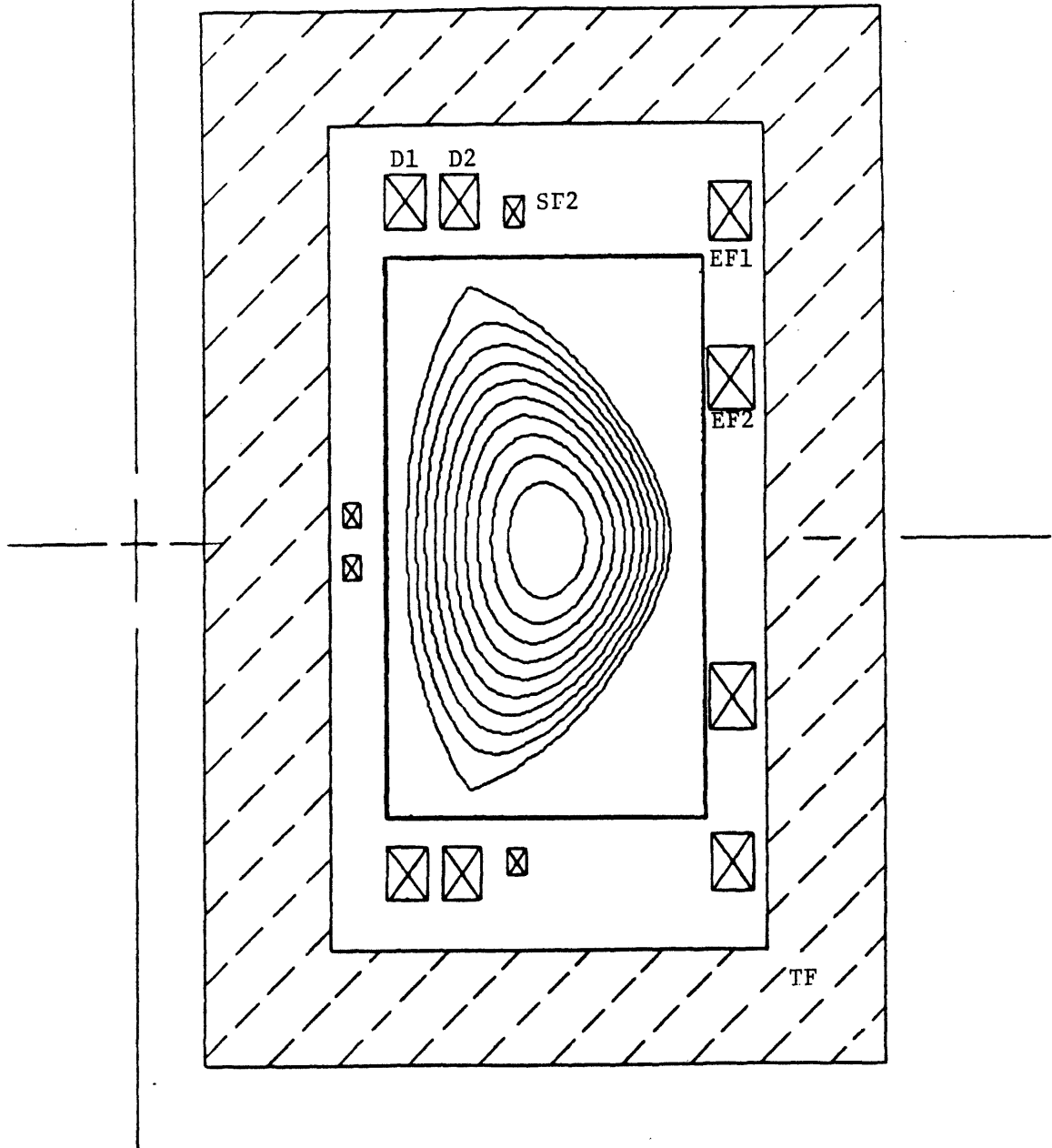
At this phase in the design we focus our attention on optimizing the configuration to obtain an operating space which is feasible from an engineering point of view. The critical beta limit is determined on the basis of ideal MHD modes. A study of MHD stability properties in terms of kink and ballooning modes and various stabilization methods for achieving high β has been carried out by several groups. We assure ourselves overall stability by keeping β less than the Troyon limit, i.e.,

$$\beta (\%) < 3.3 \frac{I}{aB_t} \quad (2.1)$$

For a standard case which has an elongation of $\kappa = 1.8$ and a triangularity of $\delta = .3$, $\beta_c = 6.6\%$. To provide disruption free operation and to model sawtooth behavior the constraints $q_\psi(a) > 2.5$ and $q_\psi(o) = 1$ are imposed throughout. Vertical position control can also be assured with these MHD guidelines.

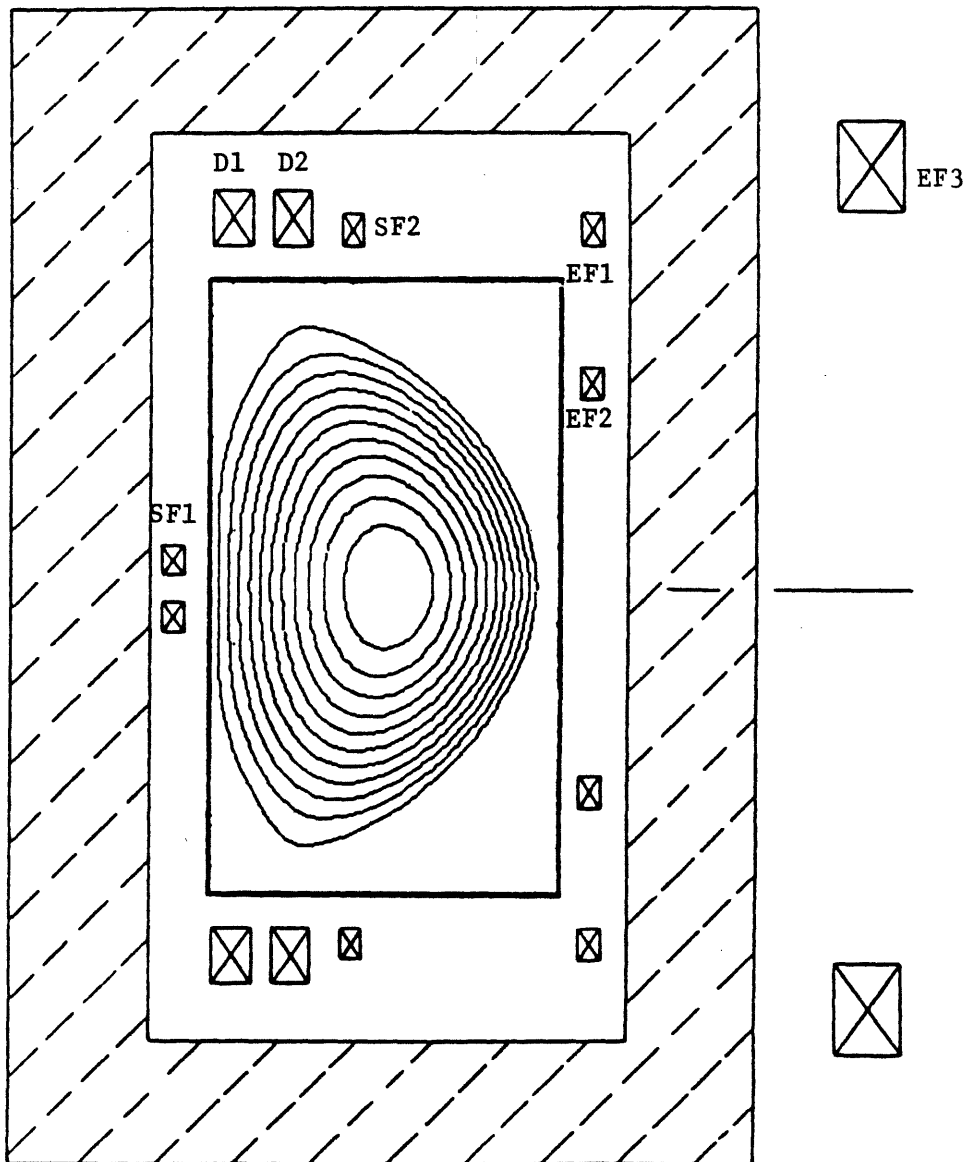
2.3.2 Basic D-Shaped Configuration

Stable D-shaped plasmas can be obtained with either limiter or poloidal divertor configurations. The limiter option makes the best utilization of the available space within the vacuum vessel. Figures 2.3.1 and 2.3.2 show the equilibria obtained for the two cases of all internal or partial external PF systems, excluding OH coils. The OH system is designed for double swing. These figures correspond to the plasma shape at the point when the OH current is crossing zero. For convenience of discussion, all the coils are classified as divertor-like coils D1 and D2, EF coils EF1, EF2 and EF3 and shaping coils SF1 and SF2. EF3 is outside the TF coil bore as shown in Fig. 2.3.2. The coil locations and currents are listed underneath the figures. The β for both



	R(m)	Z(m)	I(MA)
D1	0.50	0.63	0.75
D2	0.60	0.63	0.75
SF1	0.40	0.05	-0.15
SF2	0.70	0.61	-0.20
EF1	1.10	0.61	-0.775
EF2	1.10	0.35	-0.9706

Fig. 2.3.1: Plasma configuration with all internal PF coil system.
 $\beta_t = 3.8\%$, $q_0 = 1.05$, $q_\psi = 2.8$, $\kappa = 1.8$, $A = 3$, $\delta = 0.4$.



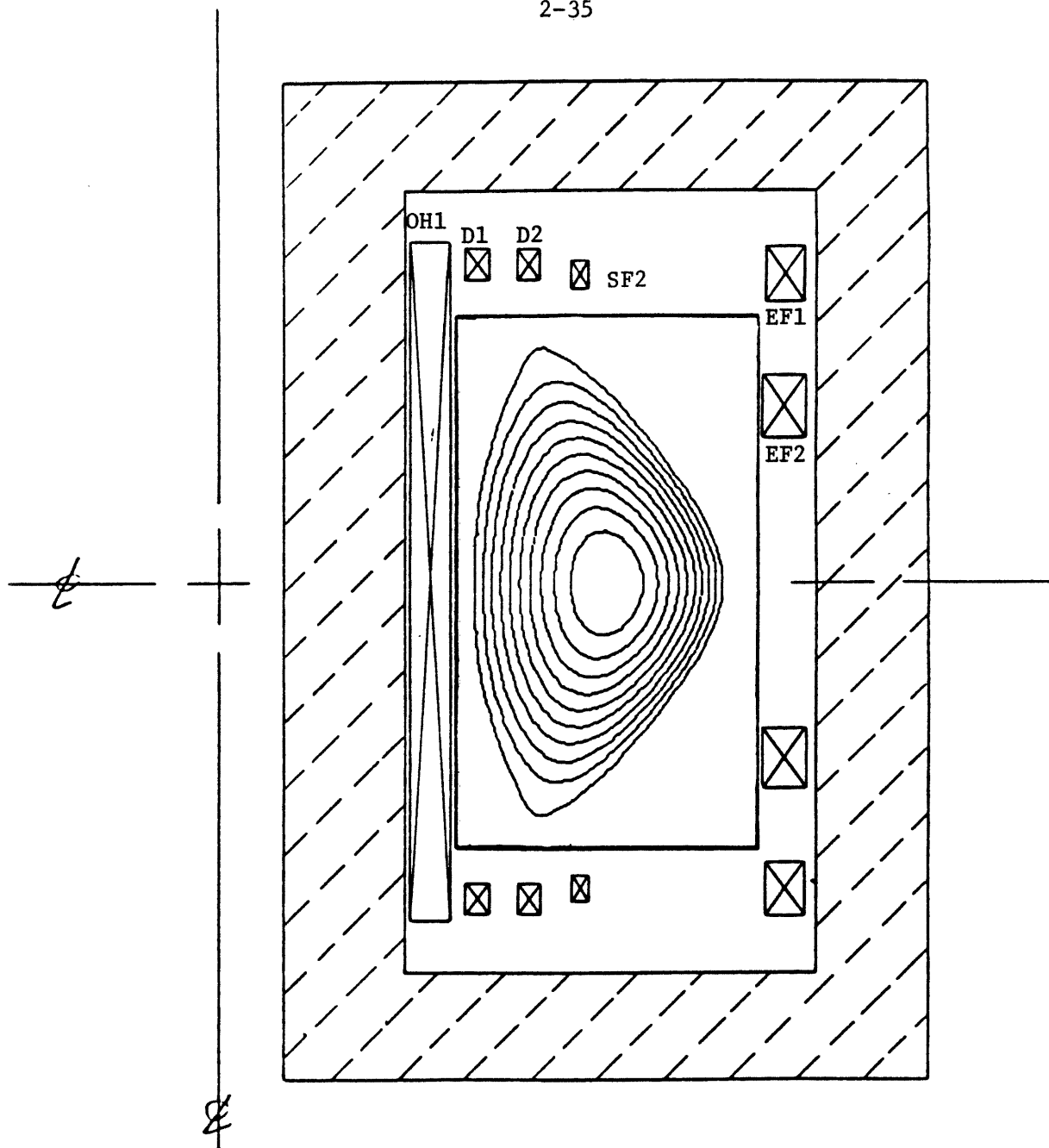
	R(m)	Z(m)	I(MA)
D1	0.50	0.63	0.65
D2	0.60	0.63	0.65
SF1	0.40	0.05	-0.20
SF2	0.70	0.61	-0.20
EF1	1.10	0.61	-0.254
EF2	1.10	0.35	-0.254
EF3	1.57	0.72	-1.907

Fig. 2.3.2: Plasma configuration with partial external EF system.
 $\beta_t = 3.4\%$, $q_0 = 1.05$, $q_\psi = 2.5$, $\kappa = 1.8$, $A = 2.7$,
 $\delta = 0.4$.

cases is $> 3\%$. The plasma is more triangularly shaped for the case of all internal coil system than it is for the partial external EF system. All the coil cross sections are drawn for 10 kAmp/cm^2 current density. EF1 and EF2 have very large cross sections in the case of the all internal PF, and there may not be enough space if the coil is designed for 5 kAmp/cm^2 current density. The current in an external EF3 is twice as large, although it is outside and is thus not constrained by space. Therefore both coil configurations have to be evaluated in terms of power consumption, force and space. However, the choice of either case will not make a major impact on the overall configuration of the device.

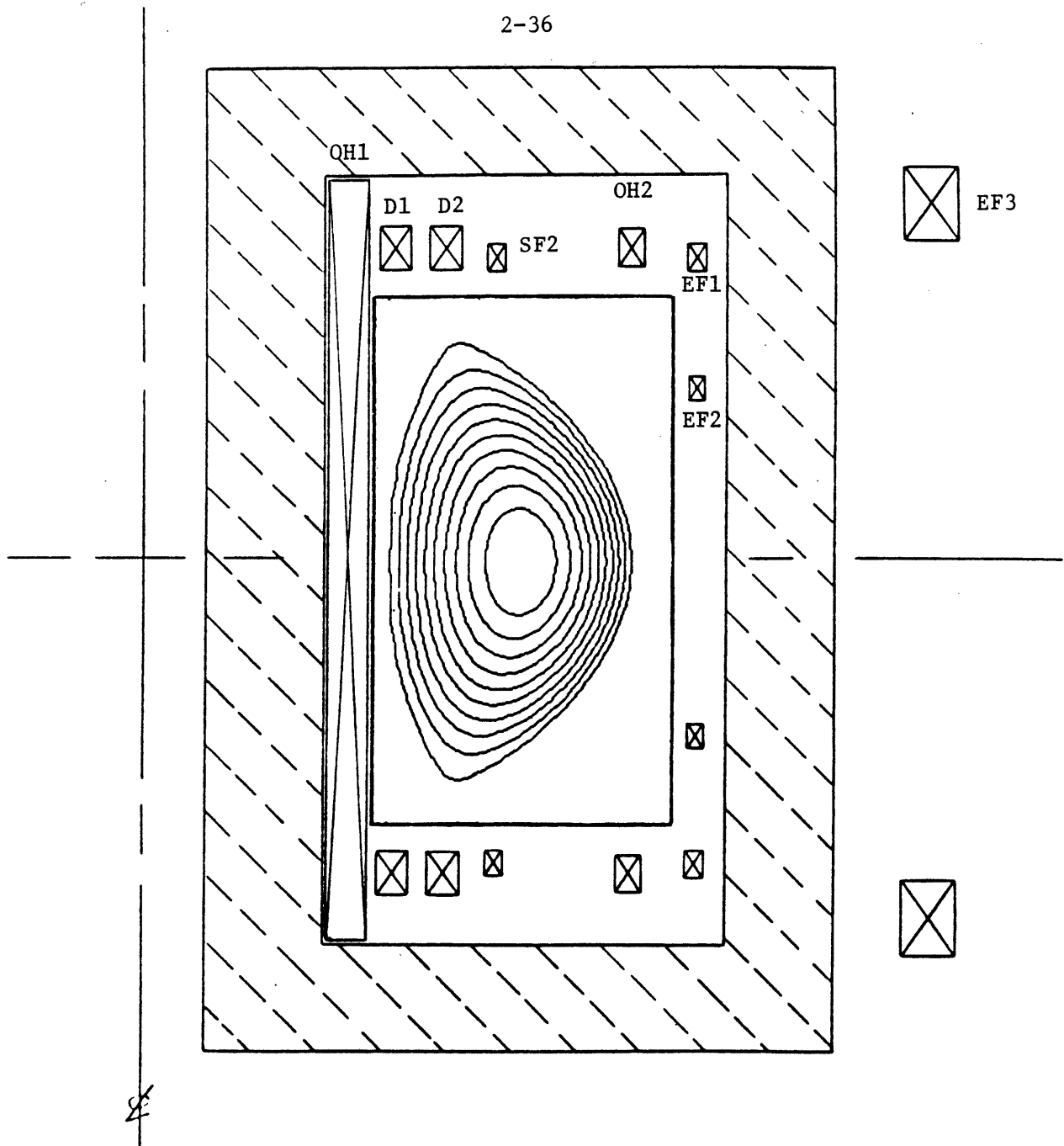
The OH coil is inside the TF coil bore in close proximity of the plasma and carries very large current (12 MA). It would have a significant effect on the MHD equilibrium configuration. It is important to optimize the PF system to obtain the same plasma configuration when the OH coil current is zero or 12 MA. Two plasma configurations with OH current = 12 MA are shown in Figs. 2.3.3 and 2.3.4 with wholly internal or partial external PF systems. The shaping coil SF1 is no longer needed. The main OH solenoid is designated as OH1. The OH1 solenoid is taller than the divertor coil and an additional OH2 coil is added to reduce the coupling of OH1 with the divertor and the EF coils (Fig. 2.3.4). The coil locations and currents for these cases are tabulated below the figure.

The requirements for divertor operation are discussed in Section 2.4. To provide sufficient target area and distance between the target plate and the plasma, divertor configurations for 2.5 MA plasma current for both wholly internal and partial external PF systems are shown in Figs. 2.3.5 and 2.3.6. This plasma still has an elongation of 1.5, triangularity of 0.4, and β of 3.5%.



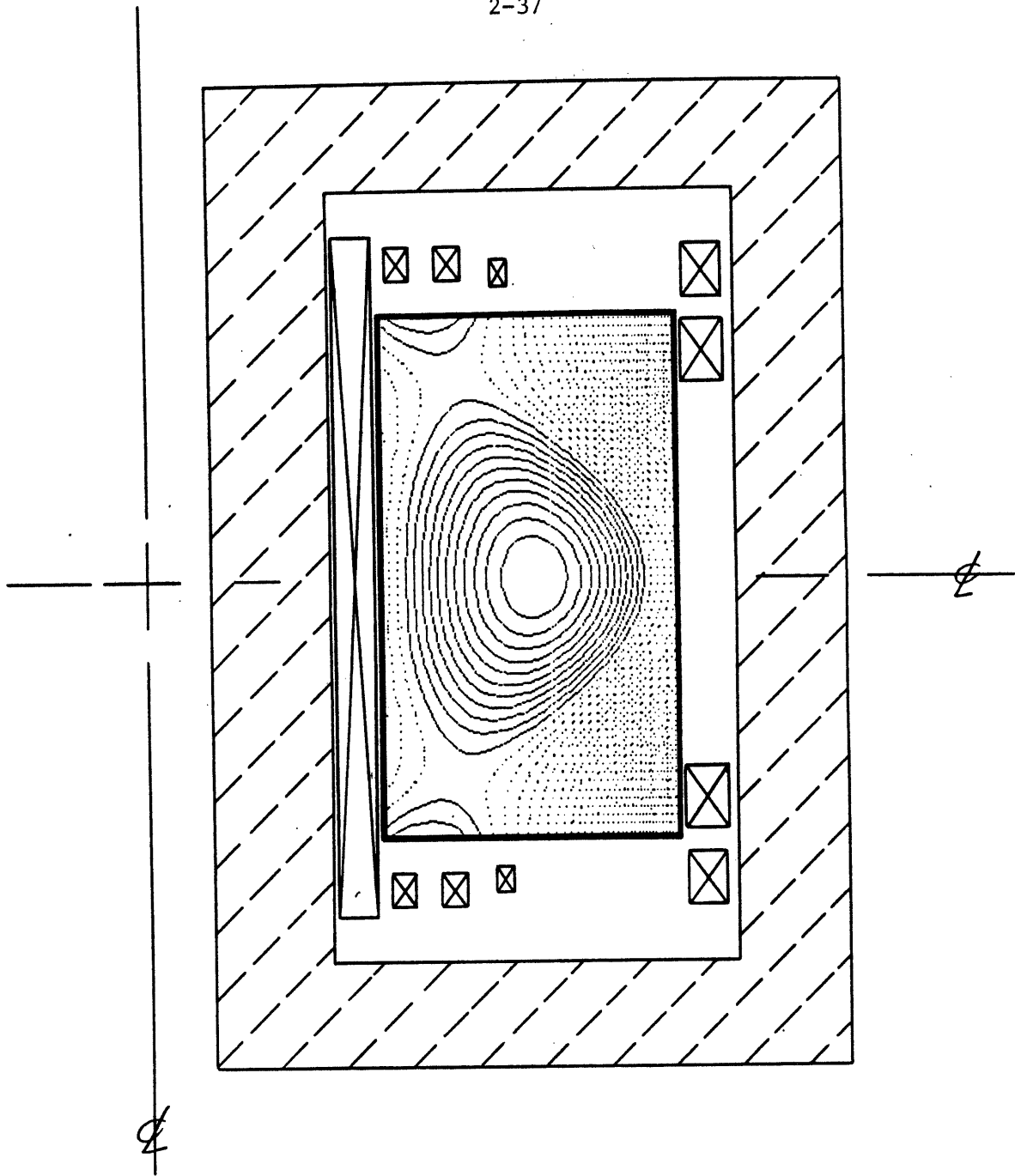
	R(m)	Z(m)	I(MA)	Height
OH1	0.41	0.0	-12.0	1.55
D1	0.50	0.63	+0.30	
D2	0.60	0.63	+0.30	
SF1	0.40	0.61	--	
SF2	0.70	0.61	-0.20	
EF1	1.10	0.61	-0.969	
EF2	1.10	0.35	-1.246	

Fig. 2.3.3: Plasma configuration with all internal PF coil and OH coil at full current. $\beta_t = 4.3\%$, $q_0 = 1.0$, $q_\psi = 3$, $\kappa = 1.8$, $A = 3$, $\delta = 0.4$.



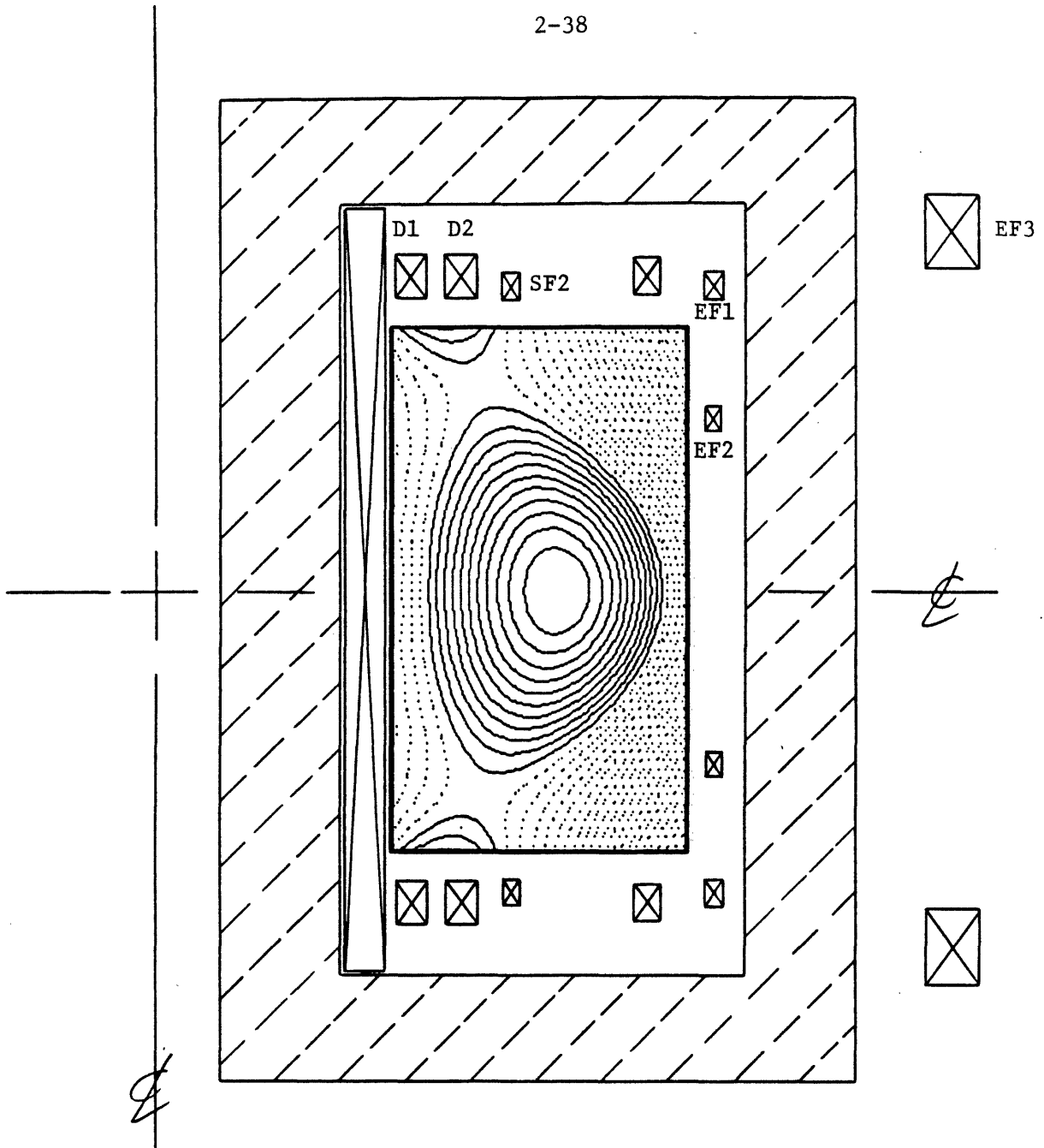
	R(m)	Z(m)	I(MA)	Height
OH1	0.41	0.0	-12.0	1.55
OH2	0.97	0.63	-0.40	
D1	0.50	0.63	+0.60	
D2	0.60	0.63	0.60	
SF2	0.70	0.61	-0.20	
EF1	1.10	0.61	-0.346	
EF2	1.10	0.35	-1.242	
EF3	1.57	0.72	-2.419	

Fig. 2.3.4: Plasma configuration with partial internal PF coil and OH coil at full current. $\beta_t = 4.3\%$, $q_0 = 1.05$, $q_\psi = 2.5$, $\kappa = 1.8$, $A = 3$, $\delta = 0.4$.



	R(m)	Z(m)	I(MA)
OH1	0.41	0.0	-12.0
D1	0.50	0.63	0.25
D2	0.60	0.63	0.25
SF1	0.70	0.61	-0.20
EF1	1.10	0.61	-0.91
EF2	1.10	0.45	-1.258

Fig. 2.3.5: Divertor configuration for all internal PF system.
 $\beta_t = 3.5\%$, $q_\psi = 2.8$, $\kappa = 1.5$, $A = 3$, $\delta = 0.4$.



	R(m)	Z(m)	I(MA)
OH1	0.41	0.0	-12.0
OH2	0.97	0.63	-0.40
D1	0.50	0.63	0.60
D2	0.60	0.63	0.60
SF1	0.40	0.05	0.00
SF2	0.70	0.61	-0.20
EF1	1.10	0.61	-0.186
EF2	1.10	0.35	-0.186
EF3	1.57	0.72	-1.857

Fig. 2.3.6: Divertor plasma configuration with partial external EF coil.
 $I_p = 2.5$ MA, $\beta_t = 4.2\%$, $\kappa = 1.6$, $A = 3$, $\delta = 0.4$.

The divertor coil can still fit the space with 5 kAmp of current density. A third divertor configuration for 4 MA plasma current has also been obtained by raising the coil against the magnet so that the chamber can be enlarged vertically to provide space for the target plate. The equilibrium configuration is shown in Fig. 2.3.7.

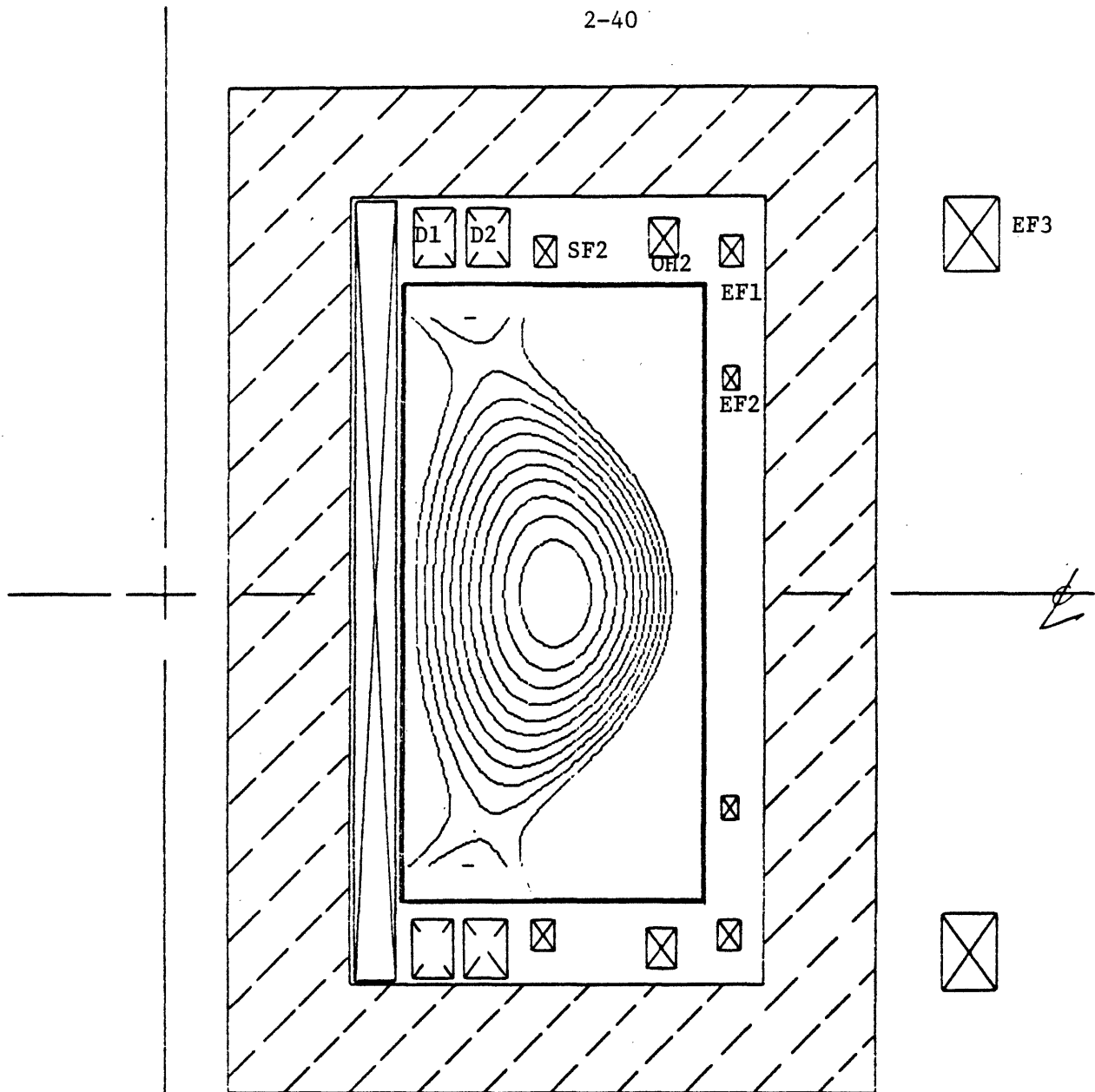
2.3.3 β -Dependence

As pointed out in Section 2.1, to facilitate disruption-free operation and to model sawtooth operation, the plasma configurations were obtained under the constraints $q_\psi(a) > 2.5$ and $q_\psi(o) \approx 1$. A series of calculations have been carried out for β ranging from 1% to 4%. The ideal and resistive criteria at $\beta = 4\%$ are shown in Fig. 2.3.8. This β is well below the Troyon limit for our device which is 6.6%. The β dependence study was done by holding the divertor coil currents and other parameters fixed, and by varying the EF coil current. The variation of the EF coil current as a function of β is given in Fig. 2.3.9.

A detailed study of the plasma stability with respect to kink and ballooning modes using the PEST code is underway. The purpose of such a study is not only to determine the β limit in terms of these modes for this device, but also to study different stabilizing methods such as profile and orbit control and triangularity to reach higher β in the first stability regime.

2.3.4 Start-up Scenario

Since the OH coil carries very large current in close proximity to the plasma, its influence on the plasma configuration has to be studied during



	R(m)	Z(m)	I(MA)
OH1	0.41	0.0	-12.0
OH2	0.97	0.715	-0.717
D1	0.50	0.715	+1.00
D2	0.60	0.715	+1.00
SF1	0.74	0.70	-0.30
EF1	1.10	0.69	-0.30
EF2	1.10	0.44	-0.251
EF3	1.57	0.72	-0.251

Fig. 2.3.7: Divertor configuration for 4.0 MA plasma and extended chamber. $I_p = 4.0$ MA, $\beta_t = 3.6\%$, $q_\psi = 2.6$, $\kappa = 1.8$, $A = 3$, $\delta = 0.35$.

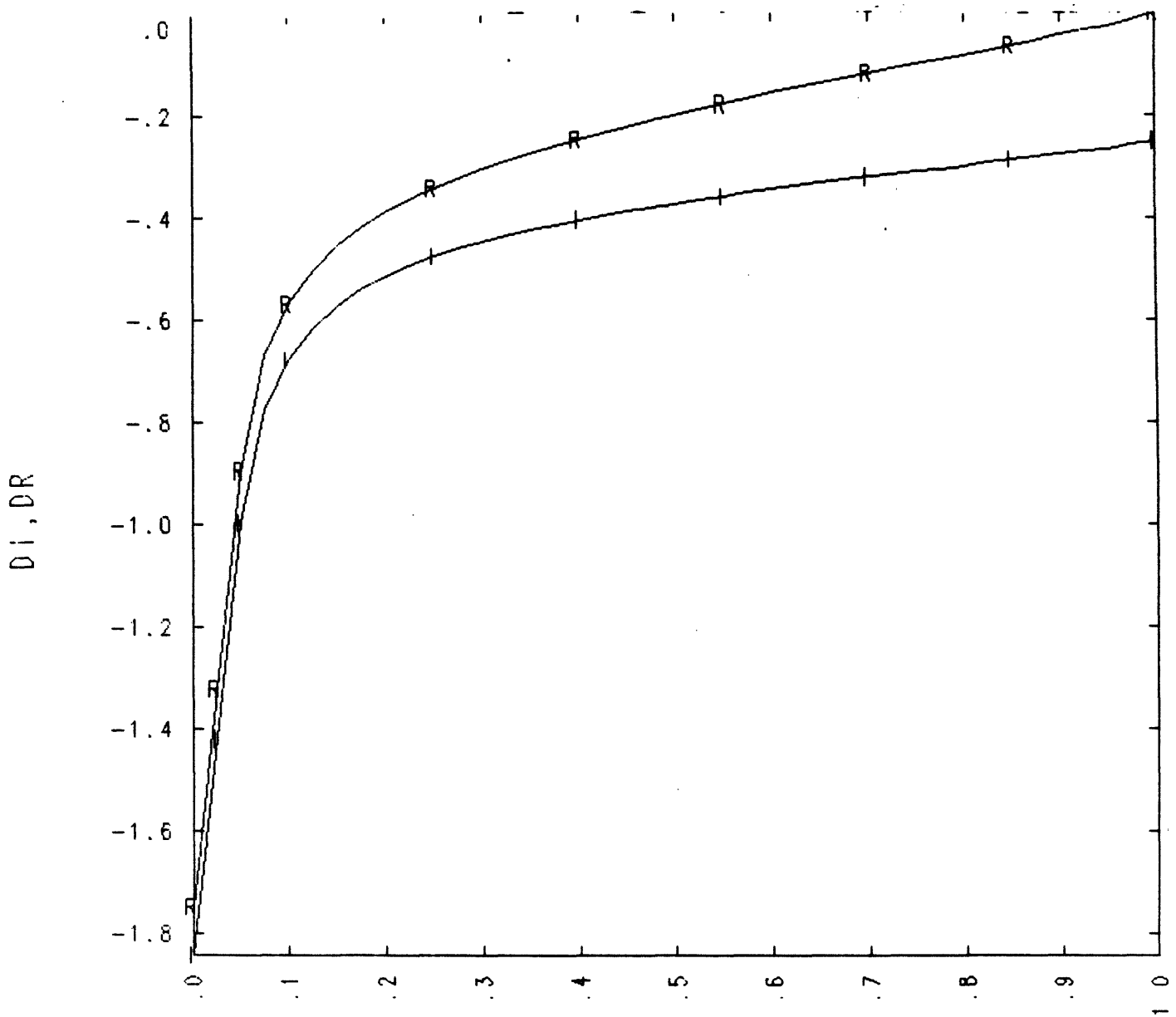


Fig. 2.3.8: The stability criteria DI , DR are negative throughout the entire plasma.

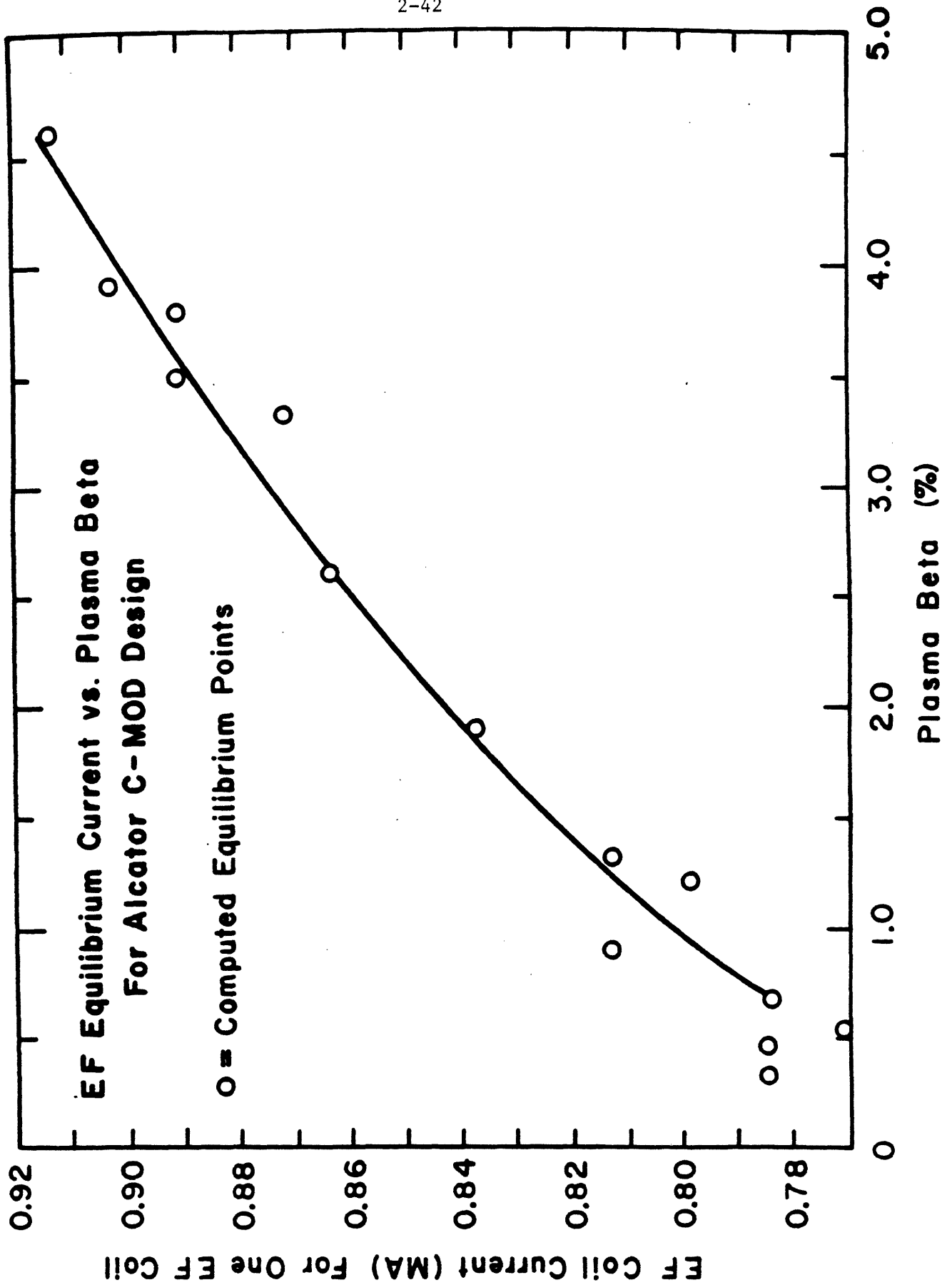


Fig. 2.3.9: Current in each EF coil as a function of β calculated based on all internal PF system.

start-up. This is particularly important when the OH current is reversed. The OH current is initially charged to +12 MA, then swung through zero to -12 MA. A series of MHD configurations for various plasma currents have been obtained. The OH current, total divertor current, total EF current, toroidal field, and plasma current are tabulated in Table 2.3.1.

TABLE 2.3.1

PF COIL AND PLASMA PARAMETERS DURING STARTUP

Time Sequence	I_p (MA)	B_t (T)	I_{OH} (MA)	I_D (MA)	I_{EF} (MA)
1	0.75	4.5	9.89	1.0	-0.75
2	1.0	5.0	9.16	1.2	-1.54
3	1.5	6.0	7.94	1.6	-2.18
4	2.0	7.0	6.50	2.0	-3.01
5	2.5	8.0	5.09	2.4	-3.76

At each point during start-up the plasma is quasi-stable. Initiation of the plasma current during the toroidal field ramp is employed to maximize the flat top pulse length. The correspondent sequence of quasi-static plasma equilibria during start-up are shown in Fig. 2.3.10 as the plasma evolves from circular to D-shape.

2.3.5 Advanced Configurations

In addition to supporting ignition physics issues, Alcator C-Mod is designed to have the flexibility and capability to pursue advanced shaping and

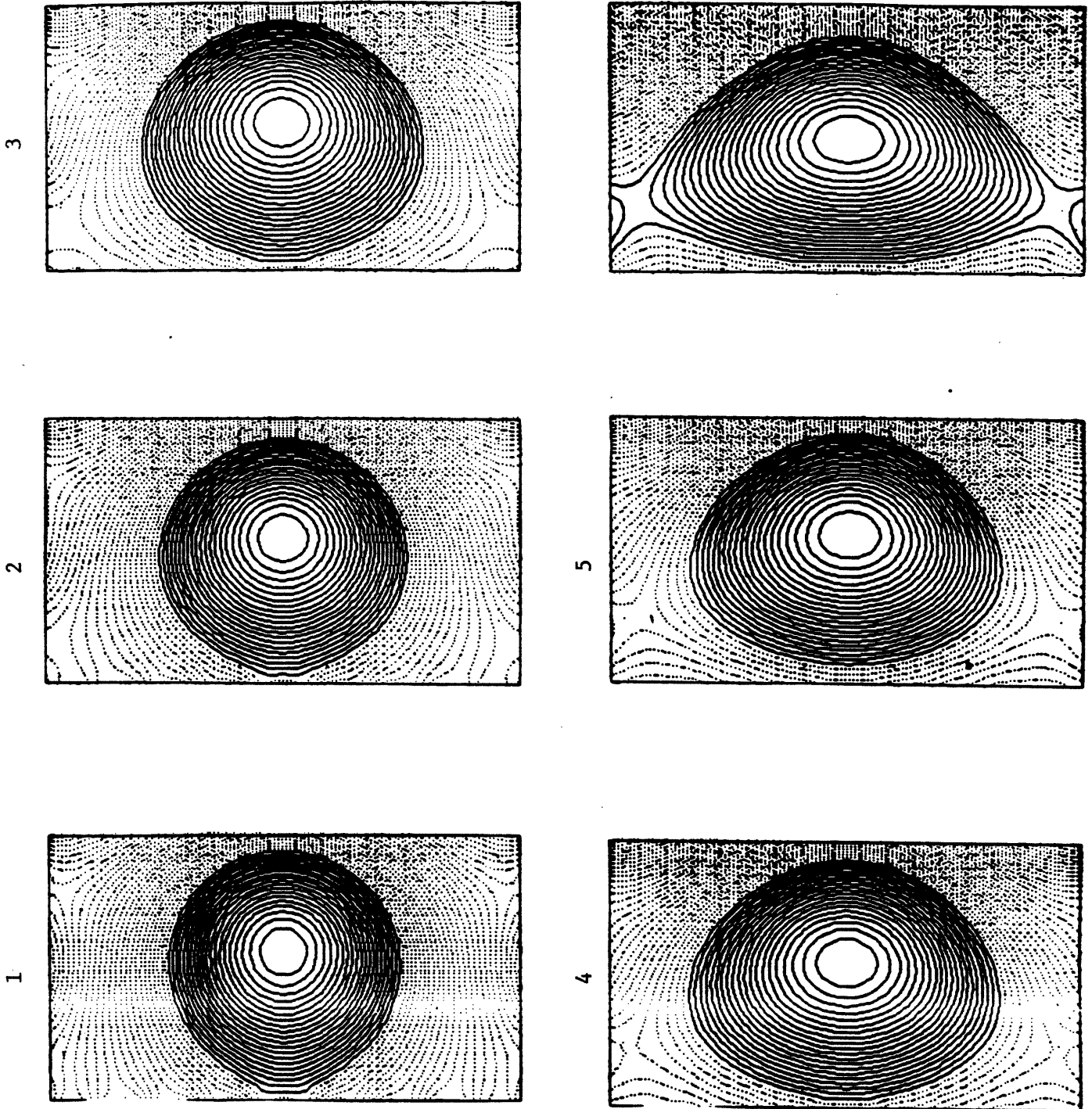
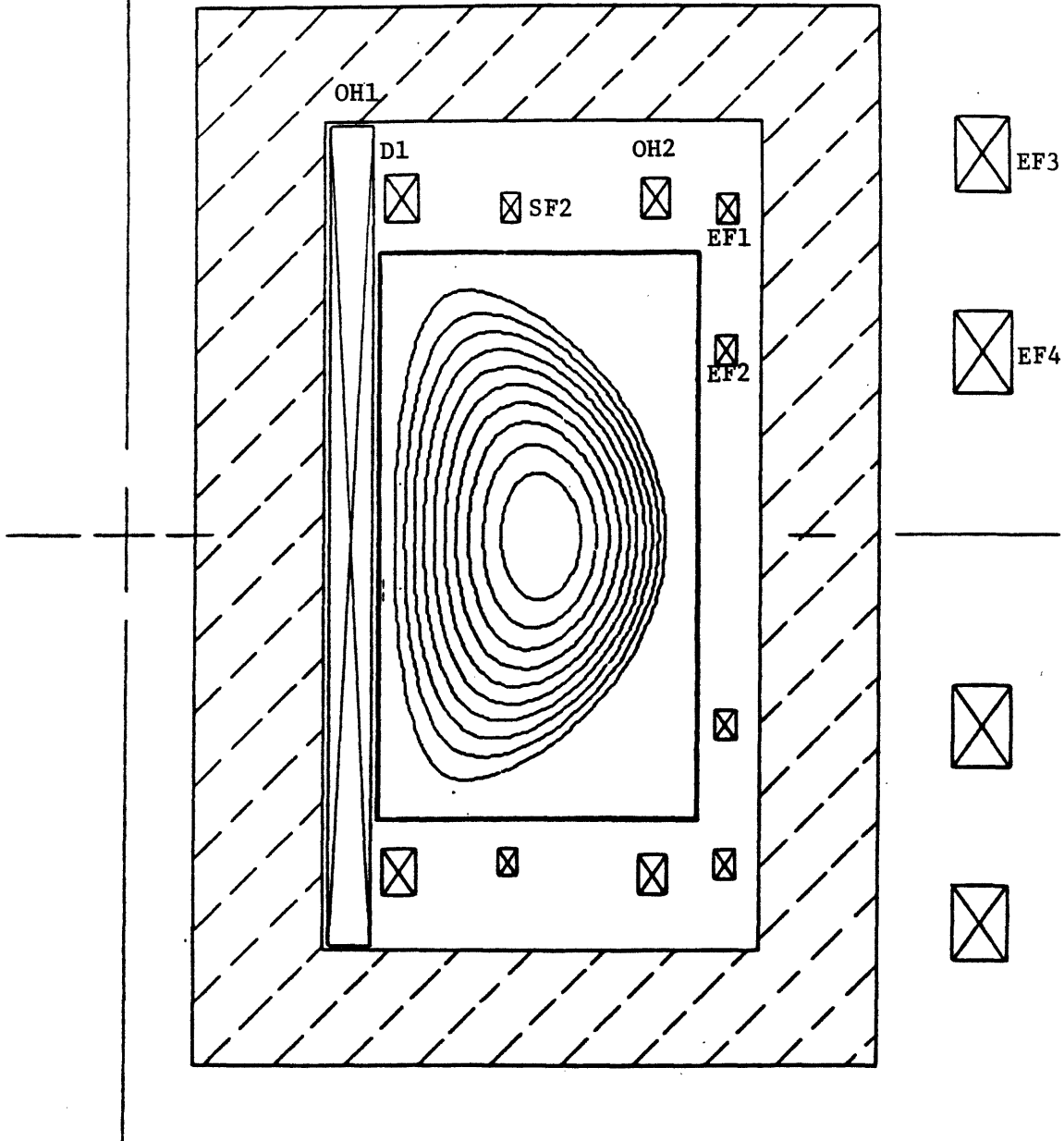


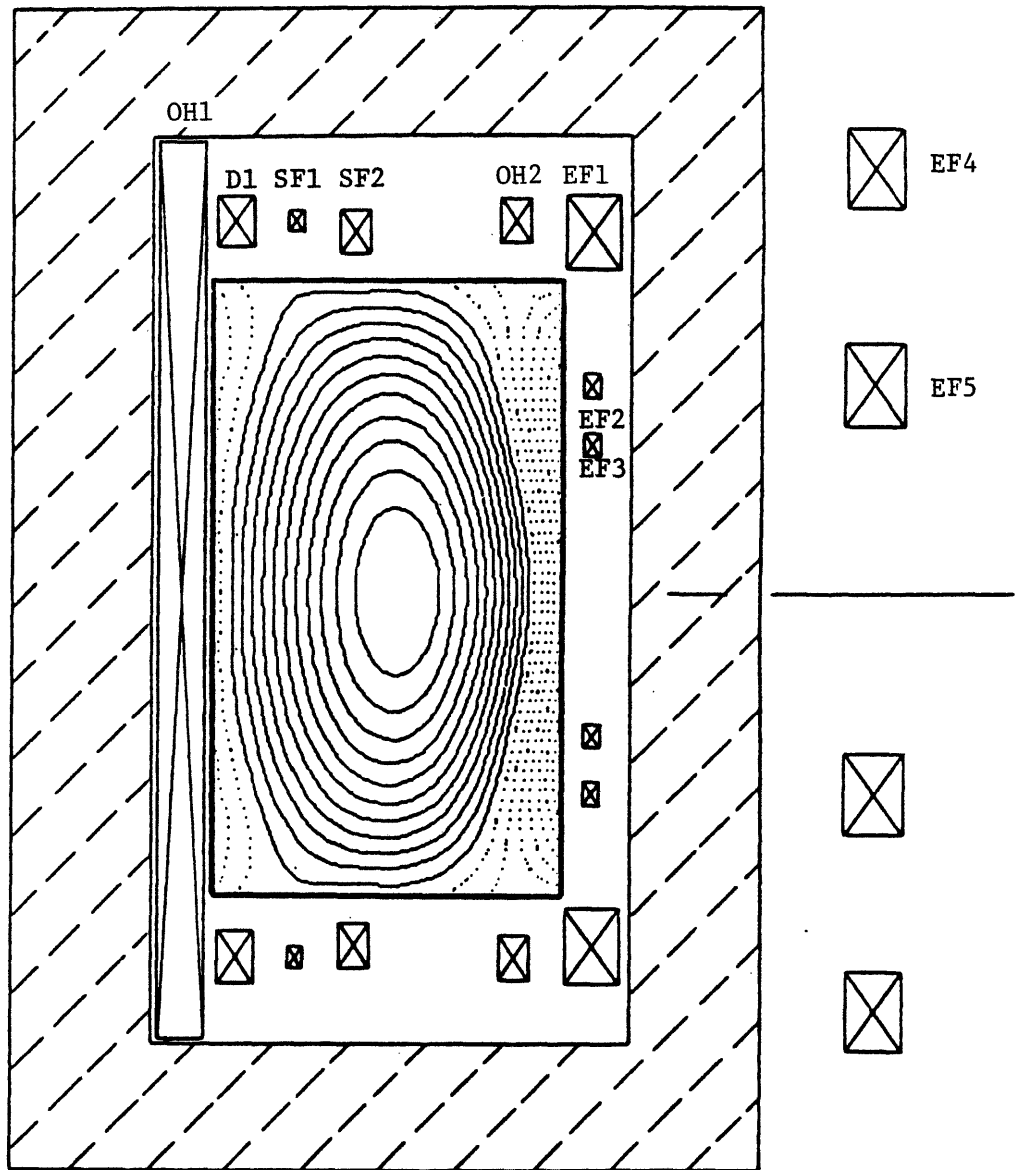
Fig. 2.3.10: Evolution of plasma configuration during startup.

physics experiments for new concepts. We have successfully obtained configurations with high ellipticity, as well as additional rectangularity or triangularity with only minor modifications of the coil system. Figure 2.3.11 shows the highly triangular plasma, and Fig. 2.3.12 the rectangular plasma. The only major modification to the PF system is the addition of a pair of external EF3 coils which are outside the TF bore. All the originally designed access ports on the top and sides of this device are still available.



	R(m)	Z(m)	I(MA)	Height
OH1	0.41	0.0	-12.0	1.55
OH2	0.97	0.63	-0.40	
D1	0.50	0.63	+0.60	
D2	0.60	0.63	0.0	
SF1	0.40	0.43	0.40	
SF2	0.70	0.61	-0.20	
EF1	1.10	0.61	-0.145	
EF2	1.10	0.35	-0.145	
EF3	1.57	0.72	-1.014	
EF4	1.57	0.35	-1.014	

Fig. 2.3.11: Highly triangular plasma configuration.
 $\beta_t = 3.4\%$, $\kappa = 1.8$, $A = 3$, $\delta = 0.6$.



	R(m)	Z(m)	I(MA)
OH1	0.41	0.0	-12.0
OH2	0.97	0.63	0.0
D1	0.50	0.63	+0.60
SF1	0.61	0.63	-0.10
SF2	0.70	0.61	-0.40
EF1	1.10	0.61	+1.20
EF2	1.10	0.35	-0.136
EF3	1.10	0.25	-0.136
EF4	1.57	0.72	-1.492
EF5	1.57	0.35	-1.629

Fig. 2.3.12: Rectangular plasma configuration with elongation of 2 and aspect ratio 3. $\beta_t = 3.7\%$, $q_0 = 1.5$, $q_\psi = 2.5$, $\kappa = 2.1$, $A = 3$.

2.4 Impurity Control

2.4.1 Introduction

In present experiments, impurity influxes generally accompany radio-frequency heating of the plasma [2.4-1]. For Alcator C-MOD to reach its design objectives, the impurity density in the plasma must be kept at a minimum. The techniques for reducing the amount of impurities in the plasma fall into two general categories: degrading the impurity confinement once they have entered the plasma [2.4-2] or limiting the impurity influx rate. The second category will be addressed in this section.

There are a number of ways to reduce the impurity influx rate. Evaporation and physical sputtering are the principal impurity source mechanisms in current tokamaks. Evaporation can be reduced by minimizing the temperature excursions of the material surfaces in the vacuum chamber. This can be accomplished either by minimizing the heat flux incident on those surfaces or by providing active cooling. On the time scale of this experiment active cooling would have little effect on the surface temperature rise for typical tile thicknesses (1 cm.). Sputtering is principally reduced by lowering the ion and electron temperatures of the plasma incident on those same surfaces. This can be accomplished, for example, by producing a 'high-recycling regime' of neutrals and plasma near the limiter/divertor plate.

Assuming that all possible methods of reducing the impurity flux off these material surfaces have been implemented, a final step can be taken to reduce the actual flux of impurities into the plasma proper: increase the distance from the material surface producing the impurity to the plasma edge. This allows the impurities generated at a surface to be

ionized before reaching the main plasma, thus binding them to an edge field line. The obvious choice for this technique is the poloidal divertor. Other, less attractive choices exist, such as bundle divertors and ergodic divertors.

2.4.2 Limiter and Divertor Configurations

Three basic types of limiter/divertor configurations have been designed for Alcator C-MOD. A standard limiter configuration is shown in Fig. 2.4-1. This limiter design has been optimized to provide the largest amount of limiter area (which reduces the local heat loads) consistent with not blocking diagnostic viewing access and a number of plasma shapes. The inside (smaller major radius) 'bumper' limiter also serves to protect the vessel wall against disruptions. The outer limiter could be tilted tangent to a variety of plasma shapes.

From the above discussion it is obvious that divertor configurations are better than the limiter configuration at minimizing the backflow of neutrals to the main plasma. Two divertor plate geometries depicted in Figs 2.4-2 and 2.4-3, have been designed. Each shape has been optimized to limit the incident heat flux to 2MW/m^2 for the particular plasma equilibrium shown and the estimated energy scrapeoff length given in Table 2.4-1. Unlike the internal-coil poloidal divertors of ASDEX and PDX, the flux surface spacing near the x-point is large. This precludes the possibility of using baffles to minimize the leakage of neutrals, created at the divertor plate, back to the plasma. To overcome the loss of these mechanical baffles, the divertor plasma must itself prevent hydrogenic and impurity neutrals from entering the main plasma; a 'high

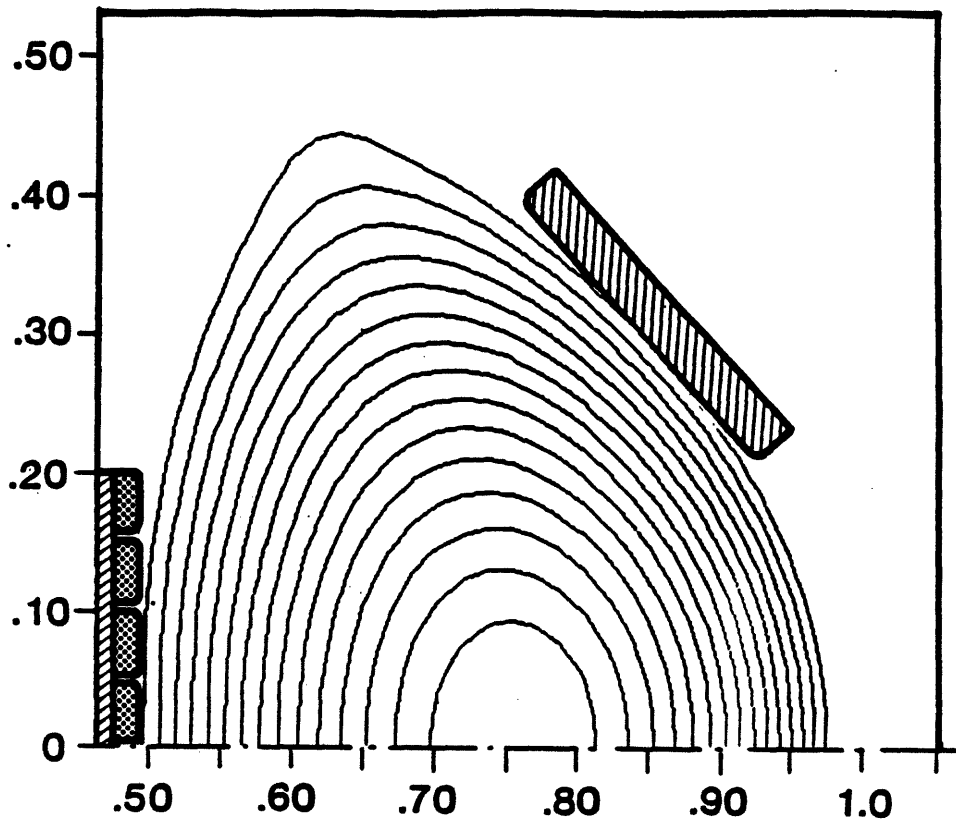


FIG. 2.4-1 Standard limiter plasma with three toroidal limiters. One is located at the inside (small major radius) edge of the plasma. The two others above and below the midplane can be tilted tangent to a variety of shapes.

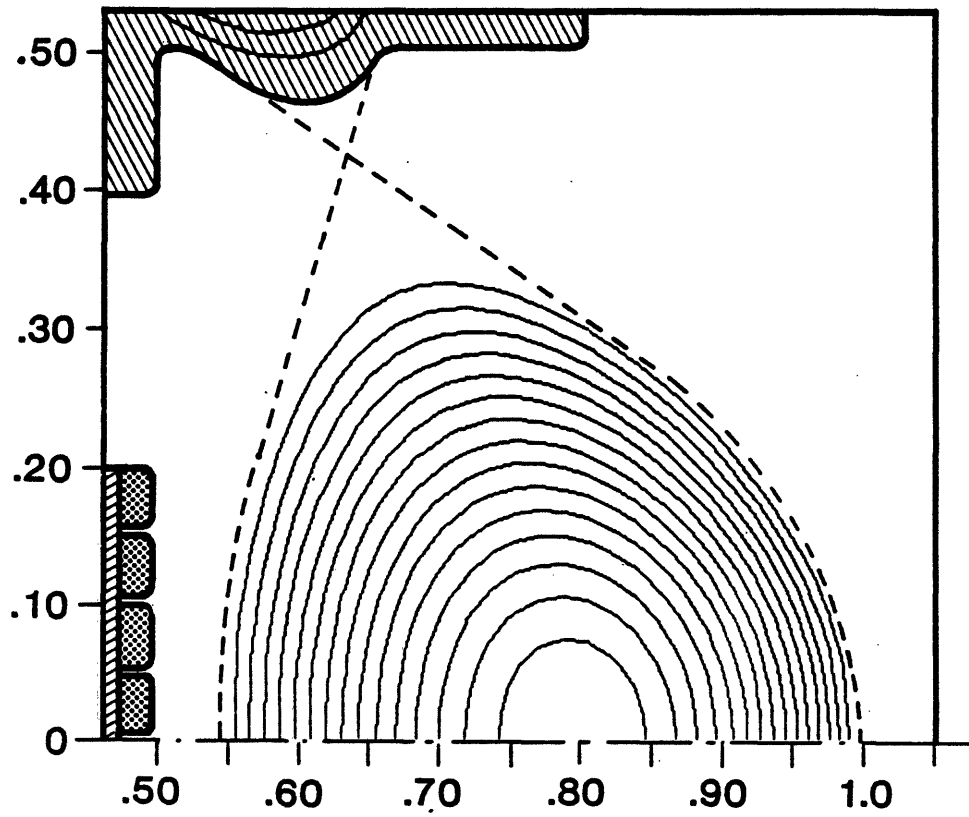


FIG. 2.4-2 First divertor plasma configuration: separatrix indicated by dashed line.

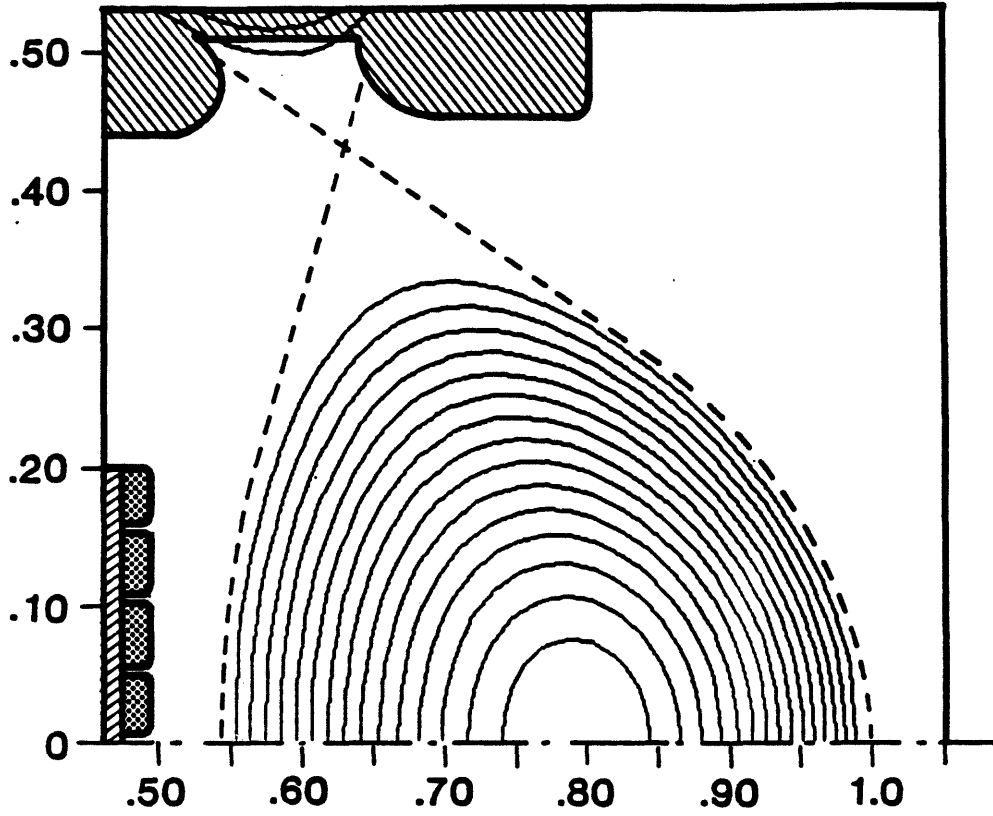


FIG. 2.4-3 Second divertor configuration.

TABLE 2.4-1

PLASMA SCRAPEOFF CHARACTERISTICS

Power entering the edge	5 MWatts
λ_E (midplane)	.5 cm
n_e (midplane)	1.5×10^{14}
T_e (midplane)	40 eV
λ_E (divertor plate)	1.5 cm
n_e (divertor plate)	5×10^{14}
T_e (divertor plate)	10 eV
P_{ave} on limiter/divertor	2-3 MW/m ²
λ_{mfp} (ionization of 30 eV H at plate)	≈ 1.0 cm
λ_{mfp} (ionization of 30 eV C at plate)	≈ 0.2 cm
Dist. from x-point to plate	6-7 cm

recycling regime'. The specifics of whether this can be accomplished in Alcator C-MOD will be discussed in the following sub-section.

The principal difference between the two divertor plate shapes shown in Figs 2.4-2 and 2.4-3 is just the angle at which the separatrix intersects the divertor plate. Because of this difference in angles, the second configuration (Fig. 2.4-3) can locate the point of intersection further from the x-point than the first configuration. Also, the normal to the divertor plate surface at this intersection point is directed further away from the main plasma. Both of these characteristics reduce the hydrogenic and impurity neutral backflow to the main plasma over that of the first divertor configuration. The surface of the first divertor

configuration is in closer contact to the vessel wall and thus would be easier to support and cool through thermal conduction.

2.4.3 High Recycling Regime

Based on experimental results from D-III, ASDEX, PDX and PBX, there are some general guidelines for achieving the 'high recycling regime' [2.4-3]: a high-density, low temperature plasma near the divertor plate. Basically, the neutrals must be ionized either before crossing the separatrix into the main plasma or crossing the scrapeoff layer into the vacuum region near the wall. Results for D-III and PBX indicate that this condition can be accomplished in an open geometry such as that of C-MOD. In other words, the internal divertor coils and baffling used in PDX and ASDEX are not needed. Indeed, measurements in D-III show that the electron density at the divertor plate ($\approx 10^{14} \text{ cm}^{-3}$) can be greater than in the center of the plasma ($\approx 3-5 \times 10^{14} \text{ cm}^{-3}$) [2.4-4]. The temperature at the divertor plate is much lower than along the same field line nearer to the plasma edge.

With the above background, the prospects for achieving the high-recycling regime in Alcator C-MOD are quite reasonable. Predicted central plasma density in Alcator C-MOD is significantly higher ($5 \times 10^{14} \text{ cm}^{-3}$) than that of D-III, and the edge parameters reflect this (Table 2.4-1). The mean free path for ionization of a 30 eV neutral near the Alcator C-MOD divertor plate will then be $< 1 \text{ cm}$. The distance from the divertor plate to the x-point or across the scrapeoff layer to open vacuum is greater than this value. These characteristics bode well for achieving the high-recycling regime and the accompanying reduction in temperature and sputtering at the divertor plate.

The high-recycling condition also enhances the natural impurity shielding effect of the divertor discussed earlier. A standard divertor is better suited for impurity control than a limiter, in that the distance from the impurity's 'birthplace', at the limiter/divertor surface, to the plasma edge is much greater in the divertor configuration (≈ 0 for limiter). The high-recycling condition further magnifies this advantage by reducing the mean free path for ionization of impurities (see, for example, Table 2.4-1). After ionization in the scrapeoff layer, the impurities are swept back towards the divertor plates through the effect of frictional drag on the background plasma.

2.4.4 Reduction of Evaporation

To minimize the evaporation-derived impurity source rate, the limiter/divertor plate heat load, and resultant surface temperature rise, must be minimized. The heat deposition profiles on the limiter/divertor plate depicted in Figs 2.4-1-3 are estimated using the scrapeoff characteristics of Table 2.4-1.

The heat flux parallel to a field line in the scrapeoff layer is calculated as a function of the major radius, R , on the plasma midplane assuming the standard form;

$$P(R) = P_0 \cdot \exp\left(-\frac{R-R_0-a}{\lambda_E}\right)$$

where a and λ_E are the plasma minor radius and energy scrapeoff length on the midplane. The flux surface geometry is given by the output, $\psi(R,z)$ of an equilibrium code. The heat flux along a field line near the limiter/divertor surfaces is assumed equal to that calculated on the midplane

allowing for changes in flux tube area (i.e., it is assumed that cross-field diffusion and energy loss mechanisms are negligible). The heat flux to the surface is then simply the dot product of the heat flux along a field line with the surface normal.

The heat loads on the Alcator C-MOD divertor plates are large but manageable. The divertor surfaces shown in Figs 2.4-2 and 2.4-3 have been shaped to limit the incident heat loads to 2 MW/m^2 for $\lambda_E = 0.5 \text{ cm}$. Figure 2.4-4 shows the variation of the heat load to the larger major-radius plate of Fig. 2.4-2 with variation in λ_E . This is typical of the heat load variations for the other divertor plates shown. The variation of this heat load with changing plasma major radius is minimal. This is due to the close proximity of the divertor coils to the plasma which does not allow the position of the x-point or separatrix intersection with the divertor surfaces to vary significantly. The heat loads to the limiter surfaces (Fig. 2.4-1) are shown in Fig. 2.4-5. These heat loads are also quite reasonable.

The evaporation rate due to such heat loads is dependent on the resultant surface temperatures. The surface temperature rise during an experiment has been estimated assuming the tile attachment design shown in Fig. 2.4-6, which is similar to that used for the 'jaws' limiter in TFTR [2.4-5]. The 1-D (space) numerical model used for this calculation fixes the inside wall temperature at 213° K , the typical vessel temperature on Alcator C. In particular, the vessel wall in Alcator C must be ohmically heated between shots to keep the surface temperature from dropping to that of liquid nitrogen ($\approx 77^\circ \text{ K}$). The thermal contact resistance used is given by the TFTR tile results [2.4-5]. Typical heat fluxes

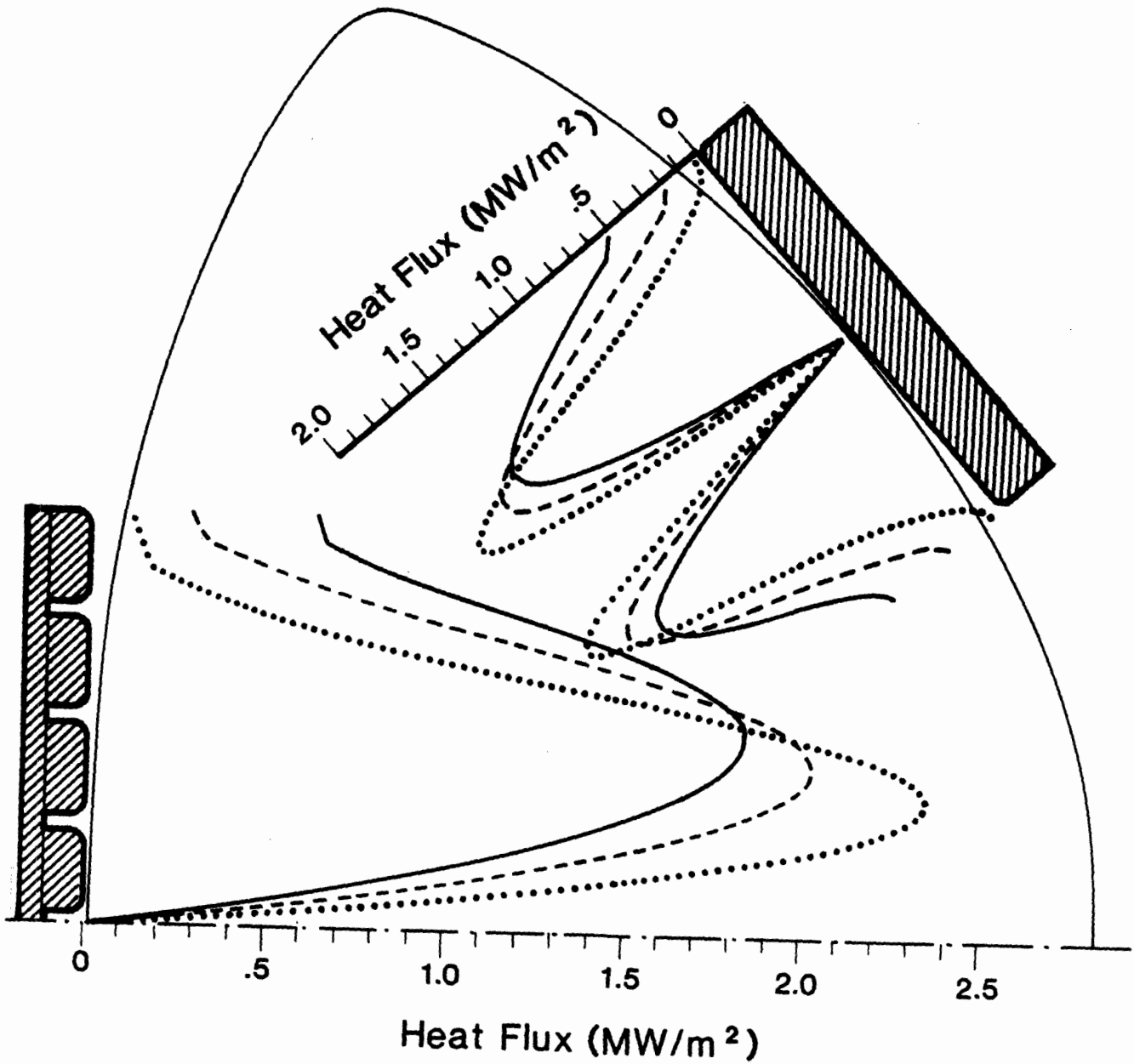


FIG. 2.4-4 Heat loads on limiter surfaces shown in Fig. 2.4-1: heat flux scale perpendicular to the surface it refers to.

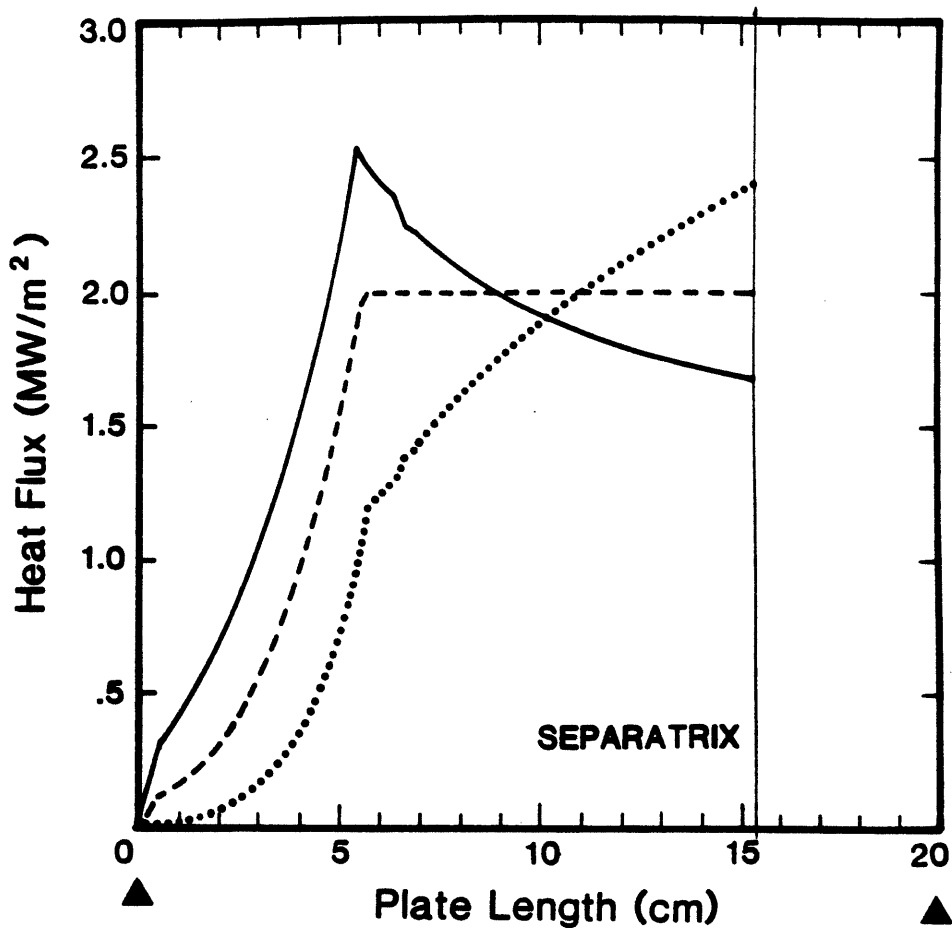
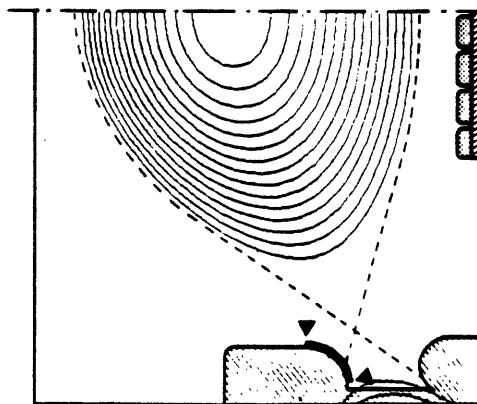


FIG. 2.4-5 Typical heat load on a divertor plate: arrows indicate correspondance between ordinate of heat flux figure (upper drawing) and actual surface (darkened area of surface shown in lower drawing).



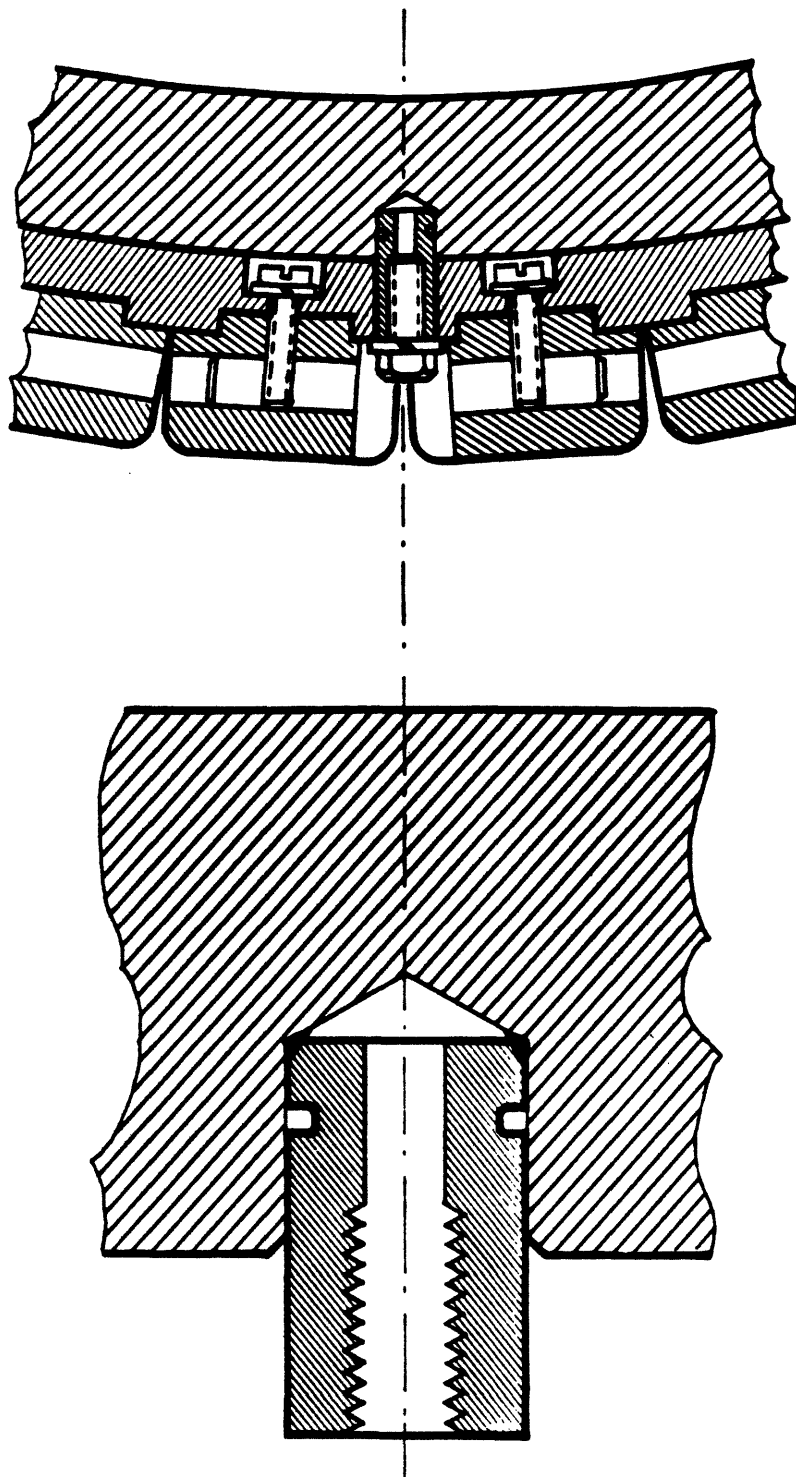


FIG. 2.4-6 Example of tile attachment method: upper figure shows Molybdenum tile mechanically attached to stainless steel spine. Spine is attached to wall by bolting to a threaded rivet which is welded to vessel wall (bottom figure - exploded view).

shown in Figs 2.4-4 and 2.4-5 are less than 2.5 MW/m^2 . Assuming a toroidal peaking factor of 2.5 the surface temperature was estimated for the worst case, 7 MW/m^2 heat fluxes for 3 seconds on molybdenum tiles. Ten minutes are allowed between heat pulses and radiative cooling was not included. The between-shot surface temperature increases over a period of ≈ 5 shots reaching the equilibrium shown in Fig. 2.4-7. The model results indicate that thermal conduction to the wall is sufficient to return the limiter/divertor surface to its starting value between shots. Evaporation from such temperature excursions would not be significant.

If the cooling by conduction fails, radiation cooling will keep the limiter from melting. Given the heat load duty cycle outlined earlier, the average rate of heat removal required between shots is $< 3.5 \text{ Watts/cm}^2$. If we were to require that all 3.5 Watts/cm^2 be removed by radiation cooling, the limiter surface temperature would rise to $\approx 1300^\circ \text{ K}$ (for) molybdenum). The surface temperature would then rise during a shot to $\approx 2000^\circ \text{ K}$, significantly below the melting temperatures of molybdenum. But more important, the resulting evaporation is still quite manageable ($\approx 5 \times 10^{17}/\text{sec}$).

References

- [2.4-1] E. S. Marmor, M. Foord, B. LaBombard, B. Lipschultz, J. Moreno, J. Nucl. Mater. 128 & 129 (1984) 69.
- [2.4-2] D. Sigmar, Appendix A-2.
- [2.4-3] D. Post ISP proposal.
- [2.4-4] M. Shimada, et al., Paper D-4, A.P.S. Topical Conference on Atomic Processes in High Temperature Plasmas, Princeton, 1983.
- [2.4-5] D.W. Doll, et al., General Atomic report GA-A16581.

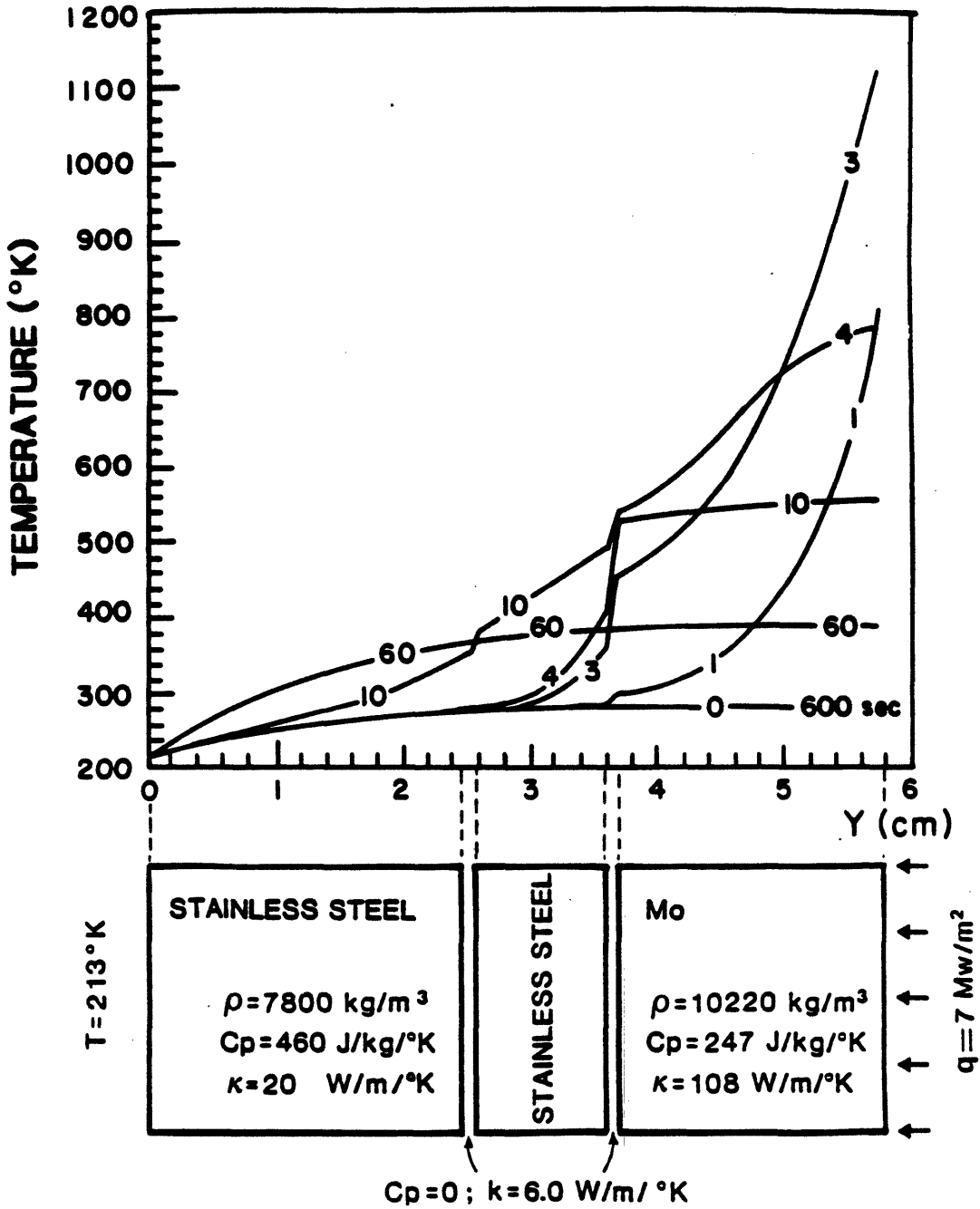


FIG. 2.4-7 Equilibrium temperature profile through tile-spine-wall configuration of previous figure for a heat load of 7MW/m^2 . Wall temperature is fixed at 213°K .

2.5 ICRF Heating of Alcator C-MOD

2.5.1 Background and Choice of Frequencies

Our understanding of ICRF heating physics has improved significantly over the past decade. This progress is a consequence of the rapid advances made in the ICRF experimental program both in the U.S. and abroad. A number of heating options are available which may be suitable candidates for heating a high density, high magnetic field ignition device. However, the experimental data available at present have been obtained at densities $\bar{n}_e \lesssim 0.5 \times 10^{20} \text{ m}^{-3}$, $B_T \lesssim 3 \text{ T}$, while a compact ignition device would operate at two to five times higher magnetic field, and at least an order of magnitude higher density. Experimental data on ICRF heating at such high densities are lacking at present. One of the purposes of the Alcator C-MOD program is to provide data on ICRF heating of such a high density, high magnetic field device.

A second unknown factor is the confinement properties in such plasmas, especially in the presence of intense ICRF heating. Alcator C-MOD is designed to explore the confinement properties in a downscaled compact ignition-type device, which nevertheless has the key ingredients, such as high plasma current and an effective divertor. This would also allow us to study ICRF antenna-plasma coupling in a compact high density device.

The ICRF power sources under consideration are the $P \sim 6 \text{ MW}$, $f = 180\text{-}215 \text{ MHz}$ FPS-17 radar transmitters (on location at MIT) and the $P \sim 10 \text{ MW}$, $f = 40\text{-}80 \text{ MHz}$ (upgradable to $120\text{-}150 \text{ MHz}$) FMIT sources (on location at PPPL). Both RF power systems require extensive upgrading. However, the FMIT sources would be useable on the compact ignition experimental device in the 1990's. In Fig. 2.5.1 we show the relevant frequencies as

ION CYCLOTRON FREQUENCIES OF INTEREST

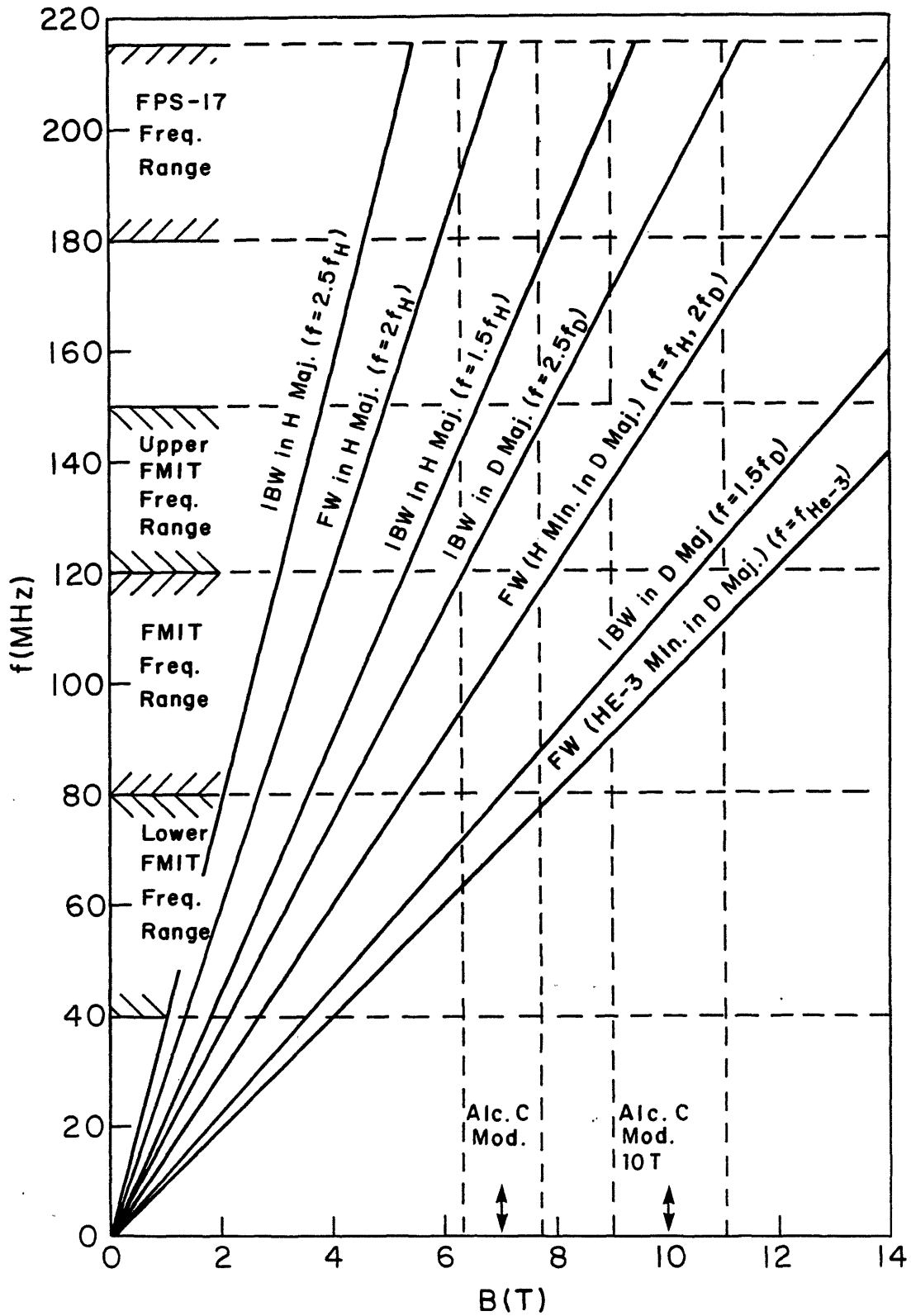


FIG. 2.5-1 Ion cyclotron frequencies of interest.

a function of magnetic field. Assuming a baseline machine operating at a central field of $B_0 = 7.0$ T, shown in Fig. 2.5.2 are the relevant fast wave ICRF frequencies. Of interest are the fast wave ion cyclotron harmonic heating ($\omega/\omega_H = 2$ at $f_0 = 215$ MHz), the fast wave minority heating in a deuterium plasma ($\omega/\omega_H = 1$ at $f_0 = 107$ MHz, or $\omega/\omega_{He-3} = 1$ at $f = 71$ MHz), or harmonic cyclotron heating in a deuterium plasma ($\omega/\omega_D = 2$) at $f = 107$ MHz. Here a range of frequencies is shown about the central value, corresponding to an acceptable off-axis power deposition profile of $|\Delta r|/a \lesssim 0.3$. Assuming an aspect ratio of $a/R \sim 1/3$, at a fixed frequency a variation in the magnetic field of $|\Delta B/B| \sim 0.1$ is allowed (i.e., $B_0 \sim 6.3-7.7$ T is acceptable). Alternatively, at $\omega/\omega_c = \ell$, at $B_0 = 7$ T, a change of $\Delta f/f_0 = \pm 0.1$ in the RF frequency is acceptable. In Fig. 2.5.2 we restrict the variations to $\Delta f/f_0 = \pm 0.10$, allowing for off-axis deposition of a fixed frequency and central magnetic field.

Possible Ion Bernstein Wave (IBW) heating scenarios are either nonlinear heating in a pure majority species plasma at $\omega/\omega_c(0) = (m + 0.5)$, where m is an integer, or minority heating using a heavy minority species (D or He-4) at $\omega/\omega_{cD}(0) = 2(m + 0.5)$, (m being an integer) and a lighter majority species, H. In Fig. 2.5.3 the frequencies of interest for IBW heating, using either the FPS-17 or the FMIT sources, are shown. Again, a $\pm 10\%$ frequency spread is allowed for possible off-axis power deposition. It may be seen that the frequencies of interest are nonlinear heating at $\omega/\omega_H = 1.5$ at $f_0 = 160$ MHz (off-axis heating at $f = 150$ MHz or $f = 180$ MHz), $\omega/\omega_D = 2.5$ at 134 MHz, and $\omega/\omega_D = 1.5$ at 80 MHz; or minority heating of D^+ or He-4 minority in a H^+ majority plasma at $f = 180$ MHz ($\omega/\omega_D = 3.0$). Possibilities in the full performance machine ($B_0 = 10$ T) include either nonlinear heating of a deuterium plasma at $f = 114$ MHz ($\omega/\omega_D =$

FAST WAVE HEATING REGIMES

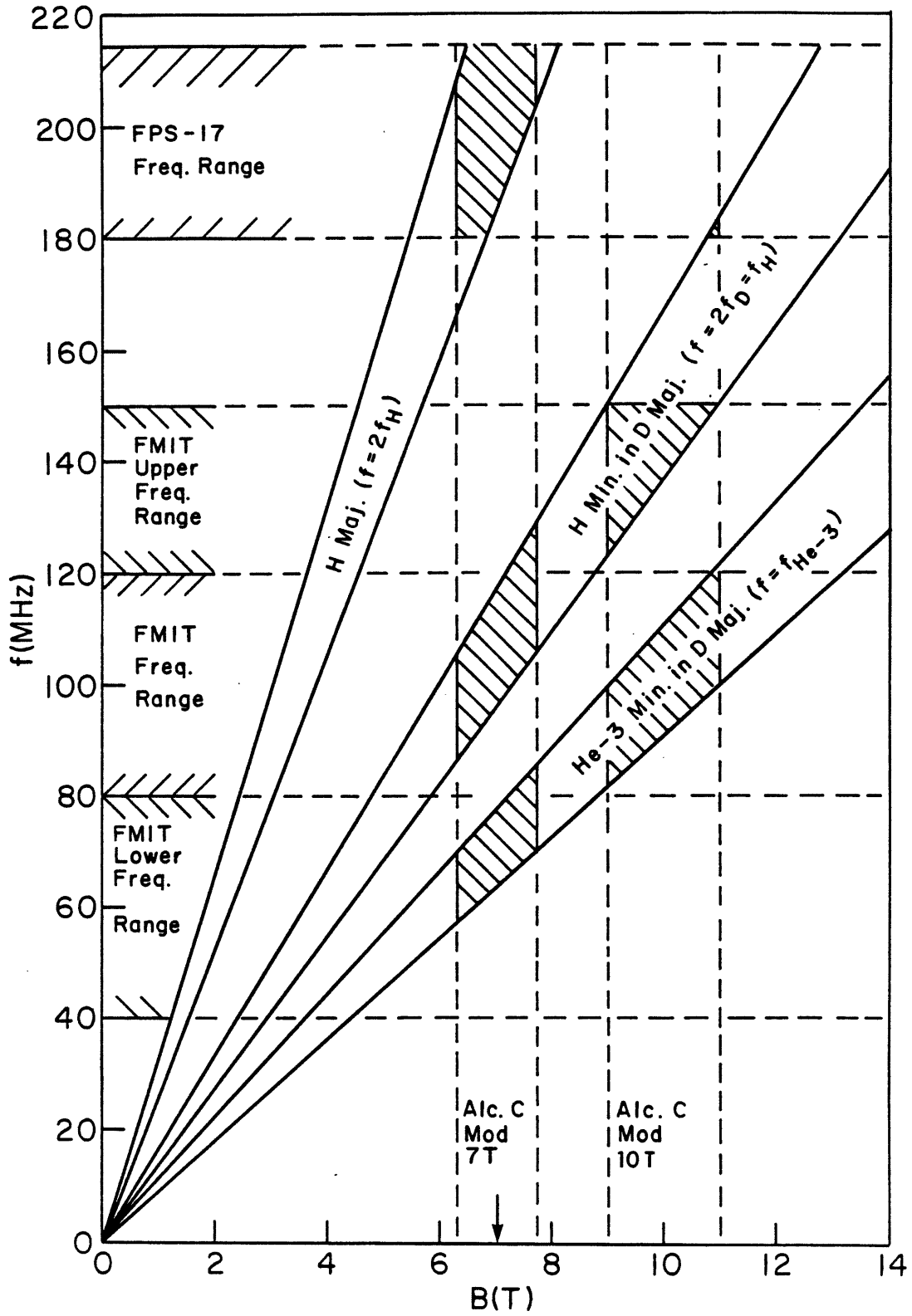


FIG. 2.5-2 Fast wave heating regimes.

ION BERNSTEIN WAVE HEATING REGIMES

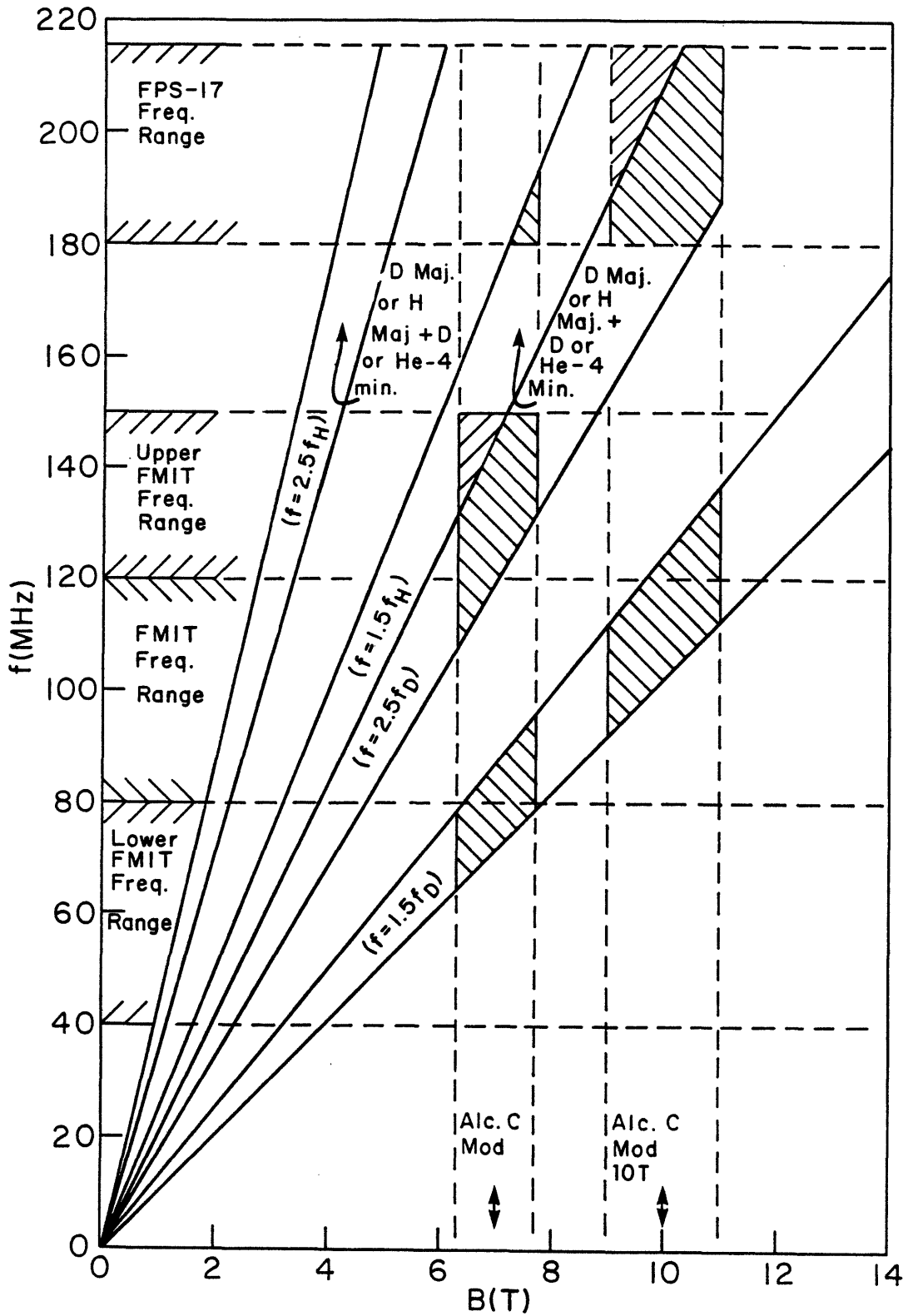


FIG. 2.5-3 Ion Bernstein wave heating regimes.

1.5) or at $f = 190$ MHz ($\omega/\omega_D = 2.5$), or off-axis nonlinear heating in a hydrogen majority plasma at $f = 215$ MHz ($\omega/\omega_H = 1.5$), with or without D or He-4 minority species.

To summarize, since a large range of possibilities exists, the availability of the RF equipment, the cost-effectiveness, and the expected degree of success should determine which scenario would be used. It should be emphasized, however, that given the scarce experimental data at high densities, the upcoming Alcator C experiments will be of considerable help in selecting the best heating scenario for Alcator C-MOD.

2.5.2. Absorption Efficiencies

a. Fast Wave Harmonic Resonance ($\omega = 2\omega_H$)

In a single ion species plasma, such as a pure hydrogen plasma, the dominant fast wave absorption mechanism is dominated by finite Larmor radius effects. Thus, absorption is enhanced at higher temperatures. Finite Larmor radius effects introduce two important effects: i) ion tail formation, which further enhances absorption, leading to increasingly larger ion tails. (ii) Coupling to the ion Bernstein wave which may propagate away from the harmonic resonance layer, thus reducing the heating effect. Bernstein waves (which propagate on the high magnetic field side) are relatively weakly damped by electrons (depending on k_z and T_e) and therefore may carry part of the power to the plasma edge. Bernstein waves which propagate above or below the midplane in the sheared magnetic field of a tokamak may be absorbed by electron Landau damping. Since this process is not well understood, it is best to design the antenna to launch waves which are not mode converted into Bernstein

waves. On the other hand, evanescent Bernstein waves, which are the by-product of mode-conversion of fast waves incident from the low magnetic field side, enhance absorption of the incident wave on ions. The situation is depicted in Fig. 2.5.4. Theory predicts that moderately large values of k_z tend to be absorbed on ions, whereas small values of k_z tend to be mode-converted. However, too large values of k_z reduce k_{\perp} and hence absorption. Further problems may occur for very large values of k_z which may be evanescent at the plasma edge, and hence do not couple to propagating modes, especially if the antenna is too far in the shadow of the limiter.

The single pass transmission coefficient of the fast wave incident from the low magnetic field side is given by

$$T_f = \exp(-2\eta),$$

where

$$\eta = \frac{\pi}{4} \beta_i R_0 \frac{\omega_{pi}}{c} \quad (1)$$

and β_i is the ion beta.

We note that when the Doppler width due to ion absorption is much less than the width of the evanescent layer, i.e., when

$$\frac{k_z v_{ti}}{\omega} \ll \sqrt{3} \beta_i \quad (2)$$

mode conversion is the dominant absorption process, with possible electron heating as the byproduct. In this case the reflected power, and the mode converted power for low-field side launch is

$$R = (1 - T_F)^2 \quad (3)$$

$$A = T_F(1 - T_F) \quad (4)$$

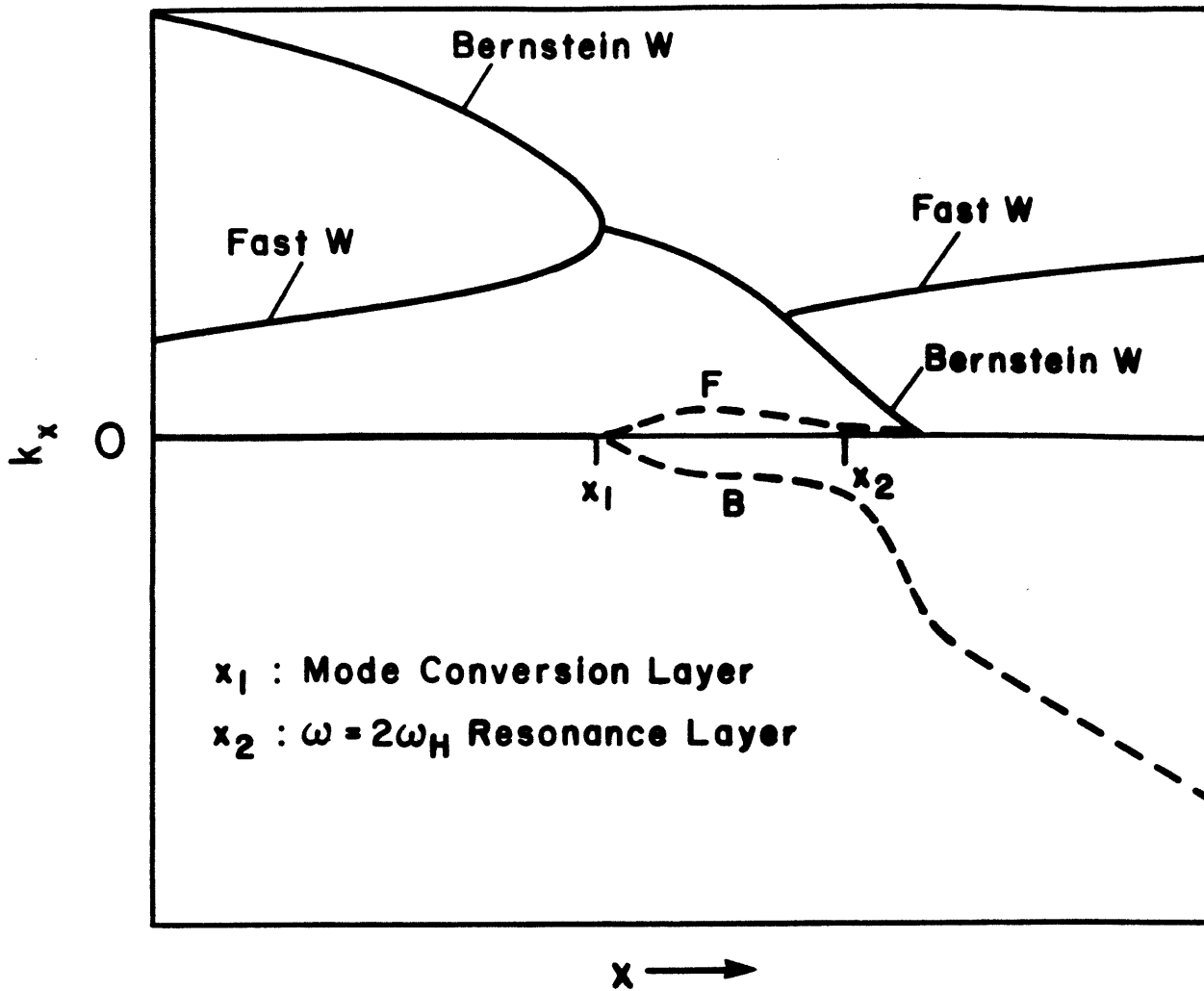


FIG. 2.5-4 Conceptualization of mode conversion and absorption processes near the $\omega = 2\omega_{ci}$ resonance layer for k_z finite. The dashed lines represent k_{IM} .

where T_F was defined by Eq. (1) (note that for high field side launch $R = 0$ and $T_B = 1 - T_F$, where T_B is the fraction of power mode converted to Bernstein waves). To achieve absorption on ions, for high field side launch we need

$$k_{zh} > \sqrt{3} \beta_i \omega / v_{ti}, \quad (5)$$

and for low field side launch one finds that typically, $k_{z\ell} \approx k_{zh}/3$. (This is a consequence of the fact that for low field side launch the evanescent Bernstein wave is absorbed more directly.) The fraction of power being transferred to ions as a function of k_z can be determined only by solving the fourth order mode coupling equation, including dissipation. Typically, the maximum power that can be absorbed by ions is

$$A_I \approx 1 - T_F \quad (6)$$

which is usually achieved at intermediate values of k_z (i.e., between $k_{z\ell}$ and k_{zh}). For example, in the present case for Alcator C-MOD, $R = 75$ cm, $B = 7$ T, $T_i = 1.0$ keV, $n_i(0) = 6 \times 10^{14}$ cm $^{-3}$, we find that $\beta_i = 0.4\%$, $\eta = 0.25$, and $T = 0.60$. Thus, at most 40% of the power is available for ion heating. Equation (5) predicts that ion heating would dominate mode conversion for high field side launch only for $k_{zh} > 0.2$, and for low-field side launch $k_{z\ell} \gtrsim 0.07$. Thus, a reasonable value of k_z for optimizing ion absorption is near $k_z \sim 0.15$. To substantiate these estimates, we used Colestock's code [2.5-1] to determine the power flow more accurately. Figures 2.5.5-2.5.9 display results of code calculations for Alcator C-like parameters ($R = 64$ cm, $B = 6$ T), which are close to the C-MOD parameters since $R_0 T_i / B^2$, and hence η remain nearly the same). It may be seen that while at $n_e \sim 1 \times 10^{14}$, $T_e = 1.5$ keV, $T_i = 0.7$ keV,

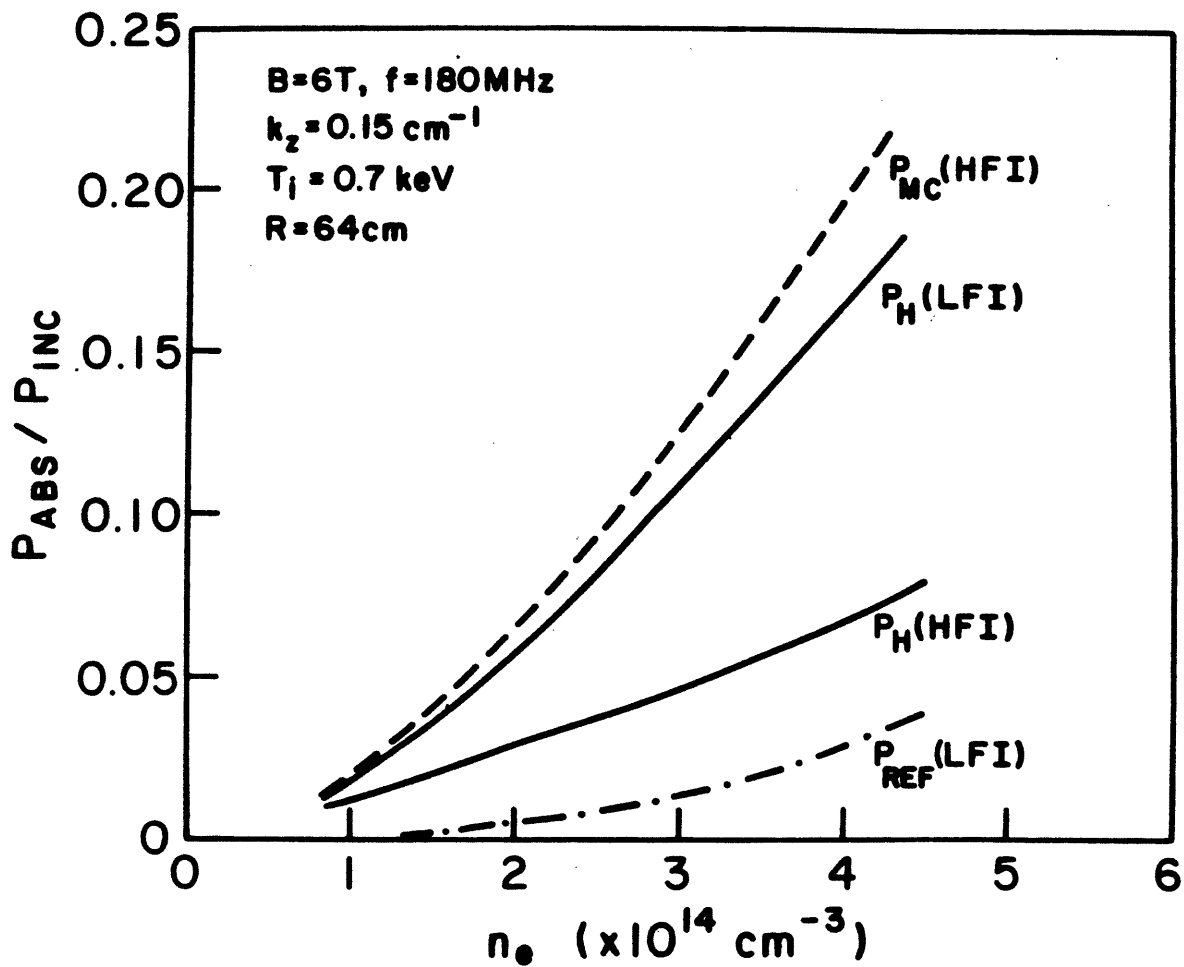


FIG. 2.5-5 Single pass absorption efficiencies as a function of density for $B = 6T, f = 180MHz, T_e = 1.5keV, T_i = 0.7keV, R = 64cm,$ and $k_z = 0.15.$

$P_{MC}(HFI)$ = mode converted power, high field incidence
 $P_H(HFI)$ = power absorbed by ions, high field incidence
 $P_H(LFI)$ = power absorbed by ions, low field incidence
 $P_{REF}(LFI)$ = power reflected, low field incidence

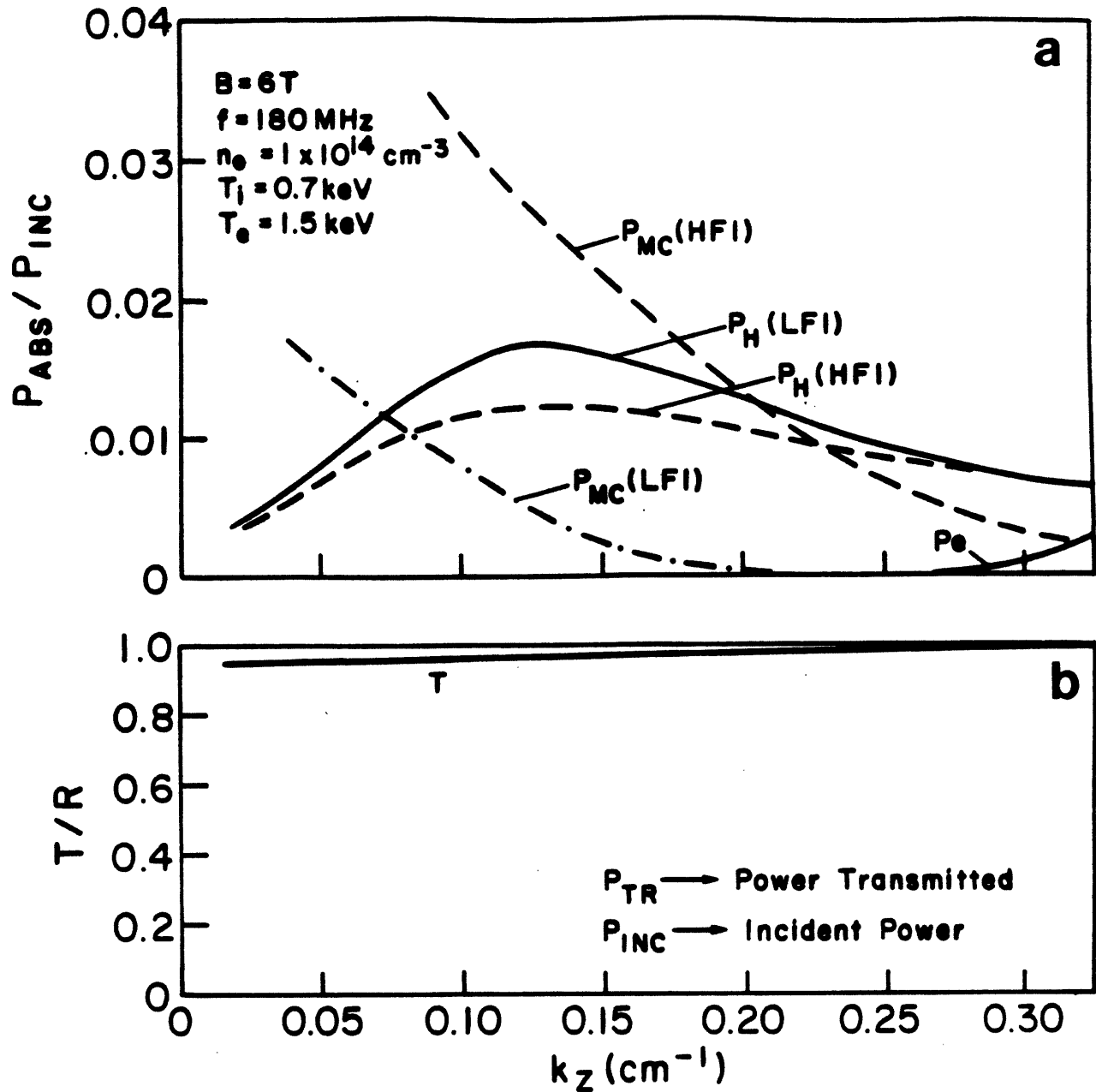


FIG. 2.5-6 (a) Single pass absorption efficiencies at $n_e = 1 \times 10^{14}\text{ cm}^{-3}$, as a function of k_z . P_e is direct electron absorption by electron Landau damping and TTMP.

(b) Transmission coefficient (T) for the same parameters as in (a).

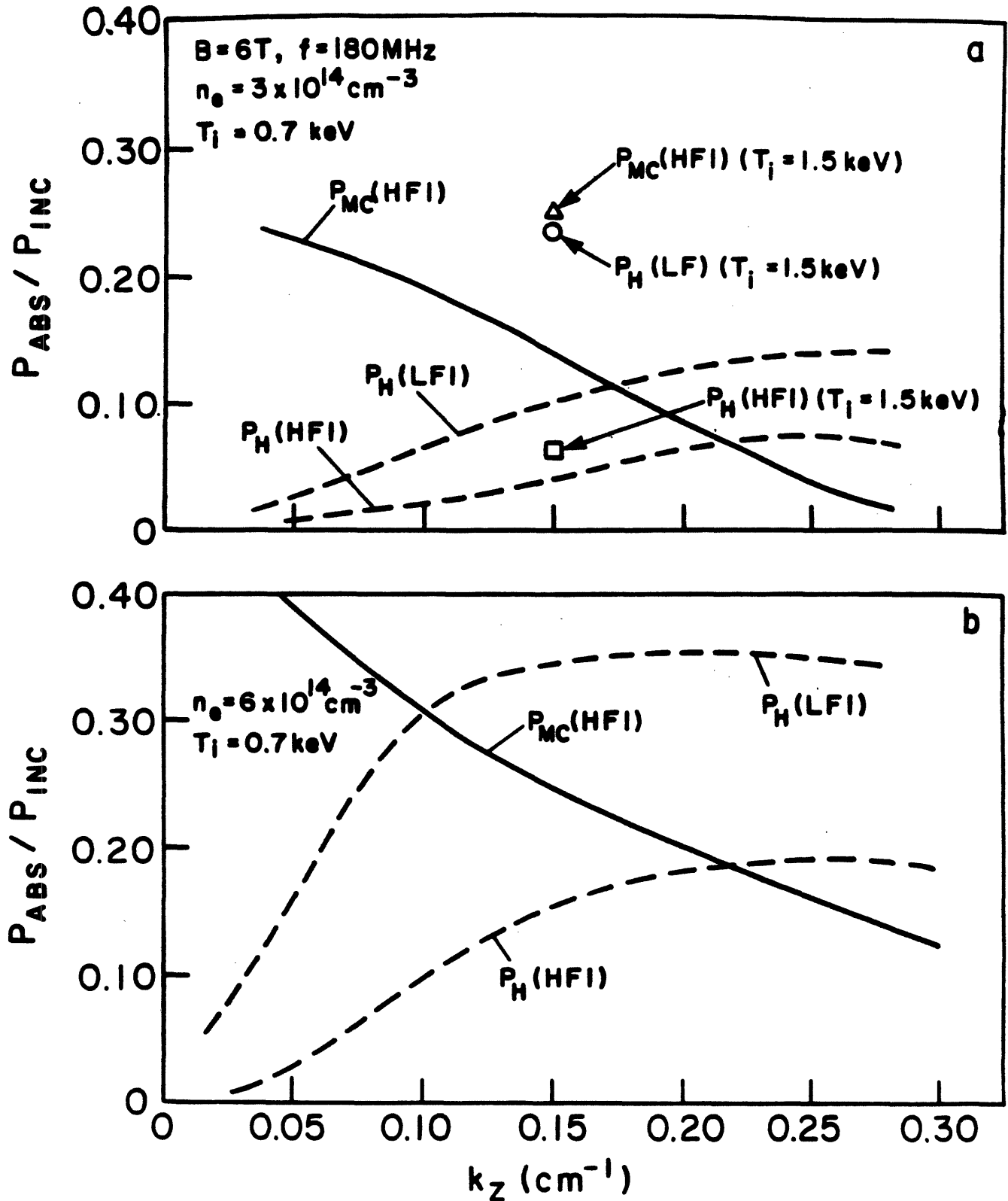


FIG. 2.5-7 Single pass absorption efficiencies versus k_z for $T_e = 1.5 \text{ keV}$, $T_i = 0.7 \text{ keV}$, $R = 64 \text{ cm}$.

(a) $n_e = 3 \times 10^{14} \text{ cm}^{-3}$ (b) $n_e = 6 \times 10^{14} \text{ cm}^{-3}$

Also shown in (a) are a few higher temperature ($T_i = 1.5 \text{ keV}$) points.

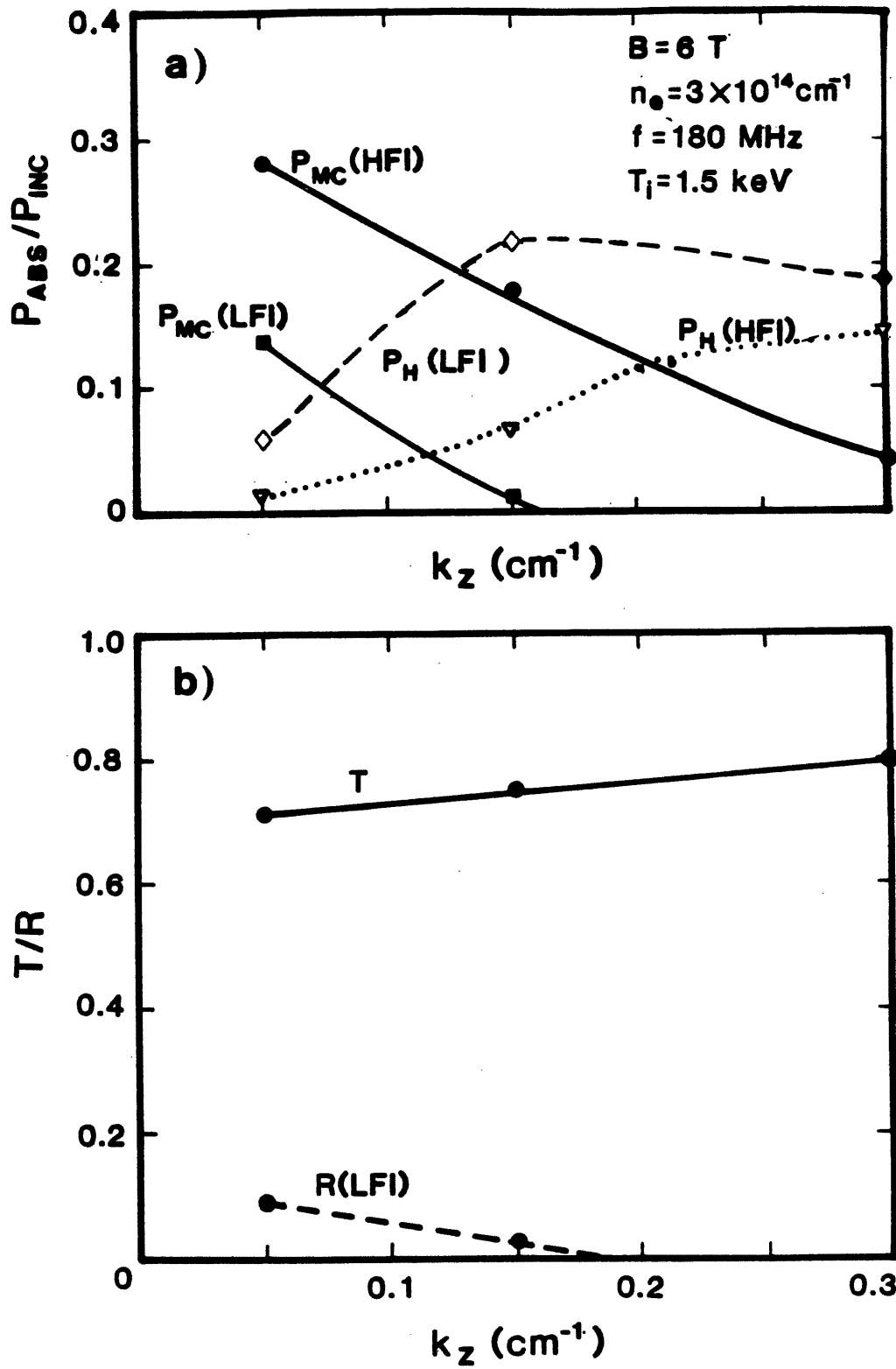


FIG. 2.5-8 (a) Single pass absorption efficiencies versus k_z at $n_e = 3 \times 10^{14} \text{ cm}^{-3}$, $T_e = T_i = 1.5 \text{ keV}$.

(b) Transmission coefficient (T) and reflection coefficient (R), the latter for low-field side incidence.

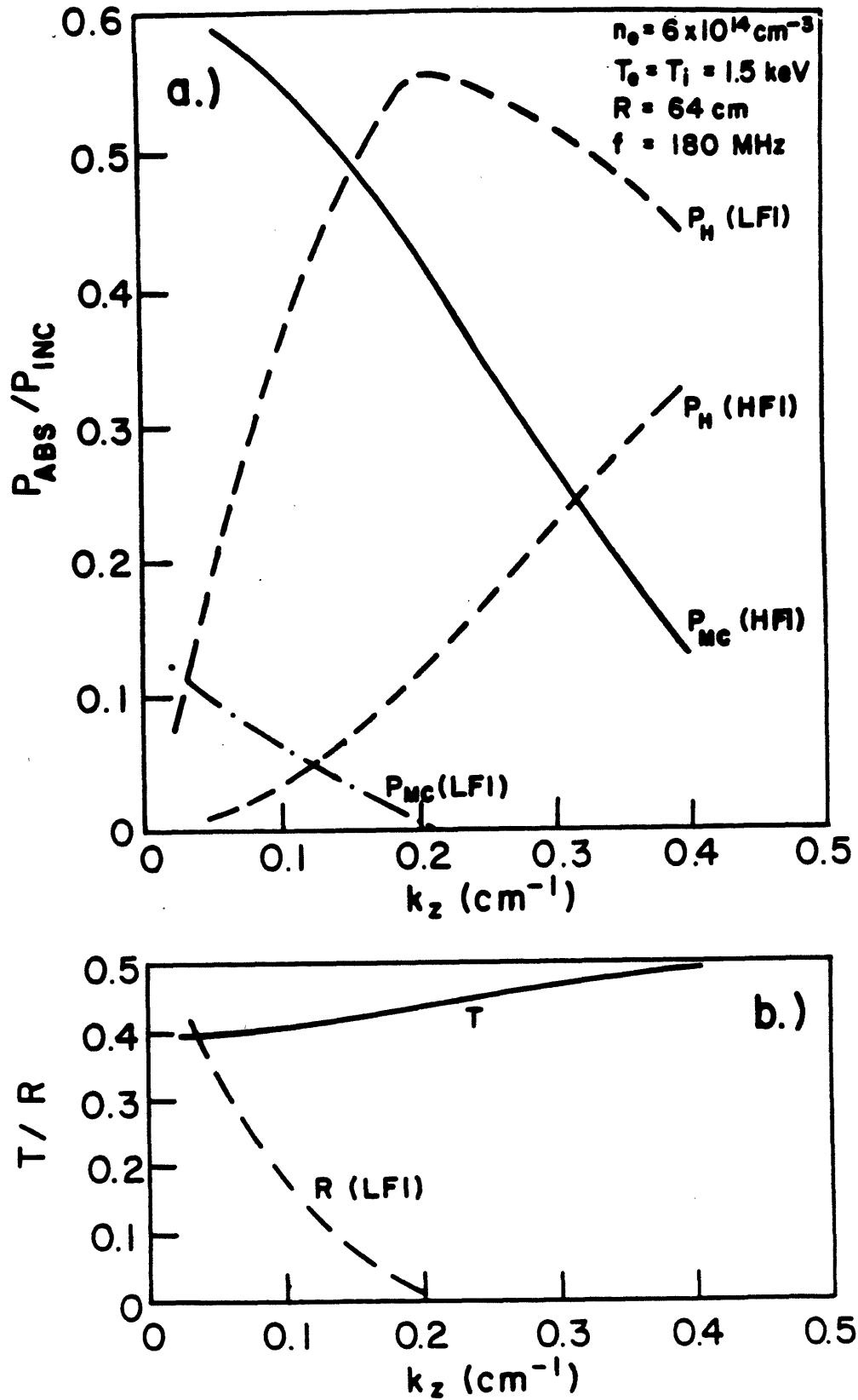


FIG. 2.5-9 (a) Single pass absorption efficiencies versus k_z at $n_e = 6 \times 10^{14} \text{ cm}^{-3}$, $T_e = T_i = 1.5 \text{ keV}$.

(b) Transmission coefficient (T) and reflection coefficient (R), the latter for low-field side incidence.

$B = 6 \text{ T}$, $f = 180 \text{ MHz}$ the absorption on ions is at most 1%, at $n_e \approx 3 \times 10^{14}$ low field side launch achieves $A \sim 0.15$ at $k_z \sim 0.25$, and at $n_e \sim 6 \times 10^{14}$, $A \sim 0.35$ is achieved for $k_z \gtrsim 0.15$. These results are in reasonable agreement with the analytic estimates. It is clear that for high field side launch mode conversion dominates absorption by ions, at least for $k_z \lesssim 0.2$. For higher values of k_z ion absorption may exceed mode conversion, but then the maximum absorption remains about one half of the low field side value due to a gradual reduction of the FLR effects. Thus, low field side launch is preferred. At higher temperatures even better absorption may be achieved (see the three points on the $n_e = 3 \times 10^{14} \text{ cm}^{-3}$ figure, where $T_i = 1500 \text{ eV}$ was assumed; the absorption for low field side launch approximately doubled). Also, Figs 2.5.8 and 2.5.9 show absorption curves with $T_e = T_i = 1.5 \text{ keV}$, at $n_e = 3 \times 10^{14} \text{ cm}^{-3}$ and $6 \times 10^{14} \text{ cm}^{-3}$, respectively. We see that for low field side launch, up to 55% of the power is absorbed in the first pass for $k_z \gtrsim 0.15$. Thus, as the plasma heats up, above a few keV temperature at $n_e = 6 \times 10^{14} \text{ cm}^{-3}$ more than 50% of the power may be absorbed during the first pass for optimal values of k_z . The optimal values are in the range $k_z \approx 0.1-0.3$. A 15 cm wide antenna (which can be fitted into the Alcator C-MOD ports) would have a characteristic Fourier spectrum of $\pi/d \sim 0.20$, a reasonable value. However, some fraction of the power will inevitably fall into the mode conversion regime (especially as the transmitted wave is reflected from the high-field side). Hopefully, at least at the higher temperatures this should lead to electron heating. To avoid large sawtooth effects, off-center location of the mode-conversion layer may be desirable. Finally, note that for $k_z \lesssim 0.05$, mode conversion dominates ion absorption for either low or high field side incidence.

As we remarked earlier, the absorption of waves on ions leads to a high energy tail formation. As an example, in Fig. 2.5.10 we display a Fokker-Planck calculation for Alcator C parameters at a density of $n_{i0} = 3 \times 10^{14} \text{ cm}^{-3}$, $P_{\text{rf}} = 600 \text{ kW}$ for $k_z = 0.2 \text{ cm}^{-1}$. Here the power was assumed to be deposited uniformly in the inner central region of the plasma ($\Delta r/a = 0.4$). It is apparent that an ion tail develops. These results may be scaled to Alcator C-MOD at $n_i(0) = 6 \times 10^{14} \text{ cm}^{-3}$, by noting that $P/\text{VOL} \times n_i^2(0)$ is smaller by a factor of two at $n_i(0) = 6 \times 10^{14} \text{ cm}^{-3}$, if $P = 4.8 \text{ MW}$ (since the effective volume is four times greater). Hence, we expect little ion tail formation even at full RF power, unless the power deposition is highly peaked near the center (not usually observed in experiments). More quantitative estimates of ion tail production are presented in the next section dealing with minority absorption, where essentially the same conclusions are reached. Thus, the absorption calculations presented here remain substantially correct, at least in the high density regime.

b. Minority Fast Wave Absorption

This mode of heating may be of some interest for Alcator C-MOD in case the FMIT sources were available, and if one were to use a deuterium majority species plasma. Then, a hydrogen minority species may be heated at $f_0 = 107(\pm 11) \text{ MHz}$, or a He-3 minority species may be heated at $f_0 = 70(\pm 7) \text{ MHz}$ at $B = 7 \text{ T}$. Furthermore, similar techniques may be used in a full-field operation ($B = 10 \text{ T}$) at $f = 150 \text{ MHz}$ or $f = 100 \text{ MHz}$, respectively. Operating with a deuterium majority plasma assumes that adequate shielding against neutron radiation is available.

Assuming low field side incidence, the power transmitted (T), reflected (R) and absorbed (A) are given by Budden factors similar to the harmonic absorption case,

$2\omega_{CH}$ HYDROGEN DISTRIBUTION FUNCTION

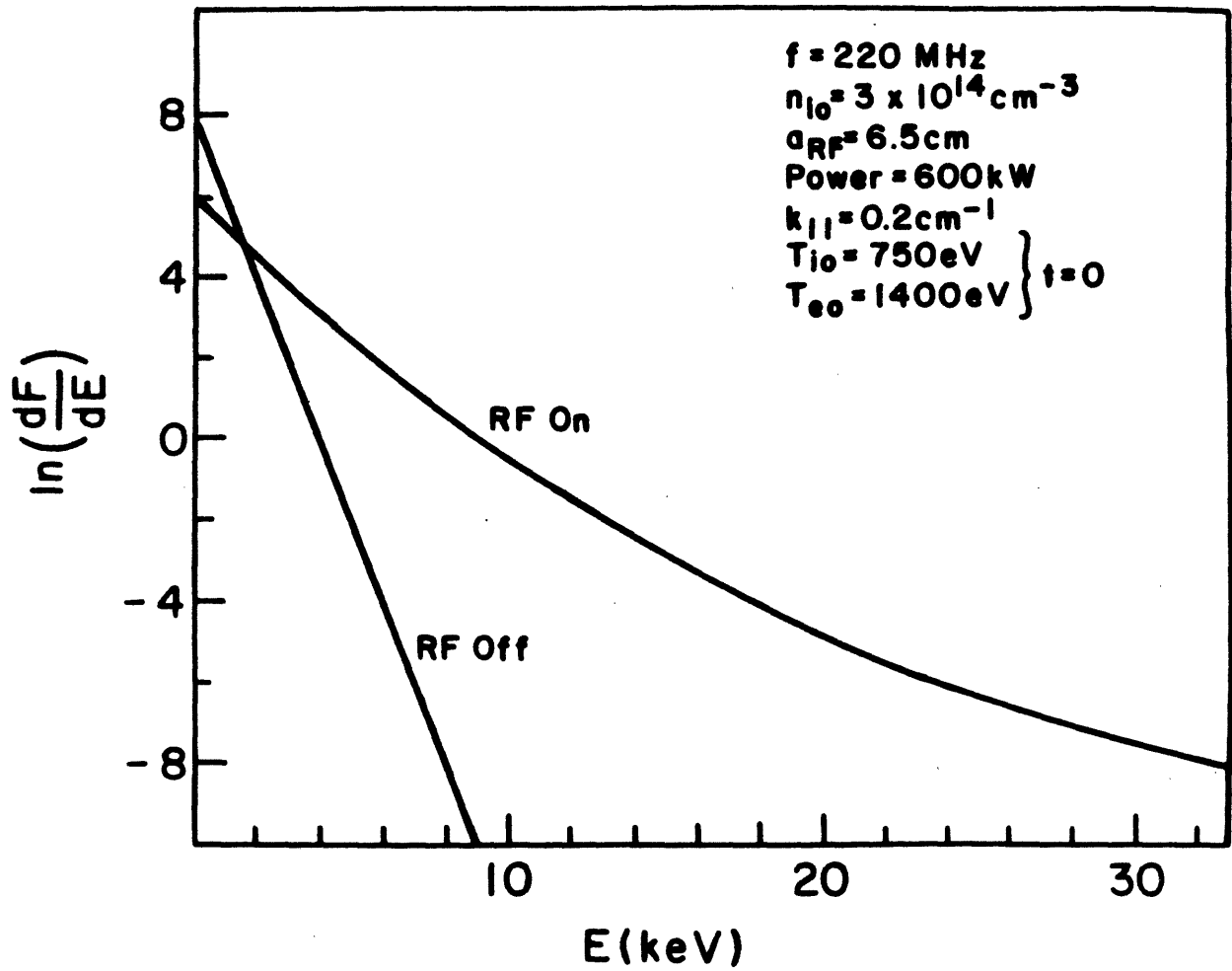


FIG. 2.5-10 Fokker Planck code calculations for Alcator-C like parameters.

$$T = \exp(-2\eta_m), \quad (7a)$$

$$R = (1 - T)^2, \quad (7b)$$

$$A = T(1 - T), \quad (7c)$$

but where the tunneling factor is given by the expression (on the midplane):

$$\eta_{\min} = \frac{\pi}{4} \frac{\omega_{PD}}{c} R \frac{n_m}{n_e}. \quad (8)$$

Here n_m is the minority species concentration (density), n_e is the total electron density, R is the major radius, and ω_{PD} is the deuterium (majority species) ion plasma frequency (in radians). Note that these expressions differ from the ion cyclotron harmonic heating only in the factor n_m/n_e replacing β_i in η . Thus, in general, using hydrogen minority in a deuterium plasma the total absorption factor is given by

$$\eta_{\text{tot}} = \eta_{2\omega_{ci}} + \eta_m \quad (9)$$

(since the two resonances coincide).

If the temperature is sufficiently high, $\eta_{2\omega_{ci}}$ may exceed η_m . Assuming $n_m/n_e = (0.01-0.05)$ for our parameters this would occur only for ion temperatures in excess of (2-10) keV, respectively. In general, for Alcator C-MOD minority absorption would then dominate. However, as before the absorption would end up in mode converted Bernstein waves on the high magnetic field side, unless k_z is large enough to spread the width of resonance (on minority ions) across the width of the evanescent layer (i.e., the region between the ion-ion mode conversion layer on the high field side, and the minority cyclotron resonance layer on the side of incidence). The width of the evanescent layer is typically

$$\Delta x \approx R_0 \frac{n_m}{n_e} \quad (10)$$

Thus, to achieve optimal ion heating, the condition on the width of the resonance gives

$$k_z \gtrsim \frac{n_m}{n_e} \frac{\omega}{v_{tH}} \quad (11)$$

in which case the absorption by ions is approximately $A \approx 1 - T$. Otherwise mode conversion into Bernstein waves dominates. For initial C-MOD parameters, Eq. (11) gives $k_z \gtrsim 16(n_m/n_e)$. Thus, for $n_m/n_e > 10^{-2}$, $k_z \gtrsim 0.16$ to satisfy Eq. (10). Meanwhile, for Eq. (8), at $n_e = 6 \times 10^{14} \text{ cm}^{-3}$, $R = 75 \text{ cm}$,

$$\eta_m \approx 45 \frac{n_m}{n_e}, \quad (12)$$

so that for $n_m/n_e \sim 10^{-2}$, $\eta \approx 0.45$. The power absorbed by ions is given by

$$A_1 \sim 1 - e^{-2\eta_m} \quad (13)$$

which for the present case yields $A_1 \approx 0.60$. It turns out that for optimal absorption it is better to have $\eta_m \gtrsim 1$, and hence $n_m/n_e > 0.01$. A desirable range of values is $n_m/n_e \sim 0.01-0.05$. This dictates that the absorption processes will be partially in the mode-conversion regime. The fraction of power absorbed by ions in the mode conversion regime may be calculated by accounting for the screening of the E^+ component of the electric field. The fraction of power absorbed by ions in the mode conversion regime is estimated to be:

$$A_2 \approx \pi \frac{\omega_{PD}}{c} R \frac{n_e}{n_H} \frac{k_z^2}{\omega^2} v_{tH}^2 \quad (14)$$

where $v_{tH}^2 = 2T_H/m_H$. This expression is valid as long as the opposite of Eq. (11) is satisfied, namely

$$k_z < \frac{\omega}{v_{tH}} \frac{n_H}{n_e} \quad (15)$$

(thus, $n_H \neq 0$).

Consider then the parameters $n_H/n_e \approx 0.02$, $T_H = 1.0$ keV, $n_e = 6 \times 10^{14} \text{ cm}^{-3}$, $R = 75$ cm, $f = 107$ MHz, so that

$$A_2 \approx 36 k_z^2 .$$

Therefore, for $k_z \approx 0.1$, $A_2 \gtrsim 0.36$, a significant fraction. For $k_z > 0.32$, Eq. (13) is valid (see Eq. (11)) and it predicts $A_1 \approx 1 - \exp(-1.8) \approx 0.84$, a very large factor (we note that A_2 cannot exceed A_1 , since A_1 is an upper limit for absorption). Therefore, it may be concluded that for ion temperatures of a few keV, and minority concentrations of a few percent, near complete absorption is obtained for parallel wavenumbers $k_z > 0.1$. Furthermore, higher effective temperatures of the minority species is easily achieved since the total number of particles is significantly less than the majority species. Therefore, using minority heating in a deuterium majority plasma (assuming the FMIT transmitters) large single pass efficiencies can be obtained. We note that the multi-mega-ampere currents available in Alcator C-MOD would be sufficient to confine the energetic minority concentration. The optimal range of parallel wavenumbers is similar to those for harmonic cyclotron heating, namely $0.1 \lesssim k_z \lesssim 0.4$. Hence, 15 cm wide antennas ($k_z \sim 0.2$) should again be

$\lesssim k_z \lesssim 0.4$. Hence, 15 cm wide antennas ($k_z \sim 0.2$) should again be satisfactory. Finally, we note that Fokker-Planck code calculations, as well as previous experiments in Alcator C at densities $\bar{n}_e \sim 2 \times 10^{14} \text{ cm}^{-3}$ demonstrated significant minority component heating.

Minority heating leads to development of a high energy "tail" type of distribution of the minority species. Stix has solved the quasi-linear equation to determine the mean effective temperature of the minority species [2.5-2]. The equivalent minority temperature is found to be

$$T_{eq} = u \xi T_e, \quad (16)$$

where for hydrogen minority ξ may be written in the form

$$\xi = 10^{26} \frac{(1 + \eta_p)}{\eta_p} \frac{P(\text{W cm}^{-3}) T_e^{1/2} (\text{eV})}{n_e^2 (\text{cm}^{-3})}$$

with $\eta_p = n_m/n_e$, and u is a coefficient slightly less than one. Equation (16) is useful when $\xi \gg 1$ (otherwise, $T_{eq} \sim T_e$). Taking $P = 5 \text{ MW}$ deposited in an effective minor radius of $r/a \sim 0.4$ and taking elongation into account, the RF power density for $a = 25 \text{ cm}$ would be $\sim 15 \text{ W/cm}^3$. Thus, taking $\eta_p = 0.03$, $n_e = 5 \times 10^{14} \text{ cm}^{-3}$, $T_e \approx 6 \text{ keV}$, we obtain $\xi \approx 0.5$. Thus, we do not expect any significant ion tail formation under these conditions (unless the power were deposited in a small central region, say $r/a \lesssim 0.2$; even then, at $T_e \sim 1 \text{ keV}$, $\xi \lesssim 1$). Note also that at the initial conditions $T_e \sim 1 \text{ keV}$, $\xi \sim 0.2$, and no tail should develop. The same conclusions hold even for $\eta_p \approx 0.02$. Hydrogen tail development begins at $\eta_p \lesssim 0.01$, $T_e \gtrsim 6 \text{ keV}$. However, as we saw earlier, for $\eta \lesssim 0.01$, the single-pass absorption efficiency decreases, an undesirable regime. Therefore, for all practical purposes at the high densities

envisaged in Alcator C-MOD, minority tail does not develop. Using a He-3 minority, the effective value of ξ is reduced; in particular, $\xi(\text{He-3}) = 0.75 \xi(\text{H})$. Thus, not even in the He-3 minority operation will an ion tail be developed. This brings up the question of the channel of power-flow during minority heating. In particular, the slowing down on electrons must be examined. It is found that for small values of ξ most of the energy ends up in majority ions by collisional equilibration between the minority and majority ions. Thus, electron heating is due only to absorption of the mode converted Bernstein waves (for $k_z < 0.1$).

c. Ion Bernstein Wave Heating

The concept of ion Bernstein wave heating utilizes short wavelength electrostatic waves which are absorbed by cyclotron harmonic damping (either linear or nonlinear) near the plasma center. Recent experiments both on JIPP-T-II-U and PLT produced very favorable results (with no apparent deterioration of confinement) at densities up to $\bar{n}_e \lesssim 2 \times 10^{13} \text{ cm}^{-3}$ [2.5-3]. The condition for direct Bernstein wave heating is that near the center of the plasma the condition

$$\omega = (m + 0.5)\omega_{ci} \quad (17)$$

be satisfied. Condition (17) may be satisfied even in a single ion species plasma, in which case nonlinear Landau absorption becomes operative at $2\omega = (2m + 1)\omega_{ci}$. Alternatively, even at low power level minority absorption may take place when condition (17) is satisfied for the majority species (say hydrogen) and for a minority species the condition

$$\omega = l\omega_{cm} \quad (18)$$

is satisfied simultaneously. Such is the case for hydrogen majority, and a minority species with $z_m/m_m = (1/2m_H)$, so that $l = (2m + 1)$. Thus, minority absorption on deuterium or He-4 would occur in a hydrogen majority plasma. The relevant frequencies were given in Figs 2.5.1 and 2.5.3 (including frequency spread). In the case of minority absorption, complete single pass absorption occurs under typical tokamak conditions. The power is absorbed by the bulk of the minority species, leading to an energetic component, which then transfers its power to the majority species by collisions. Since the wavelengths are short, the bulk of the minority species is heated ($\omega/k_{\perp} \sim v_{Ti}$). The question of efficiency, then, is determined by the efficiency of ion Bernstein wave generation. The waves are generated by an antenna with a polarization 90° relative to the fast wave. Thus, the long antenna dimensions are parallel to the magnetic field, and at the antenna surface the frequency is just slightly below the exact local cyclotron harmonic frequency of the majority species. An attractive feature of Bernstein wave launching is the possibility of utilizing a waveguide as an antenna, at least with dielectric loading in present day machines. For waveguide launching the TE_{10} mode may be used, (similarly to lower-hybrid launching). However, one or two adjacent waveguide(s) may be satisfactory at these low frequencies.

Recent experiments have shown that, at least in PLT and JIPP-T-II-U, nonlinear mechanisms were the dominant absorption processes. This leads to the attractive feature of majority species, bulk (T_{\perp}) ion heating, even in the presence of a minority species. The threshold for nonlinear pump depletion was calculated recently by Porkolab, and the following result was obtained [2.5-4]. With no minority species present, the threshold is given approximately by the expression:

$$\frac{4.7 \times 10^{18} P(W) R(\text{cm}) \omega_{ci}^2}{v_{ti}^2 (\text{cm/sec}) n_0 (\text{cm}^{-3}) T_i (\text{eV}) A (\text{cm}^2) \omega} > 1 \quad (19)$$

where $v_{ti}^2 = 2 T_i/m$ and A is the antenna surface area. Thus, for $R = 75$ cm, $f = 180$ MHz, $f = 1.5 f_{CH}$, $T_i = 1.0$ keV, $n_0 = 5 \times 10^{14}$ cm^{-3} , Eq. (19) predicts an antenna power density of

$$P/A > 5 \text{ kW/cm}^2 ,$$

which in general is somewhat on the high side (a more reasonable value is $P/A \lesssim 2 \text{ kW/cm}^2$). However, in the presence of a minority species the nonlinear threshold is greatly reduced, typically by a factor of 10^2 - 10^3 , or down to ~ 10 Watt/ cm^2 , which is easily exceeded in most experiments. Thus, the dominant heating mechanism would be nonlinear absorption on majority hydrogen, assuming that a few percent of impurities (D, He-4, etc.) were present. We note that a dielectric loaded waveguide (Alumina, Al_2O_3 , or BeO) could be used to launch the waves. In summary, for Alcator C-MOD the appropriate frequency for Bernstein wave heating is 180 MHz in a hydrogen majority plasma, with a few percent of D minority species. The dominant absorption mechanism is nonlinear Landau (cyclotron) damping, leading to bulk (T_{\perp}) absorption directly by the hydrogen majority. The absorption efficiency is expected to be 100% per single pass.

2.5.3. The Alcator C-MOD ICRF System

a. Fast Wave Antenna

A wide loop antenna or a cavity loop coupler may be used as the coupler concept for the baseline ICRF design for Alcator C-MOD. Each antenna is constructed so that it will slide into a horizontal port (each about 14 cm wide and 80 cm high). The system will consist of four (eight) antennas,

each rated at 1.25 MW (0.62), in four (eight) ports of Alcator C-MOD (the power density on each antenna is 1.1 kW/cm^2 (0.55 kW/cm^2)).

One antenna module consists of a loop $14 \text{ cm} \times 40 \text{ cm}$ (poloidally) above and below the midplane as shown in Fig. 2.5.11. The antenna is fed from the ends and terminated in a short at the midplane. Current maxima (voltage minima) occur at the midplane and at the feed point because the length is near a half wavelength, taking into account the reduction in phase velocity caused by the capacitive loading from the shield. The shield consists of horizontal conducting straps surrounding the center conductor. Alumina shielding between the Faraday shield and the center conductor may be provided if detailed design requires it.

The antenna width limits k_z to $|k_z| \lesssim 0.20 \text{ cm}^{-1}$, and the evanescent region will limit $|k_z|$ to comparable values, depending on the edge density profile. The single pass absorption is sufficiently high (30 - 90 %) so that the radiation resistance of the antenna can be approximated by considering an antenna radiating into a plasma of infinite extent. In addition, the reduced importance of reflections from the wall allows a rectangular slab model to be used, at least for radiation resistance calculations. A second type loop antenna, consisting of two phased adjacent segments, may be considered for controlling the k_z spectrum.

We define the lumped radiation resistance of the antenna (R_r) as the resistance which, when placed at the end of a transmission line with the same characteristic impedance as the antenna (Z_a), results in the same terminal impedance as the antenna. An examination of the scaling of R_r reveals that while the radiation resistance increases with the length of the antenna, it decreases as the antenna is made wider. The decrease in



FIG. 2.5-11 Alcator C-MOD fast wave ICRF antenna concept (1 MW module).

radiation resistance is compensated by a decrease in the characteristic impedance of the antenna (Z_a) so the standing wave ratio is not degraded. Further, if the impedance of the feed transmission line is matched to Z_a without sacrificing voltage stand-off, the power available to the antenna actually increases with the width of the antenna.

The antenna shown in Fig. 2.5.11 has a characteristic impedance of 20 ohms, and a radiation resistance (R_r) of 2-5 ohms, depending on the plasma density profile. Separate feeds to the upper and lower elements allow a straightforward connection to the eight sources, and provide for some control of the azimuthal mode number by phasing the elements separately. The individual RF sources can be phased at a low power level. The antenna design shown in Fig. 2.5.11 can easily be altered to form a phased double array, or a cavity-loop antenna, of the type considered for big DIII-D [2.5-5]. A typical resonant cavity antenna is shown in Fig. 2.5.12. A detailed design of such an antenna will be carried out to determine its compatibility with Alcator C-MOD ports and frequencies.

b. Bernstein Wave Antenna

A schematic of a conventional loop-type ion Bernstein wave antenna is shown in Fig. 2.5.13. It is the MIT "T-bar" type antenna design. Its advantage is easy installation into a port in the vertical direction, followed by a 90° rotation so the antenna itself is aligned parallel to the magnetic field. The length is of the order of 50 - 80 cm in the long dimension, and 13 - 15 cm wide so it may be inserted in the port. The main design consideration is that the length be long enough to avoid electron Landau damping near the plasma center for the majority of the k_z

84T0003

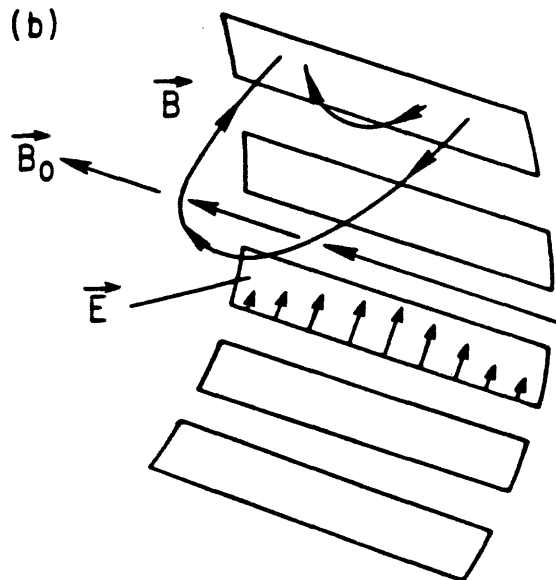
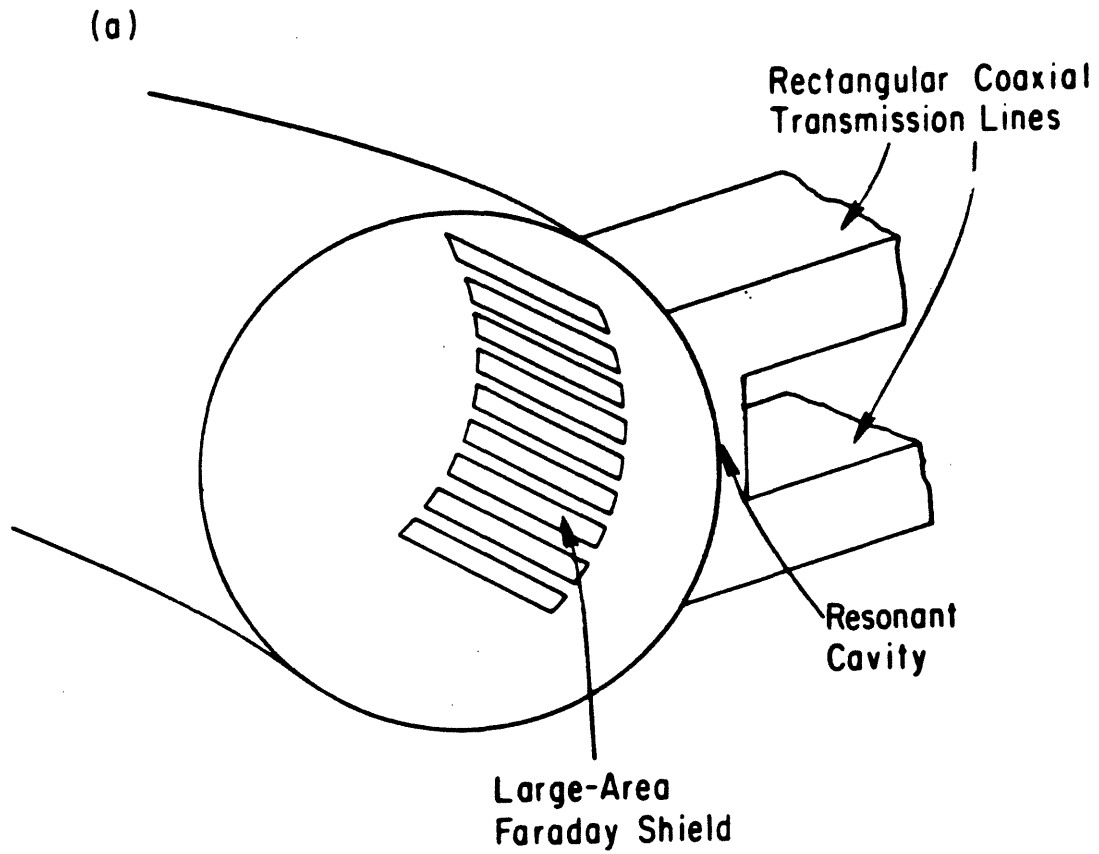


FIG. 2.5-12 Resonant re-entry type resonant cavity coupler.
(After Perkins, et al., PPPL drawing)

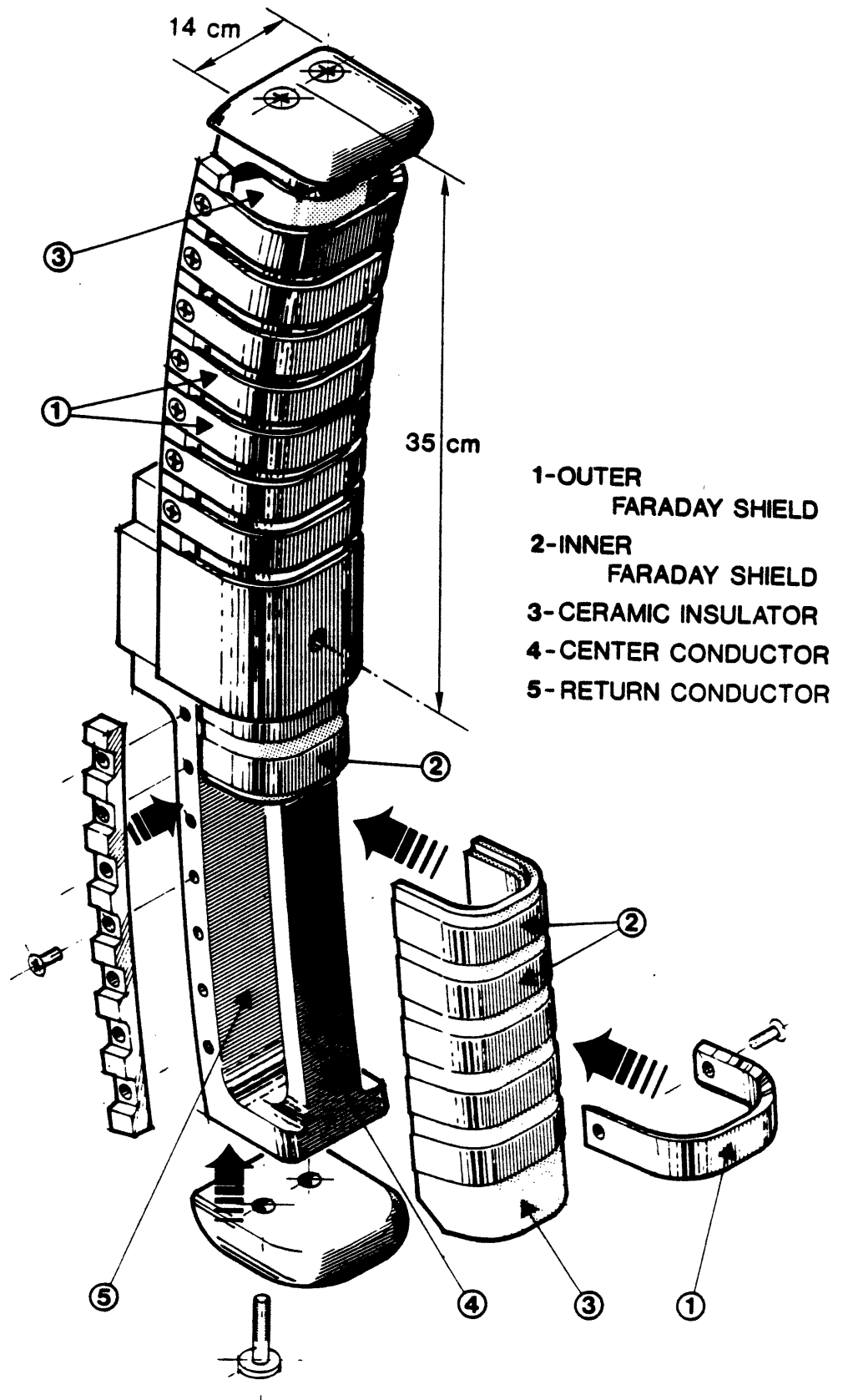


FIG. 2.5-13 Schematic of the ion Bernstein wave loop antenna.

Fourier power spectrum. Thus, taking $k_z \lesssim \pi/L$, electron Landau damping is avoided for

$$\frac{\omega}{k_z} > 2v_{te}, \text{ or } fL > v_{te}.$$

Taking $f = 180$ MHz, $L > 50$ cm, it is seen that Landau damping is negligible for the maximum envisaged Alcator C-MOD parameters of $T_e \lesssim 10$ keV. The RF power density for 1.2 MW of power is of the order of 1 kW/cm^2 on the antenna surface.

The antenna can be moved in and out radially and can be rotated about the radial support axis so as to ensure alignment with the total magnetic field (including B_p) at the plasma edge. This would optimize coupling to Bernstein waves at the plasma edge. The coaxial feed line is similar to that discussed for the fast wave launcher.

An alternative and attractive launching scheme is a dielectric loaded waveguide antenna of the type shown in Fig. 2.5.14. Using a dielectric constant of 8, the cut-off wavelength at 180 MHz is of the order $\gtrsim 60$ cm. Thus, a maximum waveguide height of ~ 50 cm would ensure launching the TE_{10} mode, which ensures coupling to the electrostatic Bernstein wave. The width of the antenna is the port width, or $\sim 14 - 15$ cm, corresponding to a waveguide area of 700 cm^2 . Thus, the power density for 1.25 MW per antenna is 1.8 kW/cm^2 , which is well below typical lower-hybrid power levels. Furthermore, multi-factor should not be a problem. Electron Landau absorption might occur, however, for temperatures $T_e > 2$ keV. Detailed ray tracing calculations must be performed to evaluate the variation of k_z near the absorption layer.

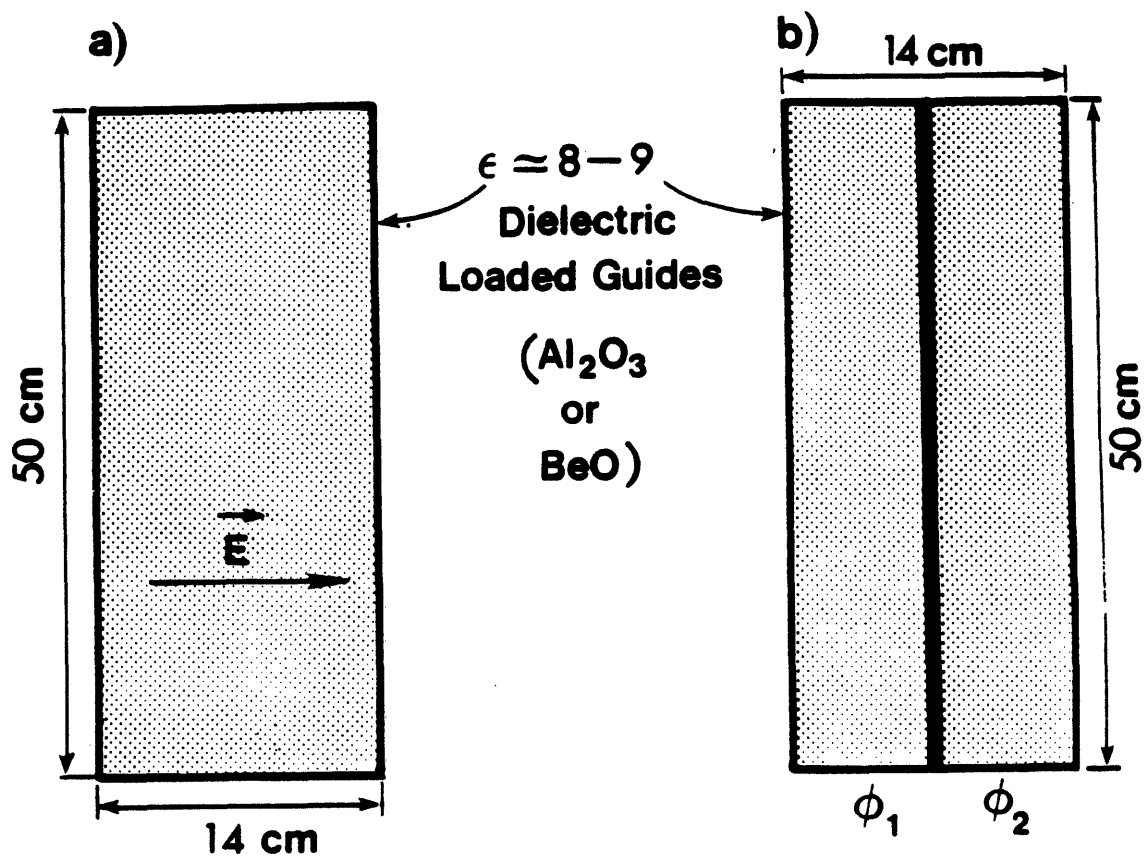


FIG. 2.5-14 Schematic of a dielectric loaded waveguide antenna for ion Bernstein wave launching.

c. Tuning and Matching

The RF system block diagram is shown in Fig. 2.5.15. A 20 to 50 ohm transformer section precedes the tuning system to keep the mismatch low. It is considerably closer to the machine than the tuning stubs and serves to limit the length of line with a high standing wave ratio. This reduces the possibility of breakdown in the transmission lines and cuts down the losses in the system. Matching is accomplished by a double stub tuner in each feed line. With a spacing of $3\lambda/8$ the range of loads accessible at any given frequency is broad enough to cover most plasma induced load variations. Fixed line sections can be changed to adjust for major loading variations or if the frequency is changed appreciably. The tuning system is diagnosed by reflectometers before and after the tuning stubs, and probes at each tuning stub monitor the current in each antenna.

d. The FPS-17 ICRF 6 MW System

The layout for the 180-215 MHz system is shown in Fig. 2.5.16. This system consists of 8 amplifier chains each with a 6950 power amplifier tube in the output. The 6950 tube will have 27 kV DC on the anode and the grid will be fixed biased off. The intermediate power amplifier stage will be control grid, screen grid, and plate pulsed. This will allow the use of the lower hybrid modulators for all eight of the ICRF amplifier chains.

Each of the lower hybrid power supply transformer/rectifiers will have two DC outputs summed with a special summing choke. Each transformer/rectifier will supply two 6950 power amplifier stages and the modulator

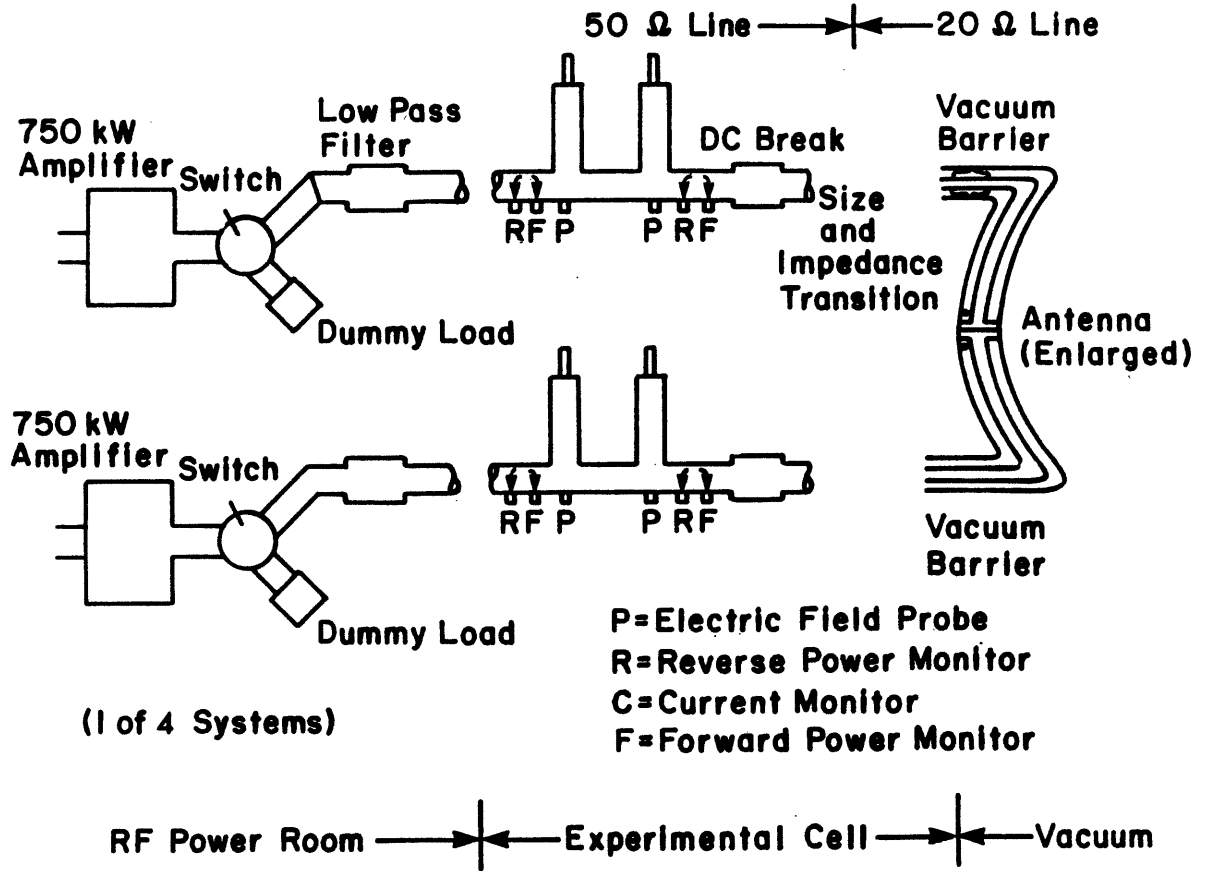


FIG. 2.5-15 Block diagram of the ICRF tuning and matching system.

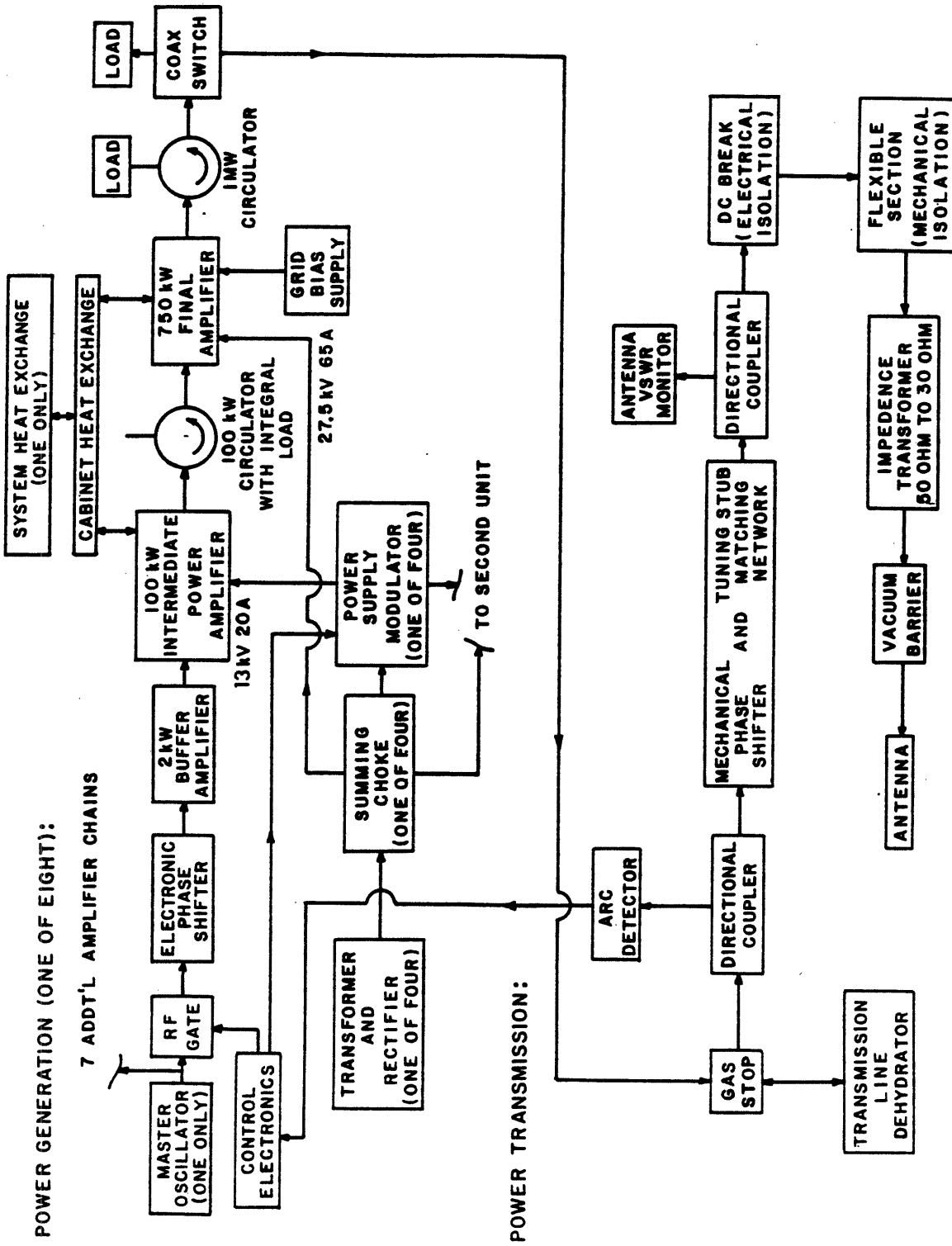


FIG. 2.5-16 Schematic of the FPS-17, 180-215 MHz, 6 MW system.

for four intermediate power amplifier stages. Only two of the four lower hybrid modulators will need to be used to pulse modulate all eight intermediate power amplifier stages.

The 6950 power amplifier will need some updating from their basic FPS-17 configuration. This consists mostly of the cooling system, the diagnostics reporting, and the grid bias supply. The intermediate power amplifier will need a total rebuild to take advantage of newer tube types that are needed to supply the minimum 100 kW of drive to the 6950 power amplifier.

The power output of each amplifier chain will be a 750 kW, 2 second pulse. A system of diagnostic reporting will include the normal forward and reverse power on each pulse plus a number of detected faults on each operating chain in the system.

e. The FMIT 10 MW ICRF System

The FMIT ICRF system is a 10 MW, 40-80 MHz system, in storage at Princeton Plasma Physics Laboratory. Assuming that it became available, it could be upgraded to operate up to 150 MHz (so it could be used in an ignition device at $B = 10$ T at the harmonic of the deuterium cyclotron frequency, or as a Bernstein wave heater at $\omega = 3\omega_{cT}$). It may be seen in Figs. 2.5.1-2.5.3 that this system could be used in Alcator C-MOD as a minority heater (H or He-3) in a deuterium majority plasma. Alternatively, it may be used at 150 MHz as an off-center Bernstein wave heater at $f = 1.5 f_H = 3 f_D$ in a deuterium minority, hydrogen majority plasma. It is assumed that the upgrade work would be carried out at PPPL, and hence details of the system will not be discussed here.

References

- [2.5-1] P. Colestock and R. J. Kashuba, Nucl. Fusion 23, (1983) 763.
- [2.5-2] T. Stix, Nuclear Fusion 15, (1975) 737.
- [2.5-3] M. Ono, et al., Phys. Rev. Lett 54, (1985) 2339.
- [2.5-4] M. Porkolab, Phys. Rev. Lett 54, (1985) 436.
- [2.5-5] F. W. Perkins, and R. Kluge, IEEE Transactions on Plasma Science, PS-12, (1984) 161.

CHAPTER 3

ALCATOR C-MOD POINT DESIGN

3.0 Introduction

A conceptual level point design for the C-MOD device has been developed, and is based on the "jointed rectangular coil" configuration under study at PPPL for the compact ignition device. This concept uses an external frame to reduce the tension loads on the inner legs of the TF magnet to near zero, leaving only radial compression loads to limit magnet performance.

The jointed coil aspect of the PPPL ISP and the C-MOD designs open up a major advantage, namely the ability to remove internal components in a relatively straightforward manner. The vacuum chamber can be made in one robust piece, and the PF coils can be internal to the TF coils, hence used to more effectively provide a controllable divertor configuration and adequate volt-seconds. In the case of C-MOD the jointed TF coil also offers flexibility for future studies of more advanced plasma shapes.

An overview of the engineering parameters for the C-MOD point design is given in Table 3.1. The table lists two performance levels for the machine, 7.5 T and 10 T, the lower field representing the limits of the present TF power supplies, and the higher field, the design capability of the magnetic systems. An upgrade of the present power supplies which would permit 10 T operation, is discussed in Appendix A.

The C-MOD point design as shown in Figures 3.1 and 3.2 would have greatly improved access over the present Alcator C machine. Twelve horizontal ports of 15 cm width are shown, compared with only four ports of 5 cm width on the present machine. This increased access will greatly improve the ability to carry out the high power RF heating program begun on

on Alcator C. The ripple for this configuration is 1% at the plasma edge, and 0.05% out to half radius. We propose to provide coil taps to allow ripple to be varied to study the impact on confinement.

The structure shown in Figures 3.1 and 3.2 is a relatively simple force containment concept consisting of top and bottom sandwich structures, and a simple cylinder surrounding the out-board legs. As illustrated, the structures have not been electrically subdivided, which is unconventional relative to present day tokamaks. These simple structures, however, should be less expensive and at the same time should be more representative of coil assembly approaches amenable to remote maintenance than are the present day individual coil-case tokamak designs. Electromagnetic modeling, discussed in Section 3.2.3, indicates that the structural elements have time constants in the 50 msec range, which we believe is compatible with current ramp-up and control requirements.

TABLE 3.1

OVERVIEW OF C-MOD POINT DESIGN ENGINEERING PARAMETERS

Major Radius	0.75 m
Minor Radius	0.25 m
Magnetic Field	7.5 T - 10 T (*)
Elongation	1.8
Triangularity	0.3
Plasma Current	4 MA
Flat-top (360 MJ)	1 sec @ 7.5 T; 10 sec @ 5 T
Flat-top-pulse (640 MJ)	1 sec @ 10 T; 20 sec @ 5 T
Volt Seconds	12 Weber
RF Heating	10 MW
Average Heat Flux (@ 10 MW)	1.0 MW/m ²
Stored Energy Required @ 7.5 T (TF and PF)	360 MJ
Stored Energy Required @ 10 T	640 MJ

(*) 10 T operation requires an additional generator; see Appendix A for the description of a suitable surplus unit.

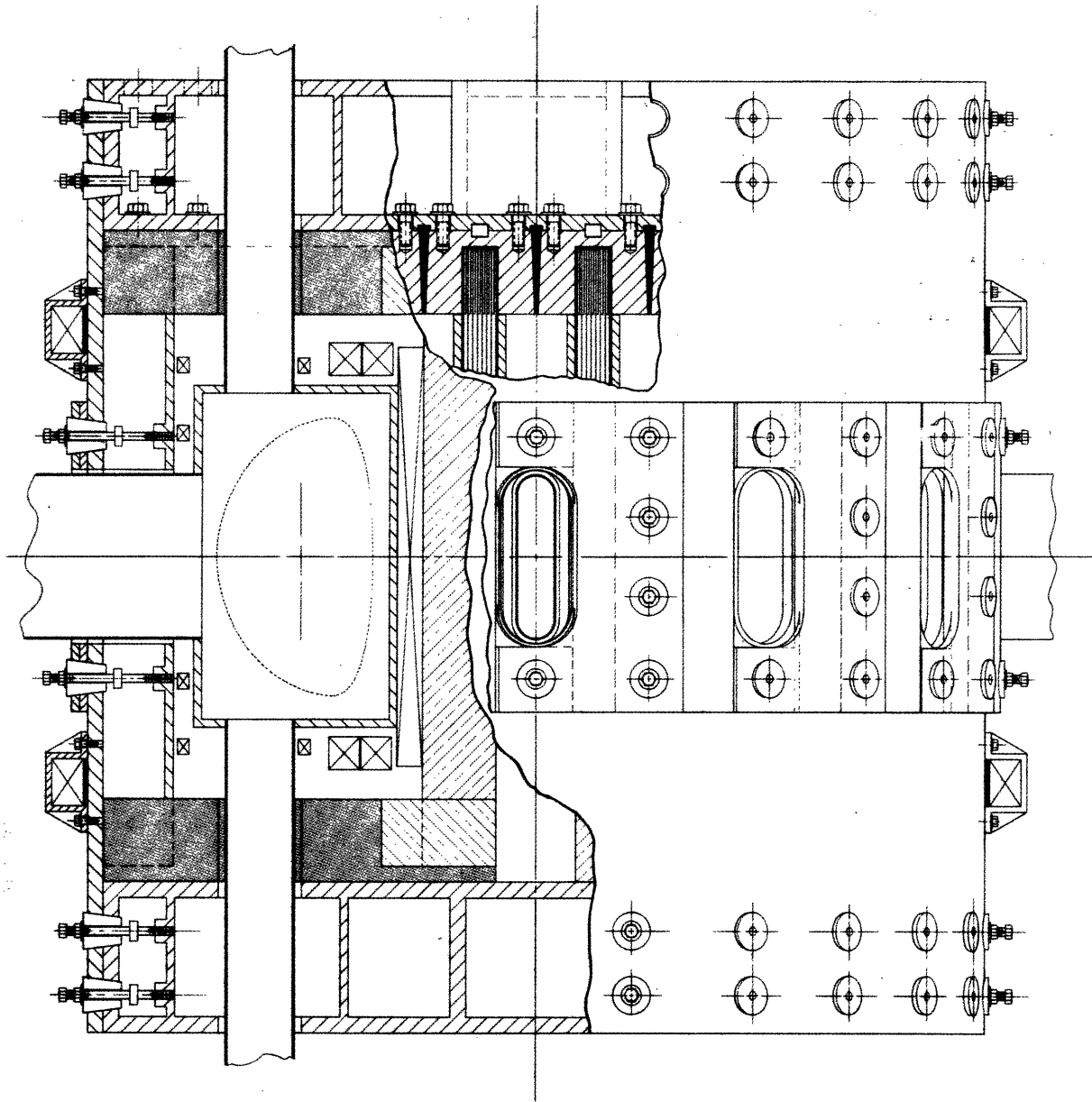


Figure 3.1: Elevation view of C-MOD point design

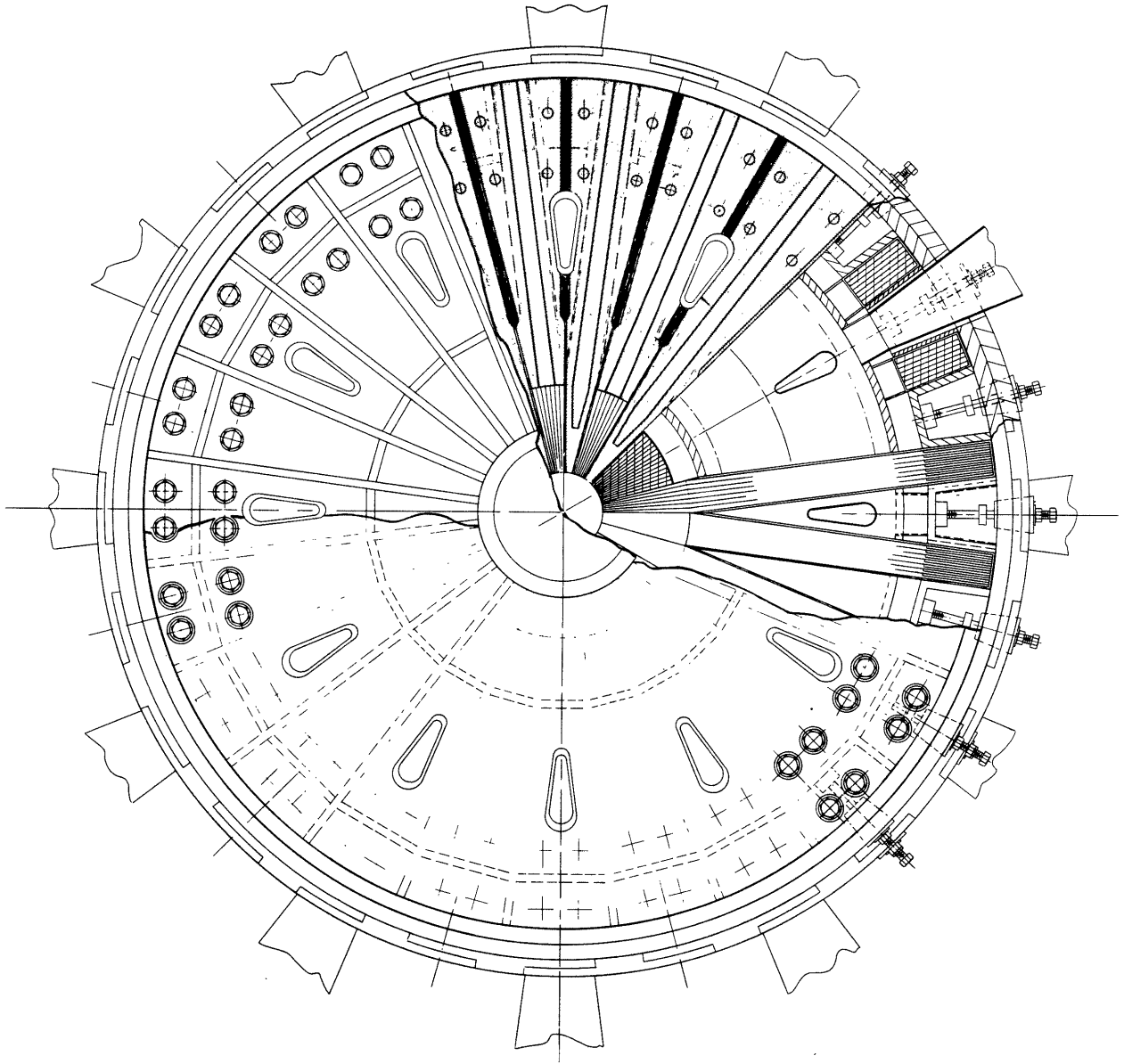


Figure 3.2: Plan view of C-MOD point design

3.1 TF Magnet System

3.1.1 General Description of the TF Coil System

The basic configuration of the picture frame coil can be seen in Figure 3.3. The central TF cylinder consists of 155-alloy copper tapered plates wedged together with thin sheets of fiberglass insulation between them. There are seven plates of constant thickness in each of the 24 radial arms and outer vertical legs, for a total of 168 turns. The central TF cylinder would be radially precompressed, tension banded, and epoxy bonded to assure an integral behavior even in the absence of radial compression from the TF field.

The TF coil has joints in all four corners (see Section 3.1.3) for ease in assembly and for access to the internally located PF coils and single piece vacuum chamber.

The coils are surrounded by a steel superstructure consisting of top and bottom sandwich covers, joined by an outer cylinder. The cylinder is split at the magnet equator to allow removal of the entire vacuum vessel as a unit, with a segmented girth band used to rejoin the cylinder halves when the magnet is reassembled.

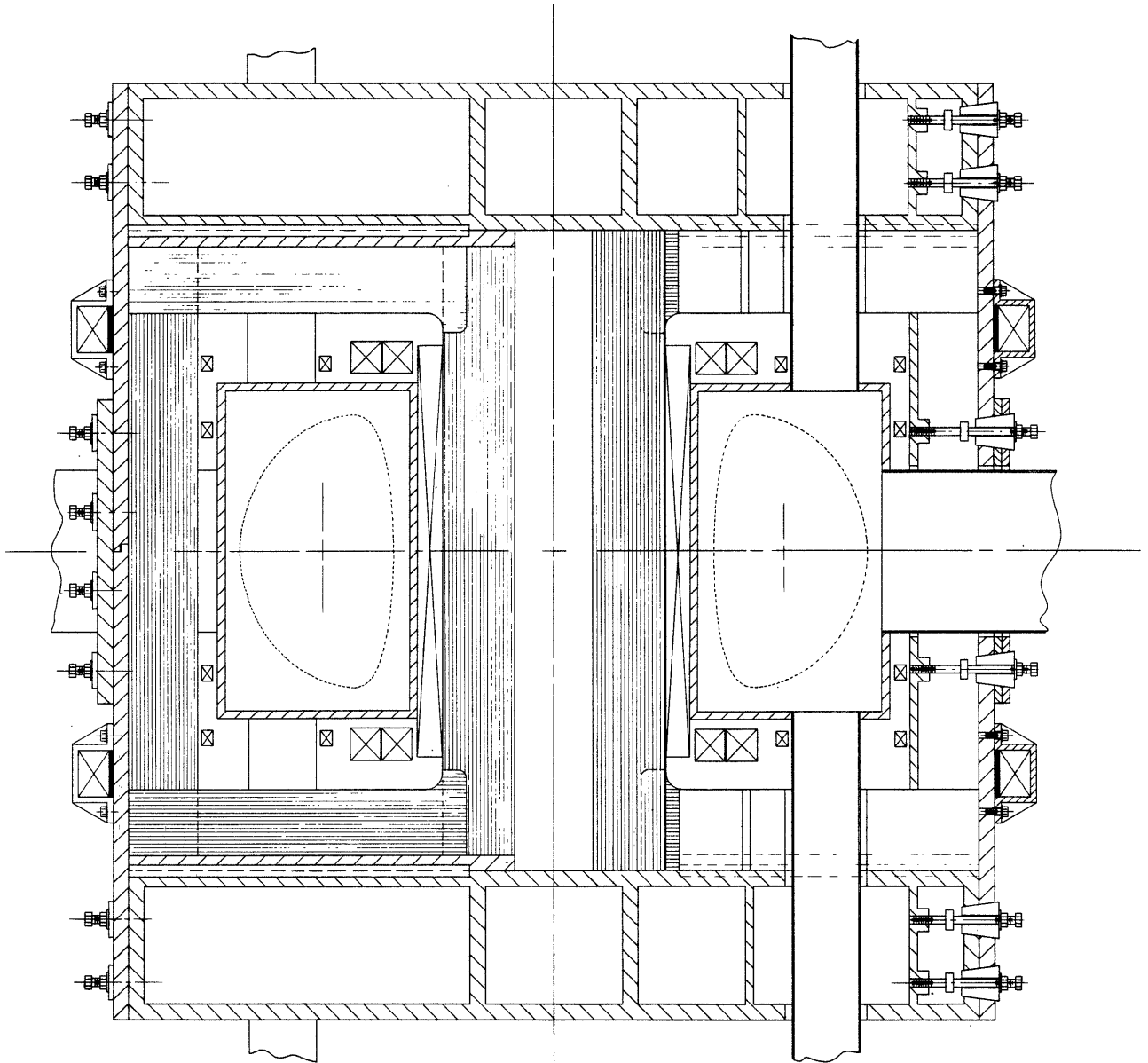


Figure 3.3: C-MOD TF picture frame coil concept utilizing Alcator C like joints at the four corners

3.1.2 Structural Behavior of the TF Coil System

The TF magnet utilizes an external frame superstructure to support all inplane loads except the radial compression on the inner leg which is carried by wedging. All out-of-plane loads on top, bottom and out-board legs are also supported by the external frame, but the inner leg out-of-plane loads must be taken by turn-to-turn shear.

The investigation of the Alcator C-MOD TF coil has been largely directed thus far toward exploring the structural behavior of the central cylinder, which appears to be the critical component of the TF coil system.

In the current PPPL ISP design, sliding joints in the TF coil are utilized in order to allow external frame to carry essentially all the tension load which would normally be shared between the TF vertical legs and the external frame. In an ideal sliding joint case only the structural response to the radial compressive loads in the inner leg remains to limit the magnet performance.

In the C-MOD conceptual design we have considered a dual function for the external frame; first to carry some of the inplane loads and second to apply preload to the inner TF leg and thereby reduce the tension to near zero even if the joints were fixed joints. This alternate strategy (utilized in IGNITOR) has the advantage of allowing the joints to be more representative of the present tokamak fixed-joint data base, and the advantage of avoiding the uncertainties in electrical and mechanical behavior of slip joints.

In the following analysis we examine both the slip joint case and the fixed joint case.

3.1.2.1 Coil Structure Behavior With Slip Joints

The radial arms and outer vertical legs are supported in statically determinate fashion by the superstructure consisting of the two covers and outer cylinder. The central cylinder is self-reacting in that it supports the radially inward TF Lorentz loads by wedging of the turns. (We also examined an optional case in which a bucking cylinder is used in combination with TF wedging). The sliding joints are intended to avoid axial Lorentz load on the coil vertical legs, but this is only partially realized, because of the Lorentz loads caused by the curved current paths in the joint regions. This residual tension load will be partially supported by the external frame and partly by the TF cylinder itself. However, because the central cylinder is a much stiffer path than the external structure, most of this tension will be carried by the TF central cylinder.

The cylinder alone must resist the major part of the out-of-plane Lorentz forces between the top and bottom joints. Partial restraint of the central cylinder twist, however, is provided by the detail shown in Figure 3.4 which shows the TF central cylinder keyed to the intercoil wedges, and, in turn, to the top and bottom covers. Out-of-plane loads contribute little to the stresses in the central cylinder provided that the cylinder behaves monolithically. However, the loads do influence the pressure distribution between plates at the slip joints.

The top and bottom covers support the vertical forces on the radial arms (Figure 3.5). The reaction is provided by the outer cylinder, which also transmits the torque due to the out-of-plane loads from the top of the magnet to the bottom. In addition, the cylinder helps support

the outer vertical legs of the coil against the inplane Lorentz loading. The outer cylinder must be split at the equatorial plane to allow assembly around the vacuum vessel, and is rejoined by an overlapping segmented shell as shown in Figure 3.6 and Figure 3.7.

The out-of-plane Lorentz loads on the radial arms are transmitted to the covers through the vertical ribs and wedges that lie between the groups of seven turns that comprise each coil (Figure 3.3 and 3.4). The vertical channels on the outer cylinder transmit the out-of-plane Lorentz loads from the outer legs to the outer shell.

The proposed location of the inboard TF joint is shown in Figure 3.8. The coil joints are loaded in toroidal compression by spring plates to achieve an acceptably low electrical contact resistance (see Section 3.1.3). Friction at the contact faces will lead to inplane loads when there is relative inplane movement of the radial arms with respect to the vertical components. This frictional load component is not significant at the 100 psi spring plate pressure. However, should there be a significant relative twist at the location of the joints due to out-of-plane loads, there could be a significant additional toroidal force between each vertical plate of the cylinder and the corresponding radial plate at the inner joint. There may also be localized twists and bends at the corners due to the elastic deformations of the coil plates.

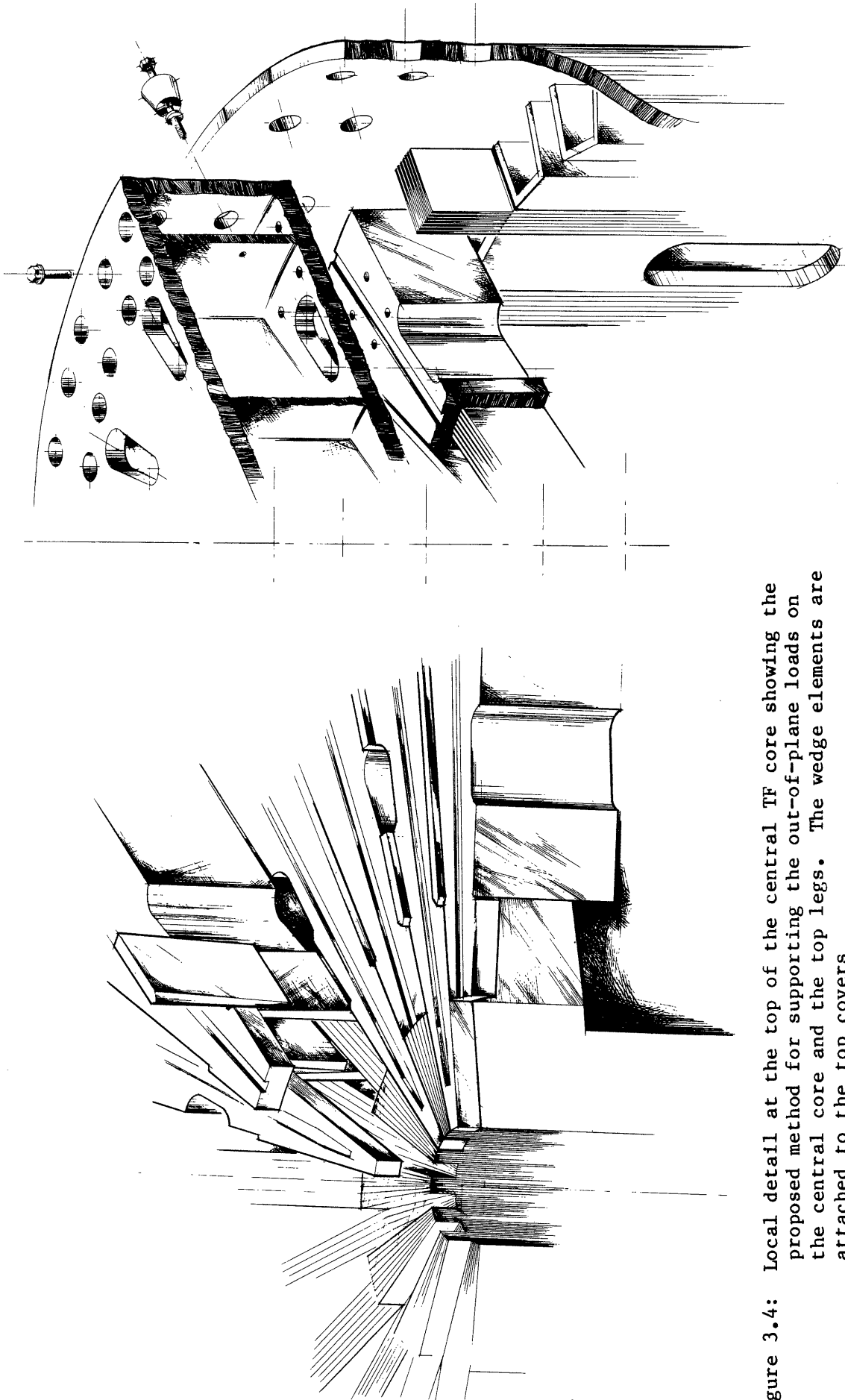


Figure 3.4: Local detail at the top of the central TF core showing the proposed method for supporting the out-of-plane loads on the central core and the top legs. The wedge elements are attached to the top covers

Figure 3.5: Local detail showing the attachment between the out-of-plane wedges and the upper cover, and between the upper cover and the outer support cylinder

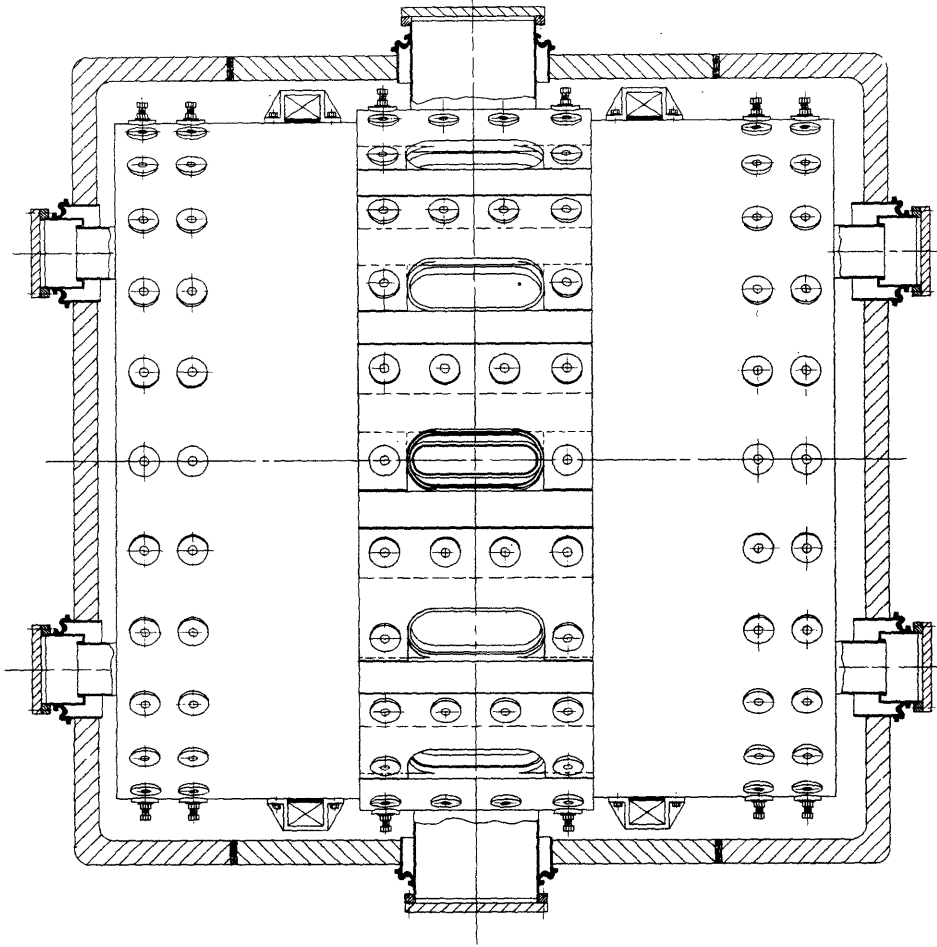


Figure 3.7: Overview of the C-MOD outer support cylinder

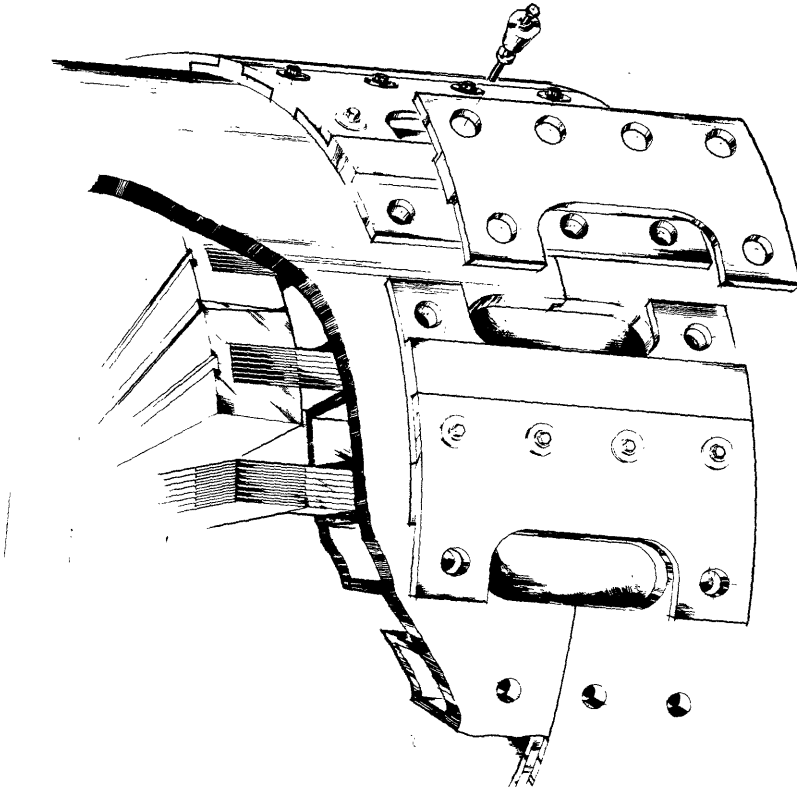
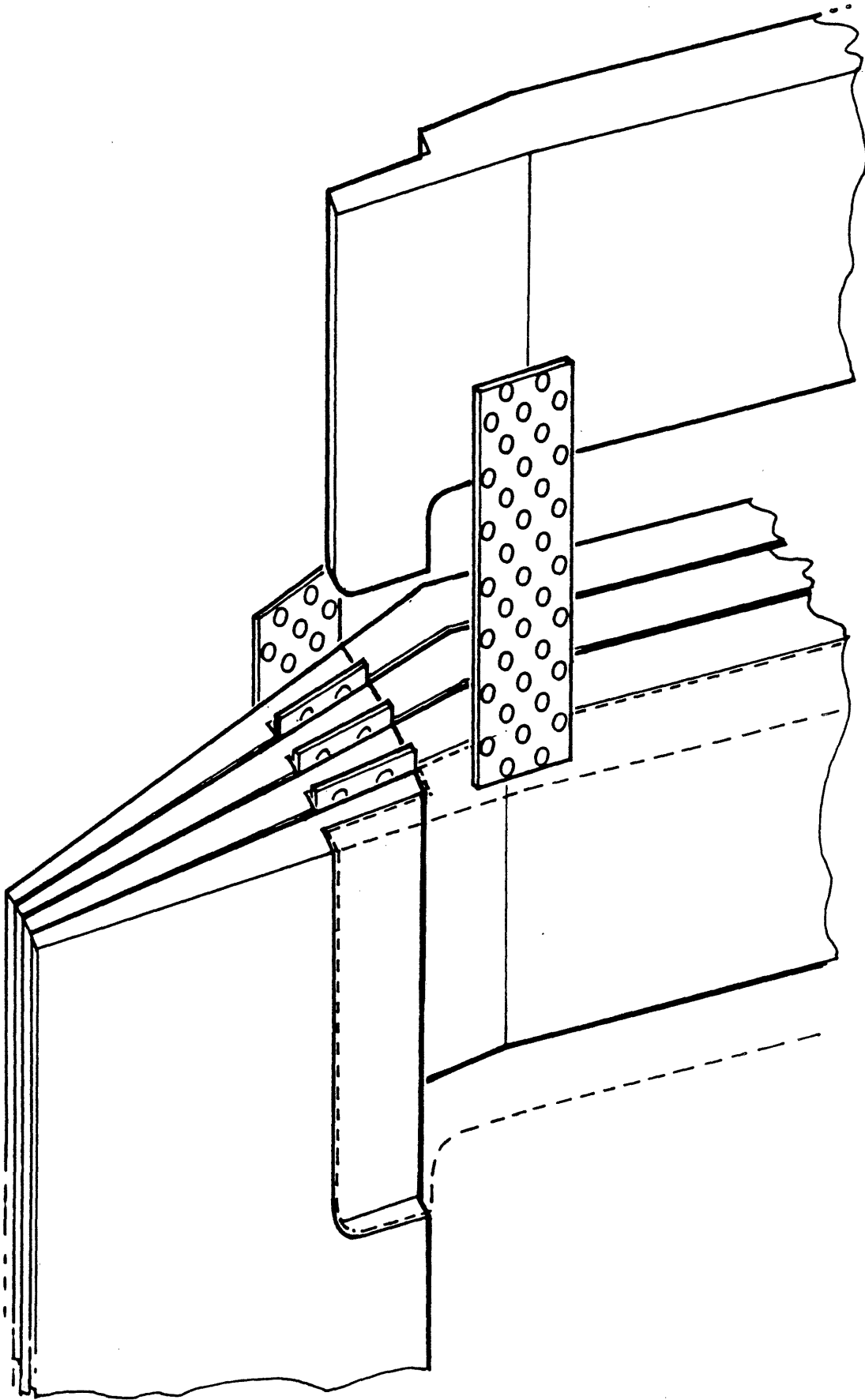


Figure 3.6: Local detail at the outer support cylinder showing the out-of-plane support of the outer TF legs, and the assembly split in the support cylinder



8675/7/7B/

Figure 3.8: Proposed TF coil joint. The joint detail is similar to the nonsliding joints in Alcator A and Alcator C

3.1.2.2 Coil Structural Behavior With Fixed Joints

A fixed joint coil could theoretically react the TF Lorentz loads up to some field level. The superstructure however, is required to keep the central cylinder tresca stress within the allowables at the field levels of interest in C-MOD. The covers also minimize bending at the corners in the turns. Alternates under consideration in this fixed joint case are to preload the radial arms and central cylinder through the superstructure, and also to provide some bucking action with a central cylinder.

3.1.2.3 Comparison of Applied Stresses With Allowables

Finite element calculations were performed on the slip joint and fixed joint coil options using the grid shown in Figure 3.9. The Lorentz vertical and radial loads are given in Figure 3.10 for 10 Tesla.

Three types of fixed joint coil-superstructure interaction were explored for response to vertical Lorentz loads:

1. The radial arms were unsupported
2. They were supported passively by the covers
3. They were preloaded and supported by the covers

In addition, cases with and without a bucking cylinder were explored. In the case with a cylinder, simultaneous wedging was assumed (i.e., perfect fit-up).

Results of Inplane Analysis

Table 3.2 and Table 3.3 display the 7.5 Tesla and 10 Tesla stresses at the equatorial plane of the central cylinder under inplane Lorentz loads. At 7.5 Tesla all the slip joint and fixed coil tresca stress are nominally within the allowables, provided they are supported by the superstructure. At 10 Tesla, the only cases that nominally satisfy the allowables are the slip-joint coil with a bucking cylinder, and the preloaded fixed-joint coil. Both techniques require careful tolerance control and assembly.

For example, the large difference in stresses between cases with and without a bucking cylinder points to the potential problems associated with controlling the level of bucking in a system likely to have tolerance uncertainties and "shakedown" radial displacements. The radial movement of the inner leg without a bucking cylinder, for example, would

be 0.4 mm, which leaves little room for gap tolerance. However, it does suggest that the coil with a bucking cylinder would probably be driven to a fully supported condition against the cylinder after shake-down. Then the question arises as to the actual amount of inner leg wedging remaining to combat the overturning loads and to avoid buckling under preloading. Calculations indicate that buckling can be avoided only if the inner leg acts as a monolith (i.e., that the bonding between turns remains intact).

The choice concerning whether to use combined bucking and wedging, or to use preloading is under study. It might in fact, be advantageous to have the ability to use both and to be able to vary the degree to which each is acting. Measurements of resulting deflections could then add considerable insight to probable behavior of the full scale ignition device.

The allowable stresses in Tables 3.2 and 3.3 are taken from the guidelines used for the ignition studies, namely 70% of ultimate strength for a constrained coil, or 60% of ultimate strength for a self supported coil. In Tables 3.2 and 3.3 all cases are considered constrained except the case of the fixed joint "free coil". The mechanical properties of copper alloy-155 assumed for the design are given in Table 3.4.

Finite element analyses show that the steel support structure operates at reasonable stress levels. The contours of constant stress for the 8 Tesla case shown in Figure 3.11 indicate a cover plate peak stress of 35 ksi (245 MPA) which would be 52 ksi (370 MPA) at 10 Tesla. The yield strength for 304 LN plate at 77°K is 98 ksi, approximate twice the peak stress. Comparable margins exist for the outer cylinder as well.

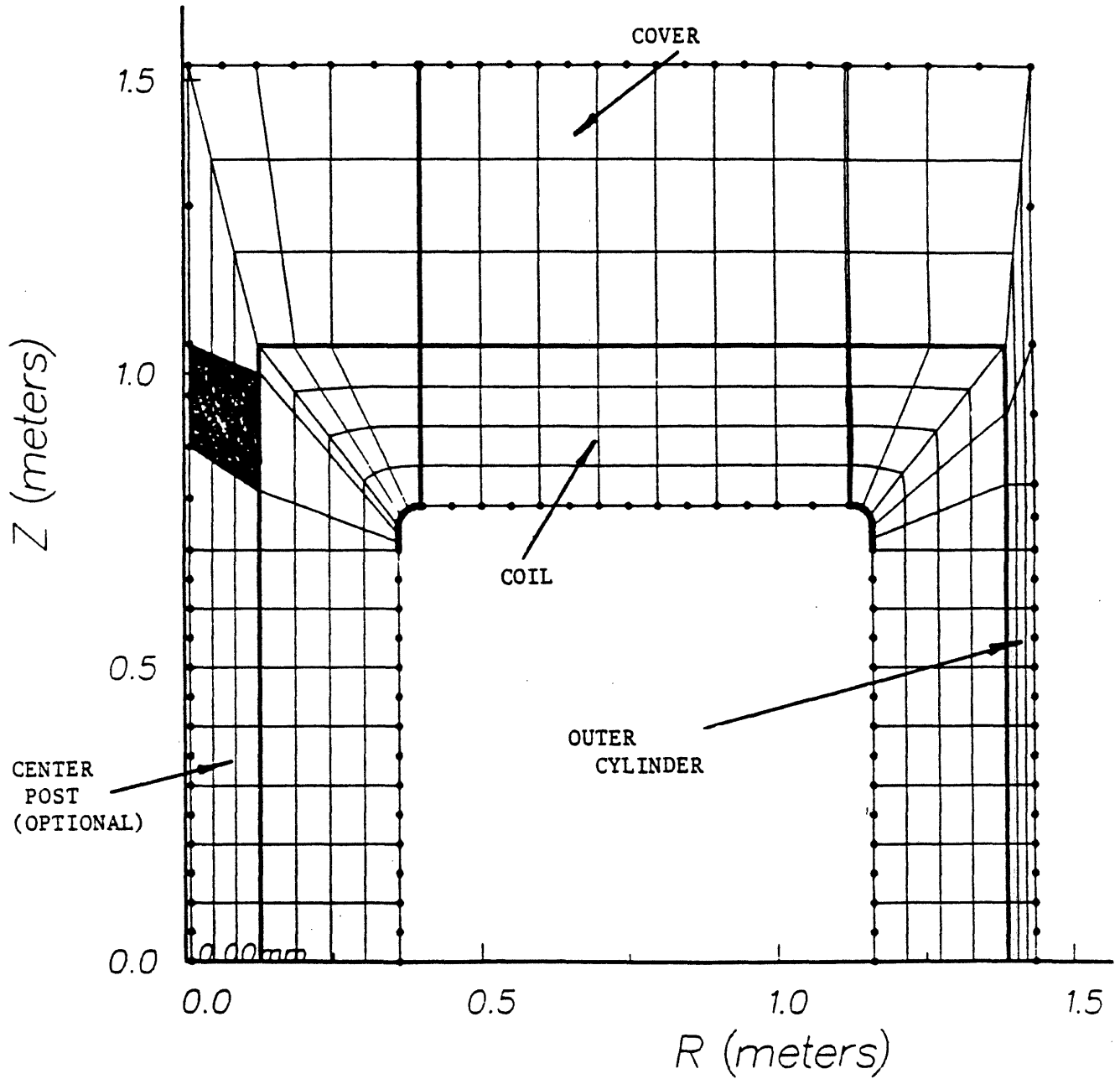
ALCATOR C-MOD
FINITE ELEMENT GRID

Figure 3.9: Alcator C-MOD finite element grid

ALCATOR C-MOD
IN-PLANE LORENTZ LOADS

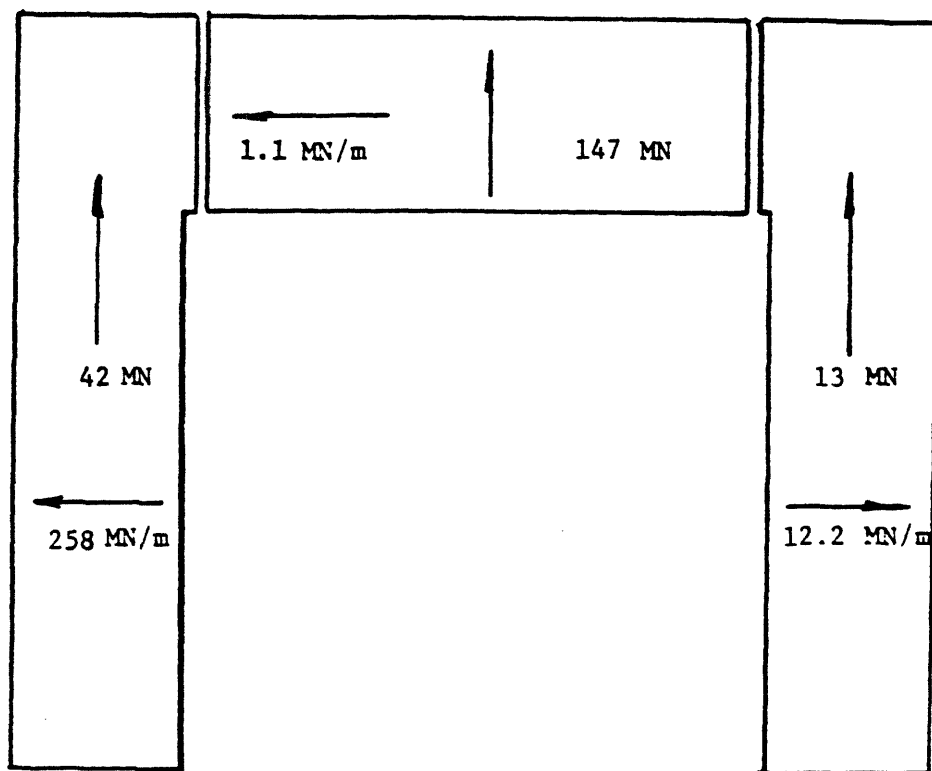


Figure 3.10: Alcator C-MOD inplane Lorentz loads

TABLE 3.2
 CENTRAL CYLINDER AVERAGE TF STRESSES AT 7.5 TESLA
 T = 200°K, ASSUMED. NO THERMAL STRESSES INCLUDED
 CENTRAL CYLINDER WEDGED IN ALL CASES

COIL TYPE	BUCKED	OTHER ASPECTS	AVERAGE STRESSES, MPa				σ_{all}^*	$\frac{\sigma_t}{\sigma_{all}}$
			$\sigma_v(+)$	$\sigma_\theta(-)$	$\sigma_r(-)$	σ_t		
Slip Joint	Yes		76	115	57	191	319	0.60
	No		76	212	93	288	319	0.90
Fixed Joint	Yes	Free Coil	221	104	97	325	273	1.22
		Coil Supported by Superstructure	142	110	95	252	319	0.80
		Supported and Preloaded by Superstructure	0	121	91	121	319	0.36
	No	Free Coil	221	217	57	438	273	1.60
		Coil Supported by Superstructure	146	217	57	363	319	1.08
		Supported and Preloaded by Superstructure	0	215	57	215	319	0.62

σ_v - Vertical stress; σ_θ - Toroidal stress (face pressure); σ_r - Radial Stress;

σ_t - Tresca stress; σ_{all} - Static allowable stress; + = Tension; - = Compression

* - Allowables taken as 70% of ultimate strength for contained coils, and 60% of ultimate strength for the free coil; properties are for C-155 copper per Table 3.4.

TABLE 3.3
CENTRAL CYLINDER AVERAGE TF STRESSES AT 10 TESLA
T = 200°K, ASSUMED. NO THERMAL STRESSES INCLUDED
CENTRAL CYLINDER WEDGED IN ALL CASES

COIL TYPE	BUCKED	OTHER ASPECTS	AVERAGE STRESSES, MPa				σ_{all}^*	$\frac{\sigma_t}{\sigma_{all}}$
			$\sigma_v(+)$	$\sigma_\theta(-)$	$\sigma_r(-)$	σ_t		
Slip Joint	Yes		119	180	89	298	319	0.94
	No		119	331	145	450	319	1.41
Fixed Joint	Yes	Free Coil	345	163	152	508	273	1.91
		Coil Supported by Superstructure	222	172	148	394	319	1.25
		Supported and Preloaded by Superstructure	0	189	142	189	319	0.56
	No	Free Coil	345	339	89	684	273	2.50
		Coil Supported by Superstructure	228	339	89	567	319	1.69
		Supported and Preloaded by Superstructure	0	336	89	336	319	1.05

σ_v - Vertical stress; σ_θ - Toroidal stress (face pressure); σ_r - Radial Stress;

σ_t - Tresca stress; σ_{all} - Static allowable stress; + = Tension; - = Compression

* - Allowables taken as 70% of ultimate strength for contained coils, and 60% of ultimate strength for the free coil; properties are for C-155 copper per Table 3.4.

TABLE 3.4
 STRUCTURAL AND ELECTRICAL PROPERTIES OF C-155 ALLOY,
 NOMINALLY T 60 TEMPER

TEMPERATURE, ° K	σ_{ty} (MPa)	σ_{tu} (MPa)	$\frac{\rho}{\rho_{cu, 300 K}}$
300	400 ¹	428 ¹	1.11
200	421 ²	455 ²	
80	469 ²	503 ²	0.22

¹ measured by MIT

² estimated by comparison with data for OFHC at cryogenic temperatures.

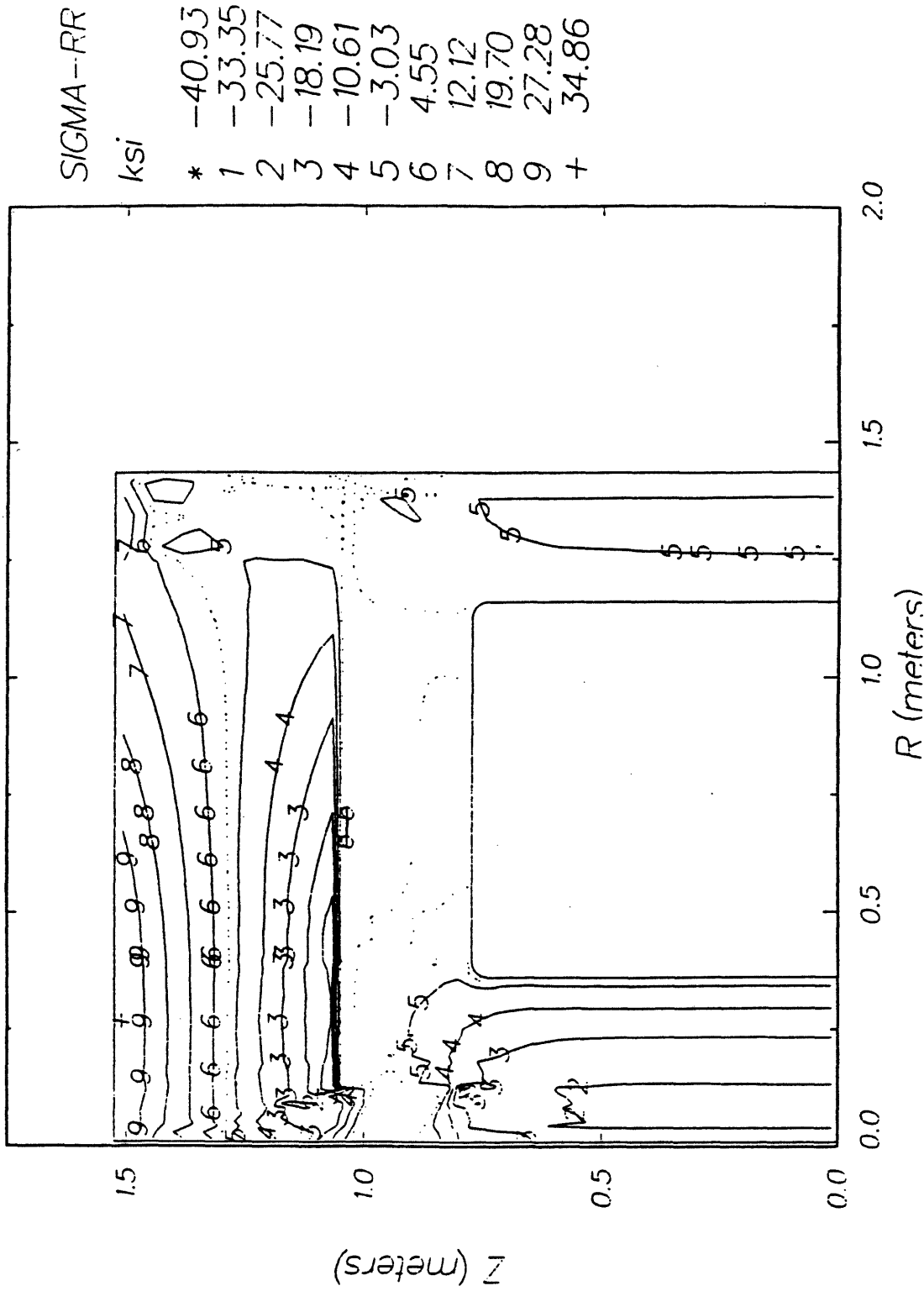


Figure 3.11: Contours of constant stress in the C-MOD TF coil and support structure

The cases shown in the tables confirm that the covers are more flexible than the coil and it is therefore necessary to preload the coil in order to appreciably reduce the Lorentz tension on the inner leg. (This was done in the finite element model with local contact between the cover and the radial arms at a radius of 0.6 m, rather than continuous contact as assumed for the passive cover condition.)

Results of Out-of-plane Analysis

The out-of-plane torques are displayed in Figure 3.12. A 6.1 ksi shear stress at the equatorial plane would result from the -3.1 MN-m torque on the inner leg alone and the 0.0734 m^3 torsional section modulus of the cylinder. The value is conservative since the radial arms and top keys provide twisting restraint to the cylinder that reduces the torque. The shear stress calculation was assumed to apply to both the slip-joint and fixed-joint coils.

The influence of the shear on the applied principal stresses is of the order of only one percent, and was therefore neglected in the comparison with allowables shown in Tables 3.2 and 3.3.

One problem area that requires further study is the behavior of the inner corners under out-of-plane loads. The keys to the covers can provide some toroidal support, and the structural continuity of a fixed-joint coil would also help. However, the plates are thin at the inner corners and can deform plastically. This local support problem is under study.

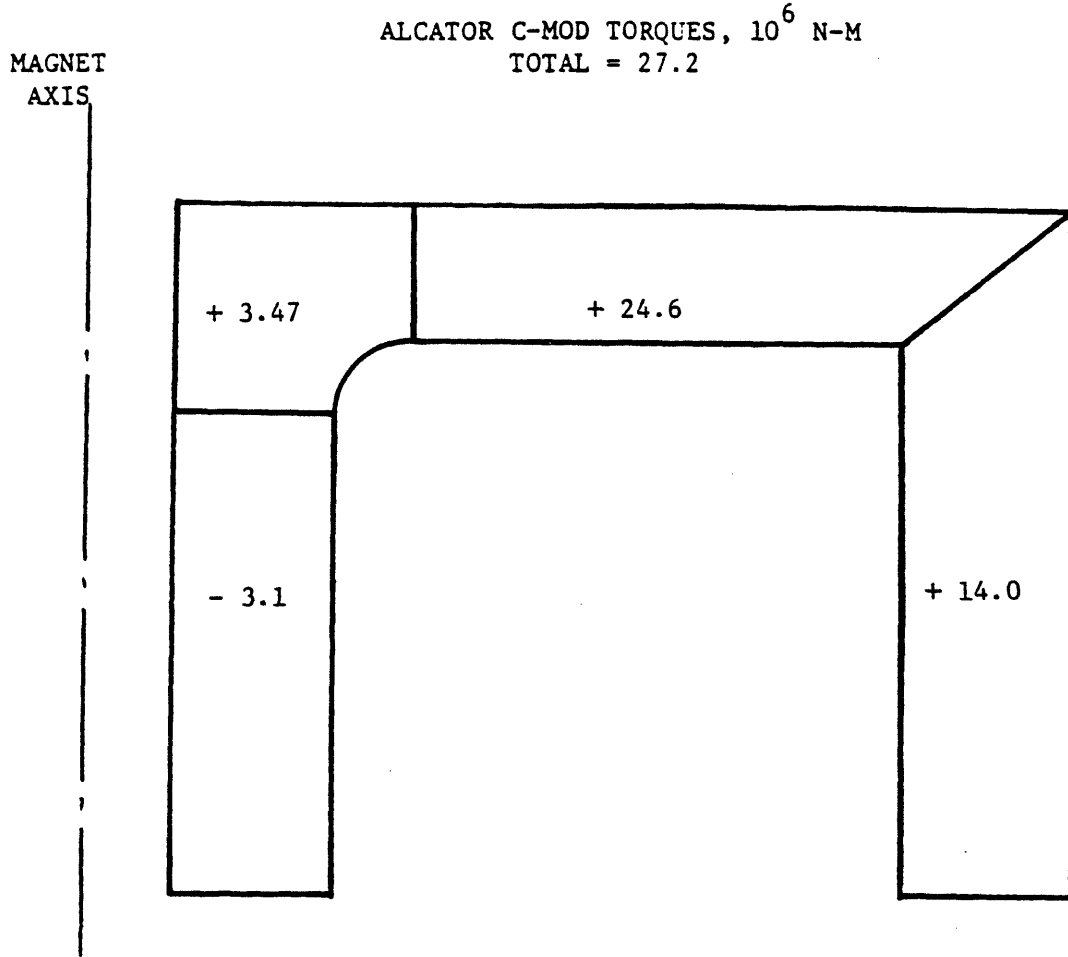


Figure 3.12: Alcator C-MOD torques, 10^6 N-m

3.1.3 TF Coil Joint Behavior

The fusion community has extensive experience with jointed TF coils, DIII, PBX and Alcator C being three examples. However, the concept of a sliding joint has not been previously used, and consequently carries a special need for analysis and test. The concept is particularly vulnerable to out-of-plane loads produced by the TF magnet interaction with the PF, raising questions of mechanical integrity of the joint area and questions of excessive wear of the joint surfaces under high transverse loading. For these reasons we are also exploring the pre-loaded coil strategy in which the joints can be fixed.

We propose to use a joint detail similar to the 250 joints used in Alcator C (see Figure 3.13). In Alcator C, the joints were loaded to approximately 500 psi and were not expected to slip. The C-MOD version of the Alcator-like joint is shown in Figure 3.8. To test the ability of this type of joint to slip, we have carried out a test on a 4 cm² model joint which consists of silver plated copper sliding on silver plated copper, and spring loaded as it would be in an Alcator-like joint. When loaded at 100 psi, the joint had a resistance of 0.5×10^{-6} ohm and completed 10^4 cycles with little apparent wear. The joint surface current density was set at 2,000 A/cm², and was operated in a steady-state mode in LN₂ at one mechanical cycle per 5 seconds. However, when the surface pressure was increased to 500 psi, the surfaces developed significant galling accompanied by a three times increase in surface resistivity after an additional 5×10^3 cycles. We are continuing experimental work to extend this life.

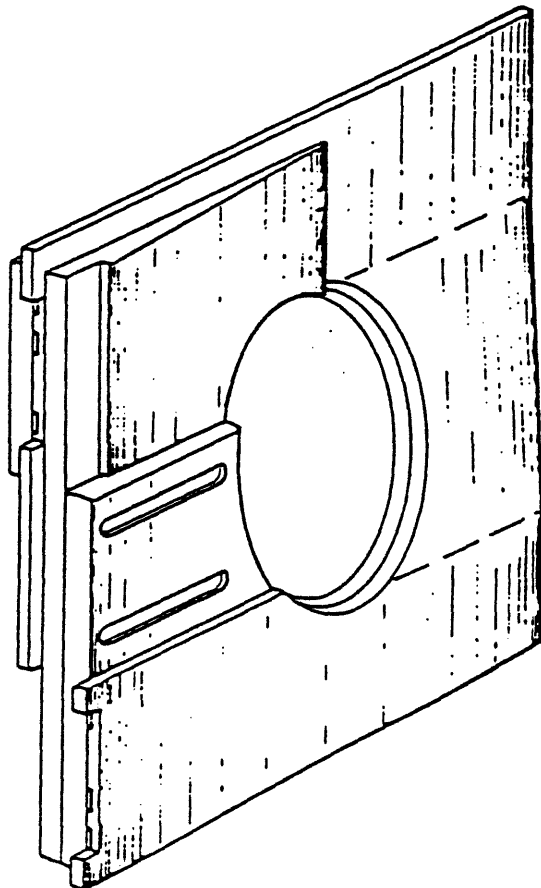
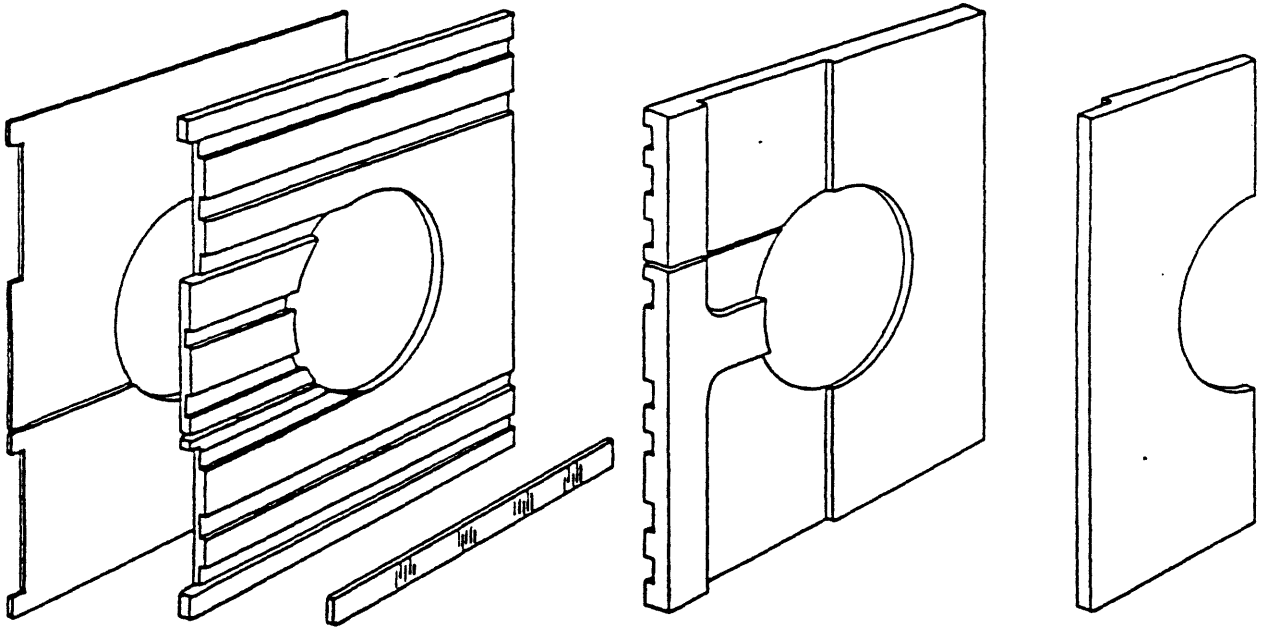


Figure 3:13: Alcatraz C turn construction showing the joint detail. The keys are rippled to provide spring follow up

If the joint surface resistance achieved in the above tests can be realized in the C-MOD magnet, there will be no significant heating associated with the joint surface. There is some local heating associated with the joint detail however, in the region where the current density is locally doubled as illustrated in Figure 3.14. The figure shows a computer model of the joint in which surface resistivity can be varied, and the effects of thermal diffusion away from the hot-spot can be taken into account. Figure 3.15 indicates the local temperature increase associated with the joint under the assumption of surface resistivity achieved in the tests. A peak temperature of approximately 300°C is reached at the end of a one second flat top at 10 Tesla. While this is acceptable, we are continuing to study corner details which can reduce this very local heating.

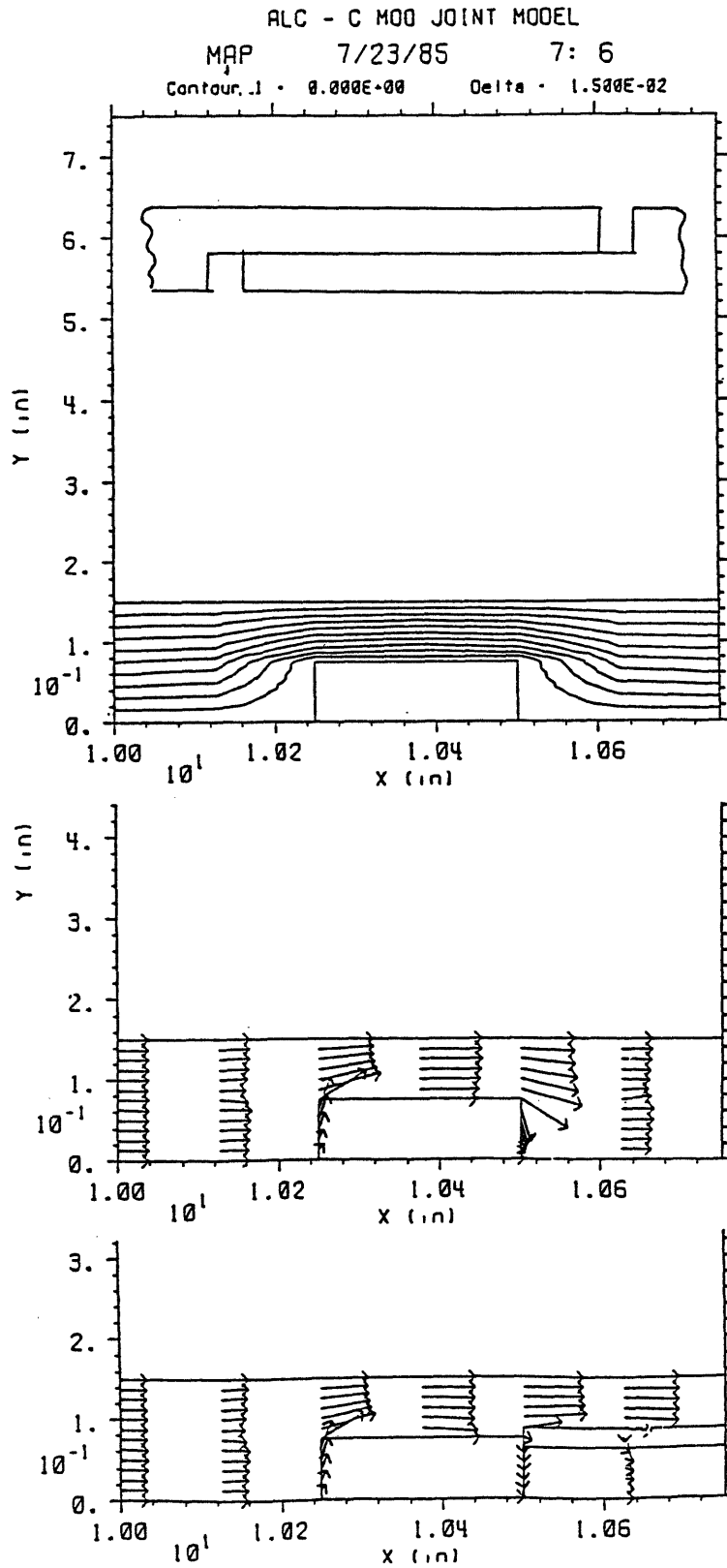


Figure 3.14: Current stream lines and relative current density near the ends of the over lapped joints. The lowest figure illustrates a case of high contact resistance

C MOD v/JOINT - CONDUCTION - 3:1 .10.0.75

MAP 8/20/85 10: 3

Contour 1 - 1.000E-09 Delta - 5.000E+01

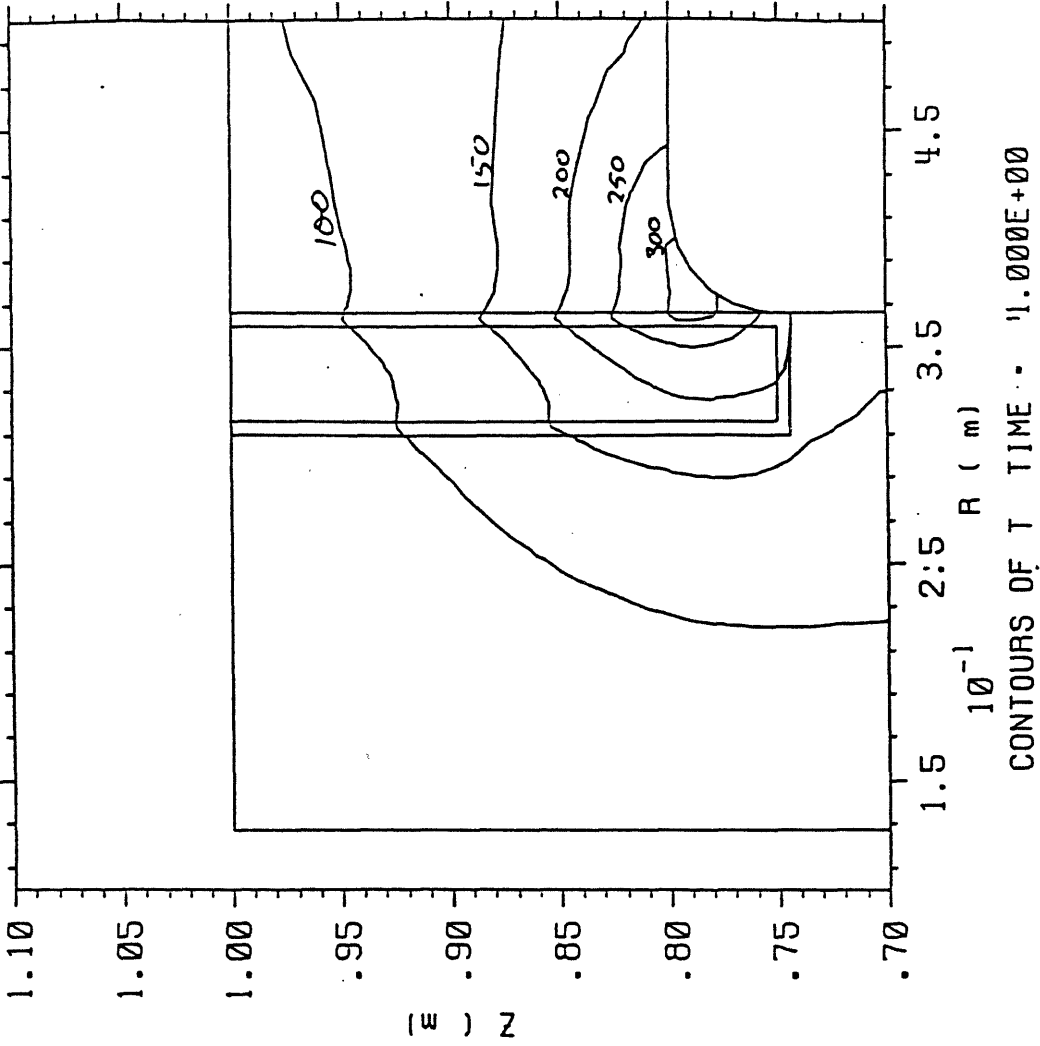


Figure 3:15: Contours of constant temperature near the inner corner joint in the TF coil at the end of a 10 T, 1 second flat top.

3.1.4 TF Power and Energy Requirements

The TF magnet is being designed for 10 Tesla operation, but this field can only be achieved through an up-grade of the present TF power system. The present power system is capable of driving the magnet to 7.5 Tesla for a 1.0 second flat top, the 1 second flat top representing a stored energy limit. For 10 T operation with the new supply described in Appendix A, the flat top would be limited by both energy and allowable temperature rise.

To determine the power and energy requirements for the TF magnet, and the peak temperatures, it is necessary to use a predictive model which takes into account the nonuniform current and temperature distribution in the magnets. The combination of LN₂ cooling, Bitter plate construction, and short pulse time results in a significant impact of magnetic diffusion on the calculations. Figure 3.16A illustrates contours of constant current density at two points in time to show the current penetration in C-MOD in the inboard corner during the pulse for a typical 2 second ramp, followed by a flat top. Such a nonuniform current distribution clearly results in a nonuniform temperature distribution as illustrated in Figure 3.16B. The peak temperature occurs at the corner of the plate, and it is the desire to reduce this local peak temperature that leads to in the corner radius shown.

Figure 3.17 summarizes the results of a number of runs of the predictive model giving the energy which must be removed from the power supply as a function of time. From the figure we note that the present 360 MJ generator (assuming a 10% over-speed), can supply approximately a 1 second flat top pulse at 7.5 T (allowing 80 MJ for the PF system). We

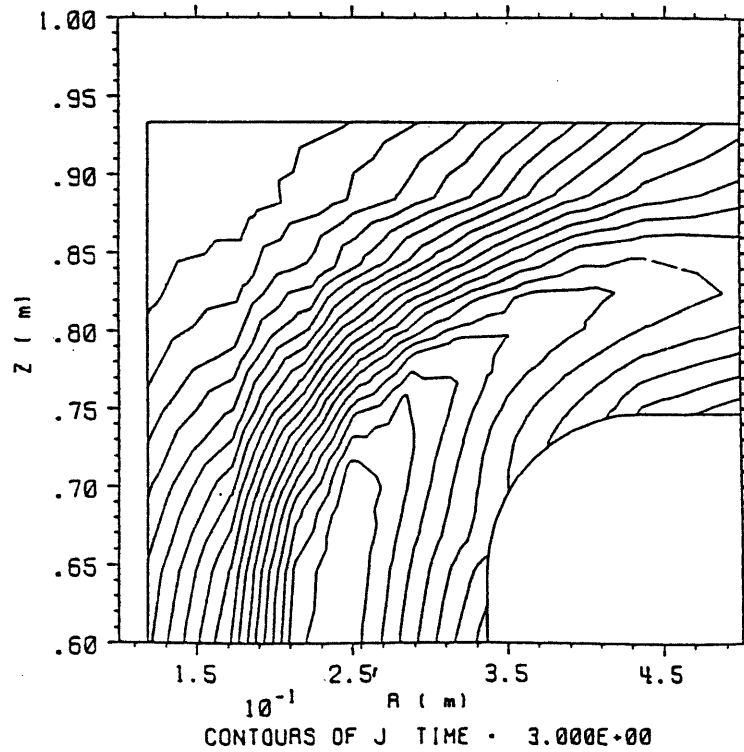
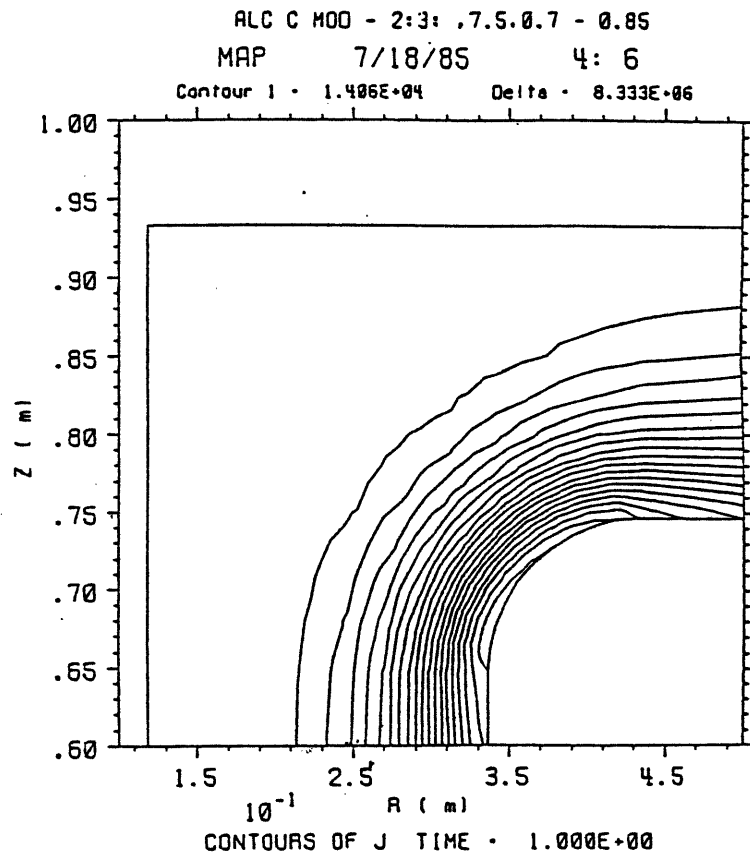


Figure 3.16A: Contours of constant current density near the C-MOD inner TF corner at 1 second into the ramp and at 3 seconds, the end of flat top.

ALC C MOD - 2:3: .7.5.0.7 - 0.85

MAP 7/18/85 4: 2

Contour 1 - 8.000E+01 Delta - 2.000E+01

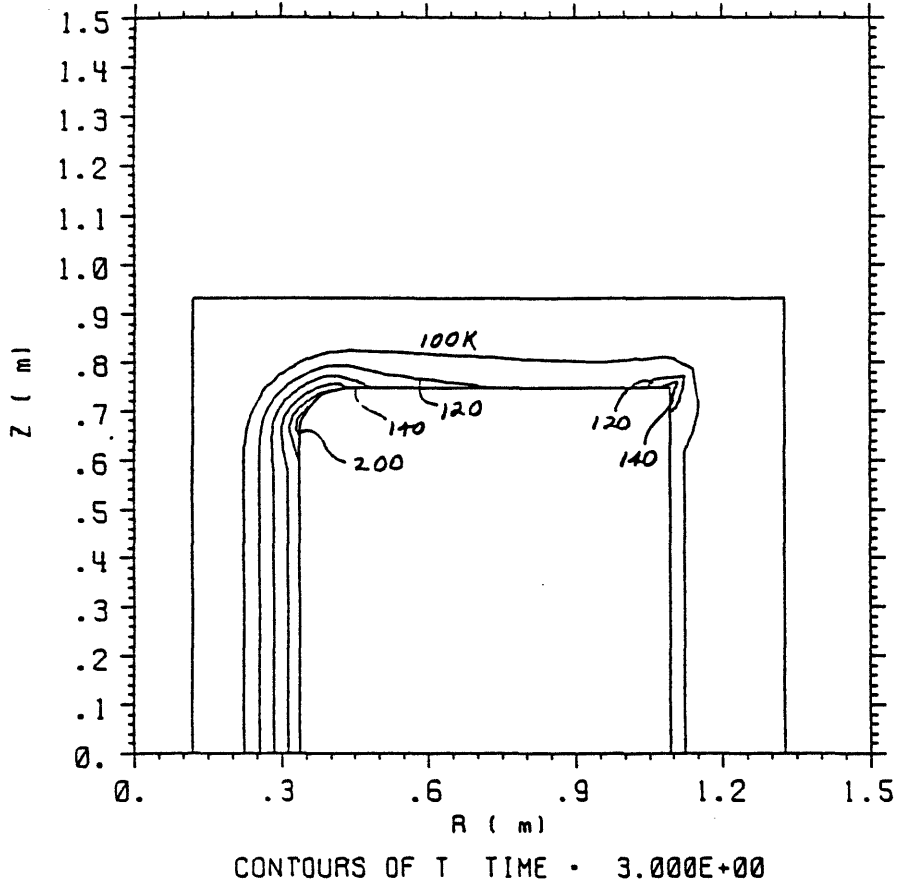


Figure 3.16B: Contours of constant temperature at the end of a 10 T, 1 second flat top

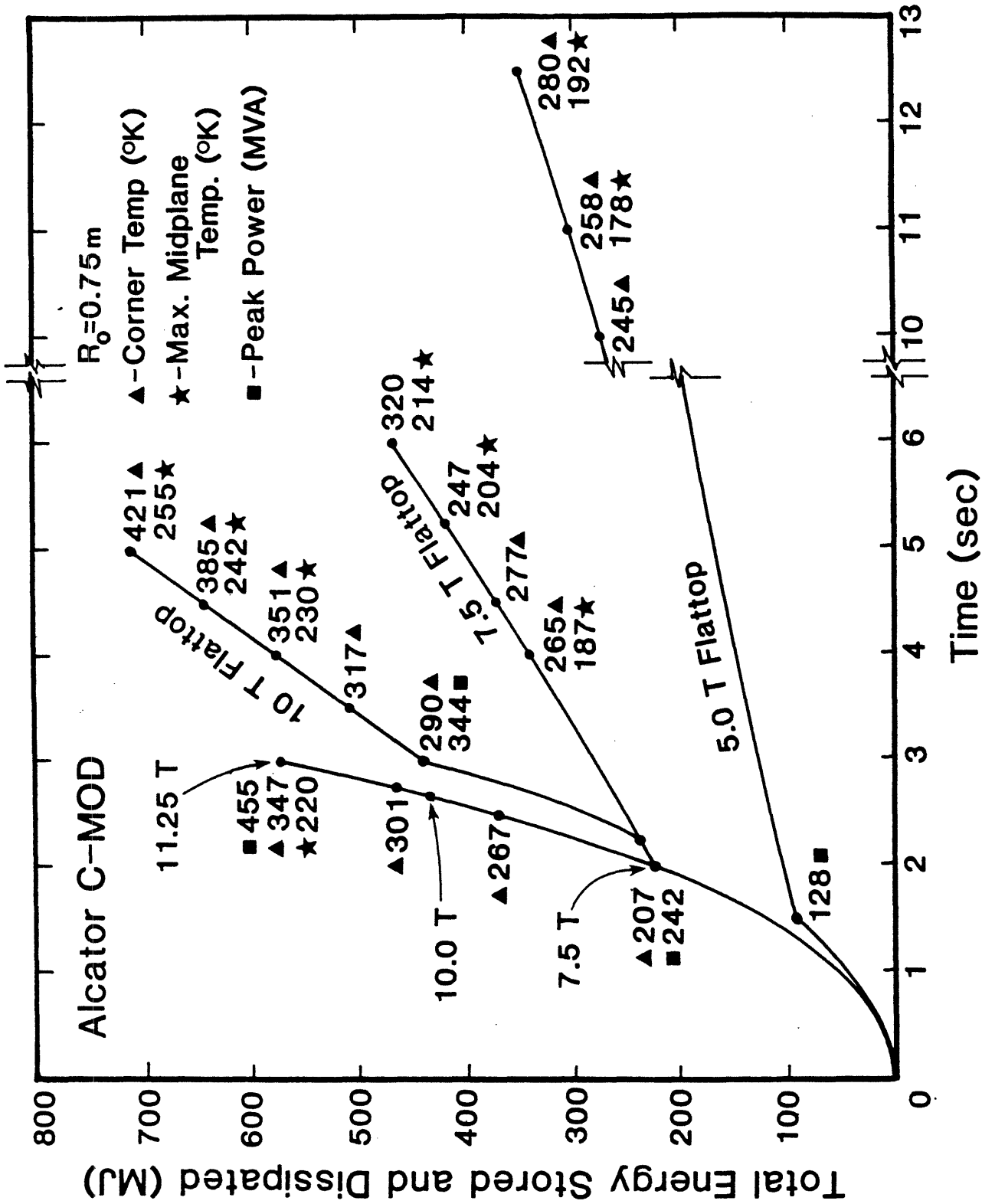


Figure 3.17: Total energy which must be supplied from stored energy for various peak fields and flat top times

8/75/7/3

also note that the proposed new 640 MJ generator could supply a flat top pulse of approximately 1.5 second at 10 T (assuming that the existing generator were used for the PF system).

Figure 3.17 also summarizes the peak corner and central leg temperatures as a function of flat top time for 7.5 Tesla and 10 Tesla. If we take 350° K as a reasonable peak corner temperature, we note that the thermal limited flat top time at 10 T is about 1 second, at 7.5 T about 5 seconds and at 5 T, about 15 seconds. Table 3.5 summarizes the energy and temperature limit flat top times for 10 T, 7.5 T and 5.0 T.

Figure 3.17 and Table 3.5 are based on the properties of 100% (IACS) conductivity alloy 102 copper. We anticipate using alloy-155 copper in at least the inner leg of the magnet. As given in Table 3.3, we note that that material is 10% more resistive at 300° K and that it has a resistance ratio at 77° K of approximately 5 as opposed to alloy 102 of approximately 7. These higher resistance properties might ordinarily result in a significant increase in stored energy requirements, but the higher resistivity is apparently largely compensated by faster field diffusion into the conductor, resulting in only modest increases as shown in Figure 3.18. The figure compares the energy which must be supplied by the rotating machine for the two alloys for a 10 T case. At the end of a one second flat top, only 25 MJ additional energy is required for the more resistive alloy.

The peak temperatures and energy requirements are also a function of the ramp rate, which is determined by the peak power capability of the supplies. The peak power capability is in-turn dependent on the

stored energy capacity of the supply, as the drop off in rotational speed has an impact on the available peak voltage. A ramp time of approximately 2 seconds to 7.5 T, and 3 seconds to 10 T is the maximum achievable, and hence has been used as the basis for the peak temperature and energy predictions.

TABLE 3.5
TF PULSE TIME LIMITS(1)

	360 MJ MACHINE(2)	640 MJ MACHINE(3)	THERMAL LIMIT(4)
10 Tesla	-	1.5 sec	1.0 sec
7.5 Tesla	1.0 sec	~ 6.5 sec	5.0 sec
5.0 Tesla	10.0 sec	~ 19.0 sec	15.0 sec

NOTES

- (1) assume alloy 102
- (2) assume 80 MJ to PF . . 280 MJ available
- (3) assume old generator supplies PF . . 640 MJ available
- (4) assume 350°K corner temperature limit at the end of flat top and without increase due to joint

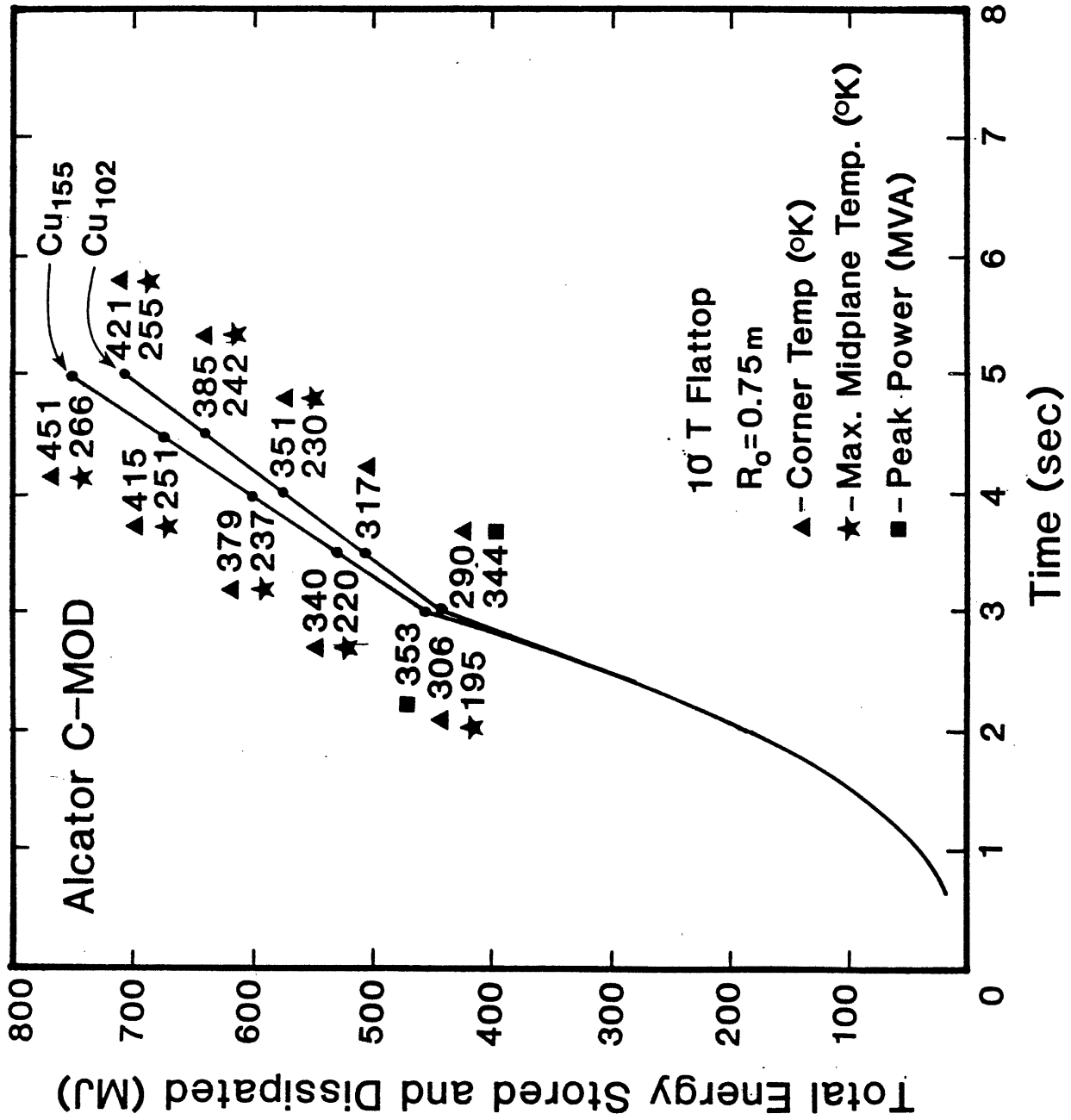


Figure 3.18: Total energy which must be supplied from stored energy for a 10 T peak field, as a function of flat top time and copper alloy

3.2 PF Magnet System

3.2.1 PF Current Requirements

The proposed C-MOD machine will utilize a combined OH/EF poloidal field system in keeping with current design practice. A typical 4 MA plasma equilibrium at the end of flat top is given in Figure 3.19.

This 4 MA equilibrium represents a double null expanded boundary where the separatrix points are only nominally inside the vacuum wall, with a 6 cm distance from the separatrix to the wall. Figure 3.20 gives a 2.5 MA double null equilibrium in which the separatrix-to-wall distance is 12 cm. An asymmetric divertor null could presumably be produced in which the 12 cm spacing would be maintained at the null, but currents in excess of 2.5 MA could be produced. Asymmetric equilibria are presently under study.

The plasma equilibria illustrated in Figure 3.19 and 3.20 are produced with a PF system in which the two outer equilibrium coils are external to the TF support structure. We have also investigated coil sets in which all the coils are internal to the structure as illustrated by Figure 3.21. The all internal PF set has certain advantages from an energy and electromagnetics point of view, but because the relatively strong dipole coils are now close to the plasma, the plasma is more subject to local field curvature effects. The present position of the internal PF coils in the point design should be taken as illustrative, with a trade-off of coil position, diagnostic access, and local plasma effects to be carried out as the design matures.

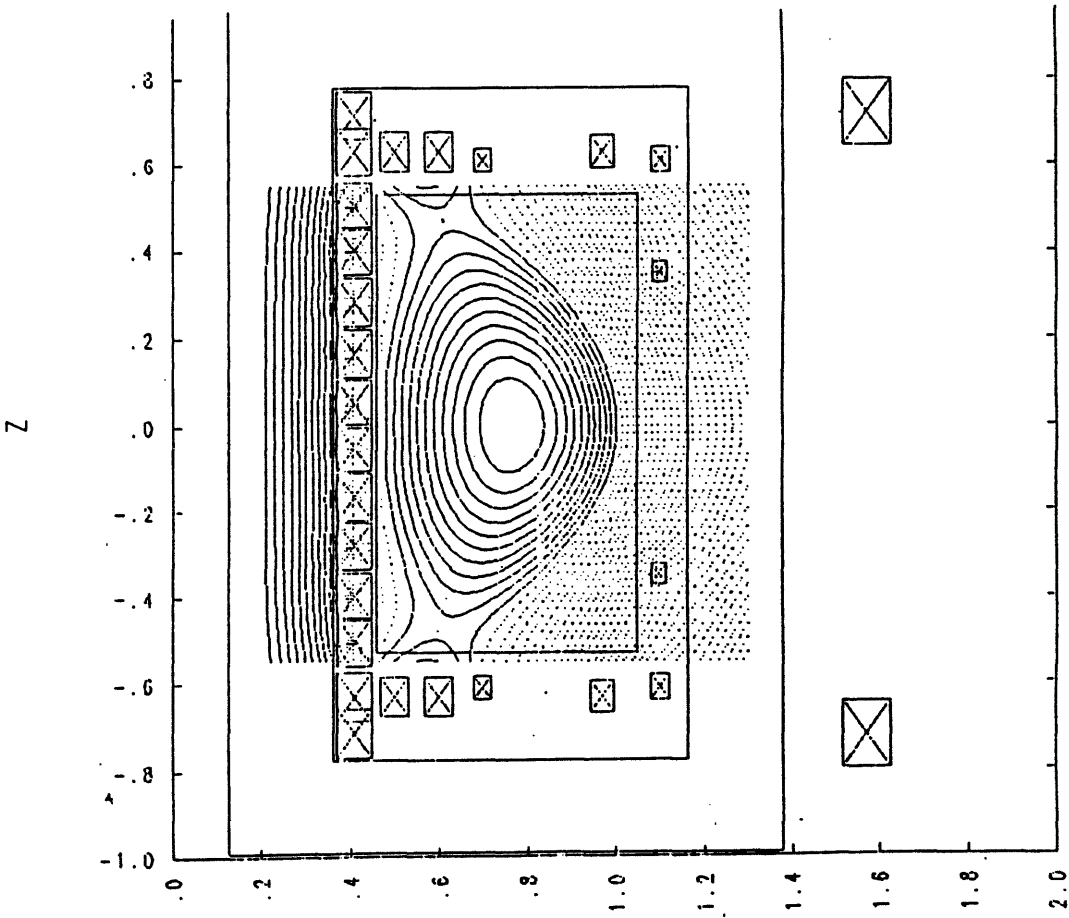


Figure 3.19: 4 MA plasma equilibrium

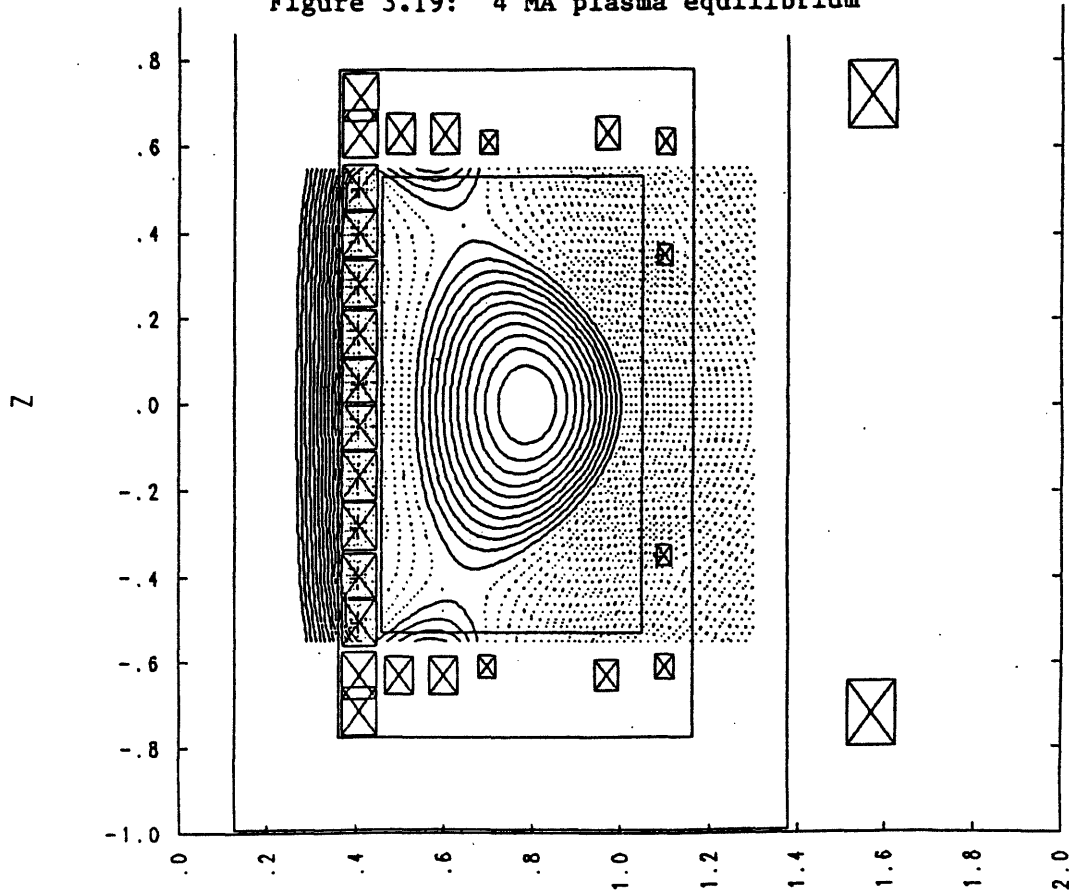


Figure 3.20: 2.5 MA plasma equilibrium

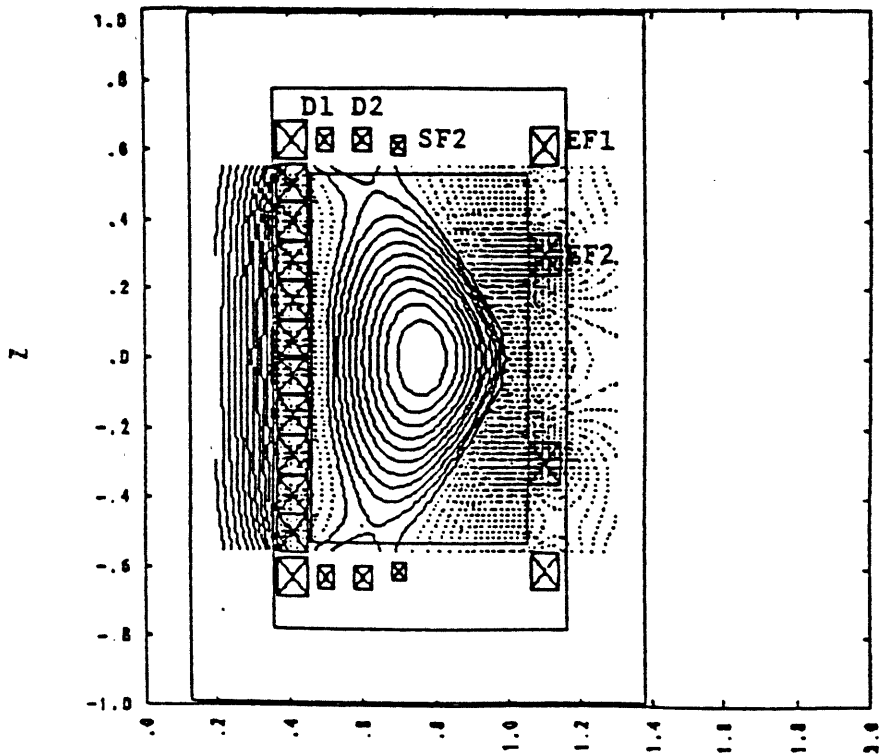
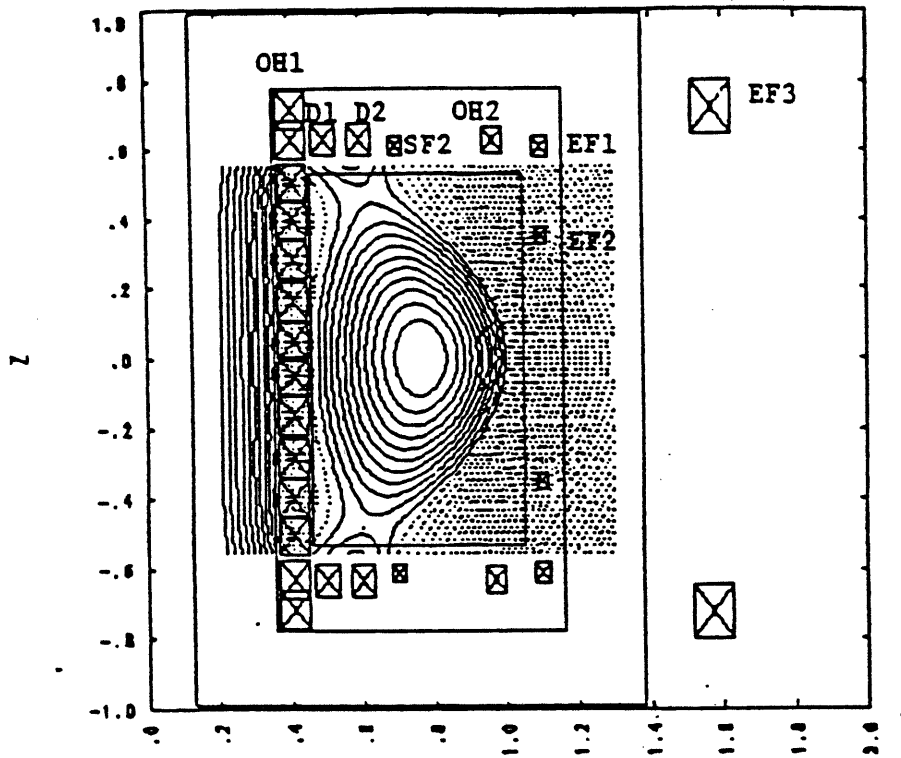


Figure 3.21: 4 MA equilibrium produced with (a) hybrid set of PF coils in which the main dipole coils are external to the support structures, and (b) an all internal set

The PF currents shortly after initiation and at the end of flat top are given in Table 3.6 for the 4 MA plasma equilibrium given in Figure 3.19, and form the basis for the power and energy considerations of the following section.

TABLE 3.6
TYPICAL PF COIL CURRENTS FOR A 4 MA PLASMA CURRENT EVOLUTION
COIL IDENTIFICATION PER FIGURE 3.21

COIL #	$I_p = 0.75 \text{ MA}^*$	$I_p = 4 \text{ MA}^{**}$
D1	+ 0.25 MA	+ 0.6 MA
D2	+ 0.25 MA	+ 0.6 MA
SF1	-	-
SF2	+ 0.08 MA	- 0.20 MA
EF1	- 0.19 MA	- 0.34 MA
EF2	- 0.09 MA	- 0.24 MA
EF3	-	- 2.36 MA
OH1	+ 9.3 MA	- 12.0 MA

* Circular plasma shortly after initiation

** Fully developed plasma of Figure 3.19

3.2.2 PF Power and Energy Requirements

The OH capability of the point design has been set at 12.0 Webers. The plasma simulation model indicates that approximately 10 volt-seconds would be required for a normal 4 MA discharge brought up in 2 seconds and flat-topped for one second. Figure 3.22 illustrates the PF coil swings and resultant volt-seconds utilizing the plasma simulation model. The plasma effective Z has been artificially increased in this model run in-order to consume the full 12 volt-seconds.

The energy requirements for the scenerio of Figure 3.22, are given in Figure 3.23 and 3.24 by individual coil, and by total resistive and magnetic energy. We note from Figure 3.23 that the energy requirements are dominated by resistive consideration largely as a consequence of the high current density in the central OH coil.

The central OH stack must operate at high current density, at a relatively high stress level, to avoid adding appreciably to the major radius and to increasing the aspect ratio. The relative build of the TF core and the OH stack have been chosen for a reasonable match of thermal capacity.

It would be extremely difficult to supply 12 volt seconds in a machine of this scale were the PF coils not internal to the TF coil. Even with the relatively large diameter, the central solenoid has a peak field of 10 T. Figure 3.25 illustrates the radial and axial magnetic loading on the central portion of the OH solenoid as a function of time, and indicates a maximum average toroidal stress of 260 MPA. This average stress is within the allowable for 155 alloy copper. An alternate choice of material would be half-hard copper co-wound with steel. The ratio of

peak to average stress in the coil is 1.13.

The plasma/coil simulation model also gives individual currents, voltage, flux linkage and peak temperature as shown in Figure 3.26 for OH1. We note a peak temperature of 172°K. The PF coil match-ups to existing Alcator power supplies are given in Table 3.7. We note that it will be necessary to supplement the present complement of Alcator C EF supplies, increasing the present 112 MVA capacity with an additional 70 MVA for the full 4 MA operation. The additional coils required for shaping (and divertor operation) are principally responsible for the increased requirements.

TABLE 3.7
PF POWER SUPPLY REQUIREMENTS

COIL #	CURRENT	VOLTAGE	CAPACITY**	COMMENT
OH1 +	22 kA	1.1 kV	60 MVA	Existing OH3
OH1 -	20 kA	1.2 kV	24 MVA	New
* OH2 +	22 kA	1.1 kV	60 MVA	Existing OH3
* OH2 -	20 kA	1.2 kV	24 MVA	New
D1	3 kA	0.25 kV	0.82 MVA	New
D2	21 kA	0.75 kV	18.75 MVA	Existing OH2
SF2	7 kA	1.0 kV	6.7 MVA	New
EF1	5 kA	2.75 kV	15.0 MVA	Existing EF1
EF2	9 kA	1.05 kV	9.05 MVA	New
EF3 +	12 kA	0.55 kV	6.06 MVA	New
EF3 -	24 kA	0.75 kV	18.75 MVA	Existing OH1

* OH2 represents the upper and lower 25% of the central solenoid, allowing additional flexibility of shaping during the fully developed plasma phase.

** Total existing capacity 112.5 MVA; required new capacity 70.0 MVA.

Plasma Volt-Seconds (Wb) vs. Time (s)

ISP 0424

VS,max (Wb) = 6.1841

VS,min (Wb) = -5.84557

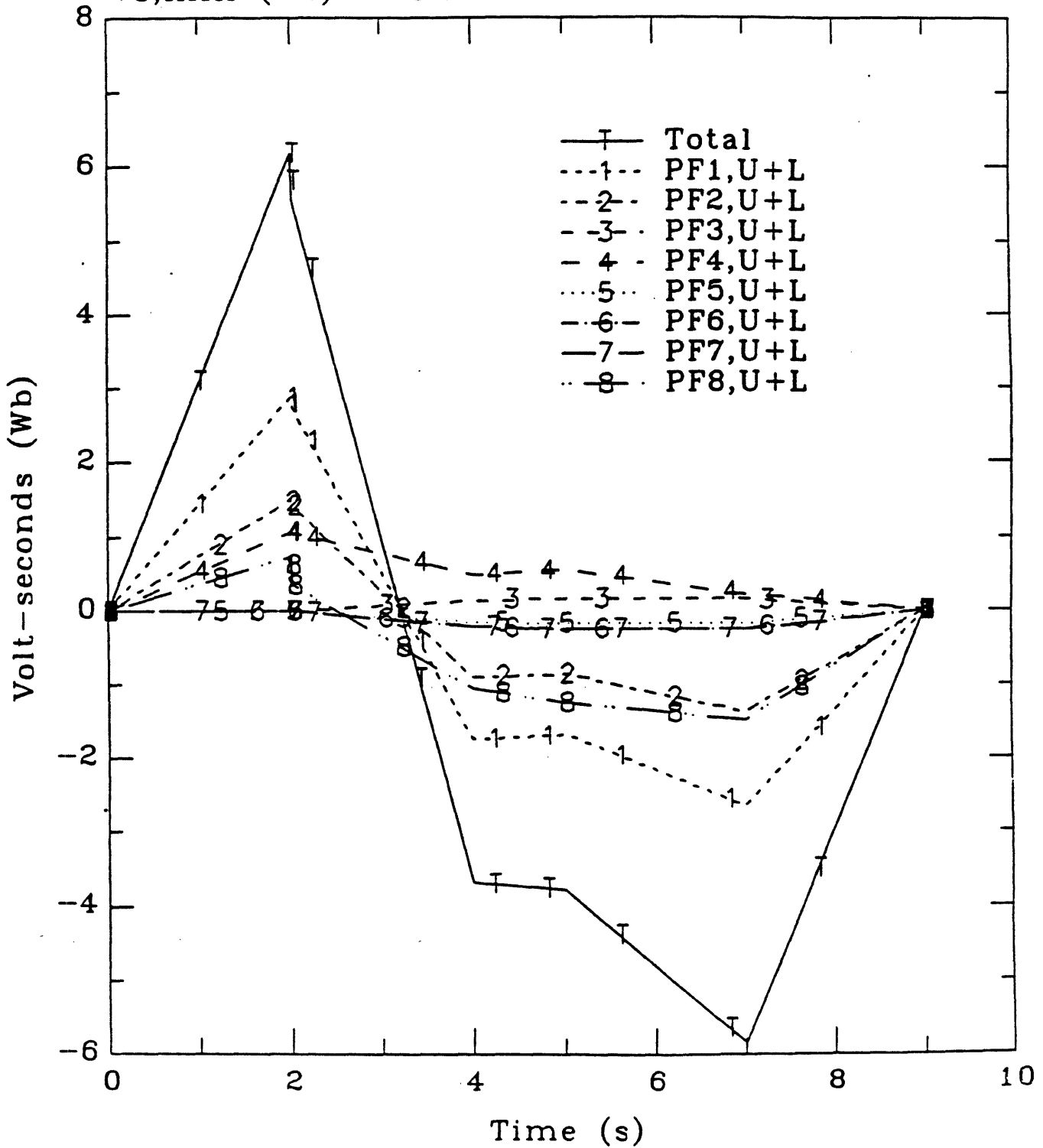


Figure 3.22: PF coil current swing and resultant volt-seconds for individual PF coils, upper and lower sets

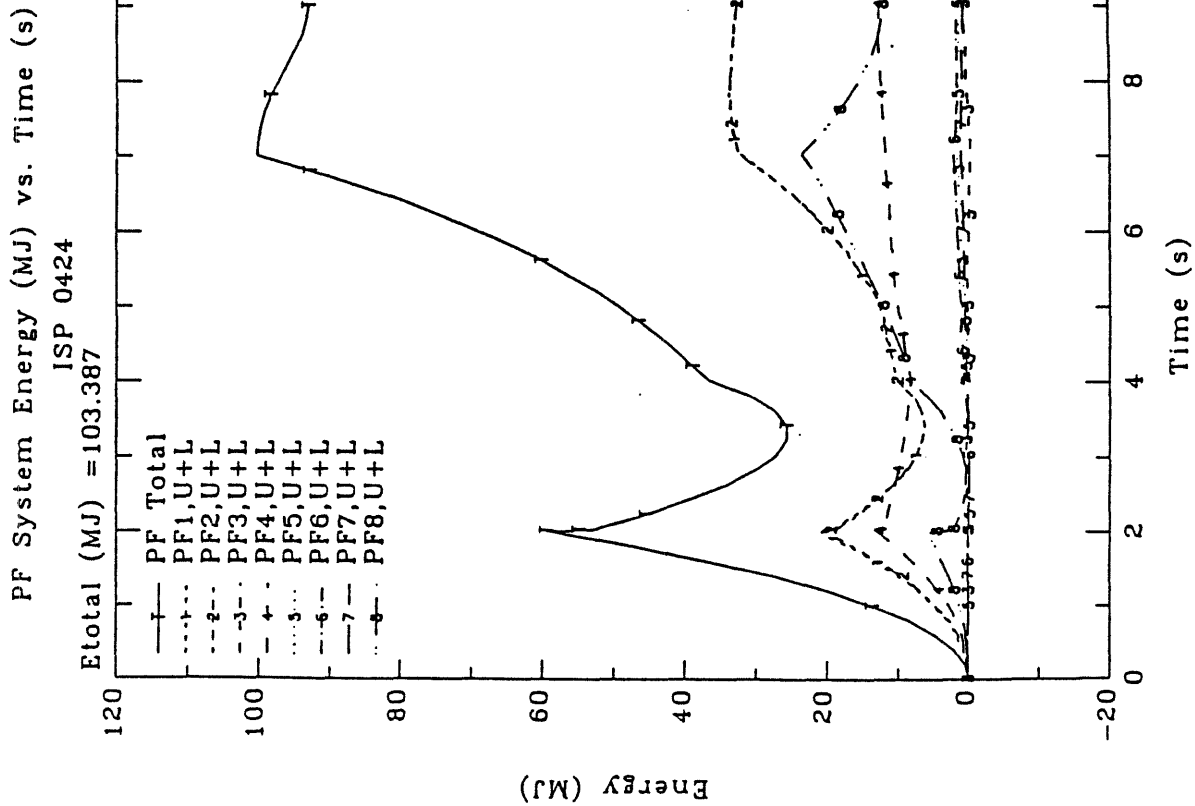


Figure 3.23: Total PF system and individual PF coil energy vs time

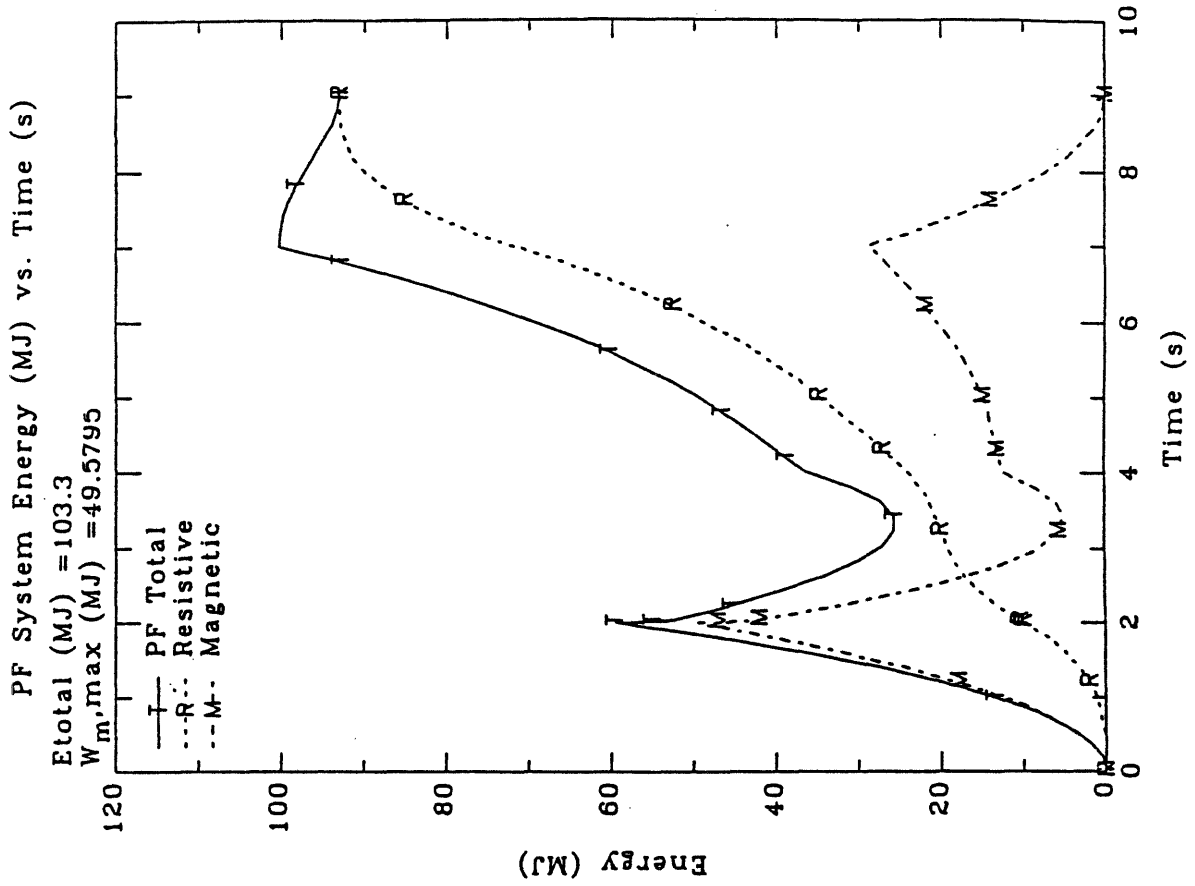


Figure 3.24: Magnetic and resistive component of PF system energy vs time

Radial Force vs. Time (s)

$$R_c \text{ (m)} = 0.410$$

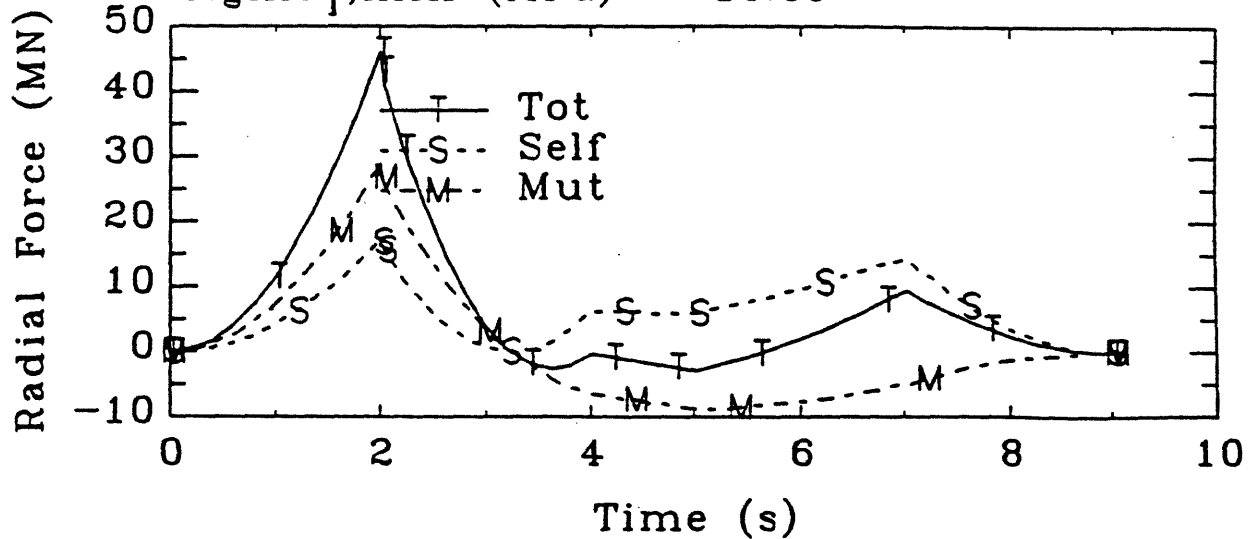
$$Z_c \text{ (m)} = 0.175$$

$$dR \text{ (m)} = 0.090$$

$$dZ \text{ (m)} = 0.350$$

$$\sigma_{T,\max} \text{ (MPa)} = 233.68$$

$$\sigma_{T,\min} \text{ (MPa)} = -14.85$$



Axial Force vs. Time (s)

$$\sigma_{z,\max} \text{ (MPa)} = 19.68$$

$$\sigma_{z,\min} \text{ (MPa)} = -3.20$$

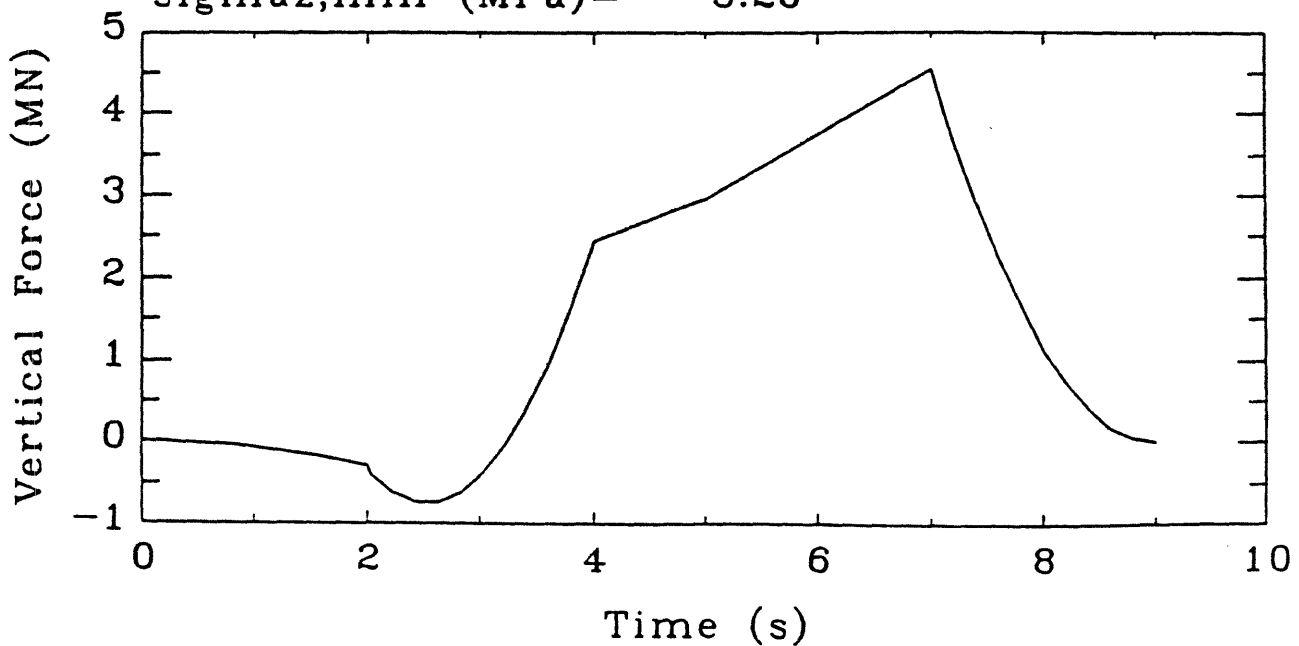
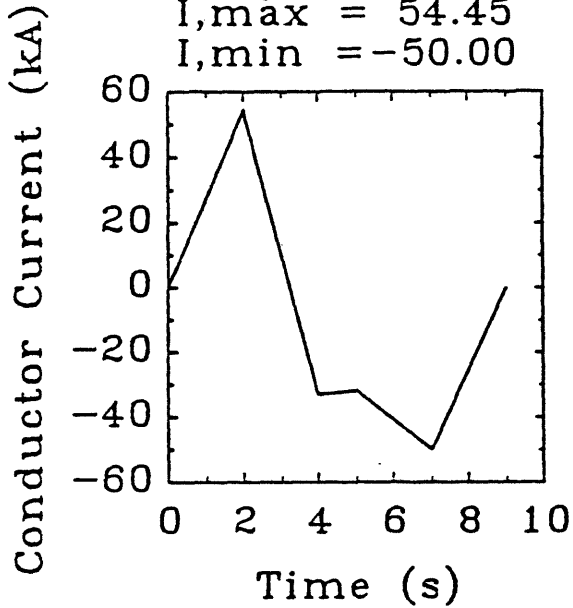


Figure 3.25: Radial and axial loading on the central portion of the central solenoid as a function of time

OH1/SF1,U

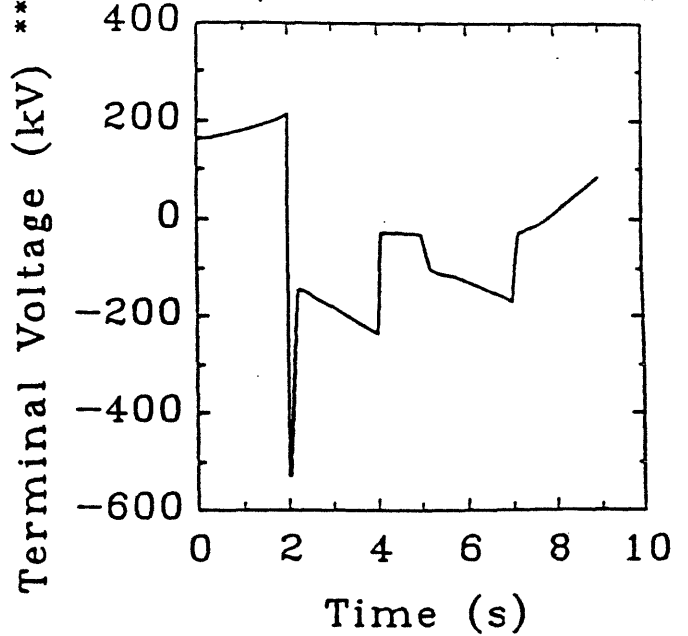
Current (kA) vs. Time (s)

$R_c = 0.41$
 $Z_c = 0.17$
 $I_{max} = 54.45$
 $I_{min} = -50.00$



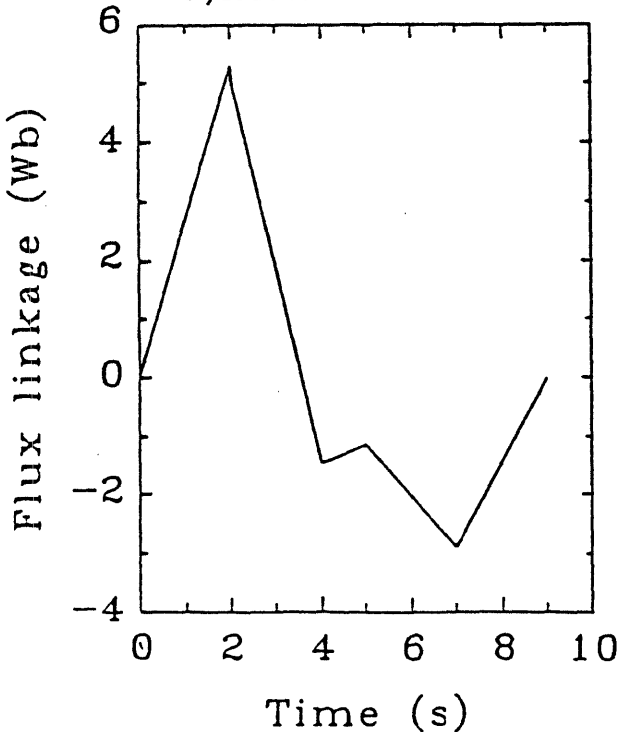
Voltage (V) vs. Time (s)

$V_{t,max} = 2.15E-01$
 $V_{t,min} = -5.31E-01$



Flux Linkage (Wb) vs. Time

$V_{S,max} = 5.29976$
 $V_{S,min} = -2.88842$



Temperature (K) vs. Time

$J^2t, \text{ norm} = 1.95174$
 $E_{spec} \text{ (J/cc)} = 235.832$
 $T_{max} \text{ (K)} = 172.451$

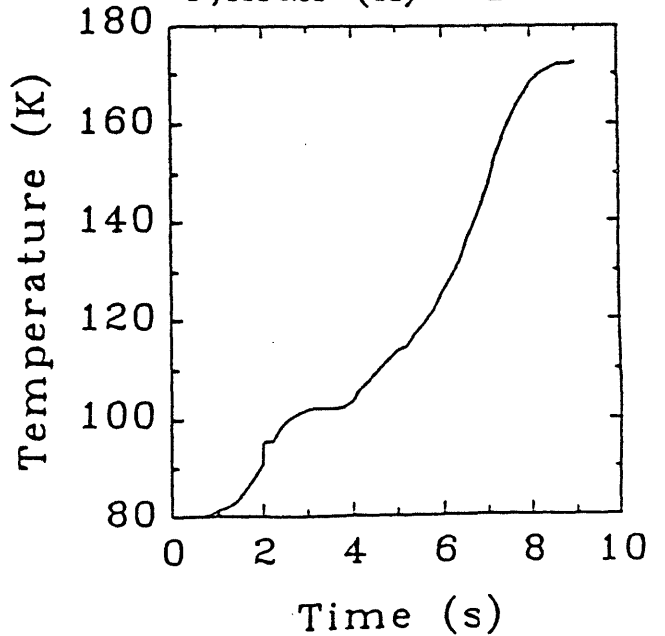


Figure 3.26: Current, voltage, flux linkage, and temperature of the central portion of the OH solenoid vs time

3.2.3 Electromagnetic Considerations

The fact that the structural elements are not electrically subdivided makes the C-MOD structural approach unconventional relative to present day tokamaks. This lack of subdivision allows relatively simple and efficient structures which lend themselves to easy assembly and disassembly.

These non-electrically divided structures, however, result in longer time delays in the penetration of start-up loop voltage and equilibrium fields, than in current tokamaks. The problem is akin to those encountered in studies of start-up and stability in INTOR-like machines in which the blanket and shield elements result in substantial delays. The general conclusions reached in the INTOR studies has been that delays in the appearance of sufficient loop-voltage are minimal relative to the plasma ramp times, and that fast vertical position stability is supplied by eddy currents in the chamber, blanket and shield elements. The INTOR studies indicate it is only necessary to supply external stabilizing fields on roughly the same time scale as the decay of the passive currents.

Radial stability (important at start-up when plasmas would presumably be circular and hence vertically stable) has not been studied in INTOR, but one might anticipate that the same consideration of cross-over between passive and active requirements will apply.

We have used a loop model simulation to study the electromagnetic impact of conducting support structure and the influence of the vacuum vessel resistivity. Figure 3.27 illustrates the loop model in which the

ALCATOR C MOD - CASE 13

C-MOD RECT. VAC. TES. SOL'S

SOLDESIGN 8/ 2/85 8:40

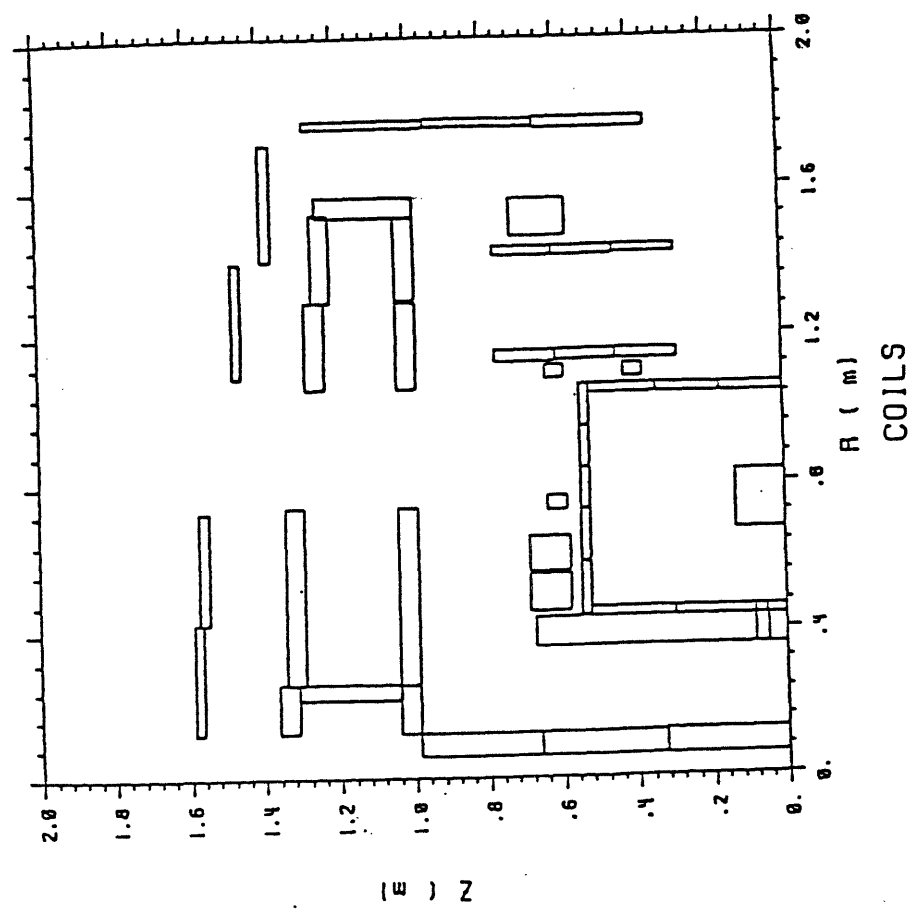
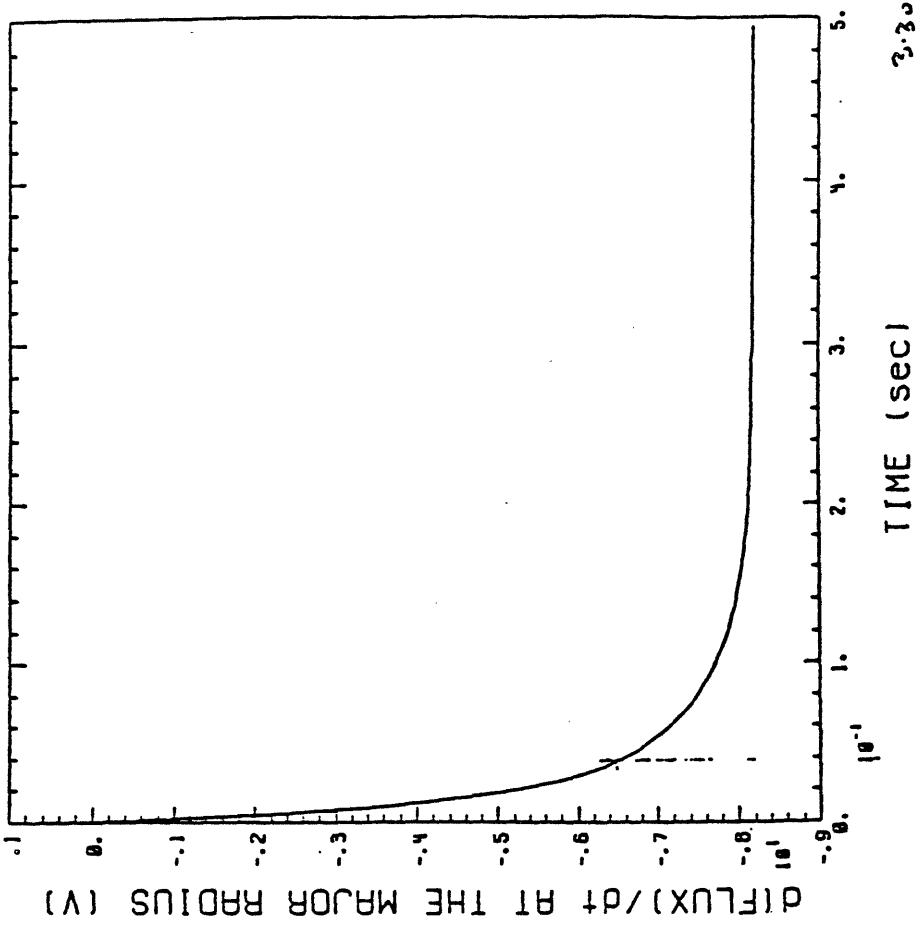


Figure 3.27: Loop elements used in Electromagnetic Model of C-MOD

Figure 3.28: Rate of change of flux at the plasma axis for a 2 second OH ramp

structure and vessel have been divided up into passive loop-like elements whose resistivity can be varied. The active coils are then driven and induce currents in the elements which decay according to the characteristic eigen values for the system. Elements which are crossed by periodic cuts (for example for ports) are assumed to carry no net current in this model and, hence, do not appear in Figure 3.27.

Figure 3.28 is a plot of rate of change of flux (proportional to loop voltage at the plasma axis) predicted by the loop model for a 2 second ramp down of the OH system. Were there no metallic elements, the resultant 8 volts of loop voltage would appear at time zero. With the structural and vacuum vessel elements included the the loop voltage achieves 80% of its final value in about 40 msec. In this simulation, the vacuum vessel is assumed to be constructed from 2.5 cm stainless steel plate, but even so, the vessel is not a major factor in limiting the initial loop voltage, that being largely determined by the support structure. When the simulation includes only the vacuum vessel for example, the 80% of final loop voltage value is achieved in 12 msec.

Figure 3.29 is a plot of the magnitude of equilibrium field at the plasma axis predicted by the loop model, where the field is intended to track a two second plasma current ramp, starting at time zero. We note that the predicted field lags the proper equilibrium field as expected. If the plasma initiation were to be delayed approximately 50 msec relative to the start of the equilibrium field ramp, a more nearly proper match would be achieved. Figure 3.30 plots the predicted rate of change of equilibrium field, and we note that 80% of the desired value is achieved in about 100 msec.

ALCATOR C MOD - CASE 13

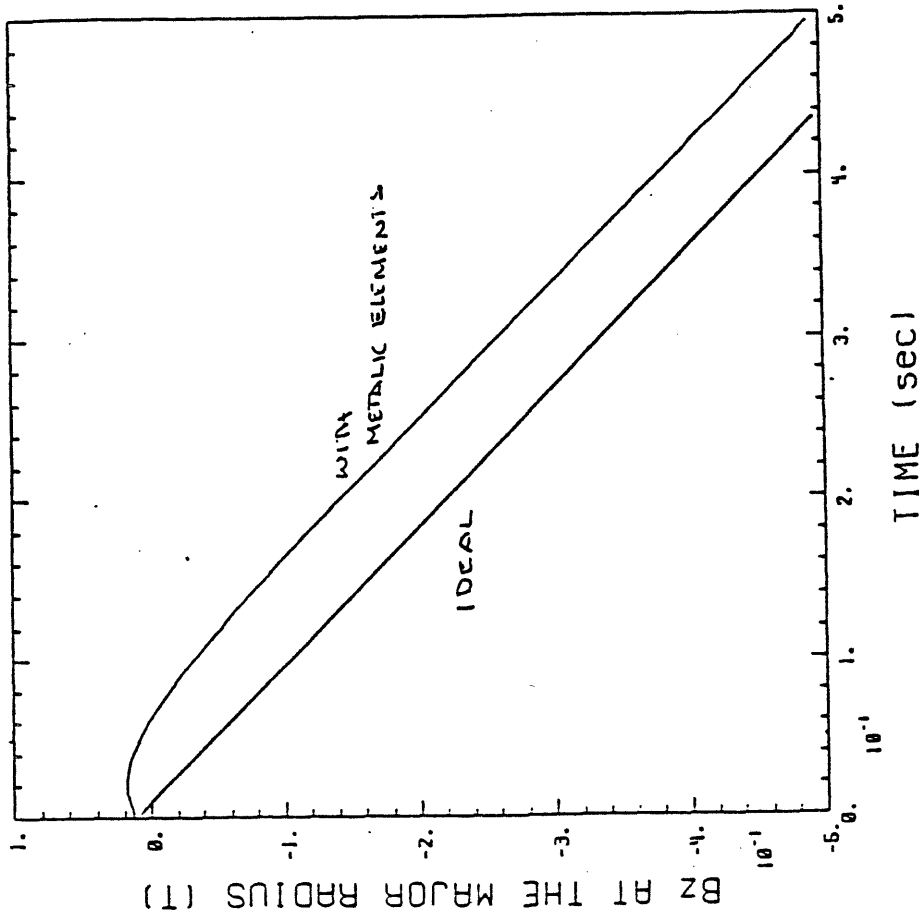


Figure 3.29: Vertical field at the plasma axis with and without metallic elements in the loop model, as the equilibrium field follows a 2 second plasma ramp

ALCATOR C MOD - CASE 13

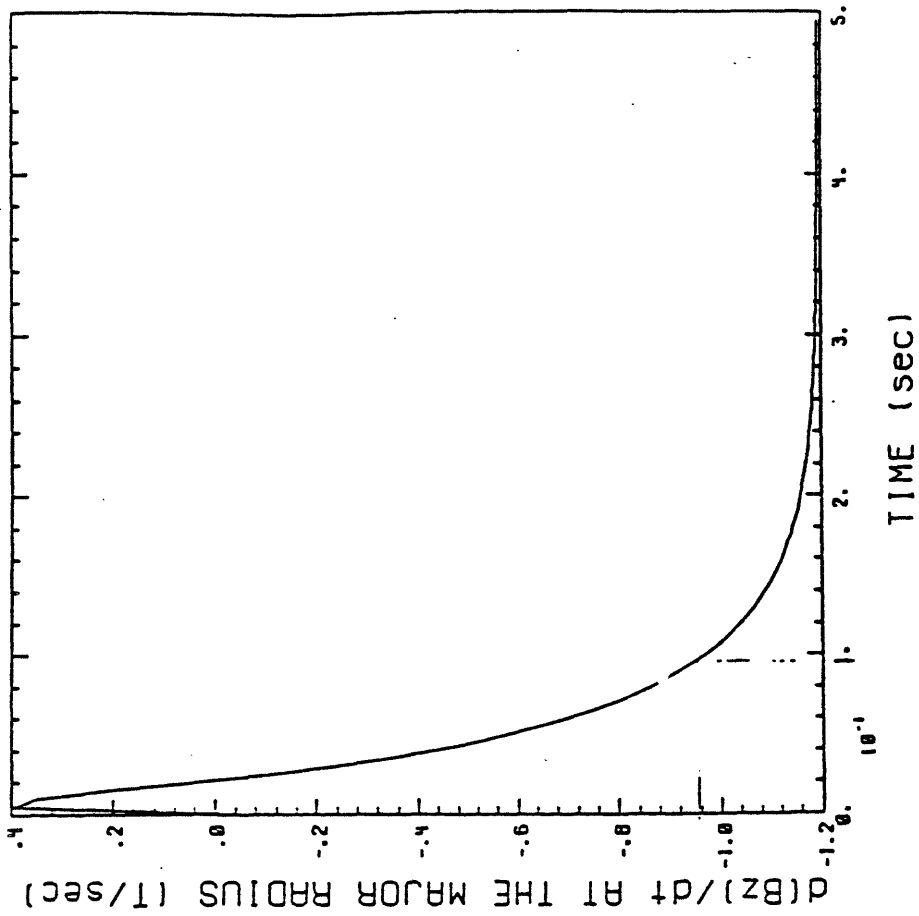


Figure 3.30: Rate of change of equilibrium field with metallic elements in the loop model, as the equilibrium field follows a 2 second plasma ramp

The loop model has also been used to carry out a study of plasma vertical position control. A preliminary estimate of peak power requirements indicate that powers in the range of 0.3 MVA would be required to return the plasma to its equilibrium position in 400 msec following a 1 cm vertical displacement. A peak power of 4.4 MVA peaking at 12 msec will return the plasma to its equilibrium position in 110 msec. However, it appears from the study that it is not possible to stabilize the plasma without adding passive elements inside the vacuum vessel. The plasma chamber walls are apparently too far away from the plasma to provide sufficient passive stabilization. A pair of 5 cm x 5 cm cross-section passive copper loops 8 cm in from the outer wall, and 30 cm above and below the equator appear sufficient. Further study will be carried out, but we note that the need for similarly placed passive elements was recognized and incorporated in Asdex-Upgrade.

3.3 Vacuum Vessel

3.3.0 Introduction

The proposed C-MOD vacuum vessel has a relatively simple rectangular cross-section form. The rectangular cross-section provides the greatest flexibility for plasma geometry variations, and provides the maximum internal volume for mounting components. The demountable nature of the TF coils allows the vessel to be constructed as a single piece and pretested prior to installation in the magnet. The single piece construction is of particular importance in coping with 4MA disruptions in a compact machine.

As discussed in section 3.1.3 on electromagnetic considerations, the electrical nature of the TF support structures dominates the electromagnetics rather than the vacuum vessel. Start-up and control strategies consistent with the proposed structural support, obviate the conventional requirements for a high resistivity vacuum vessel. This in turn greatly eases the structural problems which normally accompany large current disruptions. As discussed in Section 3.3.1, a solid wall vessel of 1.2 to 2.5 cm local thickness would be sufficient to withstand the anticipated disruption load.. A uniform thickness of 2.5 cm has been assumed in the electromagnetic field penetration calculations. A single unit heavy wall vessel further allows the robust attachment of limiters and collector plates as discussed in Section 3.3.2.

We will consider an alternate construction for the vessel as well, utilizing the DIII type sandwich panels. Vendor quotations will be obtained on both types of constructions.

The vessel need not be directly cooled according to our preliminary assessment. Liquid nitrogen cooled machines like C-MOD or Alcator C generally lose heat to the LN₂ back-ground through their thermal insulation at a sufficient rate to be compatible with the machine duty cycle. It is, in fact, generally necessary to supply some heat to promote plasma operation with chamber walls held above the condensation temperature of the plasma impurities.

The chamber pumping will be supplied by the turbomolecular pumps now used on Alcator C.

3.3.1 Disruption Structural Response

Figure 3.31 is a SPARK model simulation to determine the plasma currents flowing in the plasma chamber following a 4 MA disruption. The model includes cut-outs for the port access, but does not yet include the port extensions. We have also used the loop model described in section 3.2.3 to predict the quantitative distribution of vessel currents following a disruption. The loop model has the advantage of also including the effects of the eddy currents of the surrounding structural elements. For a case in which the disruption duration (for example, 4 msec) is comparable to the vessel time constant (for example, 6 msec for a 1.2 cm thickness), the external support structures would have a modest mitigating influence.

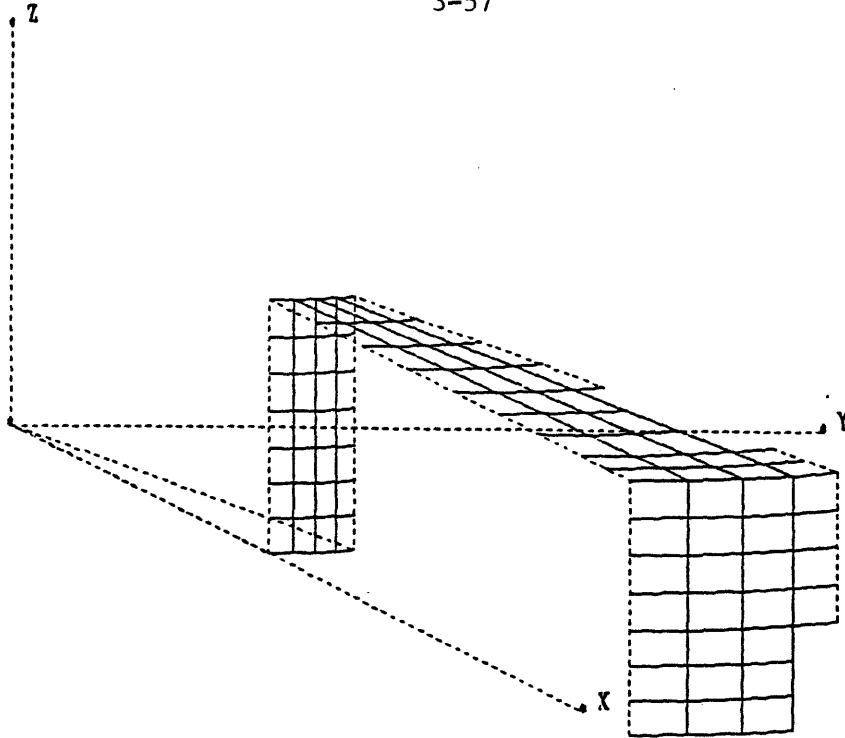
The currents induced in the vessel for a 4 MA, 4 msec disruption, peak at 4 msec, and at that time give rise to the force distribution shown in Figures 3.32 and 3.33. The resultant stresses based on relatively simple static strength-of-materials calculations are given in Table 3.8, and appear acceptable. More sophisticated shell model calculations are underway, together with stress calculations around the ports.

Future studies will examine the loads resulting from an asymmetric disruption (for example, as in the JET disruption which resulted in vacuum vessel support damage). Loads induced in limiter and collector plates will also be examined.

TABLE 3.8
VACUUM VESSEL STRESSES FOLLOWING A 4 MA DISRUPTION

VESSEL REGION	LOCAL THICKNESS	RESULTANT STRESS
Inner Wall	1.2 cm	10 ksi
Outer Wall	1.8 cm	10 ksi
Covers	2.5 cm*	30 ksi

* Local support would need to be included in selected locations



LCATOR C-MOD - VACUUM VESSEL ONLY WITH VERT. & HORIZ PORT CUTOUTS

7/31/85

08:16:17 PST

Cray d

NG= 1

NP= 0

T= 4.000e-03

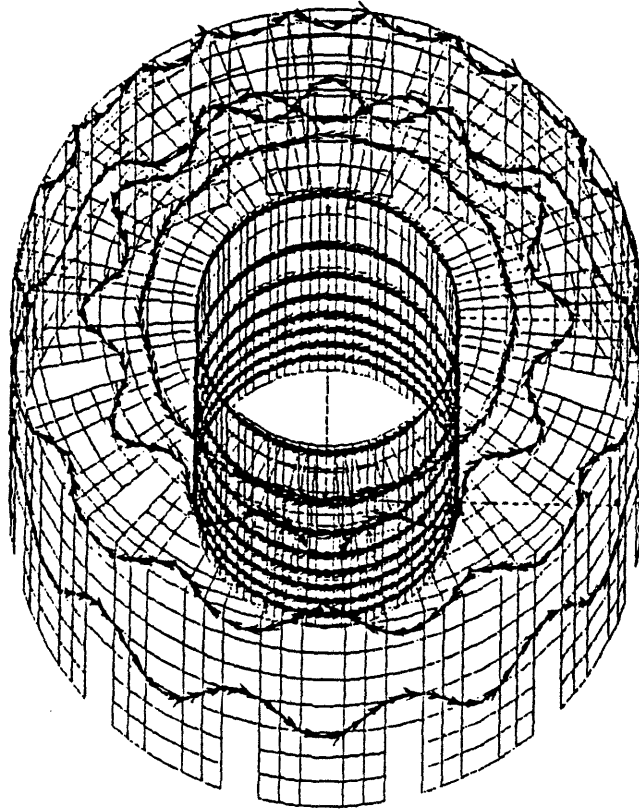


Figure 3.31: SPARK Model of the C-MOD vacuum vessel illustrating the current paths around the ports following a 4 MA disruption

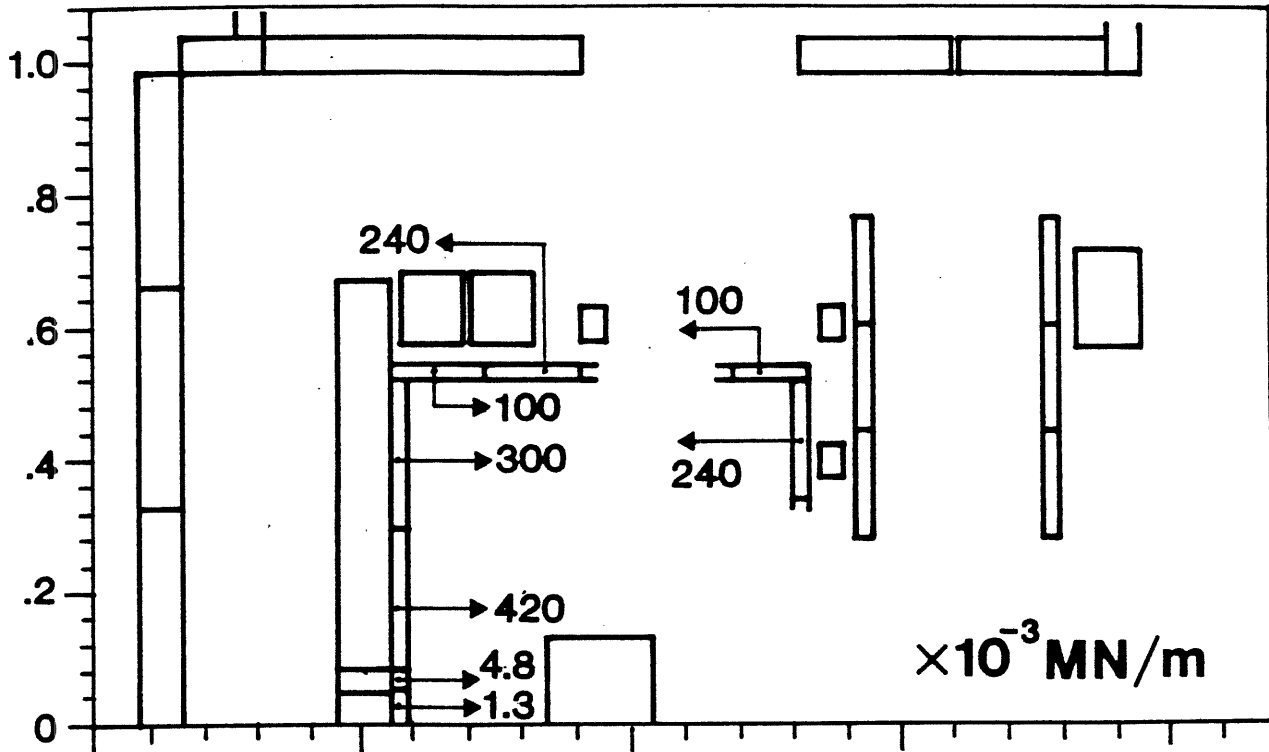


Figure 3.32: Radial component of forces per unit circumference on vacuum vessel elements. No loop current is assumed to be flowing in portions of the vessel interrupted by ports

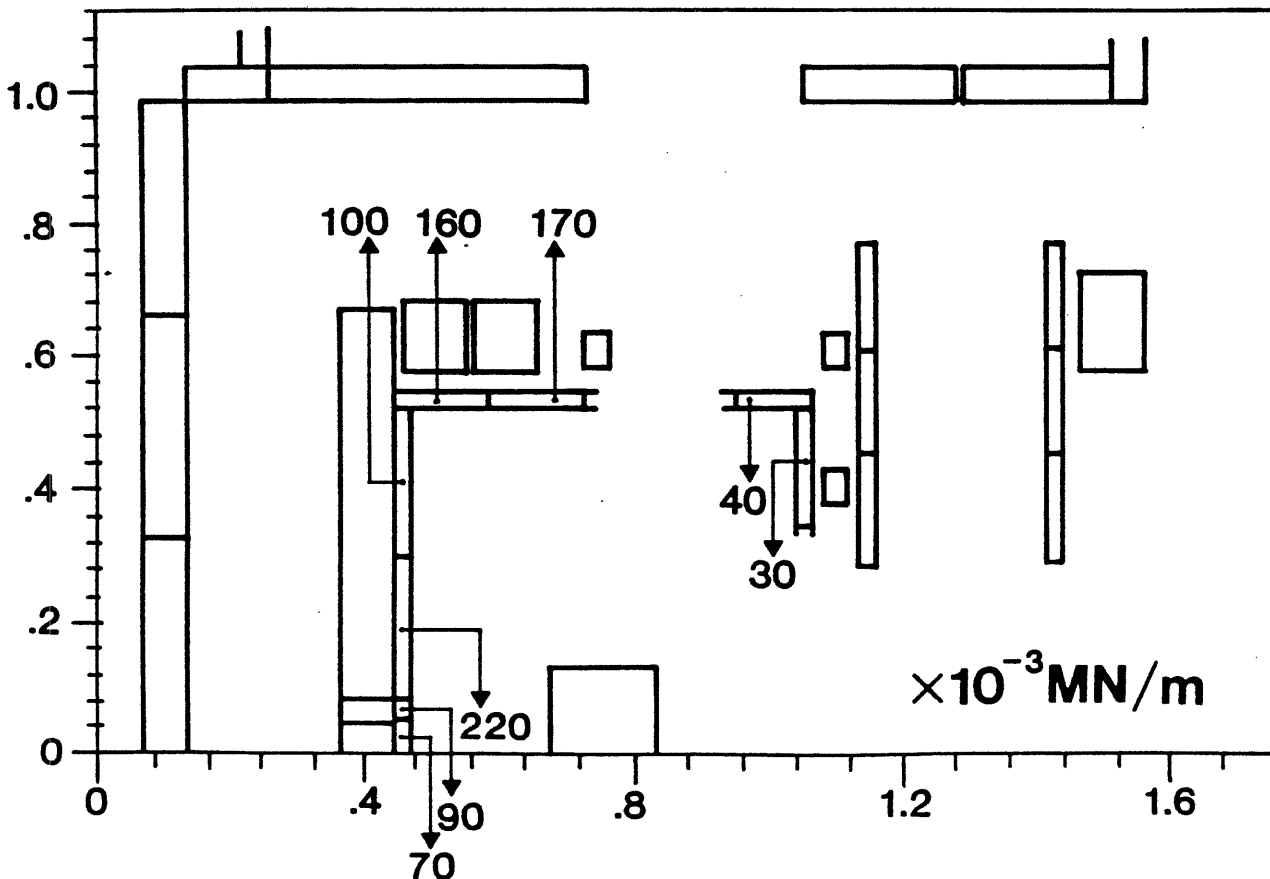


Figure 3.33: Axial component of forces per unit circumference

3.3.2 Wall Protection and Divertor Collector Plates

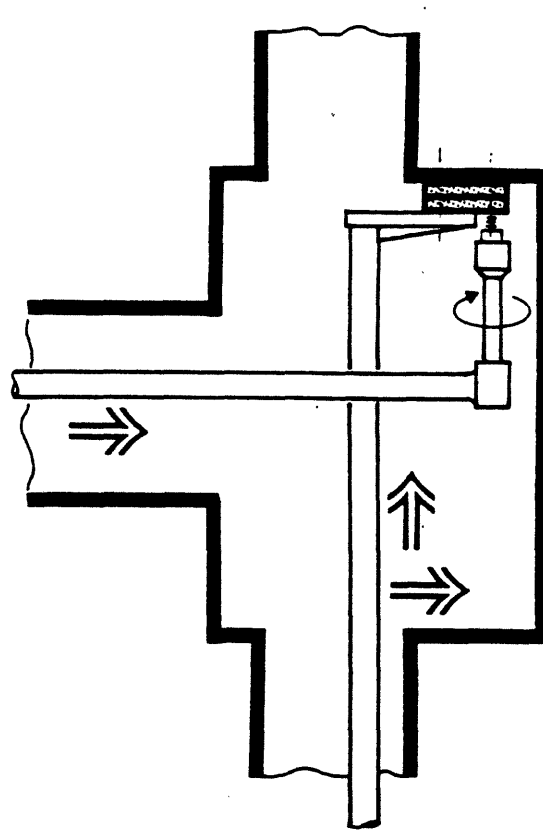
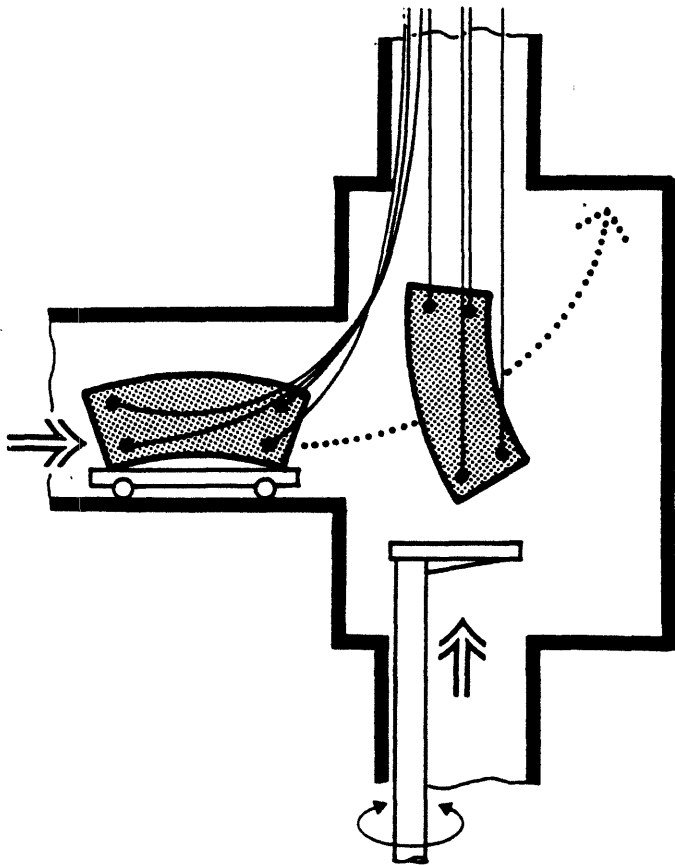
As discussed in chapter 2 under particle and impurity control, one of the major goals of the machine will be to compare limiter operation with divertor operation, and hence both configurations must be accommodated. The average heat load over the vessel is approximately 0.6 MW/m^2 with a 10 MW heat input. If we postulate limiters or collectors occupying typically 2 m^2 of the vessel area and receiving half the energy, we would have average heat loads in the 2.5 MW/m^2 class, and peak loads of approximately 7.5 MW/m^2 . The pulse time of the machine will be 1 second at maximum TF field, and we anticipate that the collectors and limiters need depend only on inertial cooling for this time duration.

All in-vessel components will be demountable. It is anticipated that they will be removable through the horizontal access ports, but one or more larger access ports, accessible only after demounting one or more TF coil copper legs, will also be provided for major installations.

An artist's conception of some reasonably simple tooling for installation of internal components is shown in Figure 3.35. Transfer tooling would be used to lift the limiter or collector panels, and to locate them on studs welded to the vacuum wall. Fasteners would then be used to attach the panels to the wall with appropriate compliance to avoid excessive thermal stress.

The inboard bumper limiter and divertor collector plates would consist of appropriate tiles (metallic or graphite) pre-mounted on stainless panels, which would then be bolted to the vessel wall. Given the electrical nature of the solid vacuum vessel (and that of the magnet

Wire Rope Loops



Wire Rope Loops

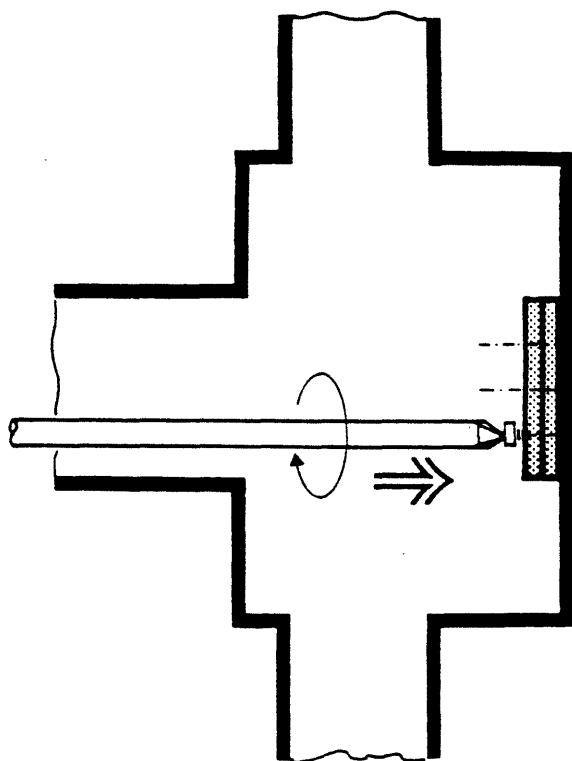
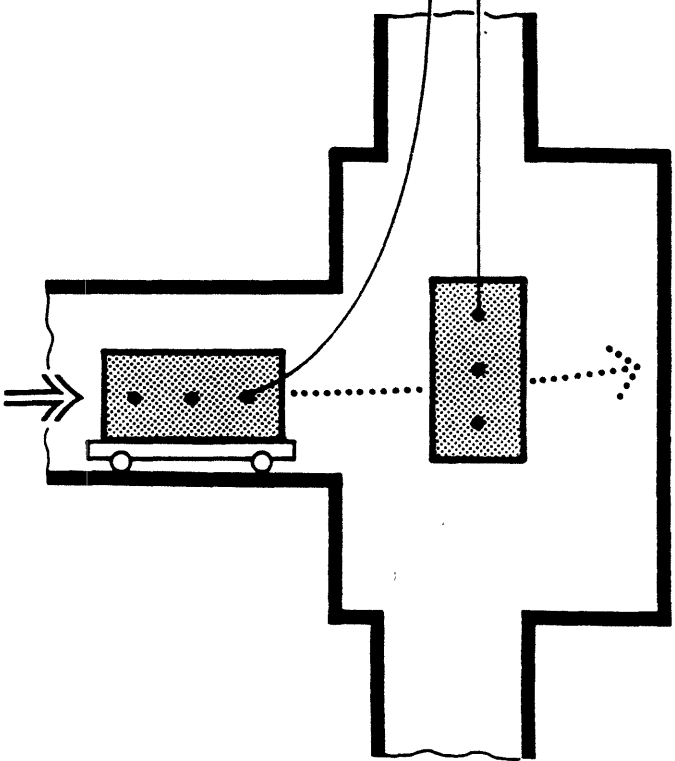


Figure 3.34: Concept for tooling to transfer bumper limiter and diverter panels to locating studs on the vessel wall, and to then tighten fasteners

structural elements) it is not necessary to electrically sub-divide these protective panels, nor to electrically isolate them from the main chamber. They can therefore be as robust as the vessel itself, greatly simplifying construction and installation. Thermal energy accumulated by the tiles during a pulse would be transferred to the panels and in turn to the vacuum vessel through the mechanical attachments (see Chapter 2).

3.4 Cryogenic Considerations

3.4.0 Introduction

The proposed machine will be liquid nitrogen cooled as in Alcator C, and the major LN₂ facilities used with the C machine will be transferred to C-MOD.

We anticipate utilizing a simple thermal barrier cryostat concept similar to Alcator C, and illustrated in Figure 3.35. As discussed below, we also anticipate using surface cooling for the TF and PF coils and structure, and allowing cold vapor to surround all elements internal to the cryostat. The vacuum chamber would be thermally insulated and provisions made to supply heat to the vessel as required to hold the chamber walls above the condensation temperature of the plasma impurities.

3.4.1 Recool Following a Pulse

The repetition rate between full-performance discharges is limited by recool of the cryocooled magnets to their initial operating temperatures of 80 K. The magnets are cooled by naturally circulating liquid nitrogen, wetting the magnet outer surfaces, therefore, the recooling rate is limited by the ability of copper to transfer heat to boiling nitrogen and by the ability of a long nitrogen column to transport bubbles.

The limiting portion of the TF magnet is the inside leg, because it is both the most strongly heated, and is the most constrained in the availability of cooling area. One option is to cool the inner leg along its inner and outer surfaces. Although the inner surface is at a very small radius, it is less constrained than the outer surface in terms of having all of its surface available for cooling and in having most of the inner vertical core available for nitrogen circulation. The outer

surface must include a spacer or winding surface for the OH coil. Using both surfaces, the recool rate from 170 K is shown in Figure 3.36. The calculated average temperature in the TF inner leg at the end of a 2 second 7.5 T flat-top is 150 K, requiring about 28 minutes to cooldown. This performance can be improved by coating the inner coil surface with a 1 mil layer of teflon, while leaving the outer surface bare. The principle is that the insulating layer allows nucleate boiling to begin at higher temperature differences between the nitrogen and the copper, while leaving about half of the available surface bare still permits good cooling at smaller temperature differences. With teflon coating on the inner surface, the recool time is reduced to 19 minutes.

An option being considered is to include cooling channels in each of the insulating sheets between TF plates, throughout all the legs of the TF magnet. This is essentially identical to the heat removal method proposed for the superconducting magnets in Alcator DCT. If 1 mm channels on both sides of an insulating sheet exposed 25% of the plate face, the face pressure on the sheets would be increased by 25%, while the cooled surface area of the inner leg would be increased by a factor of nearly 10. The recool time from 170 K for this option, assuming adequate bubble clearing, is shown in Figure 3.37. The recool time from 150 K is now only 2.5 minutes. In order to achieve that high a recool rate, 92 MJ must be removed from the inner legs at an average refrigeration rate of 613 kW. The critical boiling rate at which the nitrogen column can remove bubbles by natural convection is calculated to be 1.9 MW with the internal cooling passages, and 1.5 MW without them. An advantage of this option, which may be of some importance, is that it would allow the TF coil to dissipate as much as 1.9 MW in the inner legs on a

steady-state basis, permitting the TF coil to be energized for several hours at reduced field for plasma discharge cleaning.

It would also be convenient if the PF coils could be re-cooled by surface cooling. The relevant parameters are the Joules/gram of heat deposited in a coil, corresponding to its final temperature and the Joules/surface area, which is monotonically related to the cooldown rate. These are shown for the PF scenario option with one coil pair outside the TF coils, in Table 3.9.

TABLE 3.9
PF COIL CRYOGENIC-RELATED PARAMETERS

COIL	E/M (J/g)	E/A (kJ/m ²)
OH1/SF1	26.5	144
OH2	26.5	144
D1	0.57	2.6
D2	14.5	66.2
SF2	4.3	10.2
EF1	2.7	7.1
EF2	1.2	3.2
EF3	2.4	16.4

Table 3.9 indicates that only the central OH solenoids will present much of a problem, as might have been expected from their cramped quarters and high current densities. It should be noted that the OH ramps were predicated on an unnaturally dirty plasma, so that they could be designed for full coil capability. A relatively clean discharge requires only slightly more than half of the full OH double swing, and will thus be much less constraining on the recool time. The average value of 26.5

J/g corresponds to an average temperature of 172 K. The ratio of energy to cooled surface is half that of the TF inside legs, without internal cooling passages, but it is necessary to make cooling passages available on both the inside and outside of the OH coils, a feature not yet illustrated in the design drawings. The bubble clearing capacity of the OH coils is considerably less than that of the TF legs, unless they can communicate with the central stack through internal cooling channels in the TF legs.

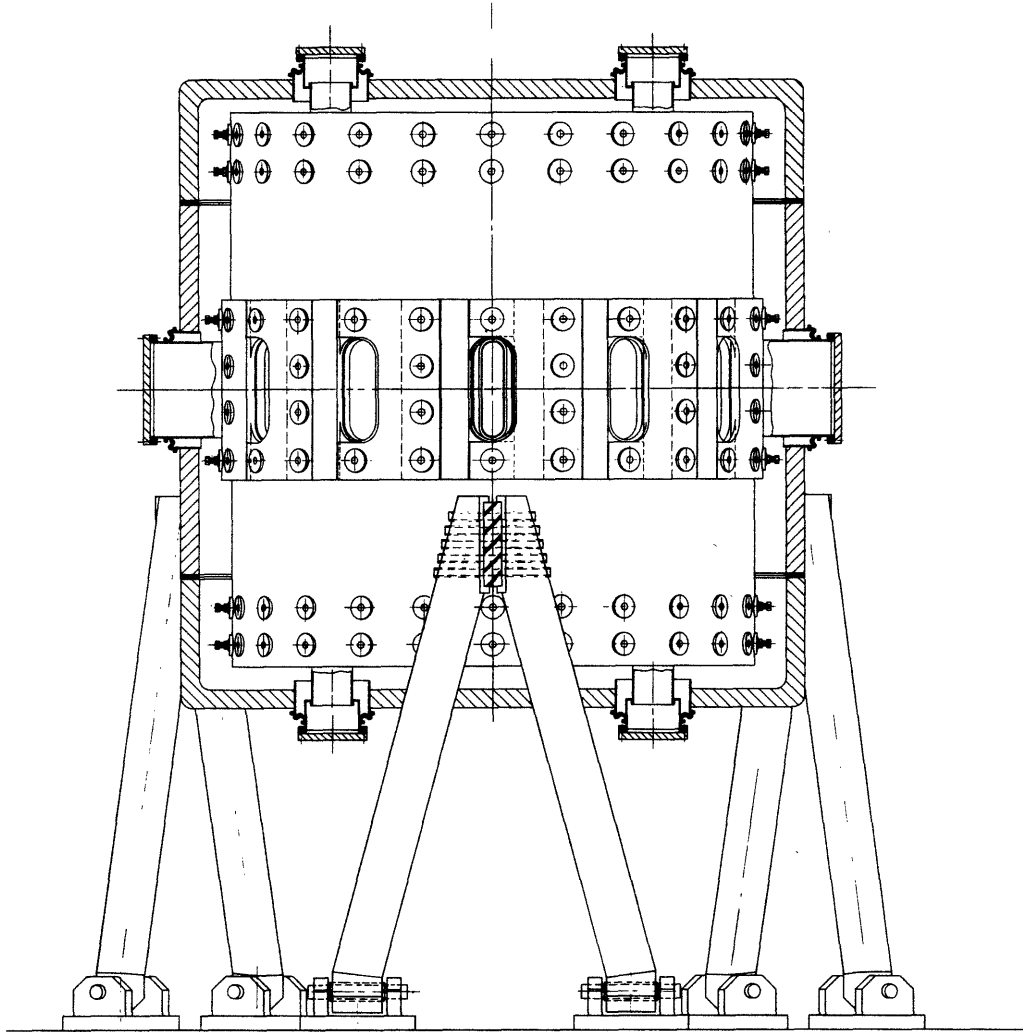


Figure 3.35: Overview of the C-MOD load assembly in the LN₂ cryostat. The cryostat detail is similar to that successfully used on Alcator A and Alcator C

**Recoil of Inner Leg of Alcator C-Mod TF Coil
by liquid nitrogen surface boiling**

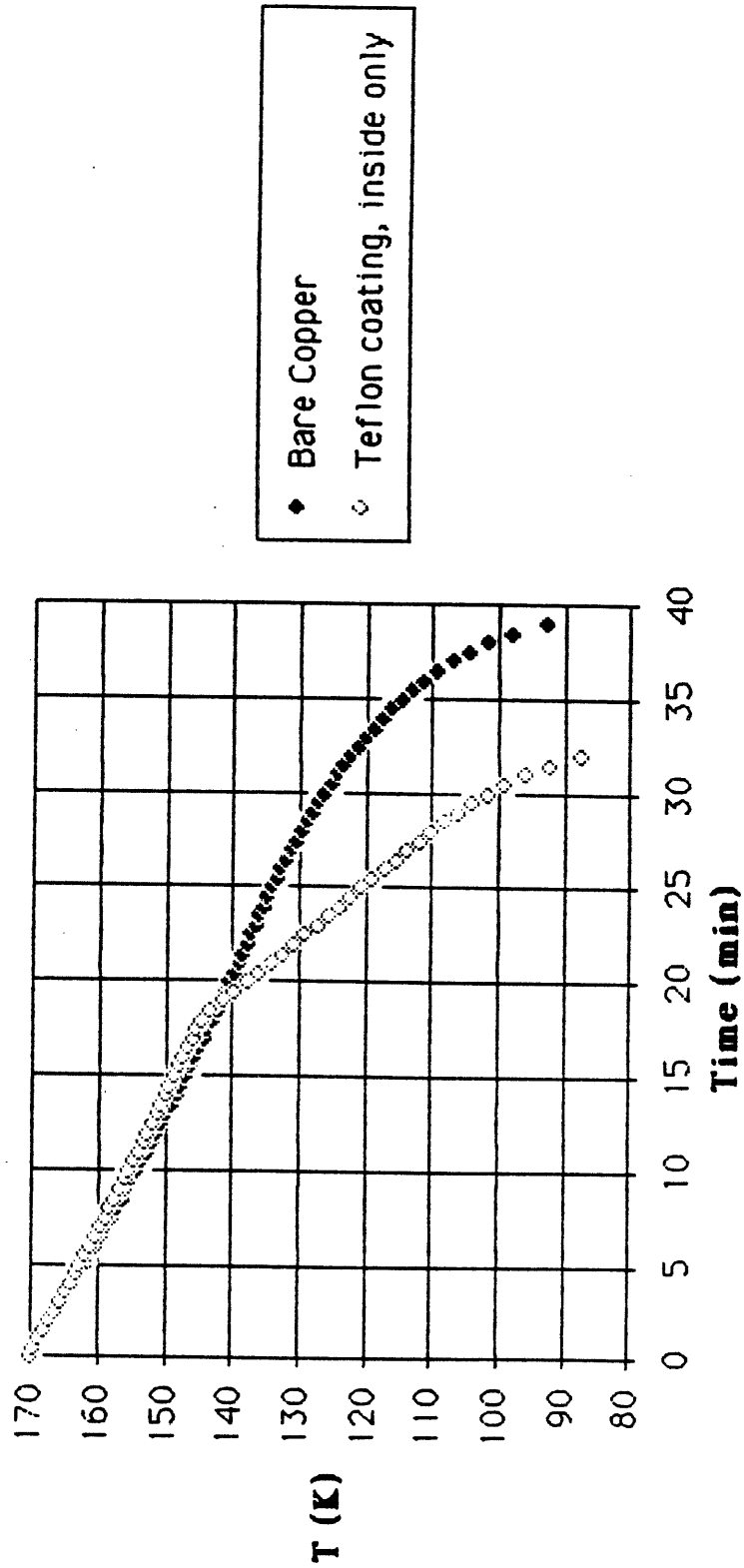


Figure 3:36: Recoil of inner leg of Alcator C-MOD TF coil by liquid nitrogen surface boiling

**Recool of Inner Leg of Alcator C-Mod TF Coil
by liquid nitrogen surface boiling
Internal cooling passages between plates**

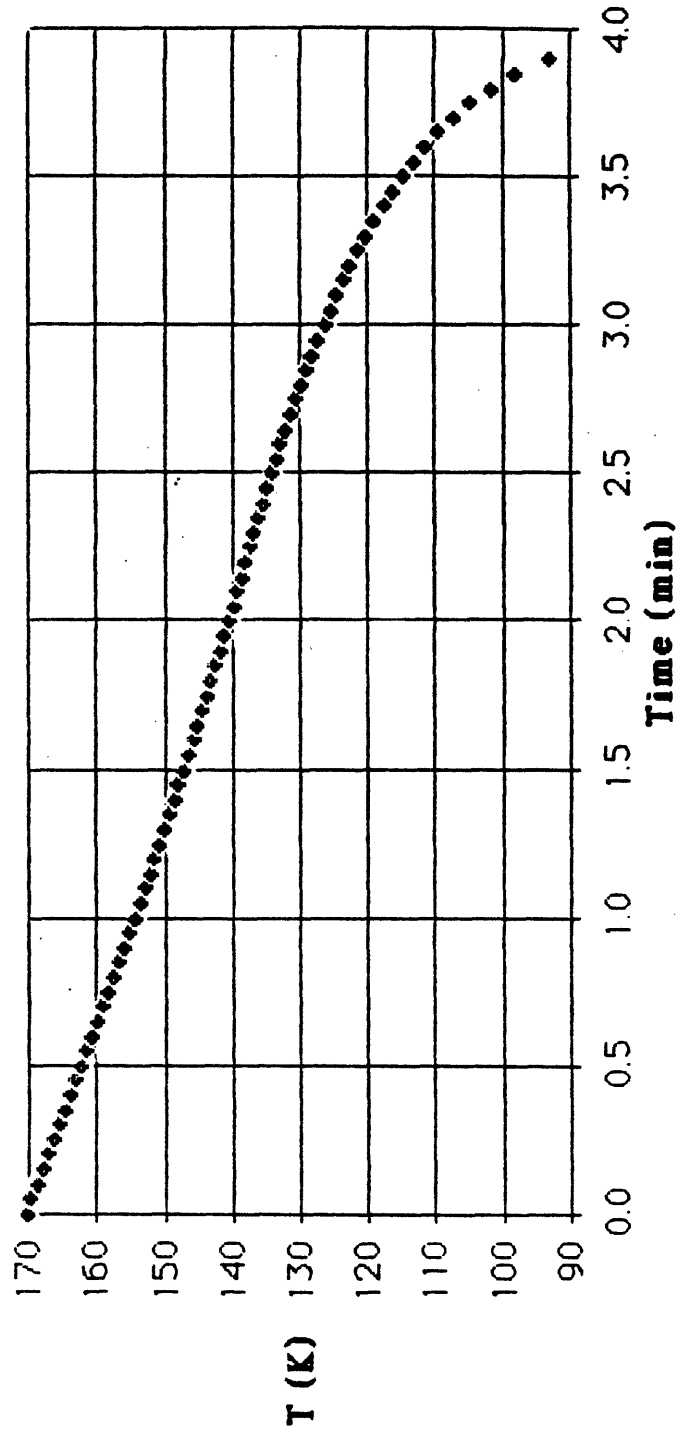


Figure 3.37: Recool of inner leg of Alcator C-MOD TF coil by liquid nitrogen surface boiling internal cooling passages between plates

3.4.2 Cooldown from Room Temperature

The simplified model of isothermal cooldown may break down at high temperatures, but it predicts a cooldown time of 4.8 hours from room temperature to 80 K. For comparison, the isothermal cooldown code predicts a 5.8 hour cooldown for Alcator C which has a measured cooldown time of 5 hours. The nitrogen consumption of Alcator C for cooldown is 2,100 gallons. The nitrogen consumption for Alcator C-MOD cooldown is calculated to be 5,330 gallons.

The cold mass and cooling surface area for C-MOD, as compared to Alcator A and C are given in Table 3.10.

TABLE 3.10
ALCATOR CRYOGENIC-RELATED PARAMETERS

ALCATOR	COLD MASS (TONNES)	COOLED SURFACE (m ²)	COOLDOWN (HOURS)	LN ₂ NEEDED (TONNES)
A	5.5	1.73	2	
C	18	3.3	5	6.42
C-MOD	45.7	10.1	4.8	16.3
<u>COIL</u>				
Inner Legs	4.74	3.32		
Outer Legs	7.50	4.47		
Upper and Lower Legs	<u>8.79</u>	<u>2.33</u>		
SUBTOTAL	21.0	10.1		
<u>STRUCTURE</u>				
Covers	14.1			
Ring	<u>10.6</u>			
SUBTOTAL	24.7			
TOTAL	45.7			

3.4.3 Nitrogen Consumption

The nitrogen consumption requirements for Alcator C-MOD are based on a desired experimental capability of running 20 equivalent full-power discharges per day, 100 per week and 2,000 per year. The standby nitrogen requirements are estimated to be 500 gallons/day. The nitrogen consumption is shown in Table 3.11. There is currently an 11,000 gallon nitrogen dewar used by Alcator C. For the proposed usage of Alcator C-MOD, in which the annual usage of nitrogen is about the same as that of Alcator C, while the highest daily usage is double that of Alcator C, the supplier would probably install a second dewar at MIT at their own expense.

TABLE 3.11
LIQUID NITROGEN CONSUMPTION

SYSTEM	ENERGY/PLUSE (MJ)	LN ₂ /DAY (m ³ /kgal)	LN ₂ /WEEK (m ³ /kgal)	LN ₂ /YEAR (m ³ /kgal)
<u>TF</u>	200	24.7/6.53	124/32.6	2,470/653
<u>PF</u>	90	11.1/2.93	55.5/14.7	1,110/293
<u>STANDBY</u>	—	<u>1.9/0.5</u>	<u>13.2/3.5</u>	<u>693/183</u>
TOTAL	290	37.7/9.96	192/50.8	4,270/1,129

3.4.4 Reliquefaction Considerations

An alternative to the purchase of liquid nitrogen to supply all cryogenic losses is to purchase a nitrogen reliquefier to convert nitrogen vapor to liquid nitrogen. A cold reliquefier should be cost and power efficient in comparison with a room temperature liquefier. This is the approach taken by the MFTF closed-cycle nitrogen reliquefaction system.

The MFTF Program is the only domestic program that has made special order purchases of closed-cycle nitrogen refrigerators in the

past decade. Laboratory and industrial-scale units are either too small or too large for the Alcator C-MOD application. Nitrogen subsystems, including a dewar, subcooler, piping, distribution system, controls and an auxiliary cooldown skid were purchased for MFTF-A and were then upgraded, along with the 500 kW reliquefier. The reliquefier alone cost \$9/W, while the cost of an entire closed-cycle system is approximately \$18/W. The current cost of nitrogen at MIT is \$0.08/l. Three nitrogen reliquefier options are considered here: (1) sized to provide the nitrogen needed for 20 full-power shots in 24 hours, (2) sized to provide 100 full-power shots over a week, (3) sized to provide standby losses only.

OPTION	RATING (kW)	COST (k\$)	SAVINGS (k\$/year)	COST/SAVINGS (YEAR)
Daily avg.	71	1,280	427	3.00
Weekly avg.	53	950	386	2.46
Standby	3.7	66	45.5	1.45

A small standby refrigerator, such as used in the Frascati FT facility, is an attractive option. It has the additional benefit of preventing machine warmup if, for any reason, a nitrogen delivery is missed. It will also have a smaller electrical power requirement than the larger reliquefier options. In reality, there are economies of scale, including a need for additional operator time, even for the smallest system. Thus, the economics don't favor the standby refrigerator as strongly as indicated in the above table. However, a small refrigerator allows two low cost alternative options, not available at larger ratings. Instead of placing a special order for a reliquefier, it would be possible to consider a 3 KW, laboratory-grade reliquefier, manufactured by Phillips, or use an existing CTI-2800 helium refrigerator as a nitrogen liquefier. If this refrigerator were run closed-cycle, it could provide approximately 18 g/s to the magnet load, or 3.6 kW, which is comparable to the rating of the standby option in the above tables.

CHAPTER 4

ALCATOR C-MOD DIAGNOSTICS

4.1 Introduction

In planning for the diagnosis of the Alcator C-MOD, we intend to draw heavily on the existing expertise and equipment which form an integral part of the present Alcator C effort. Several unique diagnostics, which will contribute greatly to an understanding of the behavior of Alcator C-MOD plasmas are presently in use on Alcator C, and at the same time, new techniques are being studied and refined for use both on Alcator C and then on Alcator C-MOD. Furthermore, we have identified diagnostic areas which require special attention on Alcator C-MOD owing to its strong shaping and the presence of the poloidal divertor. These latter include the measurement of plasma position and shape, along with n_e and T_e in the divertor region. In the following sections, we first examine in detail the diagnostics which are presently available within the Alcator C program, have been proven on Alcator C, and can in a very straightforward manner be transferred to Alcator C-MOD. A discussion of the status of diagnostics which are presently being developed in conjunction with the Alcator C program follows. Finally, we examine the special needs which result from shaped/diverted operation.

4.2 Fully Developed Diagnostic Systems

4.2.1 Multi-point Ruby Thomson Scattering

The existing Alcator C system can be used, with only very minor modifications, to measure spatial profiles of T_e and n_e on Alcator C-MOD. Accuracy of $\pm 5\%$ for T_e and $\pm 10\%$ for n_e can be realized. Because of the excellent access on Alcator C-MOD, collection solid angle can be in-

creased, and stray light levels reduced, so that it is reasonable to expect good signal to noise with n_e as low as $5 \times 10^{12} \text{ cm}^{-3}$. Single shot profiles at a minimum of six spatial positions are provided and more positions can be added at low cost.

4.2.2 Infrared Density Interferometer

The present system consists of a five chord methyl alcohol laser interferometer (119 μ), which will be well suited to the expected ranges of density for Alcator C-MOD. An upgrade of the system to provide more chords can be realized at reasonable cost, and this possibility is presently being investigated.

4.2.3 Electron Cyclotron Emission

The electron cyclotron emission diagnostics now in use on Alcator C should adapt in a straightforward manner to Alcator C-MOD. The diagnostic system consists of three parts: 1) a static Fabry-Perot interferometer which can be tuned to monitor continuously the central electron temperature; 2) a fast scanning Fabry-Perot interferometer to give T_e profiles every 2 msec with 2 cm resolution; 3) a Michelson interferometer which gives complete emission spectra over the range $50 \text{ GHz} < \nu < 1000 \text{ GHz}$. For non-circular discharges, the chord being viewed by the scanning Fabry-Perot interferometer can be swept with a vibrating mirror to give complete two dimensional electron temperature profiles.

4.2.4 Neutral Particle Energy Analysis

There are presently two neutral particle energy and mass analyzers in use on Alcator C. A ten channel analyzer measures particles in the

range $500 \text{ eV} < E < 40 \text{ keV}$ and is a routine ion temperature diagnostic on Alcator C. A second, five channel system, has been modified so that it views in the vertical direction. Both systems are mechanically scannable. Ion temperature time histories and profiles can in this way be measured.

4.2.5 Neutron Diagnostics

Operation at full plasma parameters in pure deuterium will not be routine for Alcator C-MOD. It will be possible, however, to run with modest deuterium seeding of hydrogen plasmas, and valuable diagnostic information about the ion temperature can be gained from the subsequent neutron production. The following equipment is presently available from Alcator C experiments: 1) a very high resolution ^3He spectrometer to measure the energy distribution of neutrons produced, yielding a direct measure of the ion energy distribution function; 2) a BF_3 long counter array to measure total neutron flux; 3) a Ne^{213} moderately high resolution neutron spectrometer to measure 14 MeV neutron spectra as well as 2.5 MeV spectra (from D-T and D-D reactions respectively); 4) a horizontally viewing, movable, borated water collimator which, in conjunction with one or more of the above detector systems, can be used to provide spatially resolved neutron production rate information from which both parallel and perpendicular ion energy distribution information can be inferred. At modest cost, a multichannel vertically viewing collimator can be designed to provide continuous time behavior of the ion temperature profile. These diagnostic systems will also be used to study non-fusion neutrons arising from energetic (multi-MeV) electrons through electrodisintegration and photoneutron processes, and can provide information about energetic electron populations in ohmic and RF current

driven discharges.

4.2.6 Visible and UV Spectroscopy

4.2.6.1 Survey of Intrinsic Impurity Levels

Because of the nature of Alcator C-MOD, with ICRF heating, and shaped, diverted plasmas, the monitoring of impurity levels will be extremely important. In order to achieve routine surveys of impurity levels in Alcator C-MOD, the rather complete set of instrumentation presently operating on Alcator C will be utilized. This set includes: a 1.5 meter visible and near UV time resolving spectrograph (2200 Å to 7000 Å) which can be used to observe the time histories of up to 15 lines simultaneously; an 0.125 meter far UV monochromator (1200 Å to 2300 Å) used mainly to monitor emission from low Z impurities and neutral and molecular hydrogen; an 0.2 meter extreme UV monochromator (400 Å to 1500 Å) which can monitor the low Z impurities as well as intermediate charge states of the heavier metallic impurities such as Fe and Mo which could be present; a 2.2 meter grazing incidence, time resolving spectrograph (18 Å to 600 Å) which can monitor any 40 Å section within its spectral range, having 4 msec time and 0.5 Å spectral resolution; and finally visible continuum monitors which measure chordal integrals of $n_e^2 \times Z_{\text{eff}}/\sqrt{T_e}$, thus providing a direct measurement of total plasma impurity levels. The presently operating continuum instruments include 2 single channel systems, a 20 channel imaging array, and two 16 channel imaging arrays.

4.2.6.2 Doppler Broadening and Shifts

Measurement of the Doppler broadening of far UV lines from both intrinsic and injected impurities can be used to infer ion temperature profiles. A high resolution, multichannel detector, with sensitivity

from 1200 Å to 3000 Å , has been built by the group headed by H. W. Moos at Johns Hopkins University. This new detector system is presently being tested on an existing 1 meter normal incidence vacuum instrument, which has previously been used on Alcator C with a vibrating mirror and single detector to measure Doppler widths. The new combination yields Doppler profile measurements of single impurity lines with a time resolution of about 4 msec. This instrumentation can also be used to measure shifts in the energies due to bulk plasma rotation.

4.2.7 X-ray Diagnostics

4.2.7.1 Spectroscopic

The measurement of X-rays provides information concerning the electron distribution function (from both the hard and soft continua), impurity concentrations (from $\Delta n = 1$ impurity line strengths in medium and high Z impurities) and the ion temperature (from Doppler broadening line emission). If the electron distribution function is Maxwellian, the electron temperature can be determined. Populations of RF induced non-thermal electrons, as well as run-away electron production, can also be monitored via the resulting medium and hard X-ray emissions. Systems presently in service on Alcator C include: two Si(Li) pulse height detectors ($500 \text{ eV} < h\nu < 10 \text{ keV}$, 200 eV resolution); an HgI₂ pulse height detector ($5 \text{ keV} < h\nu < 100 \text{ keV}$, 500 eV resolution); a flat crystal monochromator ($1 \text{ keV} < h\nu < 8 \text{ keV}$, 50 eV resolution); an 8 channel, collimated NaI detector system ($10 \text{ keV} < h\nu < 500 \text{ keV}$, 1 keV resolution); a compact, high resolution time resolving crystal spectrometer for measuring Doppler widths and line ratios, ($2000 \text{ eV} < h\nu < 5000 \text{ eV}$, 0.5 eV resolution); a multi-chord collimated NaI detector array to measure hard X-rays produced

at the walls and limiter/divertor plate structures ($0.5 \text{ MeV} < h\nu < 20 \text{ MeV}$). Recent results from the high resolution crystal instrument include the first quantitative intrinsic neutral hydrogen density profile measurements inferred from the observation of charge transfer recombination as well as central T_e measurements from line ratios of $\text{Ar}^{17+}/\text{Ar}^{16+}$.

4.2.7.2 Broad Band Diode Arrays

An X-ray tomography diagnostic is feasible for Alcator C-MOD. Much of the work which is required to develop such a device has been carried out for a prototype experiment on Alcator C. This includes logarithmic circuitry design, materials processing (i.e., the sealing of beryllium to stainless steel), and development of large database acquisition, processing and computer reconstruction algorithms. In addition, other potential problems such as detector noise and channel cross talk have been successfully addressed.

The 128-channel prototype has yielded tomographic reconstructions which include the $m = 0, 1,$ and 2 poloidal harmonics and better than 2 cm resolution in the radial direction. CAT scan movies have been made with data from pellet-fueled discharges showing the growth and rotation of $m = 1$ magnetic islands, as well as sawtooth activity. Enhancement of X-ray emission due to intrinsic impurities has also been studied, as well as transport of injected impurities.

The most desirable configuration for such an instrument on Alcator C-MOD would consist of about 400 detectors arranged on 20 array chips and encased in a stainless steel housing that would surround the plasma at one toroidal location. The housing should fit just inside the vacuum chamber

wall in the shadow of the limiter structure and would not necessarily have to take up significant port access space. (It could be shifted toroidally after insertion.)

The bremsstrahlung emission from an Alcator C-MOD plasma will deposit somewhat more power on the X-ray detector surfaces than is the case in Alcator C discharges, due primarily to the longer path length and higher temperatures. Nevertheless, we anticipate being able to use the same type and size detectors and apertures, and even the same circuitry.

In addition to the tomography diagnostic, we will probably want a few small detector arrays at different toroidal locations to check on toroidal asymmetry and toroidal mode numbers of instabilities. Three such arrays presently exist, and have been implemented on Alcator C. With various filters, these arrays have also been used to study the details of the transport of injected, trace impurities on Alcator C, and it is anticipated that this work would continue on Alcator C-MOD.

4.2.8 Bolometry

Radiation may contribute significantly to the power balance of the Alcator C-MOD plasma. Bolometric measurements of the power radiated to the wall will contribute to the understanding of the role played by radiation in the various regimes of operation. The present bolometer array on Alcator C has up to 16 collimated channels, covering a span of 31 cm in minor radius. Discrete thermistors were used as detectors in earlier studies; at present the detectors are individual platinum resistance gauges similar to those used on TFTR. The platinum gauges have been found to be stable and durable in their use to date, and would be used on

Alcator C-MOD. With minor modifications of the detector housing, the present bolometer array could be used to view the entire Alcator C-MOD plasma.

4.2.9 CO₂ Scattering

CO₂ laser scattering has been demonstrated to provide an important diagnostic capability during lower hybrid heating and current drive experiments on Alcator C. In addition, this technique can be used to study the low frequency edge fluctuations which have been shown to influence the propagation of driven lower hybrid waves. The device presently operational on Alcator C is a CW diagnostic for which longer machine pulses can be readily accommodated.

4.2.10 Edge Plasma and Wall Diagnostics

Some of the main goals of the Alcator C-MOD device will be to examine impurity generation, heat removal and particle recycling at walls and limiter/divertor plate structures, particularly during strongly heated heated ICRF operation. Therefore, detailed analysis of the limiter shadow and divertor plasma properties will be very important. Much attention has been paid to edge plasma and material interaction issues on Alcator C, and as a result, a substantial number of edge probes (Langmuir and electrostatic types) and their associated instrumentation have been developed. These include the Densepack poloidal probe array, which has been used to examine strong poloidal asymmetries in the edge, as well as a gridded energy analyzer which has been used to look at both the electron and ion distributions in the shadow of the limiter. There have also been numerous studies performed with limiters and calorimeter probes instru-

mented with thermocouples. As a result, both the hardware and the expertise exist within the Alcator group to design and carry out similar studies on Alcator C-MOD. These studies, coupled with the extensive spectroscopic techniques available, as described in 4.2.6, should yield an excellent understanding of the edge plasma and its interactions with the material structures of the limiter, first wall, and divertor plates.

4.3 Diagnostic Systems In Development

In a number of areas, diagnostic development continues, both for near term use on Alcator C, as well as for Alcator C-MOD. The main areas of research are detailed in the following subsections.

4.3.1 Nd:YAG Thomson Scattering

A quasi-continuous Thomson scattering diagnostic based on a repetitively Q-switched Nd:YAG laser is now installed on Alcator C and initial operation has yielded measurements of T_e and n_e at a single spatial point, at a repetition rate of 100 Hz. Additional spatial points can be readily incorporated into the design. This capability would permit profiles of T_e and n_e to be monitored as functions of time on a single discharge. No other diagnostic with the unique combination of short averaging time (the laser pulse width of 20 nsec), quasi-continuous time resolution (the interpulse period of 10 msec), and the ability to determine an entire profile currently exists.

4.3.2 CO₂ Dual Wavelength Interferometer

An interferometer system utilizing the CO₂ line, in combination with the visible He-Ne line to measure vibrational fringe shifts, is being

considered. A line average density of $3 \times 10^{14} \text{ cm}^{-3}$ and minor radius of 30 cm correspond to 1.2 fringes at the CO_2 wavelength. Such a device could provide spatial resolution of 1-2 cm over a large number of parallel chords. In addition, such a system would be very useful for monitoring the large increments in density caused by the injection of frozen hydrogen pellets.

4.3.3 Neutral Particle Analyzer

A new, expanded capability neutral particle analyzer is desirable, and would accommodate several research needs. The energy range capability should be extended to 80 keV, to be compatible with the ICRF experiments. Simultaneous dual mass resolution is also desirable for the RF experiments, as well as for pellet injection and H-D isotope exchange studies. Such an analyzer would be designed so that it could be used in a fast mode for studying transient phenomena on MHD time scales.

4.3.4 Diagnostic Neutral Beam

A diagnostic neutral beam would aid the spatial resolution of the charge exchange diagnostics, as well as providing a source of neutrals for spectroscopic measurements of charge exchanged impurity ions. In order to penetrate the relatively large, dense C-MOD plasma, a beam energy of about 50 keV would be required.

4.3.5 Time of Flight Low Energy Neutral Spectrometer

A time of flight analyzer for studying the energy and density of the edge neutrals is desirable for Alcator C-MOD. The fueling, pump out and recycling problems associated with the operation of the poloidal divertor

make this a particularly interesting diagnostic for this plasma. The current Princeton design can resolve particle energies as low as 12 eV and as high as 2000 eV and such a system could be constructed here for use on Alcator C-MOD.

4.3.6 Charged Fusion Product Measurements

If small amounts of deuterium are seeded into Alcator C-MOD hydrogen discharges, it should be possible to deduce D-D fusion reactivity profiles by measuring the direction (i.e. v_{\parallel} and v_{\perp}) of charged fusion reaction products (specifically 3.02 MeV protons in this case) which are born on unconfined orbits and are promptly lost with their full creation energy. Both v_{\parallel} and v_{\perp} must be measured in order to discriminate non-prompt losses, which have undergone collisions. Given a particle's energy, pitch angle, and gyroangle at the vacuum chamber wall, and assuming the current profile is known, the orbit can be calculated backwards into the plasma, providing a "line-integrated" emission brightness (although the "line" is not straight, it is a spiral). Multiple detectors yield chordal profiles which can be Abel inverted to get fusion reactivity profiles. It may even be possible to do tomographic reconstruction given enough detectors, but this has not been carefully examined yet.

If the deuteron temperature and density profiles, and thus the fusion reactivity profiles, are already known, the measurement can be turned around to yield information on prompt particle losses. In addition, information about the lower energy non-prompt losses may be useful in determining the energy equilibration rates of the charged fusion products.

4.3.7 Infrared Surface Temperature Measurements

In order better to understand the interaction between the plasma and either limiter or divertor plate structures, it will be necessary to monitor surface as well as bulk temperature increases. We have already implemented a pyroelectric infrared imaging system on Alcator C. We are presently investigating other detector options as well, and anticipate that such a system will be part of the initial Alcator C-MOD diagnostics package.

4.4 Summary

The diagnostic systems described in this chapter are summarized in Tables 4.4-1 and 4.4-2. Table 4.4-1 enumerates the systems which are presently fully developed and have operated successfully on Alcator C. Similarly, Table 4.4-2 lists those diagnostics which are presently in development for use both on Alcator C and then on C-MOD.

TABLE 4.4-1

Fully Developed Diagnostic Systems

<u>Technique</u>	<u>Measured Parameters</u>	<u>Features</u>
1. Ruby Thomson Scattering	$T_e(r); n_e(r)$	Minimum of 6 spatial points
2. FIR Density Interferometry	$n_e(r,t)$	$\lambda = 119 \mu\text{m}$, 5 spatial points
3. Electron Cyclotron Emission:		
a) fixed Fabry-Perot	$T_e(r,t)$	Measures time history at adjustable spatial points. Complete T_e radial profile every 2 msec. Covers $50 \text{ GHz} < \nu < 1000 \text{ GHz}$
b) Fast scanning Fabry-Perot	$T_e(r,t)$	
c) Michelson Interferometer	Emission Spectra	

TABLE 4.4-1 Cont'd.

Fully Developed Diagnostic Systems

<u>Technique</u>	<u>Measured Parameters</u>	<u>Features</u>
4. Neutral Particle Energy Analysis	$T_1(r,t)$; Ion Distribution Function	Two systems in operation
5. Neutron Diagnostics		
a) ^3He Spectrometer	$T_1(r=0,t)$	
b) BF_3 Long Counter Array	Total Neutron Flux	
c) Ne^{213} Spectrometer	Energy Spectra of both D-D and D-T produced neutrons	
d) Borated Water Collimator	$T_1(r)$	
6. Visible and UV Spectroscopy		
a) 1.5 Meter Visible Near UV Time Resolving Spectrograph	Line Emission	$2200\text{\AA} < \lambda < 7000\text{\AA}$ with 15 lines viewed simultaneously
b) 0.125 Meter Far UV Monochromator	Line Emission	$1200\text{\AA} < \lambda < 2300\text{\AA}$
c) 0.2 Meter Extreme UV Monochromator	Line Emission	$400\text{\AA} < \lambda < 1500\text{\AA}$
d) 1.0 Meter Grazing Incidence Monochromator	Line Emission	$40\text{\AA} < \lambda < 600\text{\AA}$
e) 2.2 Meter Grazing Incidence Time Resolving Spectrograph	Line Emission	Covers any 40\AA slice between 18\AA and 600\AA , with 4 msec time and 0.5\AA spectral resolution.
f) Visible continuum monitors	$n_e^2 \times Z_{\text{eff}}/\sqrt{T_e}$	one 20 channel and two 16 channel imaging arrays plus a single chord system presently operating.
7. X-ray Diagnostics		
a) Two Si(Li)Pulse Height Analysis Systems	$T_e(r, t)$	$500\text{ eV} < h\nu < 10\text{ keV}$, 200 eV energy and 50 msec time resolution
b) HgI_2 Pulse Height System	$T_e(r,t)$; Electron tails	$5\text{ keV} < h\nu < 100\text{ keV}$, 500 eV resolution

TABLE 4.4-1 Cont'd.

Fully Developed Diagnostic Systems

<u>Technique</u>	<u>Measured Parameters</u>	<u>Features</u>
7. c) Flat crystal monochromator	Line and Continuum Emission	1 keV < $h\nu$ < 8 keV, 50 eV resolution
d) NaI Multichannel Pulse Height System	Spatially Resolved X-ray Spectra; RF Induced Electron Tails	10 keV < $h\nu$ < 500 keV, 1 keV resolution, 8 channel collimated system
e) Compact Curved Crystal Time Resolving Spectrograph	$T_i(r,t)$; $T_e(r,t)$; $n_o(r,t)$	2 keV < $h\nu$ < 5 keV, Measures Doppler broadening of impurity lines.
f) NaI Array	Hard X-rays produced at walls and limiter/divertor plate structures as well as from non-thermal plasma electrons	0.5 MeV < $h\nu$ < 20 MeV spatially resolved
g) Broad Band Diode Arrays	Plasma position and shape; MHD activity; impurity transport	Fully two-dimensional tomographic reconstructions have been demonstrated.
8. Bolometry	Total radiated plus charge exchange power from plasma	16 channel, spatially resolved
9. CO ₂ scattering	Fluctuations; Driven lower hybrid waves	
10. Langmuir Probes	Edge temperature and density profiles	Poloidal and radial scanning capability with multi-probe arrays.

TABLE 4.4-2

Diagnostic Systems In Development

<u>Technique</u>	<u>Measured Parameters</u>	<u>Features</u>
1. Nd:YAG Thomson Scattering	$T_e(r,t); n_e(r,t)$	100 Hz repetition rate
2. CO ₂ Dual Wavelength Interferometry	$n_e(r,t)$	Multi-chord, CW operation. Able easily to follow density rise with pellet injection.
3. Neutral Particle Energy Analysis	$T_i(r,t);$ ICRF produced ion tails.	Extended energy range (to 80 keV); simultaneous dual mass resolution.
4. Diagnostic Neutral Beam	$T_i(r,t);$ Impurity density profiles	Improved spatial resolution for charge-exchange measurements; central T_i from broadening of impurity lines populated by charge-exchange recombination.
5. Time of Flight Low Energy Neutral Spectroscopy	Edge T_i and neutral density	10 eV < E < 2000 eV
6. UV Doppler Broadening Spectroscopy	$T_i(r,t)$	1200 Å < λ < 3000 Å, multi-channel system to yield line profile every 4 msec.
7. Infrared Surface Temperature Measurements	Limiter/divertor plate surface temperatures	
8. Collimated Charged Particle Detectors	Production rate and Confinement of D-D produced 3 McV protons	
9. Array of high resolution crystal spectrometers	$T_i(r,t)$ with profiles from the center to the edge	

CHAPTER 5

DATA ACQUISITION and CONTROL

5.1 Data Handling

The end product of a magnetic fusion experiment is a tremendous quantity of raw data. For Alcator C, 2 - 5 megabytes of data are acquired per shot; 100 - 200 megabytes are accumulated per day. Requirements for C-MOD should be similar. To be useful this data must be efficiently acquired, stored, displayed and analyzed.

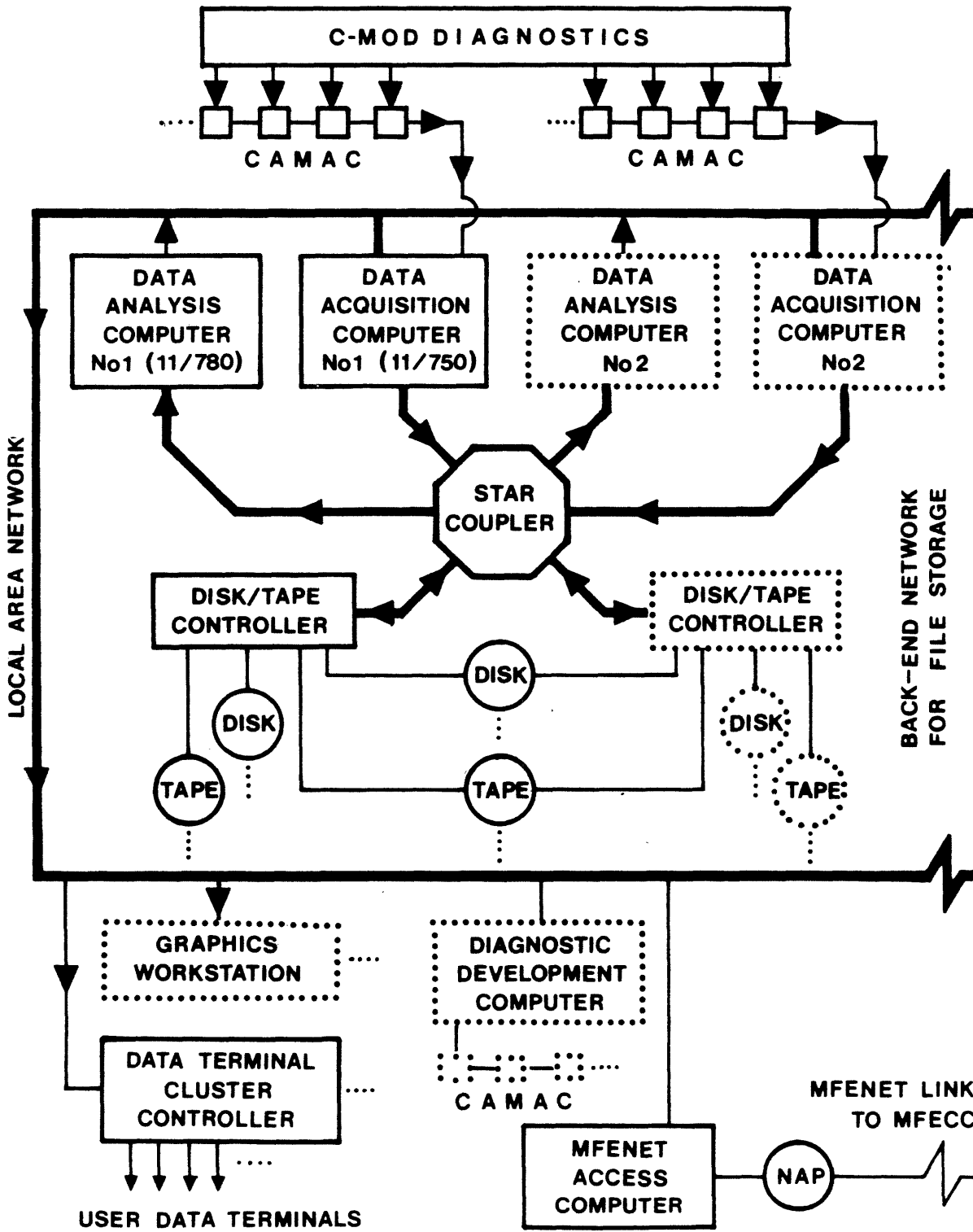
There are substantial advantages in having data available for analysis immediately after a shot, and in completing preliminary processing between shots. Operational parameters can be adjusted in response to the results and machine performance can be more quickly optimized. In addition, systematic parameter scans can be carried out more efficiently. In all cases, the physics staff can work most effectively when data are made available quickly.

The data acquisition system for C-MOD will be taken from Alcator C, more or less intact. Software development will continue during construction but only modest improvements in the hardware will be required to meet the acquisition and analysis needs for initial operation. As the experiment matures, new computational power will be added. Demands on the computers in use on Alcator C already equal or exceed capacity.

5.1.1 System Description

Figure 5-1 shows a schematic of the Alcator C data acquisition system with a growth path indicated. The interface to individual plasma diagnos-

C-MOD DATA ACQUISITION SYSTEM



..... FUTURE SYSTEM EXPANSION

FIG. 5-1

tics is through CAMAC modules. Some front-end intelligence may be provided in the CAMAC crates. These crates communicate with the computer system over a fast serial link. In the diagram, one computer is dedicated to data acquisition and one to analysis. The system can be expanded by adding additional computers for either application. There is a back-end storage network to facilitate rapid data sharing. The computers also communicate over a local area network which also links the data acquisition system through the PFC VAX to the MFE computational facility. A smaller diagnostic development system, with its own CAMAC loop, may be provided to allow off-line development of diagnostic hardware and software. Display stations provide rapid presentation of raw or slightly processed data. Users access the analysis computers through the local network. Work stations for local graphics processing may be provided to off-load those tasks from the main computers.

The architecture shown in the figure offers many advantages. Each of the computers is of the same type, although not necessarily the same model, and each runs the same operating system. This simplifies software development, eases hardware and software maintenance and provides a level of redundancy. Similarly, communications links are standardized. The CAMAC and serial highway are intrinsically standard and modular. The back-end storage allows acquired data to be immediately available for full analysis. Often, distributed processing systems trade their processing problems for communications problems. With much diagnostic data, information from several sources must be combined for analysis. With the system we propose, the data base for all diagnostic data is unified, eliminating the communications difficulties. With a

single data base we can maximize the storage at a single node, allowing us to keep data on line longer. Finally, the modular nature of the structure allows for easy development and growth.

5.1.2 Data Acquisition Hardware - CAMAC

The Alcatraz C-MOD data acquisition system utilizes CAMAC hardware from the Alcatraz C experiment. CAMAC, an acronym for Computer Automated Measurement And Control, is an internationally accepted interface standard offering increased system flexibility, reduced hardware and software efforts, and increased system longevity. CAMAC modules are available to perform a wide variety of tasks: A/D, D/A, scalars, digital interfaces, clocks, display interfaces, terminal interfaces, etc. The standardization to CAMAC allows a standard interface to the computer system with great savings in software development time.

The link from CAMAC crates to the computer is over a serial highway interface. The serial highway signal is carried by fiber optics at rates up to 50 MBaud. The fiber optic provides high-voltage isolation. The highway structure simplifies wiring in the experimental cell. Two fiber optic cables circumnavigate the cell and connect all data acquisition hardware. Expansion is modular and easily accomplished.

5.1.3 Computers

In the Alcatraz C configuration we have two mini-computers, a VAX 11/750 for data acquisition and archiving and a 11/780 for data analysis. While these machines should be adequate for initial operation of C-MOD, we expect that computational needs will approximately double

as the experiment matures. This determination is based on our experience on Alcator C. The present system is already saturated; we cannot acquire more data, display more data, or analyze more data than are presently handled. We have an uncomfortable load during run time. The system is heavily utilized into the late evening for interactive data analysis, and on through the night for CPU-intensive batch jobs. For C-MOD, which is a larger more complex experiment than Alcator C, we predict an increase in the data to be acquired and analyzed. Decisions on the type or number of computers that will ultimately be needed can wait for experience on C-MOD and developments in the industry.

5.1.4 Back-End Network

It is the "back-end network" for file storage that makes the use of separate computers for data acquisition and for data analysis efficient. Disk storage and magtape archival facilities are shared among multiple computers via the back-end network. As at MFECC, each computer has access to the shared file storage devices.

The back-end network also facilitates growth. Compatible peripherals and computers can be added to the network without serious impact on the ongoing experiment. If the data acquisition computer proves to have inadequate bandwidth, a second data acquisition computer might be added to the configuration painlessly. Replacement of a computer with a larger system often involves a great deal of effort and much downtime. The back-end network allowed us to add an 11/750 to the existing Alcator C VAX-11/780 to increase the data acquisition capacity, accessing the same database on the same storage devices on both computers.

Without the back-end network, the use of two separate computers to analyze and modify the same database is quite inefficient, and might have led to a decision to replace those two computers with one larger system.

The total disk storage capacity of this back-end network should be on the order of three gigabytes. The present disk storage capacity of the Alcator C VAX-cluster is approximately two gigabytes. The additional requirement is equivalent to two Winchester disk drives, each with a capacity on the order of half a gigabyte in a 10.5 inch high rack-mounted module. The target for data storage capacity here is to allow online disk access for only the most recent months' data. Access to older data will require recovery from the archive tapes. If video disk technology were to mature during the lifetime of the machine, it could be incorporated into the archive system.

5.1.5 Local Area Network

The Local Area Network (LAN) is not a new concept, although the versatility of these networks is constantly improving. The computers supporting the Alcator Experiment, the Tara Tandem Mirror Experiment, and access to the MFE Network for the Plasma Fusion Center community are connected together via an Ethernet LAN. We expect to connect the Alcator C-MOD computers into this same network.

It is this network that provides the communications path between the analysis computers and the MFECC via the MFENET access computer and NAP. The diagnostic development computer communicates with the other

computers via this network, also. Although this computer is not connected to the back-end network, the LAN provides access to all of the files available through that back-end network.

When a data terminal is connected directly to one of the computers on the LAN, that terminal can be "logged in" to any other computer on the network and used as if connected directly to the latter computer. However, such use imposes an unnecessary burden on the first computer just to handle the communications. In the future, we would hope to make use of data terminal cluster controllers, inexpensive boxes that support up to eight data terminals and connect directly to the LAN for communication with any of the associated computers. Graphics work stations can also be connected directly to the network instead of to a specific computer when such work stations might benefit from access to multiple computers. Network overhead is an important consideration here. When any terminal's function is primarily related to a specific computer, it will still be appropriate to use a direct connection.

5.1.6 Data Display System

The Alcatraz C-MOD data system includes several experimenter display stations to provide graphical display of data acquired during a shot. Some of these display stations, dedicated to displaying unprocessed shot data, are tied directly into the CAMAC data highway. They show raw data rapidly and without intervention of the main computers. They provide variable scaling on the time base and amplitude in the manner of a digital oscilloscope. A prototype of this system is in use on Alcatraz C. Other similar display stations would be provided for dis-

playing processed data as well as unprocessed data from any of the computers in the network. These more general displays do not require the immediate response characteristics of the former stations.

5.1.7 Data System Software

A software system to efficiently store and retrieve raw data as well as the results of numerous analysis programs must be included in the project. The data system software is comprised of purchased software packages to the extent they are available to handle data manipulation, statistical analyses, plotting and display, reports and networking among the multiple computers. The use of purchased software reduces the development and support requirements that would exist if the software were predominantly developed in-house. Unfortunately, no single package or collection of software products provides all the functionality required. Several man-years of local effort has been required as well. The resultant data system (MDS, described below) allows the experimenters to spend more time analyzing the content of the data and less time worrying about where or how the data is stored.

MDS or MIT Data System is a software package developed at MIT for acquiring experimental data using CAMAC hardware, performing data analysis and displaying the data graphically. MDS was developed for use on Digital Equipment Corporation's VAX computers using the VMS operating system. The system is designed to be general purpose and flexible. Data acquisition is configured by simply filling out a form for the particular CAMAC digitizer type the experimenter is using. Once data are acquired they can be displayed and analyzed using inter-

active command languages. The software job of adding a new diagnostic can usually be completed in hours or days with no new coding required compared to weeks or months with system requiring special coding for each new diagnostic. Usually experimenters can set up their entire diagnostic without the aid of a programmer. MDS works over a DECNET VAX to VAX network and is compatible on a VAX cluster configuration. MDS is currently being used on the Alcator C, Tara, and Constance experiments at MIT and will shortly be used on PLT and PBX in Princeton. Seven additional fusion experimental sites have expressed interest in obtaining more information about the MDS system.

MDS is constantly being improved and enhanced. A major effort is currently underway to provide more comprehensive system and user documentation. New CAMAC module types are continually being added to the library of supported modules. MDS has been interfaced to commercially available data analysis packages such as IDL (Interactive Data Language) from Research Systems, Incorporated. There is interest in adding some database functionality through the use of database products like Digital Equipment's RDB (relational database) software.

5.2 Automated Control System

The interface between man and machine for Alcator C-MOD is a programmable controller (PC). Commercial systems are available which can replace much of the customized, hard-wired control system used for Alcator C. The PC is a micro-computer with a modest amount of memory and interfaces to switch contacts, relays, motor starters, thermocouples, etc. Programming is accomplished with a standard video terminal. Operational control can be through a terminal with touch-panel

display, trackball, or light pen. Alternately, standard switches and knobs can be read by the PC which will perform a function (if allowed by the stored control program) and drive a pilot light to indicate what it has done. Some link between control system and the data acquisition computers is provided to log the control sequence and machine parameters with the data acquired for each shot.

The advantages of automated control over a hardwired system are considerable. First, there is a substantial savings in time and money. Commercial PC's are relatively inexpensive because they are produced in large numbers. Much of the hard-wiring is replaced by programmable logic; there will be lower labor costs. The control configuration is modular, which should shorten the installation time. PC's are rugged and reliable. They are often installed in factories and production facilities where the environmental control is minimal. Because the control functions are programmed, PC's offer versatility and flexibility. System documentation is excellent. After any modifications, hard copies of the control flow diagrams can be produced and distributed. Maintenance and system growth are eased by the good documentation and the modular nature of the system.

For Alcator C-MOD it is straightforward to automate power supply controls, vacuum systems, liner temperature control, cryogenic systems, gas injection systems, RF systems and some diagnostic subsystems. Redundant programmed and hard-wired safety interlocks would be included.

Fast programming and sequencing on a time scale much faster than 1 second are difficult with currently available PC's. Typically timing

must be controlled to better than .1 msec and programming for the poloidal fields or gas injection must have resolution of a few msec. A separate CAMAC system could be used for these functions. CAMAC modules with these capabilities are already available and CAMAC interfaces suitable for use with a DEC MicroVax II will soon be ready. We will vigorously pursue alternatives which meet the functional requirements and allow for an integrated control system.

Considerable effort will be put into the human controller interface. Safe and efficient operation of Alcator C-MOD depends on clearly displaying the system status and in providing a good mechanism for quickly and accurately entering control parameters. The programmable logic of the PC can help by alerting operators to problems and by preventing controls from being set outside of programmed limits.

CHAPTER 6FACILITIES6.1 Siting and Building Layout6.1.1 Overall Site Description

The Alcatraz C-MOD will be located in the east side of the Nabisco Laboratory. The Tara tandem mirror experiment is on the west side. Figure 6-1 gives an overview of the proposed modifications to the Nabisco site. The square footage of various areas are given in Table 6-1.

We propose to retain the large "garage" area, using the front portion to house power conversion equipment. The internal space within the existing one and two story Nabisco building will also be retained, and portions will be up-graded for use as control room, computer, and support areas.

The rear portion of the garage will house an experimental cell approximately 50 × 50 feet overall. The cell area will be served by a 10 ton crane, large enough to lift the heaviest subsystem component.

The east side of the Nabisco site is flanked by the 220 MVA alternator and the main switch yard. The rectifier units and RF modulators, currently in the basement of the Magnet Laboratory, will be relocated into the garage area. It is considerably less expensive to relocate the equipment than to construct bus systems to the new site.

6.1.2 Experimental Cell and Power Equipment Area Description

The experimental cell as shown in Fig. 6-1 is 50 × 50 feet square and excavated to the standard basement level of the surrounding buildings.

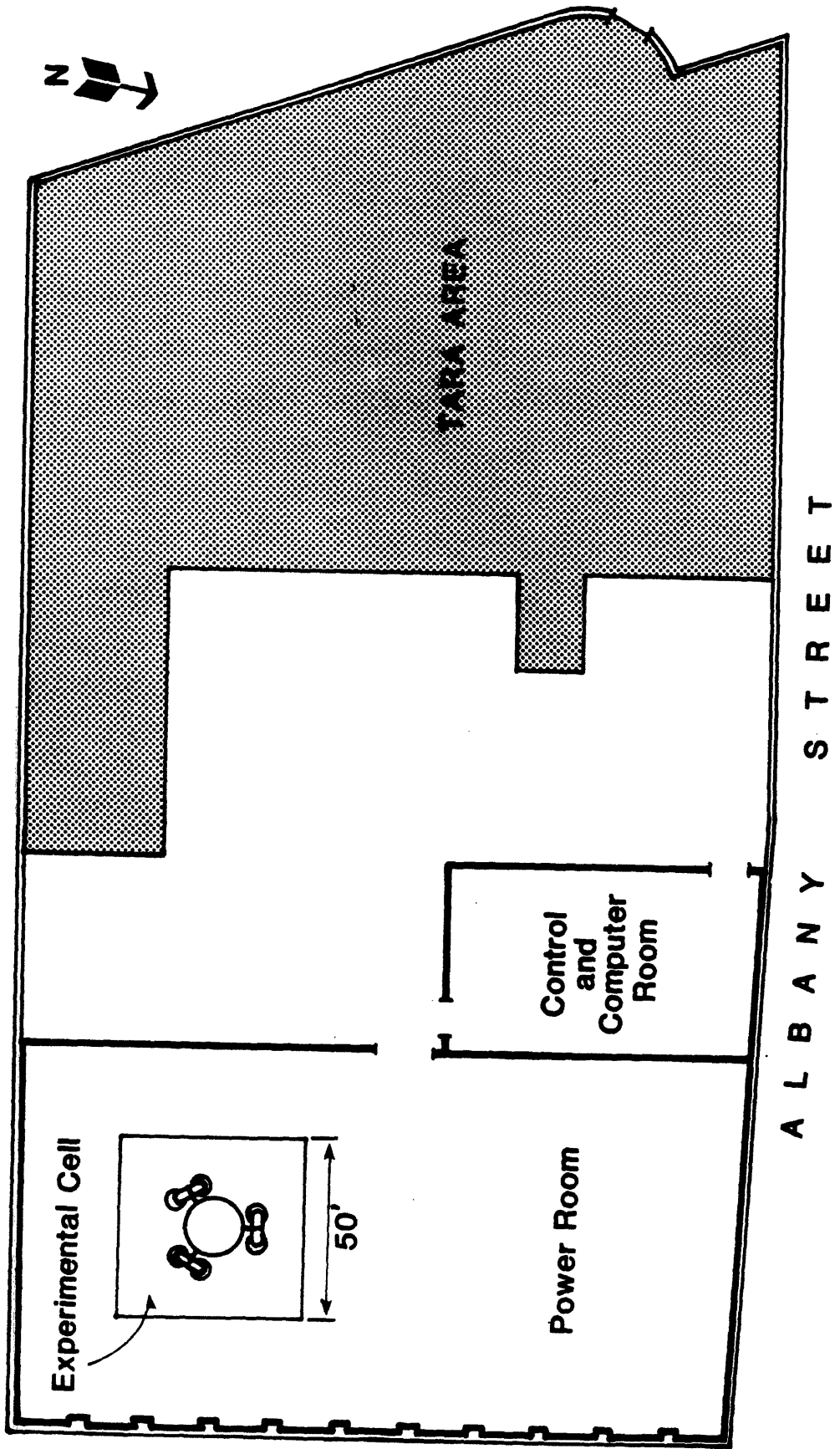


FIG. 6-1

8682

Water-table considerations make it uneconomical to go deeper. A clear horizontal width of 20 feet from the machine is allowed.

The power room shown in Fig. 6-1 will contain the RF transmitters and the magnet power supplies, including all the relocated Alcatraz C TF and OH supplies, which will be used to supply the Alcatraz C-MOD OH and EF systems.

6.1.3 Support Areas

Figure 6-1 shows the control area, data acquisition and general preparation areas immediately flanking the cell and power areas. These will be completed in a manner similar to the Tara facility.

TABLE 6-1

EXPERIMENTAL AREAS

FUNCTION	SQUARE FOOTAGE
Experimental Cell	2,500
Power Room	12,000
Control Room	2,000
Computer	1,000

6.2 Power Systems

6.2.1 Prime Power

Present prime power (13.8 kV AC) at the PFC site consists of a 220 MVA alternator with over 200 MJ available stored energy and a 750 MCM cable tie to the Cambridge system. It is rated as a 13 MVA steady-state cable with higher power ratings for limited duty cycles.

Cambridge Electric currently limits the PFC to a peak short duration pulse load of 22 MVA on top of a 10 MVA steady-state load based on their desire to avoid "flicker" on their system. This is adequate to supply the RF heating power for Alcator C-MOD.

The 220 MVA alternator was installed at MIT with the provision for adding a 1:1.1 gear box to increase the available stored energy to approximately 350 MJ. This modification will be required to provide sufficient energy for the magnet systems.

We propose to use the various high current supplies from Alcator C to supply the TF system and part of the PF system. The installed power conversion capacity at Alcator C is approximately 265 MVA, and an additional 70 MVA of power conversion equipment will be required. Table 6-2 shows a typical power supply assignment.

TABLE 6-2

POWER SUPPLY ASSIGNMENT

OH1/SF1	21.8 kA	1.075 kV	OH3
	20.0 kA	1.2 kV	New
OH2	21.6 kA	1.04 kV	OH3
	20.0 kA	1.2 kV	New
D1	3.0 kA	0.25 kV	New
D2	20.4 kA	0.75 kV	OH2
SF2	6.7 kA	1.0 kV	New
EF1	5.0 kA	2.74 kV	EF1
EF2	8.75 kA	1.03 kV	New

CHAPTER 7

COST AND SCHEDULE

7.0 Introduction

The C-MOD Project has been scoped to enable construction of the device under a constant dollars flat budget. The machine will be constructed over the period FY86-FY88 utilizing funds made available by shutting down the Alcator C device in January 1986, and by transfer of some physics personnel.

The device has been costed by drawing heavily on the unit cost data base which has been assembled for costing the ignition devices. This data base comprises historical costs (FY84 dollars) throughout the Fusion Program and we believe that it represents a reasonably conservative costing basis.

The unit cost basis will be up-dated with vendor quotes on specific components as the conceptual design matures. We have received one informal vendor estimate for the magnets, structure, vacuum vessel and preassembly based on our conceptual level drawings. That estimate from ANSALDO (currently constructing Frascati FTU, Asdex Upgrade and Tore Supra) is somewhat lower than our historical basis estimates (see Section 7.1.12).

7.1 Cost Basis

The cost basis being utilized to cost the ignition devices divides costs into direct costs and indirect costs. Indirect costs are considered overall project costs not directly tied to subsystems, and are taken as 13% of the direct costs. Direct costs are hardware costs, engineering costs associated with specific hardware, and installation costs associated with specific hardware. By way of example, in the case of the ignition device

TF structure, 15% of the TF structure hardware costs is added for engineering, and 5% for installation.

In this proposal we have followed the ignition device cost methodology, but have further divided "hardware costs" into purchased and fabrication categories to reflect that in certain specific subsystems significant MIT labor will be utilized in fabrication, rather than simply in installation or in engineering. This follows our tradition in Alcator C and in Tara of significant on-site subsystem fabrication.

A summary of the C-MOD costs are given in Tables 7.1 and 7.2, with justification given in the following sections.

TABLE 7.1
 C-MOD SUBSYSTEM HARDWARE COSTS (K\$):
 INCLUDES PROCUREMENTS AND ON-SITE FABRICATION

	PROCURE UNIT COST	PROCURE COST	ON-SITE FABRICATION COST	TOTAL HARDWARE COST	TOTAL HARDWARE UNIT COST
TF COIL	\$ 60/kg	1450	1090	2540	\$ 105/kg
TF STRUCTURE	\$ 30/kg	1265	-	1265	\$ 30/kg
PF COIL	\$ 73/kg	540	200	740	\$ 100/kg
VACUUM CHAMBER	\$ 5.3/cm ²	1540	-	1540	\$ 5.3/cm ²
WALL PROT.	\$ 14/cm ²	485	145	630	\$ 18/cm ²
THERMAL SHIELD	\$3200/m ²	160	-	160	\$3200/m ²
CRYO SYSTEM	-	160	100	260	-
SITE MOD	-	1000	-	1000	-
POWER SYSTEMS MODIFICATION	-	1200	-	1200	-
CONTROL MOD	-	300	200	500	-
RF MOD	-	<u>1900</u>	<u>265</u>	<u>2165</u>	-
		<u>10,000</u>	<u>2,000</u>	<u>12,000</u>	

TABLE 7.2
 C-MOD COST SUMMARY (K\$):
 INCLUDES HARDWARE COSTS FROM TABLE 7.1, ENGINEERING, INSTALLATION AND
 INDIRECT COSTS

	TOTAL HARDWARE COST	% ENGINEERING	ENGINEERING COST	% INSTALLATION	INSTALLATION COST	TOTAL COST
TF COIL	2540	15%	380	5%	127	3047
TF STRUCTURE	1265	15%	192	5%	97	1554
PF COIL	740	35%	259	10%	74	1073
VACUUM VESSEL	1540	10%	154	20%	308	2002
WALL PROT.	630	35%	220	15%	94	944
THERMAL SHIELD	160	15%	24	30%	47	231
CRYO SYSTEM	260	20%	52	30%	78	390
SITE MOD	1000	17%	170	-	-	1170
POWER SYSTEMS MODIFICATION	1200	10%	120	11%	130	1450
CONTROL MOD	500	20%	100	30%	150	750
RF MOD	<u>2165</u>	10%	<u>216</u>	10%	<u>216</u>	<u>2597</u>
	12,000		1,887		1,321	15,208
INDIRECT COSTS @ 13% SUBSYSTEMS COST						<u>1,977</u>
TOTAL COST						17,185

7.1.1 TF Coil Costing Basis

Table 7.3 compares the unit cost for the TF coil to the ignition device (ISP), Alcator C and DIII. A unit cost modestly less than ISP has been chosen by subtracting \$14/kg for terminals and coolant feed. We believe that the LN₂ surface cooling and the simple coil to coil joints do not add to the basic coil cost. We further believe that the C-MOD plate elements are simpler than those in DIII, hence it is reasonable that they should cost somewhat less than the DIII unit costs.

We note from the table that the total unit cost of the Alcator C plates was \$100/kg, about 25% less than that chosen for C-MOD. The purchased components for the Alcator C TF coil had a unit cost of \$64/kg, with on site fabrication, engineering and installation increasing the total subsystem unit cost to \$100/kg. We note from Table 7.1 that this is comparable with the \$60/kg purchased component element assumed for the C-MOD plates. The C-MOD plates are considered to be somewhat simpler than the Alcator C plates, in as much as the top and bottom legs as well as the outer vertical leg need not be tapered.

The TF plate elements will be assembled into a central TF core and into 24 TF subunits using on-site labor. Insulation, turn-to-turn bonding, and ground wrapping will also be done on site. These operations are similar to those performed on Alcator C.

TABLE 7.3
TF COIL COSTING BASIS

	HWD UNIT COST	ENG. %	INST. %	TOTAL UNIT COST	UNIT
<u>ISP</u>					
<u>TF MAGNET (LESS STRUCTURE)</u>					
WINDING	\$ 95/kg	15	5	\$114	300 x 10 ³ kg
TERM/COOLANT FEED	\$ 14/kg	15	5	\$ 17	
JOINTS	<u>\$ 10/kg</u> \$119/kg	15	5	<u>\$ 12</u> \$143/kg	
<u>DIII</u>					
TF MAGNET	\$108	15	(5)	\$130/kg	131 x 10 ³ kg
<u>ALC C</u>					
TF MAGNET	\$ 64/kg	(156)		\$100/kg	18 x 10 ³ kg
<u>C-MOD</u>					
TF WINDINGS	\$105/kg*	15	5	\$126/kg	24.2 x 10 ³ kg

* Includes on-site fabrication (Table 7.1)

7.1.2 TF Structure Cost Basis

Table 7.4 compares the unit cost for the C-MOD structure with ISP and preliminary vendor quotes for the earlier proposed Alcator DCT. We have chosen a value equal to that of the ISP TF case unit costs. The Alcator C-MOD structural components are essentially all rather case like. The structures are weldments needing little finish machining. The fit-up between TF copper elements and the structure will be done by epoxy-glass which will form part of the ground wrap.

The earlier proposed Alcator DCT was to be a superconducting machine, but was designed around the same structural principles, namely large unitized structures. Preliminary cost estimates were obtained from several large and small vendors. The largest vendor, Combustion Engineering, quoted a unit price of \$27/kg for the 44×10^3 kg structure. The lowest bid, by the Bath Iron Works, was a unit cost of \$12/kg.

TABLE 7.4
TF STRUCTURE COSTING BASIS

	HWD UNIT COST	ENG. %	INST. %	TOTAL UNIT COST	UNIT
<u>ISP</u>					
<u>MAGNET STRUCTURE</u>					
SUPPORT BASE	\$ 28/kg	25	10	\$ 35/kg	66.7 x 10 ³ kg
PRE-COMP. RINGS	\$ 42/kg	25	10	\$ 57/kg	72.8 x 10 ³ kg
TF SUPPORT STRUCTURE	\$285/kg	15	10	\$ 356/kg	2.2 x 10 ³ kg
TF INTER COIL	\$ 44/kg	15	10	\$ 55/kg	95.6 x 10 ³ kg
TF CASE	\$ 30/kg	15	5	\$ 36/kg \$ 46 kg	158.2 x 10 ³ kg 396 x 10 ³ kg
<u>DCT</u>					
TF STRUCTURE QUOTES	\$12-27/kg	(15)	(5)	\$15-32/kg	44 x 10 ³ kg
<u>C-MOD</u>					
TF STRUCTURE & SUPPORT BASE	\$ 30/kg	15	5	\$ 36/kg	42 x 10 ³ kg

7.1.3 PF Coil Costing Basis

Table 7.5 compares the C-MOD PF coil basis with that of ISP, DIII and Alcator C. There is a wide range of historical costs in the PF coil area (perhaps depending on the type of tooling used, on the high voltage requirements, or on the method of coil coiling?) We anticipate that C-MOD coils will be strip-wound coils, surface cooled with LN₂ as in the Alcator C PF system. We have however, chosen a unit cost substantially higher than that of Alcator C to reflect a desire for a higher quality product, and to accommodate an "internally cooled ground wrap" construction similar to that used on the Frascati FT tokamak. The total unit cost chosen is comparable with DIII PF coil costs.

The C-MOD PF unit hardware cost contains a purchased component of \$73/kg and an on-site fabrication component of \$27/kg as shown in Table 7.1. The on-site fabrication will largely involve terminal, coolant, and structural support details.

TABLE 7.5
PF COIL COSTING BASIS

	HWD UNIT COST	ENG %	INST. %	TOTAL UNIT COST	UNIT
<u>ISP</u>					
<u>PF MAGNETS</u>					
WINDING	\$155/kg	35	10	\$225/kg	20.7 x 10 ³ kg
TERM/COOLANT FEED	\$ 23/kg	35	10	\$ 34/kg	
<u>OH MAGNETS</u>					
WINDING	\$155/kg	35	10	\$225/kg	8.75 x 10 ³ kg
TERM/COOLANT FEED	\$ 23/kg	35	10	<u>\$ 34/kg</u> \$259/kg	<u>29.5 x 10³ kg</u>
<u>DIII</u>					
PF WINDING	\$ 72	11	(10)	\$ 87/kg	57 x 10 ³ kg
<u>DIII</u>					
PF WINDING	\$ 72	(35)	(10)	\$104/kg	
TERM/COOLANT FEED	(23)	(35)	(10)	<u>33/kg</u> \$137/kg	
<u>ALC C</u>					
EF WINDING	\$ 33/kg				4.4 x 10 ³ kg
<u>C-MOD</u>					
EF & OH WINDINGS	\$100/kg*	35	10	\$145/kg	7.4 x 10 ³ kg

* Includes on-site fabrication (Table 7.1)

7.1.4 Vacuum Vessel Costing Basis

Table 7.6 compares the C-MOD vacuum vessel costing basis with ISP, DIII and PDX. A design decision has not yet been made on the method of construction for the vacuum vessel. We note from Table 7.6 that there is a wide range in historical data between the sandwich panel vacuum vessel used in DIII, and the solid wall vessel used in PDX. We have chosen a hardware unit cost reflective of the DIII type of construction in the interest of conservative costing. Our preliminary point design however, is carrying the solid vessel because of its simplicity and rugged construction.

The C-MOD vessel is uncooled (except by conductive transfer to the cold gas atmosphere inside the thermal shield), and is rather simply insulated as was the Alcator C chamber.

The vacuum pumping systems are to be transferred from Alcator C, and are mounted directly on the horizontal ports.

TABLE 7.6
VACUUM CHAMBER COSTING BASIS

	HWD UNIT COST	ENG. %	INST. %	TOTAL UNIT COST	UNIT
<u>ISP</u>					
<u>VACUUM VESSEL</u>					
VESSEL STRUCTURE	\$ 6/cm ²	15	(20)	\$ 8.1/cm ²	88.2 m ²
INSULATION	1.6/cm ²	35	45	2.9/cm ²	
COOLING	~ 1.6/cm ²	30	15	~ 2.3/cm ² \$13.3/cm ²	
<u>DIII</u>					
VACUUM VESSEL (FAN STEEL)	5.3/cm ²	10	(20)	\$ 6.9/cm ²	70 m ²
<u>PDX</u>					
VACUUM VESSEL (SOLID)	1.9/cm ²	(15)	(20)	\$ 2.6/cm ²	40 m ²
<u>C-MOD</u>					
VACUUM VESSEL	\$ 5.3/cm ²	10	20	\$ 6.9/cm ²	29 m ² *

* Includes allowance for port area

7.1.5 Wall Protection Costing Basis

Table 7.7 compares the C-MOD wall protection costing basis with ISP, TFCX, TFTR and JET. One of the experimental goals for C-MOD will be to compare limiter and divertor operation, and hence both are expected to be installed in the machine. There is, again a wide variation in the historical costs in Table 7.7. We are convinced that the C-MOD protection will not require in-vessel cooling, and we do not anticipate movable limiter or collectors. We have therefore chosen a unit cost equal to that of the uncooled JET belt limiter, and approximately equal to that of the ISP unit costs.

The hardware unit cost contains a 30% component for on-site fabrication as given in Table 7.1. On-site fabrication will largely involve structural supports and tooling for mounting the limiters and collector assemblies.

TABLE 7.7
WALL PROTECTION COSTING BASIS

	HWD UNIT COST	ENG. %	INST. %	TOTAL UNIT COST	UNIT
<u>ISP</u>					
<u>LIMITER</u>					
STRUCTURE	(PER TILE)	20	15	~ \$13.5/cm ²	18.8 m ²
ARMOR	\$ 5/cm ²	35	15	7.5/cm ²	
INSTRU.	(PER TC)	30	15	~ $\frac{4.0/cm^2}{\$ 25/cm^2}$	
<u>TFCX</u>					
PUMPED LIMITER (MDAC EST)	\$ 56/cm ²	(35)	(15)	\$ 84/cm ²	21 m ²
<u>TFTR</u>					
MOVEABLE LIMITER	\$ 57/cm ²	43	(15)	\$ 90/cm ²	1.5 m ²
<u>JET</u>					
UNCOOLED BELT LIMITER	\$ 18/cm ²	(35)	(15)	\$ 27/cm ²	20 m ²
<u>C-MOD</u>					
CHAMBER PROTECTION LIMITER	\$ 18/cm ² *	35	15	\$ 27/cm ²	1.75 m ²
DIVERTOR	\$ 18/cm ² *	35	15	\$ 27/cm ²	1.75 m ²

* Includes on-site fabrication (Table 7.1)

7.1.6 Thermal Shield Cost Basis

Table 7.8 compares the C-MOD cost basis with ISP, LCP, MFTF-B, and Alcator C. A fiberglass/foam construction very similar to Alcator C is proposed. We have however, carried sufficient incremental unit cost to utilize a more effective port sealing technique, and to cover the cost of thermal extensions for the bus system.

TABLE 7.8
THERMAL SHIELD COST BASIS

	HWD UNIT COST	ENG. %	INST. %	TOTAL UNIT COST	UNIT
<u>ISP</u> EXTERNAL VESSEL (THERMAL SHIELD)	\$ 880/m ²	15	30	\$ 1275/m ²	460 m ²
<u>LCP</u> EXTERNAL VESSEL				\$ 4000/m ²	470 m ²
<u>MFTF-B</u> EXTERNAL VESSEL				\$16,000/m ²	1860 m ²
<u>ALC C</u> (THERMAL SHIELD)				\$ 1200/m ²	24 m ²
<u>C-MOD</u> EXTERNAL VESSEL (THERMAL SHIELD)	\$3200/m ²	15	30	\$ 4600/m ²	50 m ²

7.1.7 Cryosystem Cost Basis

Table 7.9 compares the C-MOD cryo distribution cost basis with ISP. The Alcator C installation currently has sufficient LN₂ storage, vacuum insulated line and pumping capacity. New work will involve local distribution using foam insulated lines.

We have included a component of on-site fabrication (Table 7.1) in the cryosystem, to reflect the Alcator C experience that much of the fabrication takes place using on-site labor.

TABLE 7.9
CRYOSYSTEM COST BASIS

	HWD UNIT COST	ENG. %	INST. %	TOTAL UNIT COST	UNIT
<u>ISP</u>					
CRYO DISTRIBUTION	\$200 K	65	70	\$830 K	-
<u>C-MOD</u>					
CRYOSYSTEM	\$260 K*	20	30	\$390 K	-

* Includes on-site fabrication (Table 7.1)

7.1.8 Site Modification Cost Basis

Table 7.10 lists a breakdown of site modification costs and is a summary of a next level breakdown of costs supplied by the architect-engineering firm who did the Tara construction.

The proposed site is in the present Nabisco Laboratory "garage" area immediately adjacent to the motor-generator building. It is proposed to excavate a 45' x 45' pit and pour foundations for the new machine. The existing roof would be left in place. A control room area similar to the adjacent Tara control room is proposed. It is currently proposed to relocate the HVAC equipment from the present Alcator C location. Allowances has been made for local electrical and water cooling facilities (additional allowance has been made under power relocation).

TABLE 7.10
SITE MODIFICATION COST BREAKDOWN

GENERAL REQUIREMENTS	160 K
SITE WORK	130 K
CONCRETE	215 K
MASONRY/METALS/WOOD/PROT/DOORS/	105 K
CONTROL AREA	65 K
SHIELD ROOM	50 K
MECHANICAL	125 K
ELECTRICAL	85 K
FEE	<u>65 K</u>
TOTAL	1000 K
ENGINEERING @ 17%	<u>170 K</u>
	1170 K

7.1.9 Power Systems Modification Cost Basis

Table 7.11 gives a cost breakdown for the modification of the power systems. The 10% over-speed gear-box represents a quotation from General Electric by the group who installed the present machine. We are also considering a comparably priced AC drive unit which would circumvent the need for the gear box and motor control modification. Motor control modification would require replacement of the motor control rectifiers to allow operation at the slower motor speed (45 hertz at the generator now reflected back to the motor through the gear box).

The relocation of electrical power involves relocation of the present rectifier units and relocation of the electrical bus. The bulk of this work is handled by contract, and hence has been listed as a procurement rather than on-site labor.

The additional PF supplies required to handle the divertor coils and additional shaping coils require approximately 70 MW of new pulsed power capacity (compared to approximately 110 MW of presently available PF systems.) The Alcator C OH3 supply was purchased at \$0.01/W, which almost exactly matches the recent Tara OH3 supply unit cost purchase. We have therefore allowed \$700 K for this item.

To these procurement we have added 10% for engineering on the total value, and 20% installation for the PF supplies (installation of the MG modification is included in that procurement).

TABLE 7.11
POWER SYSTEMS MODIFICATION COST BASIS

GEAR BOX	\$ 350 K
MOTOR CONTROL MODIFICATION	\$ 50 K
RELOCATION ELECTRIC POWER	\$ 100 K
PF POWER SUPPLIES @ \$0.01/WATT	<u>\$ 700 K</u>
TOTAL	\$1200 K
ENGINEERING @ 10%	\$ 120 K
INSTALLATION OF PF SUPPLIES @ 20%	<u>\$ 130 K</u>
	\$1450 K

7.1.10 Control Modification Cost Basis

The C-MOD control modification will be based on the Tara controller. Tara purchased a commercial GOULD Industrial controller and modified it as required. CAMAC units are used for local control.

As shown in Table 7.1 and Table 7.2, \$300 K has been set aside for procurement, and \$450 K for on-site fabrication, engineering and installation, again based on the Tara experience.

No additional computational capacity is included in the modification as the Alcatraz C computers will be transferred.

7.1.11 RF Modification

Table 7.12 lists a detailed breakdown of procurement costs associated with modification of the FPS-17 units to provide 6 MW of ICRH amplifier output. The costs are based on our experience with current installation of a portion of the equipment on Alcatraz C. Some of the capacity will not be installed until FY89.

The anticipated labor costs associated with modification of the 8 MW are listed in Table 7.1 and Table 7.2 and are:

Fabrication	\$265 K
Engineering	\$216 K
Installation	<u>\$216 K</u>
	\$697 K

TABLE 7.12
RF MODIFICATION COST BREAKDOWN

DESCRIPTION	COST PER UNIT	UNITS REQUIRED FOR 6 MW CAPACITY	
POWER SUPPLY:			
Transformer and Rectifier Cables	0.5 K/unit	4 required	2 K
Heat Exchange (a)	5 K/unit	4 required	20 K
Transformer Repair	60 K/unit	1 required ⁽³⁾	60 K
Summing Choke	5 K/unit	3 required ⁽¹⁾	15 K
Modulator Cables Light Pipe Resistor Dividers	2 K/unit	4 required	<u>8 K</u>
		SUBTOTAL	105 K
RF DRIVE:			
Master Oscillator		none required ⁽¹⁾	
8-way Power Divider		none required ⁽¹⁾	
Electronic Phase Shifter	1 K/unit	8 required	8 K
2 KW Buffer Amplifier	4 K/unit	7 required ⁽¹⁾	28 K
Control Electronics (b)	10 K/unit	8 required	80 K
RF Shielded Enclosure	2 K/unit	7 required ⁽¹⁾	<u>14 K</u>
		SUBTOTAL	130 K
INTERMEDIATE POWER AMPLIFIER:			
RCA Tube (or equivalent)	15 K/unit	8 required	120 K
Socket Assembly	3 K/unit	8 required	24 K
Cavity Manifold	10 K/unit	8 required	80 K
Miscellaneous Assembly & Fittings	2 K/unit	8 required	16 K
		SUBTOTAL	<u>240 K</u>

- (a) required for 2 sec operation
(b) includes arc detector and VSWR monitor circuits
(1) one unit available on site
(2) two units available on site
(3) three units available on site
(4) four units available on site

TABLE 7.12 (CONTINUED)
RF MODIFICATION COST BREAKDOWN

DESCRIPTION	COST PER UNIT	UNITS REQUIRED FOR 6 MW CAPACITY	
POWER TRANSMISSION:			
140 ft Transmission Line	10 K/unit	8 required ⁽⁵⁾	80 K
Gas Stop	0.5 K/unit	4 required ⁽⁴⁾	2 K
Dehydrator	1.5 K/unit	7 required ⁽¹⁾	10.5 K
Directional Coupler	4 K/unit	12 required ⁽⁴⁾	36 K
Mechanical Phase Shifter	10 K/unit	7 required ⁽¹⁾	70 K
Stub Tuner	10 K/unit	4 required ⁽⁴⁾	40 K
DC Break	10 K/unit	6 required ⁽²⁾	60 K
Flexible Bellows	2 K/unit	4 required ⁽⁴⁾	8 K
Impedance Transformer	5 K/unit	6 required ⁽²⁾	<u>30 K</u>
		SUBTOTAL	336.5 K
WAVE LAUNCHING:			
Vacuum Barrier	20 K/unit	6 required ⁽²⁾	120 K
Antenna (d)	100 K/unit	4 required	<u>400 K</u>
		SUBTOTAL	520 K
TOTAL, ICRF Power Generation and Transmission			1925.5 K

(d) 1.5 MW/antenna or $\sim 1.5 \text{ kW/cm}^2$ at Faraday Shield

(1) one unit available on site

(2) two units available on site

(3) three units available on site

(4) four units available on site

(5) 520 ft available on site

TABLE 7.12 (CONTINUED)
RF MODIFICATION COST BREAKDOWN

DESCRIPTION	COST PER UNIT	UNITS REQUIRED FOR 6 MW	
FINAL AMPLIFIER:			
Grid Bias Supply 2 KV, 2A, Variac Control	5 K/unit	8 required	40 K
Cables	2 K/unit	8 required	16 K
Termination Resistors	2 K/unit	8 required	16 K
Capacitors (100 x 40 kV, 40 pf)	5 K/unit	8 required	<u>40 K</u>
		SUBTOTAL	112 K
OTHER:			
100 kW Circulator	10 K/unit	7 required ⁽¹⁾	70 K
1 MW Circulator	20 K/unit	8 required ⁽⁵⁾	140 K
Coax Switch	10 K/unit	4 required ⁽⁴⁾	40 K
High Power Load	8 K/unit	14 required ⁽²⁾	112 K
Cabinet Heat Exchanger ^(c)	10 K/unit	8 required	80 K
FPS-17 Relocation	5 K/unit	8 required	<u>40 K</u>
		SUBTOTAL	482 K

(c) system heat exchange assumed available

(1) one unit available

(2) two units available on site

(3) three units available on site

(4) four units available on site

(5) based on present unit price of 0.1 sec pulse; may be higher for 2 sec pulse unit

7.1.12 ANSALDO Preliminary Cost Estimate

A preliminary cost estimate was obtained from ANSALDO (Italy) on the basis of our point design conceptual level drawings. ANSALDO is currently finishing construction of the Tore Supra TF coils, and have contracts for construction of Frascati FT-U and Asdex Upgrade.

	ANSALDO ESTIMATE	MIT ESTIMATE
Toroidal Coils		\$2540 K
Poloidal Coils		\$ 740 K
Structure		\$1265 K
Vacuum Chamber		\$1540 K
Preassembly		-
	<u>\$4900 K</u>	<u>\$6085 K</u>

A follow-up of this estimate will be made in September. We anticipate obtaining further machine estimates as the design matures. At the present time, however, we do not anticipate contracting for an overall machine construction, but rather for specific components.

7.1.13 Cost Basis for Future Reconfiguration Options

The C-MOD jointed TF coils allow a great deal of flexibility for a future reconfiguration of the machine (see Appendix B). Without knowing exactly which options might be chosen, it is possible to estimate the range of costs which might be involved.

The costs would need to cover only procurements, in as much as the actual conversion, i.e., disassembly, replacement of components, and reassembly would be handled by the engineering and technical support available within the C-MOD group. It would be typical for the machine to be down about three months for such a conversion.

Perhaps the most likely conversion of the machine would be to allow plasmas of elongation 3 to be formed, controlled and studied. Present studies at GAT and Lausanne suggest that such plasmas need rather tight-fitting PF coils. The present C-MOD reference design would not have a sufficient number of PF coils, and probably would not be sufficiently closely coupled to the plasma to meet the requirements. The present C-MOD PF coil set is estimated to have a procurement cost of \$540 K. It is reasonable therefore, to estimate that the cost of a PF conversion would certainly not exceed that value, and as a number of existing PF coils would undoubtedly be reutilized, the cost might be expected to be approximately \$300 K. Additional PF power supplies might be expected to add \$200 K for a total conversion procurement cost of \$500 K.

Another possible conversion might be in the area of advanced Bean shaping. In this case, it would be necessary to add shaping coils and to replace the inner section of the vacuum vessel. We might estimate \$300 K for a PF conversion, plus \$300 K for a new vacuum vessel inner wall and \$200 K for new internal wall protection, for a total of approximately \$800 K. The vacuum vessel and wall protection costs are based on area, and on the appropriate unit costs.

A third possible conversion might be the replacement of the current TF core with a core allowing smaller aspect ratio plasmas. Based on unit costs, the baseline TF core has a procurement value of about \$1450 K. A core suitable for low aspect ratio would weight only a fraction of the baseline core, but could easily be more complex (i.e., special materials or techniques). We believe that a cost approximately half that of the baseline core, namely \$750 K would be a reasonable estimate. The new

chamber extension and wall protection would add another \$500 K, and necessary PF and OH conversion, \$250 K. The total conversion cost for this option then, would be approximately \$1500 K.

7.1.14 Relationship of C-MOD Costing to Cost Projections for Ignition Scale Devices

It is of interest to compare the C-MOD costing with that of ignition scale devices since the unit costs used have a close relationship to those of the ignition devices.

There are two alternate ways of looking at the scaling. The simplest would be to hold the C-MOD field constant at 10 T and scale all linear dimensions until a B^2a adequate for ignition is achieved. This assures that all stresses remain constant, as they scale strictly with B^2 for a given concept if all dimensions are similarly scaled. The C-MOD has a $B^2a = 25$, the ISP, 42 and IGNITOR, 61.

Table A below gives the results of this simple scaling for the basic tokamak, and also suggests the cost scaling that would accompany the linear dimension change: magnetic systems scale as weight, vacuum related components, as area, and the cryosystem, approximately as TF power, which scales with linear dimension. We note that a 10 T field ISP-like device with $B^2a = 42$, should cost about \$42 M based on C-MOD scaling. The basic machine portion of the PPPL ISP, with its lower field and larger radius, was estimated at \$95 M by the FEDC.

If we scale up the 10 T constant field C-MOD to achieve an IGNITOR level $B^2a = 61$ at 10 T, we would project a basic machine cost of \$115 M.

We have not attempted to scale other costs, for example, buildings, power or auxiliary heating, because the C-MOD costs are totally dominated by existing credits.

An alternate scaling, would not hold the C-MOD field at 10 T, but rather would choose a minor radius and field equal to that of the ignition device in question; for example, 8.9 T for ISP and 12.5 T for IGNITOR. Preliminary studies of C-MOD indicate that if precompression and combined bucking and wedging are used, a 12.5 T field could be achieved (at the additional expense of more support structure weight.)

Table B below gives the results of this alternate scaling, together with the suggested cost scaling that would accompany a given field and scale change. We note while the minor diameters match ISP and IGNITOR, the major radii do not quite match as the C-MOD aspect ratio is different.

Using this alternate scaling technique we note that the basic ISP scale machine projects at \$69 M, and as the scale is now much closer to the PPPL ISP, the cost is now closer to the \$95 M projected by the FEDC. The principle differences appear to be in the area of vacuum chamber/first wall protection. For example, the projected C-MOD magnetic systems were \$46 M vs \$57 M for FEDC, whereas the vacuum related projections were \$14 M vs \$37 M for the FEDC. This difference is probably reasonable given the sophistication required for R/M and tritium in the ignition chamber.

The 12.5 T C-MOD scale-up to ignitor level $B^2a = 61$ is now much more economical than was the constant B^2 scaling. A projected cost of \$38 M is made for the basic IGNITOR scale machine.

TABLE A
C-MOD SCALE-UP MATCHED TO B²a AT 10 T

	SCALING	B ² a = 25 C-MOD	B ² a = 42 R = 1.26 m	B ² a = 61 R = 1.83 m
TF Coil	R ³	3,047	14,442	44,181
Tf Structure	R ³	1,554	7,336	22,533
PF Coil	R ³	1,073	5,086	15,558
Vacuum Chamber	R ²	2,002	5,646	11,912
Wall Protection	R ²	944	2,662	5,617
Thermal Shield	R ²	231	651	1,374
Cryosystems	R	<u>390</u>	<u>655</u>	<u>952</u>
SUBTOTAL		9,241	36,508	102,127
Indirect @ 13%		<u>1,201</u>	<u>4,746</u>	<u>13,277</u>
TOTAL		\$10,442 K	\$41,254 K	\$115,404 K

TABLE B
C-MOD SCALE-UP MATCHED TO B²a, B AND a

	SCALING	C-MOD	B ² a = 61 B = 12.5 T R = 1.18 m	B ² a = 42 B = 8.9 T R = 1.6 m	
TF Coil	R ³	3,047	11,853	29,556	
TF Structure	B ² R ³	1,554	9,448	11,950	45,852 (57,300)*
PF Coil	(BR)R	1,073	3,326	4,346	
Vacuum Chamber	R ²	2,002	4,945	9,109	14,455 (37,200)*
Wall Protection	R ²	944	2,332	4,295	
Thermal Shield	R ²	231	571	1,051	
Cryosystems	B ² R	<u>390</u>	<u>952</u>	<u>655</u>	
SUBTOTAL		9,241	33,427	60,962	
Indirect @ 13%		<u>1,201</u>	<u>4,346</u>	<u>7,925</u>	
TOTAL		\$10,442 K	\$37,773 K	\$68,887 K	

* Comparable total, FEDC costing of ISP

7.2 Schedule

The simplified bar chart schedules for the core machine and the power system/site modifications are given in Figures 7.1 and 7.2. They are based on the ability to place long term procurement (i.e., copper) on January 1, 1986, 3 months into FY86. This is consistent with the level of conceptual design activity now underway, and with the receipt of project approval at the start of the fiscal year.

The schedule shows the machine ready for start-up in the middle of FY88. Much of the balance of FY88 would be spent bringing the machine up to a significant level of performance. We anticipate construction and installation of 5 MW of ICRH prior to the end of FY88. An additional 3 MW would be added in FY89 utilizing FY89 operating funds.

The thirty month schedule shown is as aggressive as the funding constraints permit it to be. It already causes a difficult peak in funding requirements in FY87 (see Section 7.3). Thirty months is roughly the period required for construction of both Alcator C and Tara as indicated in Figure 7.3.

An example of the more detailed C-MOD schedule is shown in Section 7.6.3 and is an example of the management software which will be utilized to track the program schedule and resources.

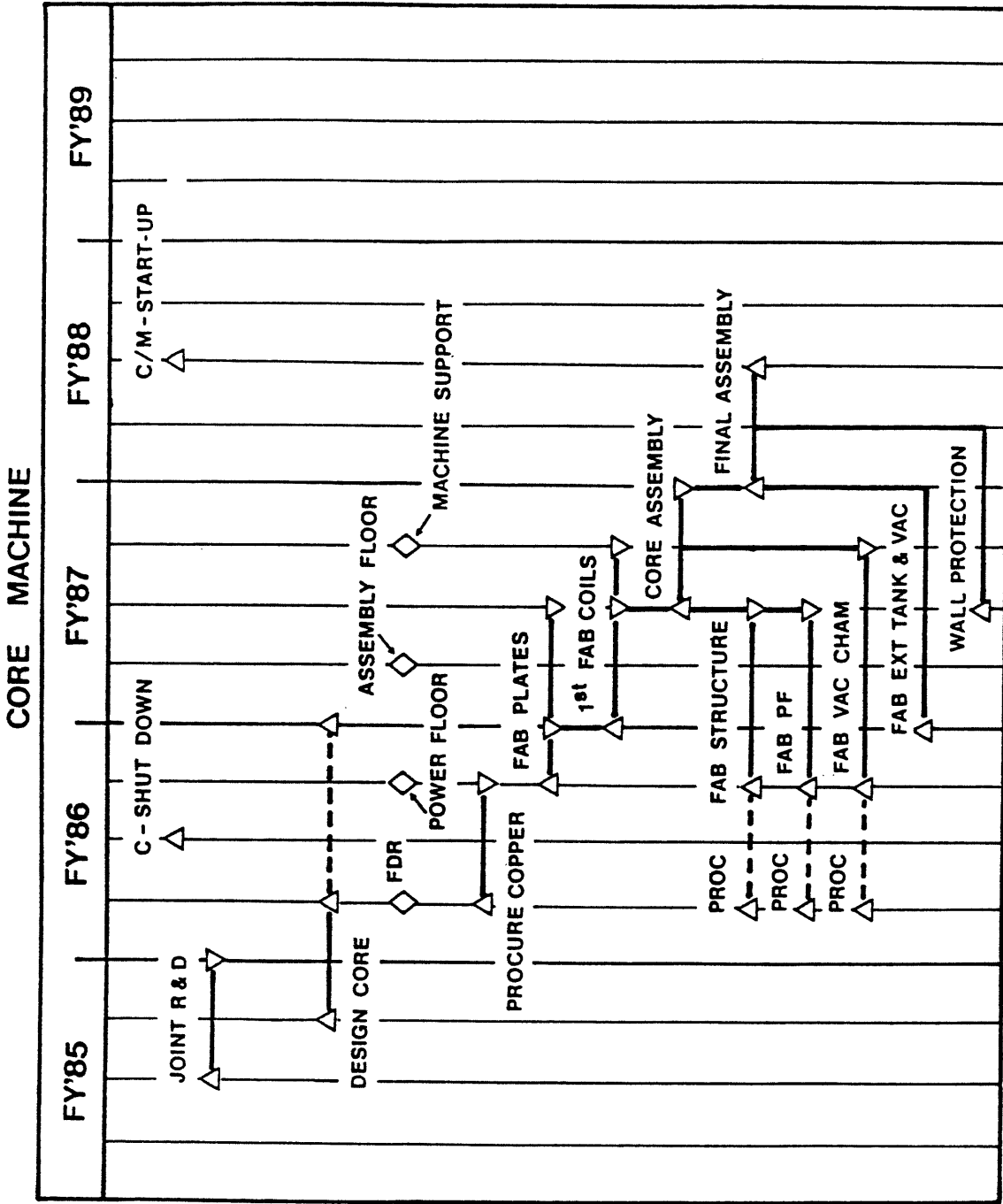


Figure 7.1: C-MOD schedule for the core of the machine

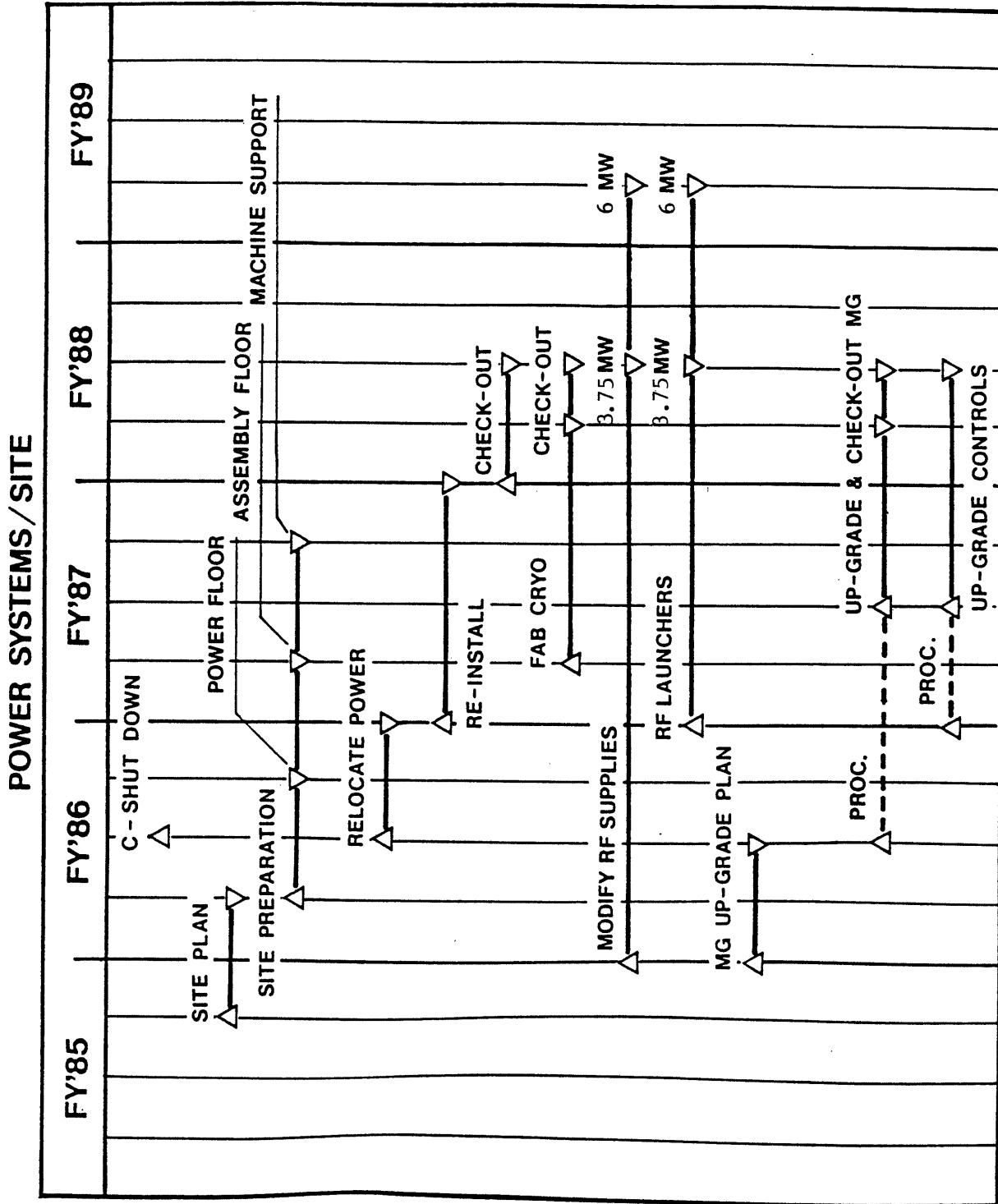
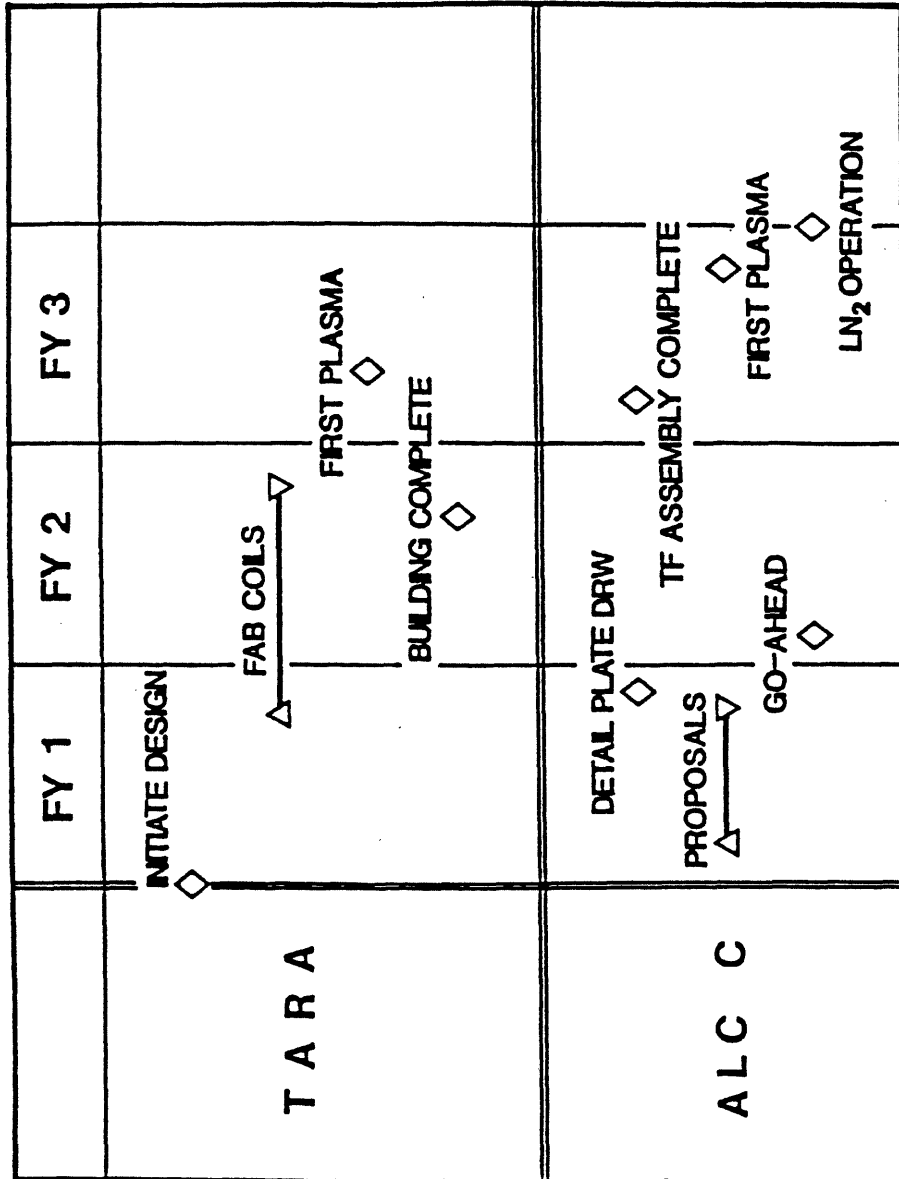


Figure 7.2: C-MOD schedule for the site and auxiliary systems



8/31/3/3/

Figure 7.3: TARA and Alcator C construction completion schedules

7.2.1 Relationship of ISP and C-MOD Schedules

While the proposed C-MOD machine represents an experimental facility at the frontier of current toroidal research in its own right, it is useful to look at it from the point of view of the Ignition Studies Program.

A recently proposed accelerated schedule for the ISP would start detailed design in mid-FY87, and start construction in FY88. The machine would then be ready to carry out preoperations testing in FY91, and begin full operation in FY92.

The C-MOD machine would begin operation in mid-FY88, allowing 3 years of operation prior to full operations in ISP. C-MOD can therefore carry out an important role in optimization of confinement and heating prior to ISP start-up. This early operation optimization can save valuable time, and resources, and minimize nonproductive use of the limited field cycles for the ISP.

By way of example, the information gained during this period would be invaluable in making sound decisions concerning the ISP RF needs. In particular, it should be noted that a 50% uncertainty in the ICRF confinement time translates to a 100% uncertainty in the heating power required for ignition. Alcator C-MOD is the only device in the proposed Toroidal Program capable of establishing a data base for ICRF heating at the fields and densities typical of ISP operation.

When examining the relative schedules it appears at first that the C-MOD engineering tests at start-up came too late to influence the ISP design. It is true they came too late to influence the overall concept

choice, but coming one year in advance of the beginning of ISP installation they can have an important influence on required fit-up, level of precompression necessary, and a host of other installation details.

Even if the schedules were almost parallel, there would be clear advantage in a smaller prerunner project which can serve to prototype many fabrication details; materials Q/A, tooling development, and bonding techniques would be typical prerun activities.

7.3 Cost Profiles

Table 7.13 profiles the procurement hardware costs for C-MOD over the FY86-FY89 period. These profiles have been carefully constructed from the schedule, and clearly show a peak burden in FY87.

Table 7.14 shows the impact of the procurement profile on the Alcator C Program resources over the period FY86-FY89. To provide the required funds for procurements, it will be necessary to shut down Alcator C by January 1, 1986 and to transfer certain personnel not primarily concerned with C-MOD to other research projects, such as TFTR. A total transfer of \$566 K must be made in FY86 and \$543 K in FY87. In FY88, it will not be necessary to transfer personnel, and in fact, it will be possible to establish a modest C-MOD M&S operating budget of \$287 K. In FY89, a nearly full return to FY85 operating levels can be made, with \$400 K going to complete installation of the remaining 3 MW ICRH capacity.

During the FY86-FY88 period, a certain base level of personnel and M&S expenses will be maintained in what is called the "C personnel base", and "C M&S". The base personnel reflect all Physics Research Staff, Research Assistants, and some Technical and Administrative Support. Only Engineering Staff and the majority of technical support personnel are shown as C-MOD personnel. The base personnel (less transfers) will remain involved in the physics aspects of the C-MOD design, in modification of existing diagnostics, and in preparation for resumption of operations. The C M&S account is reserved largely for travel, publications, etc.

Table 7.15 lists the full time equivalent of the FY85 staff by category.

TABLE 7.13
ALCATOR C-MOD BUDGET SUMMARY PROFILE

	TOTAL COST (\$K)	FY86 (\$K)	FY87 (\$K)	FY88 (\$K)	FY89 (\$K)
TF COIL SYSTEM Subtotal	1450	366	984	100	
TF STRUCTURE Subtotal	1265	555	610	100	
PF COIL SYSTEM Subtotal	540	185	305	50	
VACUUM CONTAINER Subtotal	1540	720	670	150	
WALL PROTECTION Subtotal	485	0	223	262	
EXTERNAL VESSEL Subtotal	160	0	0	160	
CRYOGENIC SYSTEM Subtotal	160	0	0	160	
SITE MODIFICATION Subtotal	1000	550	450	0	
POWER SYSTEM MODIFICATION Subtotal	1200	490	290	420	
CONTROL MODIFICATION Subtotal	300	0.00	250	50	
RF HEATING Subtotal	<u>1900</u>	<u>200</u>	<u>300</u>	<u>1000</u>	<u>400</u>
GRAND TOTAL	10,000	3,066	4,082	2,452	400

TABLE 7.14
 DETAILED PROPOSED DISTRIBUTION OF COSTS FY85-FY89 (IN FY85 DOLLARS)

	FY85 (\$K)	FY86 (\$K)	FY87 (\$K)	FY88 (\$K)	FY89 (\$K)
<u>OPERATIONS</u>					
C PERSONNEL BASE	6,710	4,754	3,942	3,942	0
C-MOD PERSONNEL	0	1,850	2,725	2,725	6,700
C M&S	2,330	896	594	594	0
C-MOD HARDWARE M&S	0	2,066	2,282	1,452	400
C-MOD OPS M&S	0	0	0	287	1,900
TOTAL ESTIMATED OPS NEEDS	9,040	9,566	9,543	9,000	9,000
OPERATIONS FUNDING	9,040	9,000	9,000	9,000	9,000
PERSONNEL TRANSFER	0	(566)	(543)	0	0
<u>EQUIPMENT</u>					
C EQUIPMENT	800	-	-	-	-
C-MOD EQUIPMENT		1,000	1,800	1,000	-
C-MOD OPS EQUIPMENT					1,000
SUBTOTAL ESTIMATED EQUIPMENT NEEDS	800	1,000	1,800	1,000	1,000
EQUIPMENT FUNDING	800	1,000	1,800	1,000	1,000

TABLE 7.15
ALCATOR C STAFF - FY85 (FTE)

FACULTY AND RESEARCH STAFF	20
RESEARCH ASSISTANTS	22
ENGINEERS	18
TECHNICAL SUPPORT	32
OTHER SUPPORT	14

7.4 Contingency and Cost Escalation

The method of handling contingency given our use of a historical costing basis, merits further discussion. The unit costs used have been derived from the finished cost of previous projects and should thus include an historical average cost contingency. There is however, an additional contingency associated with design uncertainty. The present C-MOD design is only at a conceptual level with all the attendant uncertainties.

We believe that the best way to handle contingency in the C-MOD is to allow for a 15% contingency against the hardware procurement costs of \$10,000 K, and to cover that contingency of \$1500 K against a project delay into FY89. This amount represents approximately 69% of the projected C-MOD M&S operating account in FY89.

The cost profiles of Table 7.13 and 7.14 assume constant FY85 dollars. MIT salaries have in-fact increased at 4% annually for the last two years, and we might take this as a typical level of escalation to use against personnel costs and procurement during the FY86-FY89 period. Table 7.16 repeats Table 7.14 with a 4% escalation in costs and in anticipated cost-of-living program funding.

Were there to be no cost-of-living increases in program funding, it is clear that the machine could not be built on the same schedule. We could not make a sufficient number of transfers to cover the difference over a 30 month period. It would appear however, that the machine could be built over an additional period of approximately one year. For example, were the program funding to remain at \$9000 K/year (plus \$1000 K/year equipment) while all costs grew at a rate of 4%, by the end of FY88 we

would have an accumulated short fall of \$2500 K over the constant dollar strategy of Table 7.14. This could presumably be made up out of operation M&S by delaying operation for an additional year.

TABLE 7.16
DETAILED DISTRIBUTION OF COSTS FY85-FY89
(ALL COSTS AND FUNDING INCLUDE 4% ANNUAL INCREMENTS)

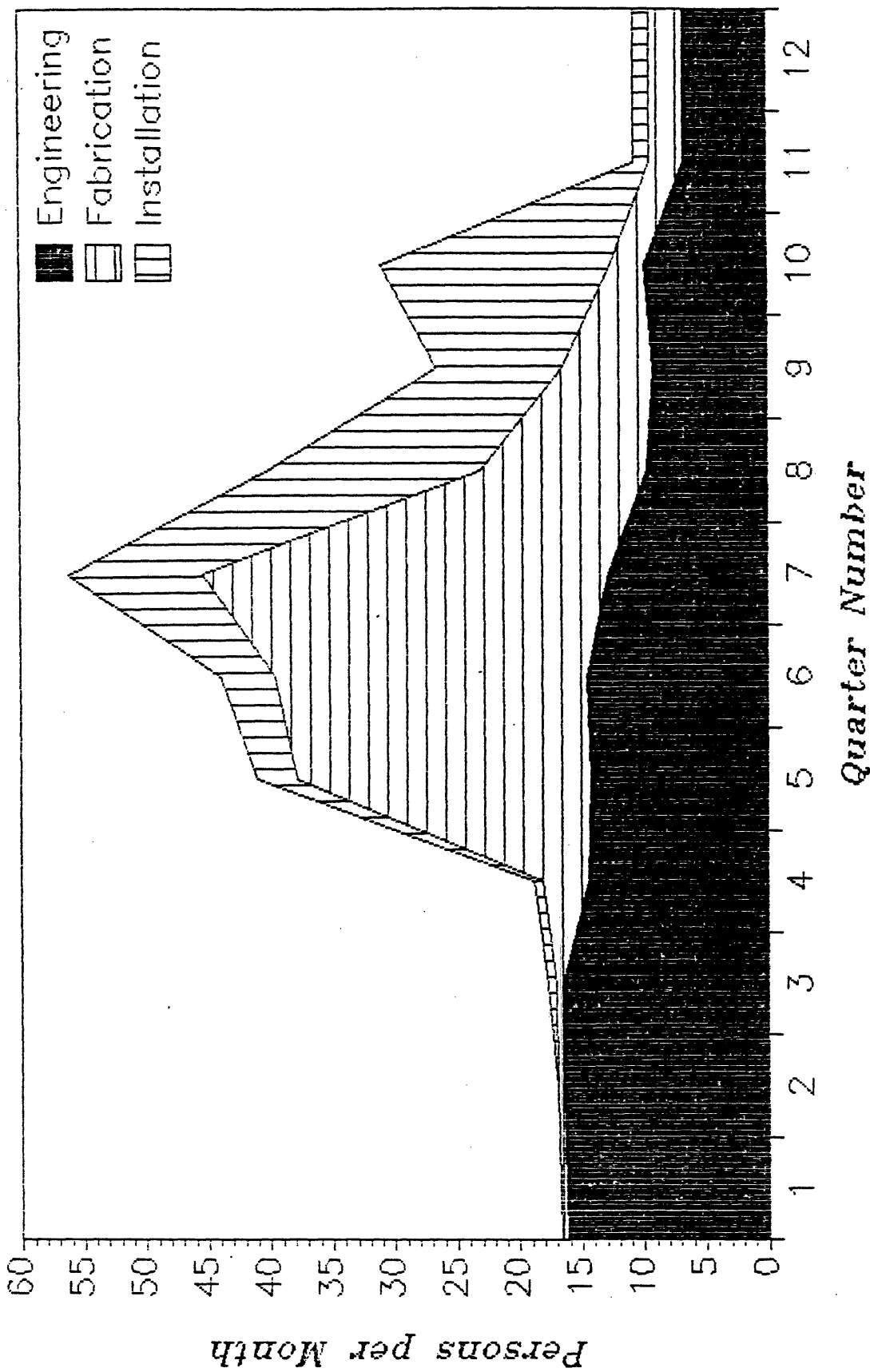
	FY85 (\$K)	FY86 (\$K)	FY87 (\$K)	FY88 (\$K)	FY89 (\$K)
<u>OPERATIONS</u>					
C PERSONNEL BASE	6,710	4,941	4,283	4,454	0
C-MOD PERSONNEL	0	1,921	2,964	3,083	8,213
C M&S	2,330	932	642	668	0
C-MOD HARDWARE M&S	0	2,149	2,465	1,626	0
C-MOD OPS M&S	0	0	0	249	2,434
TOTAL ESTIMATED OPS NEEDS	9,040	9,943	10,354	9,831	10,647
OPERATIONS FUNDING	9,040	9,360	9,720	10,080	10,647
PERSONNEL TRANSFER	0	(583)	(634)	0	0
<u>EQUIPMENT</u>					
C EQUIPMENT	800	-	-	-	-
C-MOD EQUIPMENT	-	1,040	1,880	1,120	1,160
C-MOD OPS EQUIPMENT	-	-	-	-	-
SUBTOTAL ESTIMATED EQUIPMENT NEEDS	800	1,040	1,880	1,120	1,160
EQUIPMENT FUNDING	800	1,040	1,880	1,120	1,160

7.5 Manpower Levels

Figures 7.4 and 7.5 plot the manpower requirements derived from the subsystem tasks. The technical support category clearly peaks during the assembly period in FY87, and would modestly exceed the current Alcator technical support during that period by approximately 20% if no smoothing were done. We are examining the possibility of anticipating some TF tasks and delaying some first-wall tasks to smooth out the peak. We are also examining the details of borrowing technical support from Tara in exchange for returning technical support during a non-peak C-MOD period.

The engineering manpower level shows a gradual reduction following the peak design period in FY86 and does not exceed the available resource.

C/Mod Manpower Summary



Multipliers: Engineering...1.0
Fabrication...1.5
Installation...1.0

Figure 7.4:

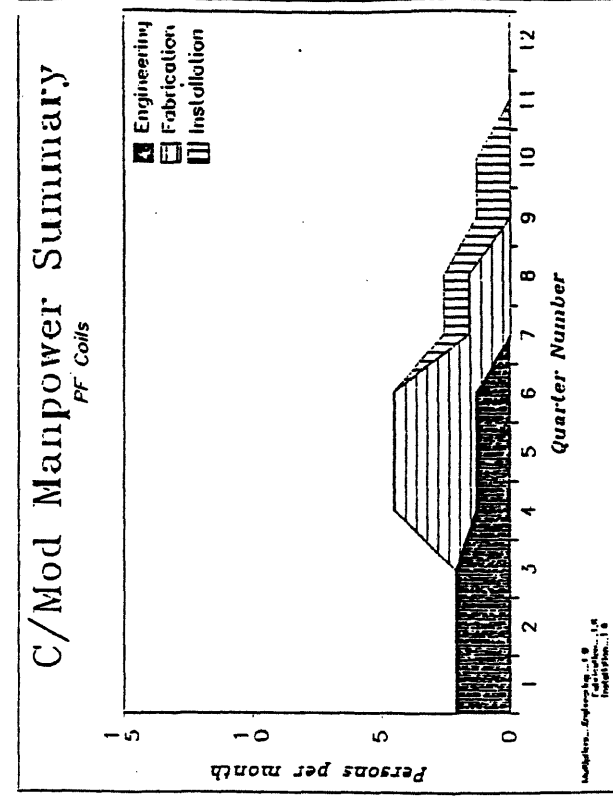
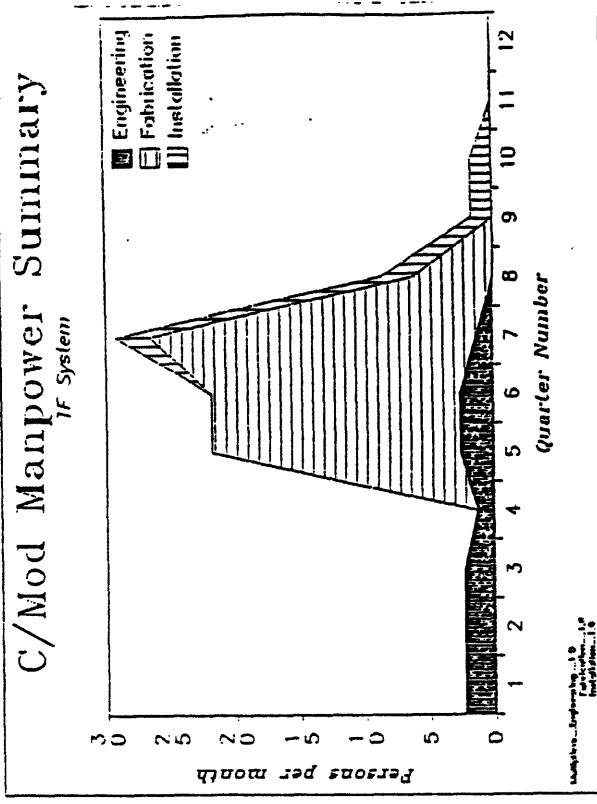
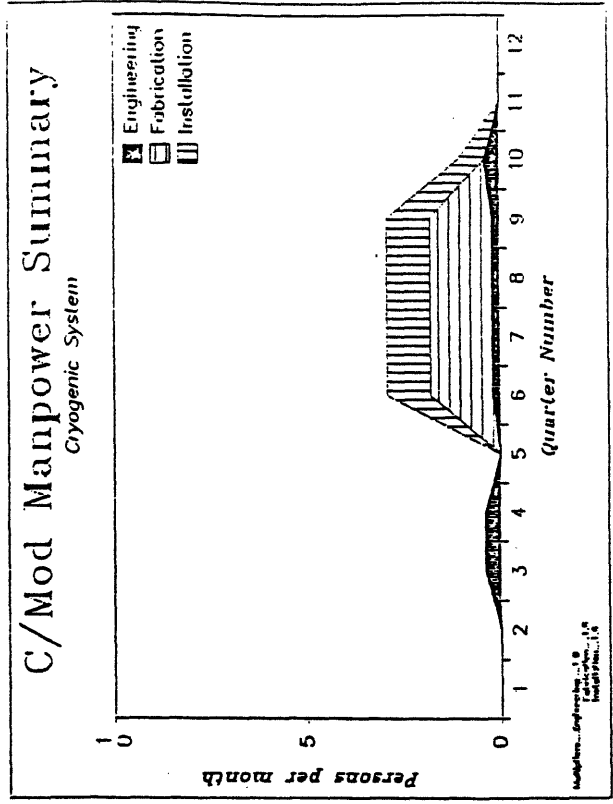
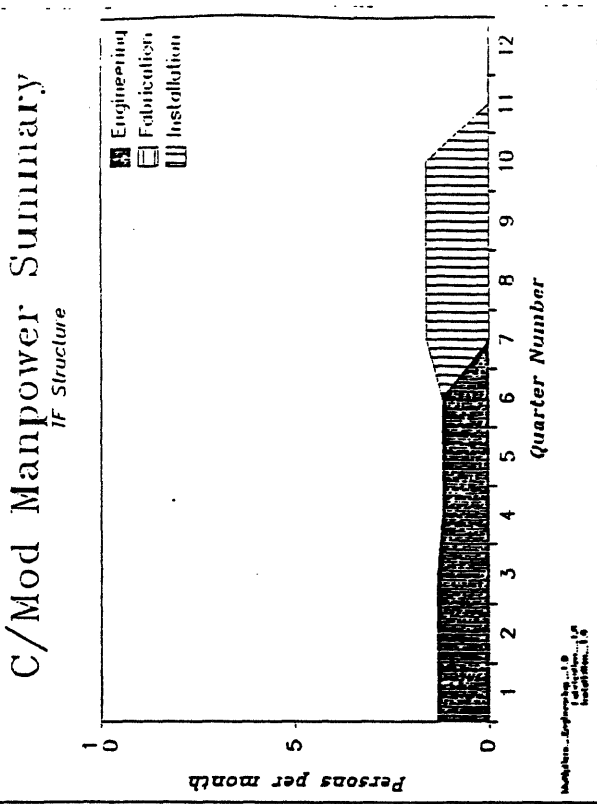


Figure 7.5A:

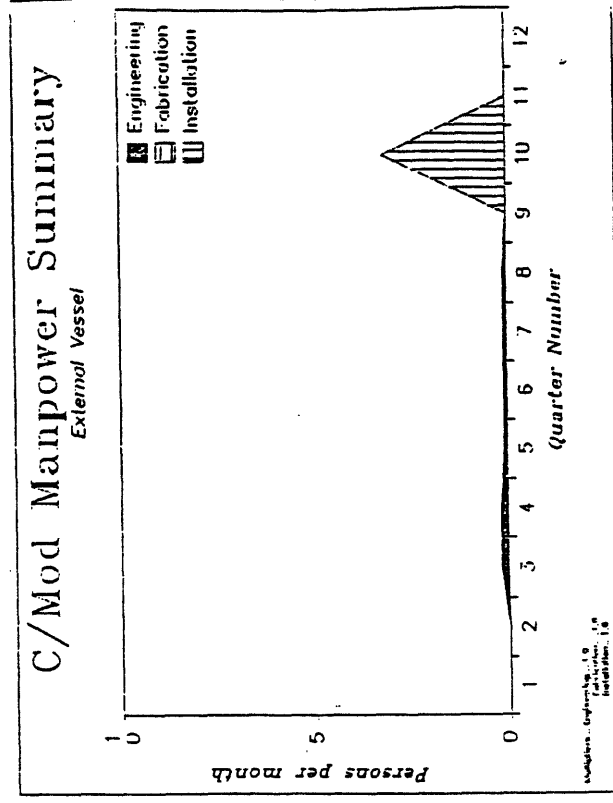
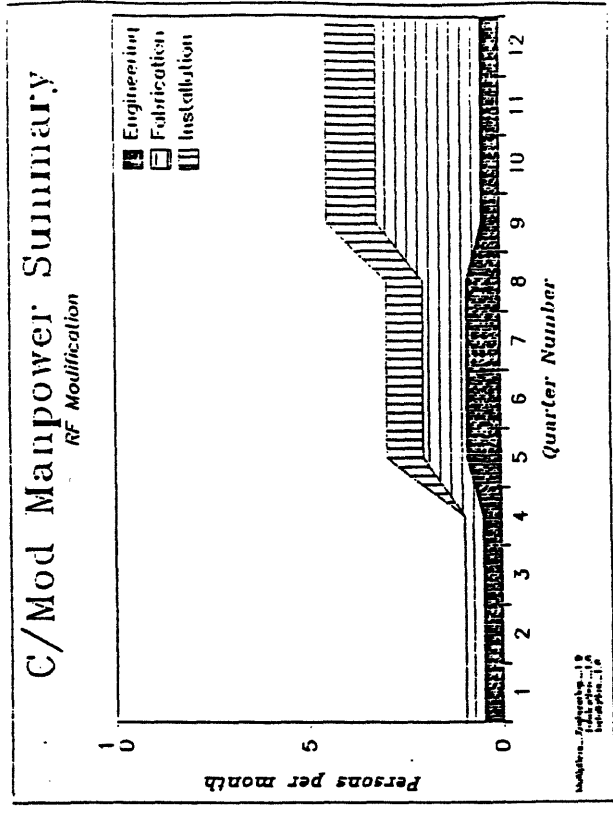
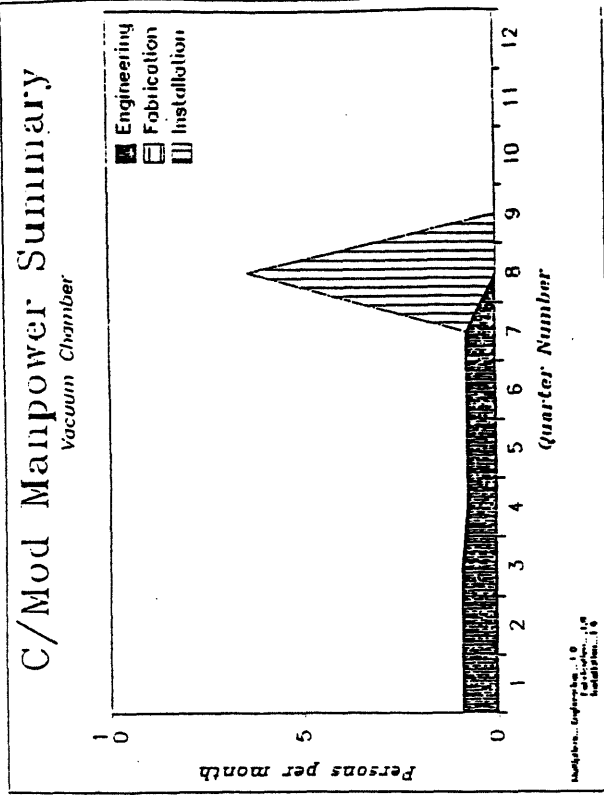
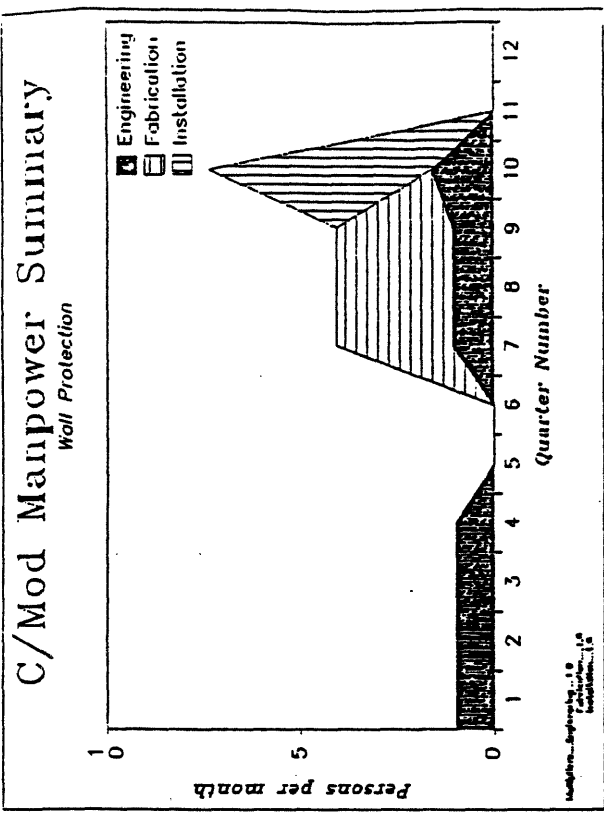


Figure 7.5B:

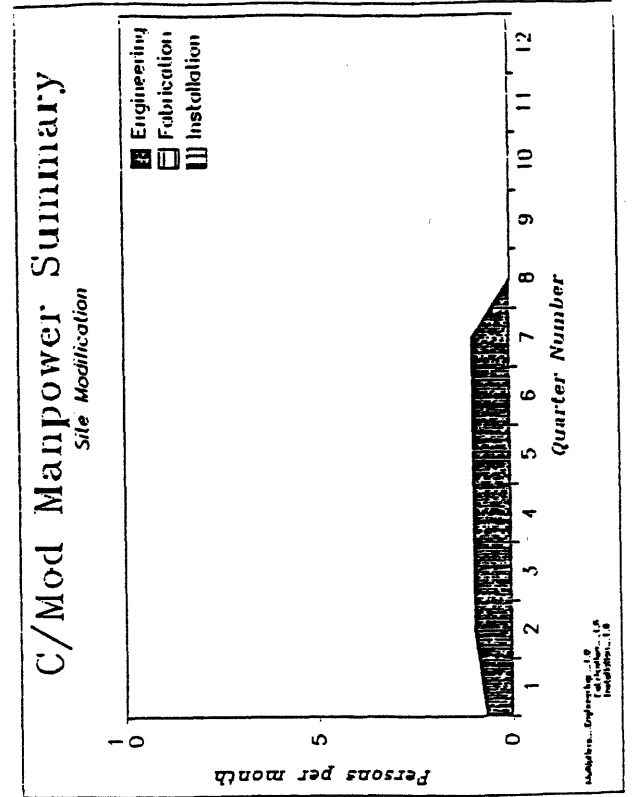
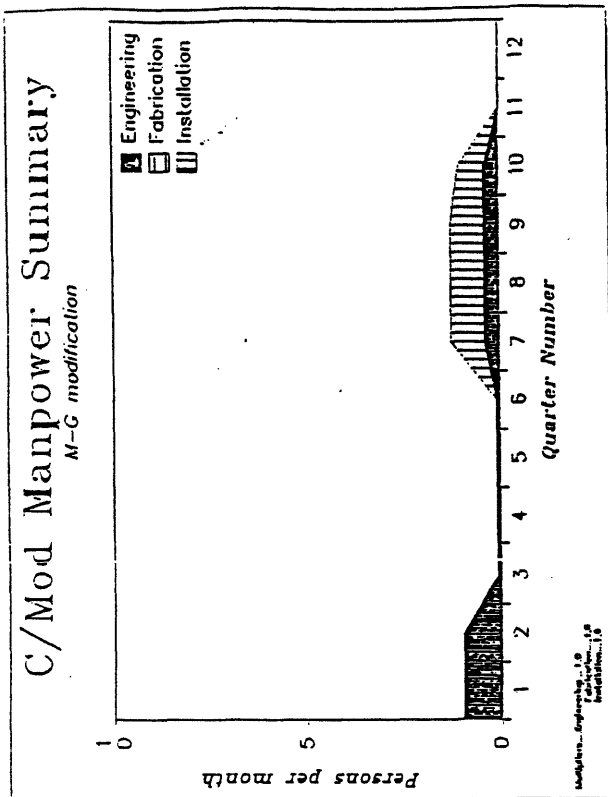
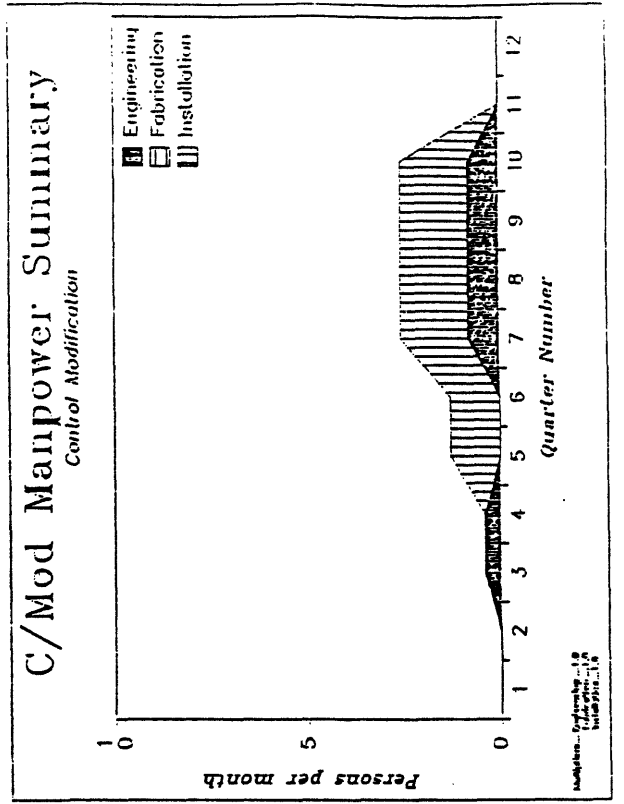
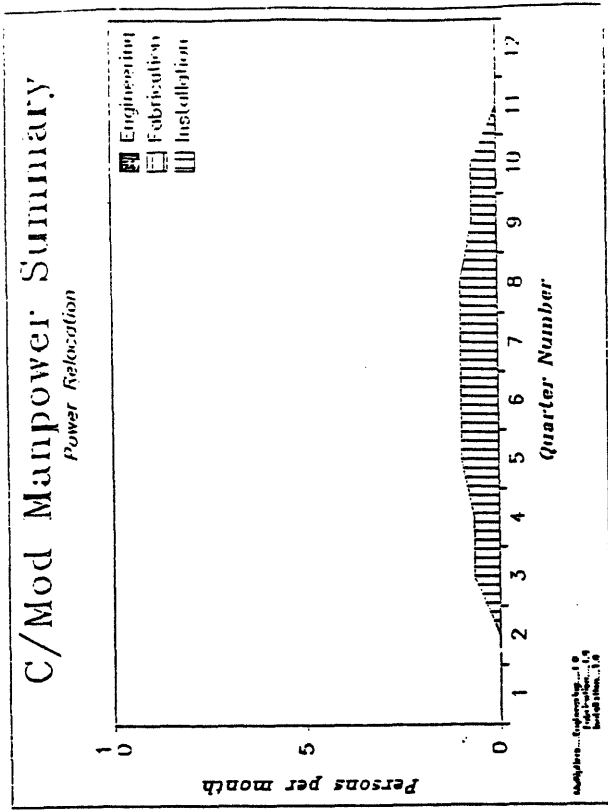


Figure 7.5C:

7.6 Project Management

We propose to organize the Alcator C-MOD Project following guidelines similar to those developed between MIT, OFE and CORO for the Tara Project. That machine construction was the same size as the C-MOD Project and was accomplished on time and on budget over a 2 1/2 year period.

7.6.1 Management Plan

A formal management plan would be written within the first three months of the project and will be negotiated with OFE. The Tara management plan provides a useful model and has the following elements:

- 1.0 Introduction - Describe the purpose and scope of the management plan.
- 2.0 Objectives - Describe the major technical, schedule, and cost objectives of the project. Include descriptions of, and definition of the boundaries between, MDF, site modification, and base program. Define the completion of the MDF.
- 3.0 Performance Criteria - Define the performance criteria for each major subsystem (i.e., the subsystem performance requirements in terms of engineering parameters rather than the experimental physics objectives of the overall system).
- 4.0 Organize - Define the project organization. Include PFC organization, relationship of OSP, PFO, subcontractors, and DOE (OFE, Field Office, and Procurment). Describe the responsibilities of all parties, identify key personnel, and describe the staffing plan for the project.
- 5.0 Work Plan - Describe the major subsystems, including subsystem design description which relate project performance requirements to design parameters. Describe what is going to be done and how it will be accomplished, in accordance with the WBS. Discuss quality assurance and quality control for each subsystem.
- 6.0 Schedule - Provide a summary schedule for the project using form DOE 535 (Milestone Schedule and Status Report), based on detailed logic diagrams. Include a log of major milestones which ties into the summary schedule. Indicate the critical path(s).
- 7.0 Cost Plan - Provide a summary cost plan. Provide time-phased cost details by WBS. Include costs, commitments, and need for funds as a function of time.

- 8.0 Manpower Plan - Provide a summary manpower plan with time-phased manpower details by WBS.
- 9.0 Management Systems - Describe the systems that will be used to manage the cost, schedule, and technical performance of the project. Include funds for management and control.
- 10.0 Documentation and Reporting Plan - Briefly summarize all project documentation including content, frequency of issue, distribution, and responsibility for preparation, review, and approval.
- 11.0 Procurement Plan - Discuss the acquisition strategy for the project. Identify and discuss anticipated major subcontracts, including scope of work, planned award date, estimated cost, need for DOE approval, and potential contractors. Identify the need for long-lead procurements. Discuss plans for Government-furnished and MIT-furnished equipment and facilities.
- 12.0 Test Plan - Discuss the rationale for all tests planned for the project. Relate the test effort to the project's technical risks, operational issues and concepts, performance criteria, and system availability. Include component, subsystem, integrated system, and operational tests.
- 13.0 Change Control Plan - Define the need and the procedures for approval of changes to the technical, schedule, and cost baselines.
- 14.0 Environmental, Safety, and Health Plan - Describe the plan for ensuring compliance with ES&H requirements.
- 15.0 Work Breakdown Structure - Provide a three-level WBS for the project.
- 16.0 Logic Diagram - Provide a logic diagram (activity net) for each major subsystem.
- 17.0 Management Plan Approval - Provide a signature page for MIT and DOE approval of the management plan.

7.6.2 Project Organization

We propose to organize the overall Alcator DCT Project as shown in Figure 7.6. R. Parker and B. Montgomery will serve as co-project leaders as they did for Alcator C.

The project managers will be advised by a Review Board which will be chosen to reflect a broad input from inside and outside MIT.

The project office would be responsible for monitoring financial affairs, for contracting, and for reporting.

An independent quality assurance function is shown to monitor all technical activities reporting to the project managers. It is our intention to give this individual broad responsibility for assuring independent review and analysis of design specifications, fabrication, acceptance and installation of major components and systems.

The project is shown as divided into two main branches, a project physics branch, and a project engineering branch. This reflects our strong view of the need for a project oriented, interactive contribution from physics as well as engineering.

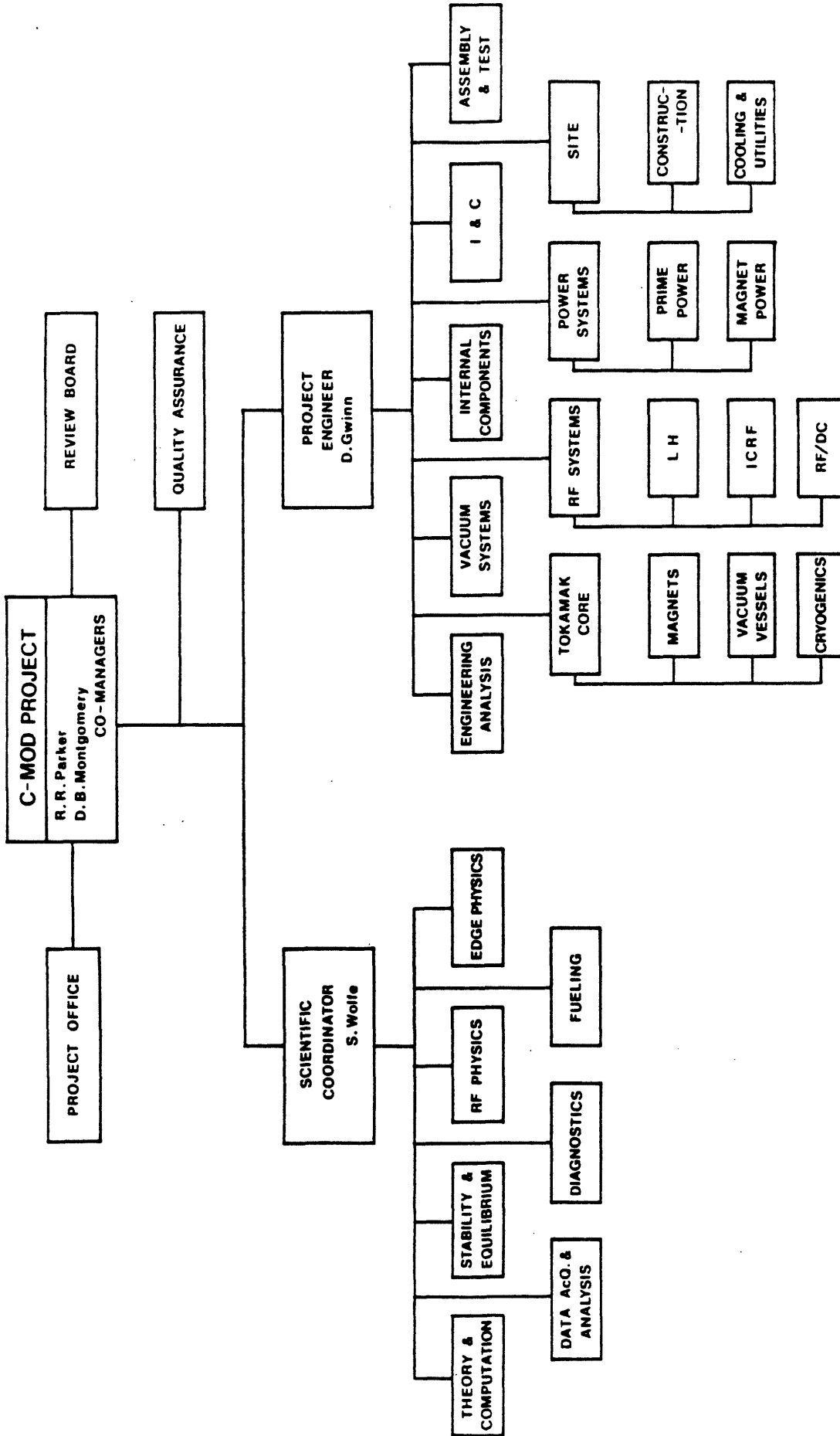


Figure 7.6: C-MOD Project Organization

7.6.3 Program Management Software

We intend to use the HTPM (Harvard Total Project Program Manager) software to track the C-MOD Project. This program is based on construction of an activity network, with inputs of time, resources and manpower that are required to accomplish each activity. Typical examples of output for the C-MOD Project are shown in Figures 7.7-7.11.

Alcator C/Mod Project Plan, Version 01 Rev. 0

Project: cmod2

19-Aug-1985

Page 1

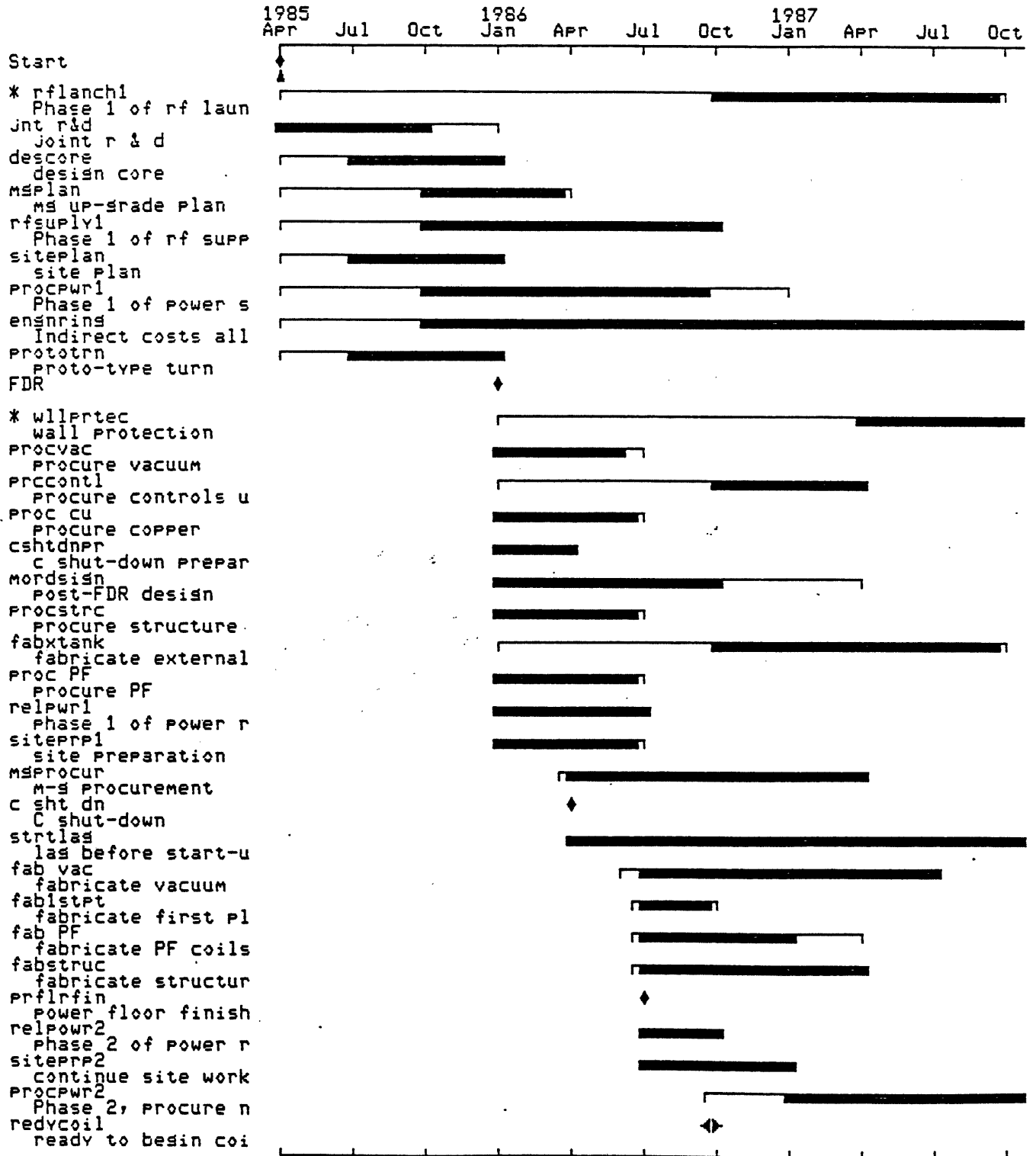


Figure 7.7: Example of HTPM Project Manager software C-MOD detailed schedule

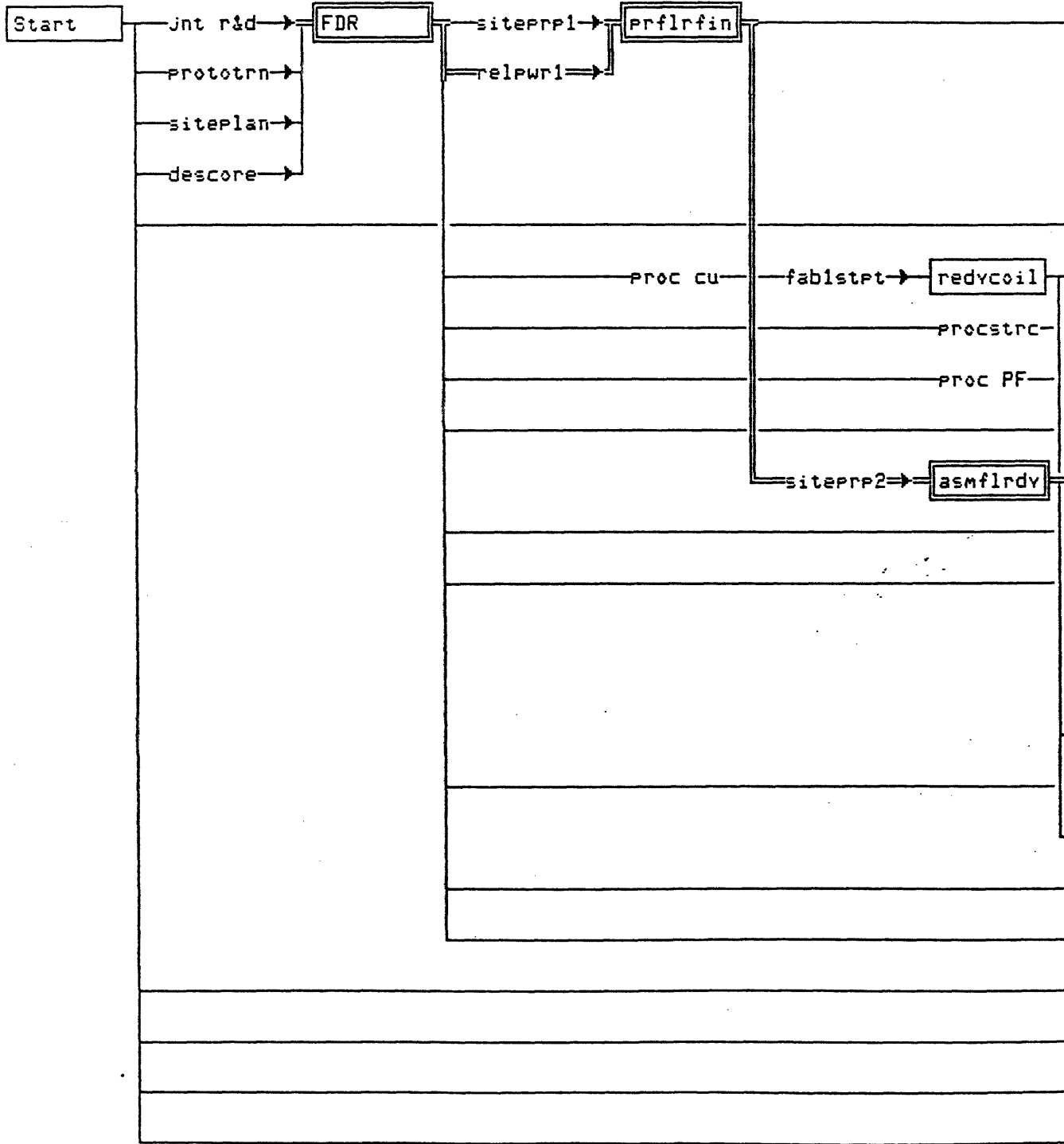


Figure 7.8: Example of HTPM Project Manager software C-MOD overall activity network

Project: cmod2

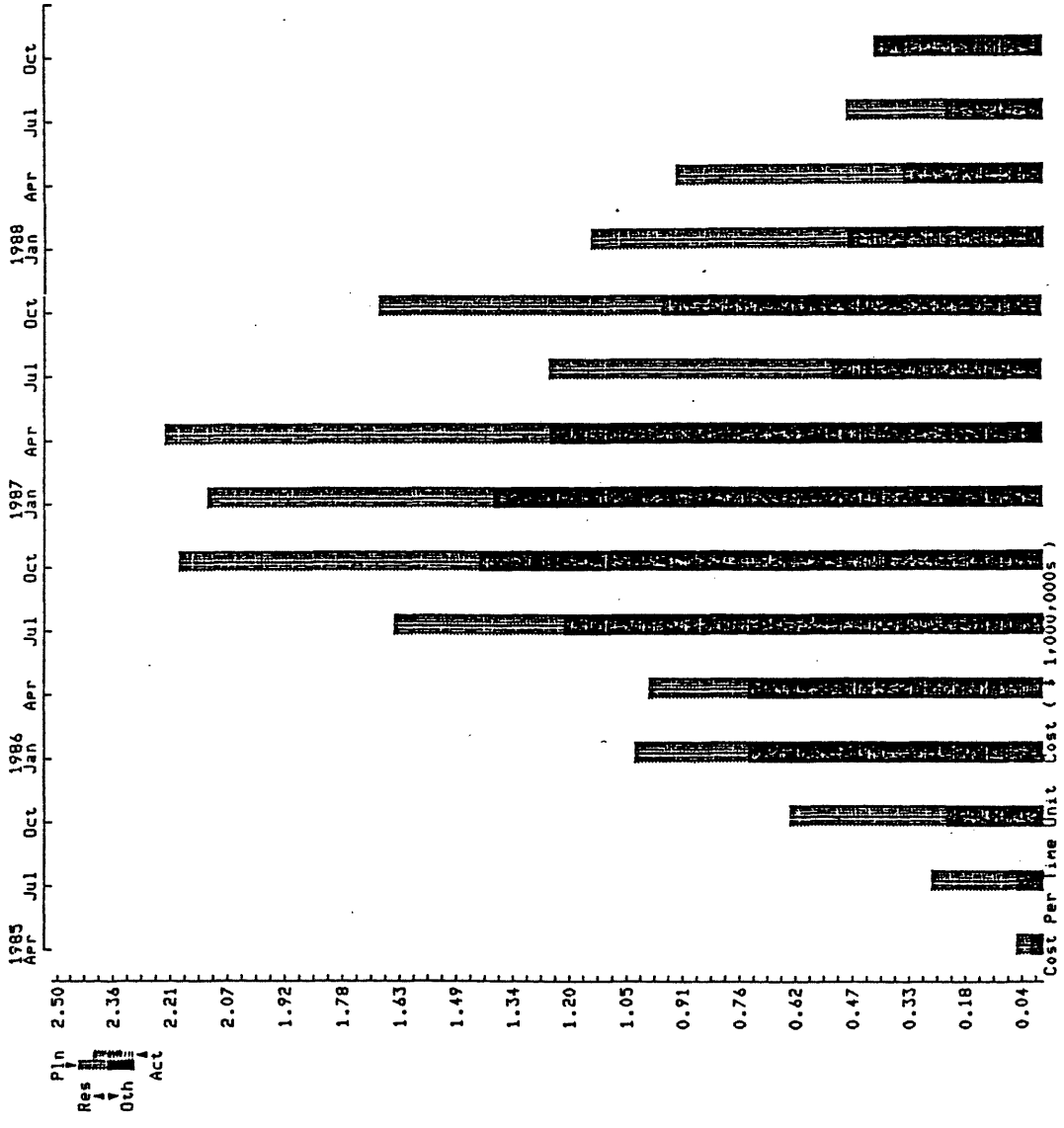


Figure 7.9: Example of HTPM Project Manager software C-MOD quarter by quarter expenditure

Alcator C/Mod Project Plan, Version 01 Rev. 0

19-Aug-1985

Page 1

Alcator C/Mod Project Plan, Version 01 Rev. 0

19-Aug-1985

Project: cmod2

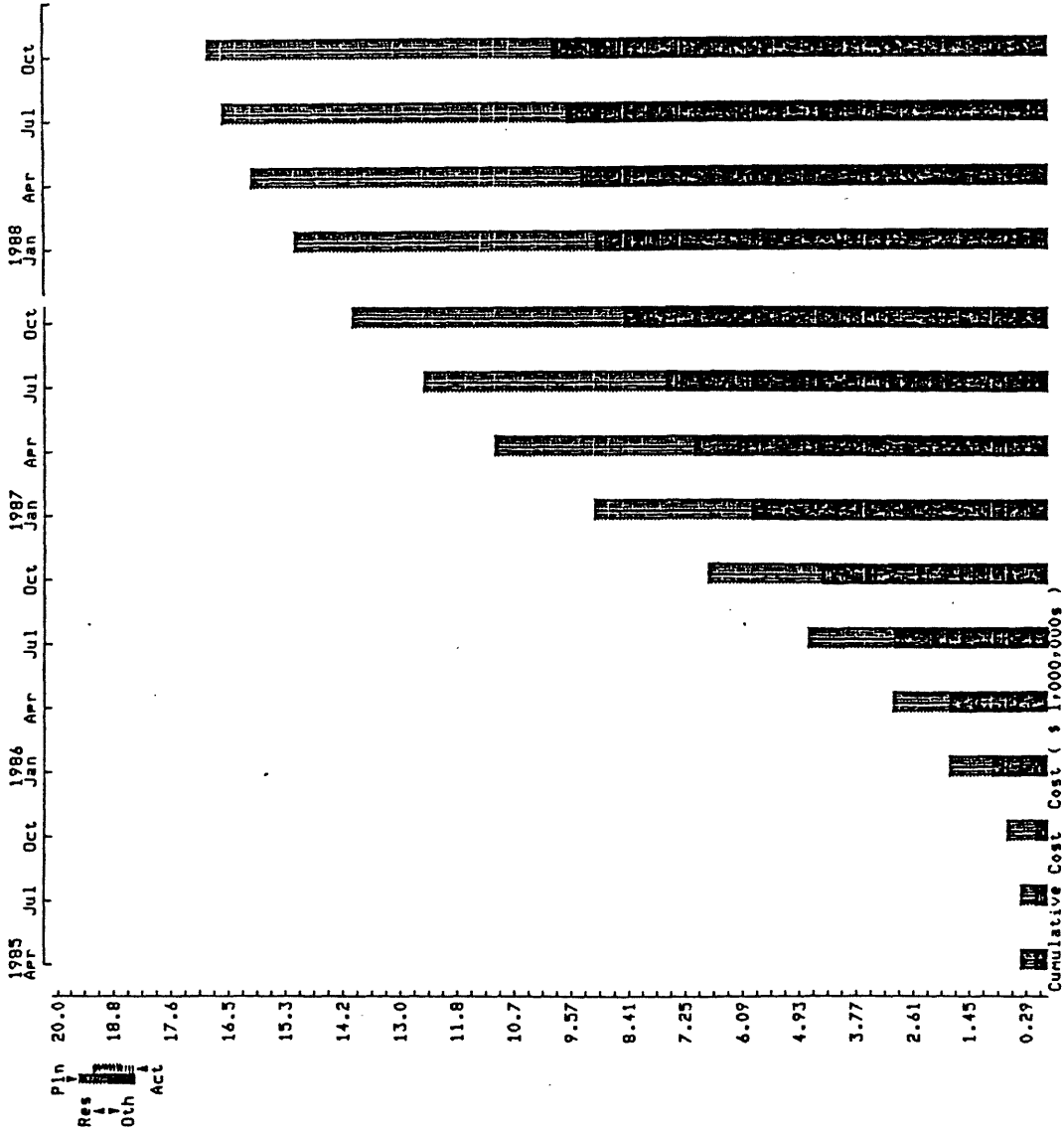


Figure 7.10: Example of HTPM Project Manager software C-MOD cumulative expenditure

Alcator C/Mod Project Plan, Version 01 Rev. 0

Resource: technicians

19-Aug-1985

Page 1

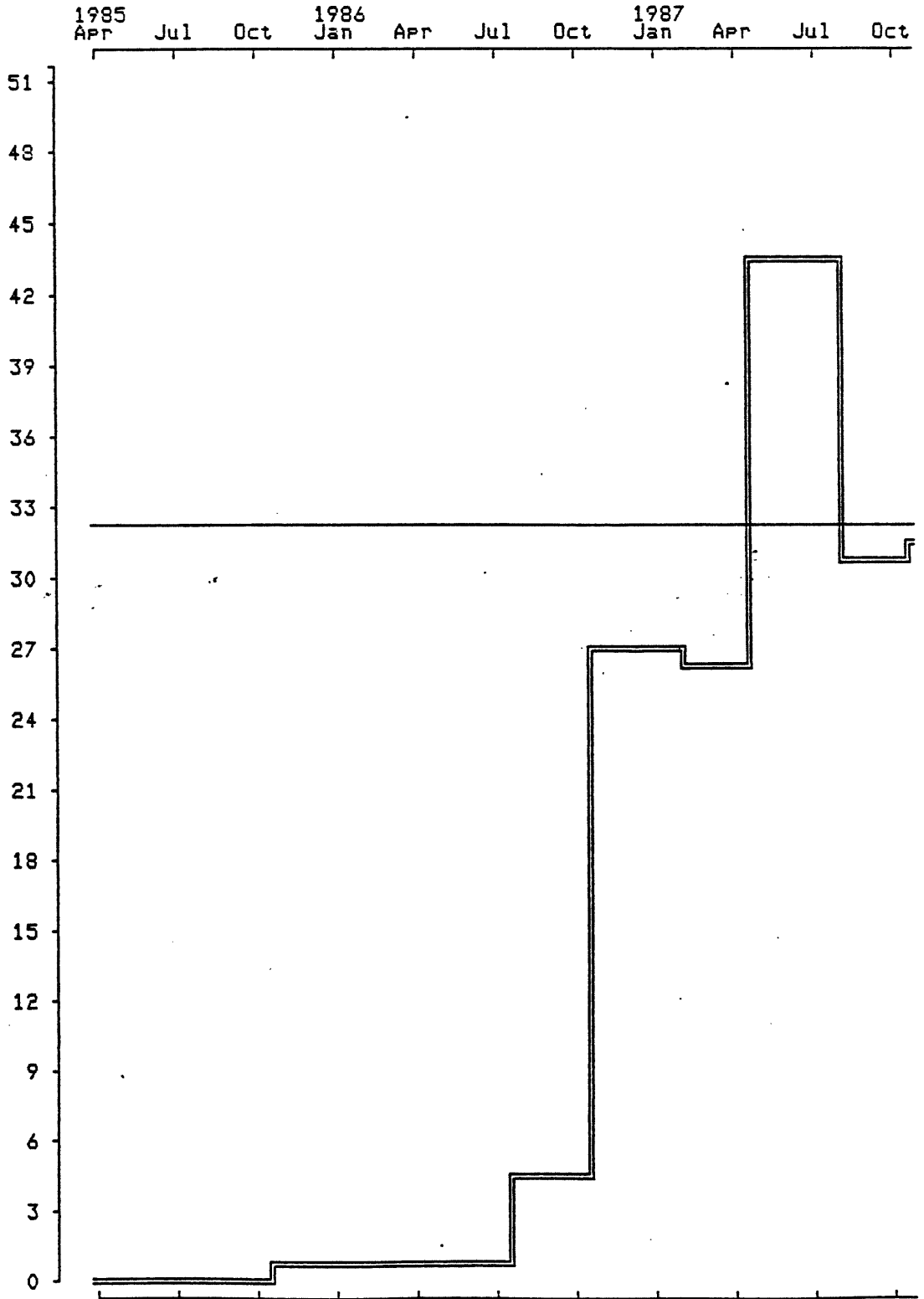


Figure 7:11: Example of HTPM Project Manager software C-MOD manpower requirements

CHAPTER 8
PROGRAM PLAN

While the details of the experimental program on Alcator C-MOD will depend on developments in the physics base and the perceived needs of the national fusion program, as well as the availability of personnel and resources, it is possible to outline a general format at this time, consistent with the assumptions and goals outlined in this proposal. We assume that the project follows the nominal "baseline" profile described above, resulting in commissioning of Alcator C-MOD with an initial 7.5 Tesla capability in mid-1988. We further assume that the FPS-17 (Shemya) RF transmitters have been upgraded and modified during the same period, and that fabrication of the ICRF launchers is either completed or well advanced on the date of first plasma.

The initial run period will commence with "shake-down" activities, establishment of operational procedures and requirements, feedback and programmed control optimization, implementation and testing of diagnostic systems, and machine clean-up. Since the magnet and power supply systems will have undergone full testing during the final stage of the MDF project, we anticipate initial operation will be at the nominal field of 7.5 Tesla. A major goal of the first operating period will be to establish equilibrium control required to produce fully elongated, D-shaped plasmas, and to increase the plasma current as rapidly as possible to the design value ($I_p > 3.0$ MA, $q_\psi < 3$). This program will entail determination of optimal current rise rates, programming of shaping fields, and tuning and optimization of feedback control, particularly with respect to control of the axisymmetric mode. Particular attention will be given to maximizing the

flat-top plasma pulse length subject to limitations imposed by the extractable stored energy in the alternator system. Internal component testing and qualification, under relatively low power loading conditions, will also be carried out during this period. While initial operation will probably rely on a mechanical limiter, preliminary assessment of expanded boundary operation will be made during this phase.

This initial operating period will last from six to eight months, with machine availability projected to rise from less than 50% during the first three months to at least 80% as the operation becomes established. Physics activities will concentrate on equilibrium studies and discharge evolution, preliminary assessment of discharge characteristics, including confinement, and mapping of the available operating space. Particular attention will be paid to the operating limits, including disruption characteristics, impurity effects, etc., and to scaling of ohmic confinement in the high current, high density regime. While no substantial RF heating experiments will be scheduled during this period, we expect to install prototype launchers in order to conduct low power coupling studies in conjunction with the equilibrium studies. This program should establish the requirements for positioning and shielding of the high power antennas to be employed during the next stage of operation. Meanwhile, final testing of these antennas at high power would be carried out simultaneously on a test stand.

By the end of the first run period, the operational characteristics of the device will have been established, the basic diagnostic set will be largely complete, and preliminary assessments of the ohmic operation and equilibrium will have been made. At this point, operation will be

suspended for the installation of ICRF components and divertor hardware. The second extended run period should begin approximately nine months after first plasma and extend over the next nine months to one year. The experimental program will be principally concerned with high power ICRF heating studies, employing the FPS-17 sources. While the precise scenario for the ICRF physics program cannot be defined at this time, we would anticipate that the full 6 MW source capability of the FPS-17 system will be installed during this period. A likely initial implementation would feature both fast wave launchers and Bernstein wave antennas installed simultaneously, so that a direct comparison of the two techniques can be made. Determination of heating efficiency and transport effects will occupy a major share of the physics activity. Establishment of the scaling of confinement in the high density, high current regime with intense ICRF heating, and comparison with results from NBI experiments, and with ICRF in lower density discharges will contribute to the understanding of the relevant physical processes underlying transport. Impurity generation and transport during the high power ICRF experiments will also be a topic of interest. Requirements for divertor components and operation will have been established during the first set of experiments, and full divertor operation will be implemented during this time. Coupling of the RF through the separatrix and scrapeoff layer, which will have been studied at low power earlier, will be an important consideration during these experiments. Use of the divertor configuration to control impurity influxes associated with the RF and for potential confinement enhancement (H-mode) will be a major focus of this phase of the program.

During the second run period we will also carry out a more detailed study of confinement physics in the ohmic plasma. Direct comparison with

the ICRF data will help determine whether a power or pressure dependent degradation occurs in the ohmic case. Particular attention will be paid to the ion thermal transport, which should be small if neoclassical scaling is relevant. We will also investigate the effect of shaping and aspect ratio on the transport properties by extending the range of equilibria, both in ohmic discharges, and to the extent permitted by restrictions on coupling and launcher geometry, with ICRF. Fueling and particle transport experiments will be carried out in conjunction with the RF heating. More specialized diagnostic systems will be brought on as indicated during this period, permitting, for instance, study of the scrape-off and divertor plasma, fluctuations which may be related to transport, determination of the propagation and damping of the RF, etc.

Following the second operating period, i.e. between 18 months and two years after first plasma, many of the basic physics issues will have been clarified, and it is likely that new questions and problems will have been identified in the course of the experiments. The program for the next operating phase will be largely based on these results. Examples of experiments which might be carried out in this period include optimized ICRF heating employing improved coupler concepts, and based on the more efficient of the techniques investigated earlier or on new concepts to be developed, implementation of more efficient divertor configurations or advanced equilibria, or use of profile and edge control to improve confinement and stability properties.

A likely topic for the Alcator C-MOD program following completion of the 6MW ICRF experiments would be the investigation of confinement and stability properties of more advanced geometries. Preliminary studies

indicate that plasmas with elongations of about three will be achievable with only minor modifications to the PF system and internal hardware. Some adaptations to the RF launchers would also be required. The advanced shaping experiments could be carried out either at high field and current in order to study confinement scaling with high B_p , or at somewhat reduced field to study the behavior of the β limit.

The subsequent direction of the Alcator C-MOD program will depend partially on results on the device and partially on external factors. We have assumed that only existing MIT resources have been available during the construction phase, i.e. the present Alcator C alternator and the FPS-17 radar sources. In this case a decision will have to be made on whether to acquire the new generating capacity necessary for full-field operation of the facility and on the possible use of the FMIT sources. Depending on these decisions, the next phase of the program could be devoted to investigation and exploitation of higher field operation, especially with respect to ohmic heating; to study of different ICRF heating schemes using the FMIT sources, which would also provide higher power capability (up to 10 MW at the source); or to further investigations of advanced shaping or profile control.

The latter topic, and the possibility of application of current drive techniques and advanced impurity control methods are examples of the tokamak improvement program to be addressed on Alcator C-MOD. These issues are addressed more fully in Appendix B.

APPENDIX A

Cost Estimate for Installation of Additional Energy

The 10 T option requires more stored energy than can be achieved by overspeeding the present generator. We have been informed by the General Electric Company, however, that a number of 1200 MVA 1800 RPM units are potentially available. These units were built in anticipation of the completion of various nuclear plants which have now been canceled. The units could supply about 650 MJ of extractable stored energy utilizing the stored energy of the rotor alone and this would be sufficient for the 10 T option.

We have received a pricing estimate and detailed work scope from the General Electric Apparatus and Engineering Services Operation, the same group who installed our present 220 MVA ConEd unit. The estimate of \$4,250 K is given in Table A-1. General Electric estimates a project length of 20 months, set largely by the manufacture of the new drive unit. There would be a credit of approximately \$400 K because the present generator would not be equipped with an overspeed drive.

TABLE A-1

MIT INSTALLATION COST ESTIMATE

Generator Foundation	\$ 800 K
Generator Package Inspection	100 K
Generator Package Transportation	600 K
Building Modification	200 K
Rotating Equipment Rigging and Installation	600 K
Generator Auxiliaries	800 K
Drive System	550 K
Plant Electrical System	600 K
	<hr/>
	\$4,250 K

The additional energy of the new unit would permit current-time profiles which would be somewhat in excess of the thermal ratings of our present pulse rectifier supplies. We would therefore propose to increase the rectifier capacity, which would require an additional investment of approximately \$750 K.

APPENDIX B

THEORETICAL CONSIDERATIONS FOR ALCATOR C-MOD AS A TOKAMAK

CONCEPT IMPROVEMENT EXPERIMENT

- I. Introduction
- II. Shaping Options
- III. Advanced Impurity Control
- IV. Lower Hybrid Current Drive and
MHD Stabilization Experiments

I. Introduction

While in its base configuration C-MOD will explore ICRH heating and its ensuing confinement in support of the high field ignition physics program, the toroidal field design with its sliding joints provides a flexibility enabling a substantial range of advanced shaping options for tokamak concept improvement. Here, we expand on the reasons for shaping already given in the bulk of this proposal. In addition to shaping, further concept improvements concern advanced impurity control and current drive.

II. Shaping Options

The reasons for advanced shaping fall into three categories:

1. Higher beta.
2. Confinement Improvement:

Compensating for $\tau_E \sim P_{aux}^{-.6}$.

Increasing the current density.

Improving $n\tau-T$.

Extending the Murakami limit.

3. New regimes of other parameters.

II.1 Higher Beta

The universal agreement that tokamak improvement will have to involve achievement of higher betas and improved confinement through shaping mandates that new experiments be performed in high performance, i.e., non-circular flux geometry. Although C-MOD is not planned to be a high beta experiment per se, the presence of ICRH produced ion bananas may lead to low mode number internal kinks (fishbone oscillations) or high mode number

ballooning modes, both destabilized below the Troyon limit by toroidal precession resonance of the energetic particles. (cf. Refs [II-1a, II-1b])

The Troyon MHD stability criterion

$$\beta_{\text{crit}} = .03 I/aB_t \quad (1)$$

indicates the stability benefits through shaping. In a shaped plasma, the plasma current is given by

$$I = (5a^2 B_t / Rq_\psi) F(\epsilon, \kappa) \quad (2)$$

where q_ψ is the MHD safety factor.

The shaping factor F results from fitting numerical equilibria. Todd et al., finds for Doublet III equilibria

$$F \approx \left(\frac{1+\kappa^2}{2} \right) [1 + \epsilon^2 (1 + \Lambda^2/2)] \cdot [1.24 - .54\kappa + .3(\delta^2 + \kappa^2) + .13\delta] \quad (3)$$

where $\Lambda \equiv \beta_p + \lambda_1/2$. Neglecting the triangularity δ for the moment, the elongation factor

$$\hat{F}(\kappa) \equiv [1 + \kappa^2]/2 [1.24 - .54\kappa + .3\kappa^2] \quad (4)$$

is given as

TABLE 1

κ	1	$\sqrt{2}$	$\sqrt{3}$	2	$\sqrt{5}$	$\sqrt{6}$
$\hat{F}(\kappa)$	1	1.62	2.42	3.4	4.59	6.02

(For larger elongations Eq. (3) would require higher power of κ). Thus,

for $\kappa \equiv b/a = 2.45$ the plasma current has grown by a factor of 6.02, at constant inverse aspect ratio ϵ and q_ψ . The advantages for β_{crit} follows from Eq. (1). E.g., for $\epsilon = 1/3$, $q_\psi = 2.5$, $\kappa = \sqrt{6}$ and $\Lambda = 1$, $\beta_{\text{crit}} = 13.9\%$. Including indented equilibria produces a yet stronger result since indentation increases the flux surface circumference.

The program is now entering the second stage of shaping, i.e. from moderately elongated D-shapes to stronger triangularity and concomitant indentation. [II-1c] While indentation is shown to be necessary to reach the second stability regime, Alcator C-MOD will employ advanced shaping mainly to increase performance in the first stability regime. The dangerous modes are ballooning, external kinks, internal kinks and, to a lesser degree, the axisymmetric modes. The external modes have recently received attention in PBX (cf. Ref. [II-1a]) and may have to be stabilized by special nearby wallsegments. We focus the present discussion on the ballooning modes, following. [II-1c]

The most relevant conclusions of Ref. [II-1c] (whose relevant figures are attached here for convenience) when interpreted for C-MOD are as follows:

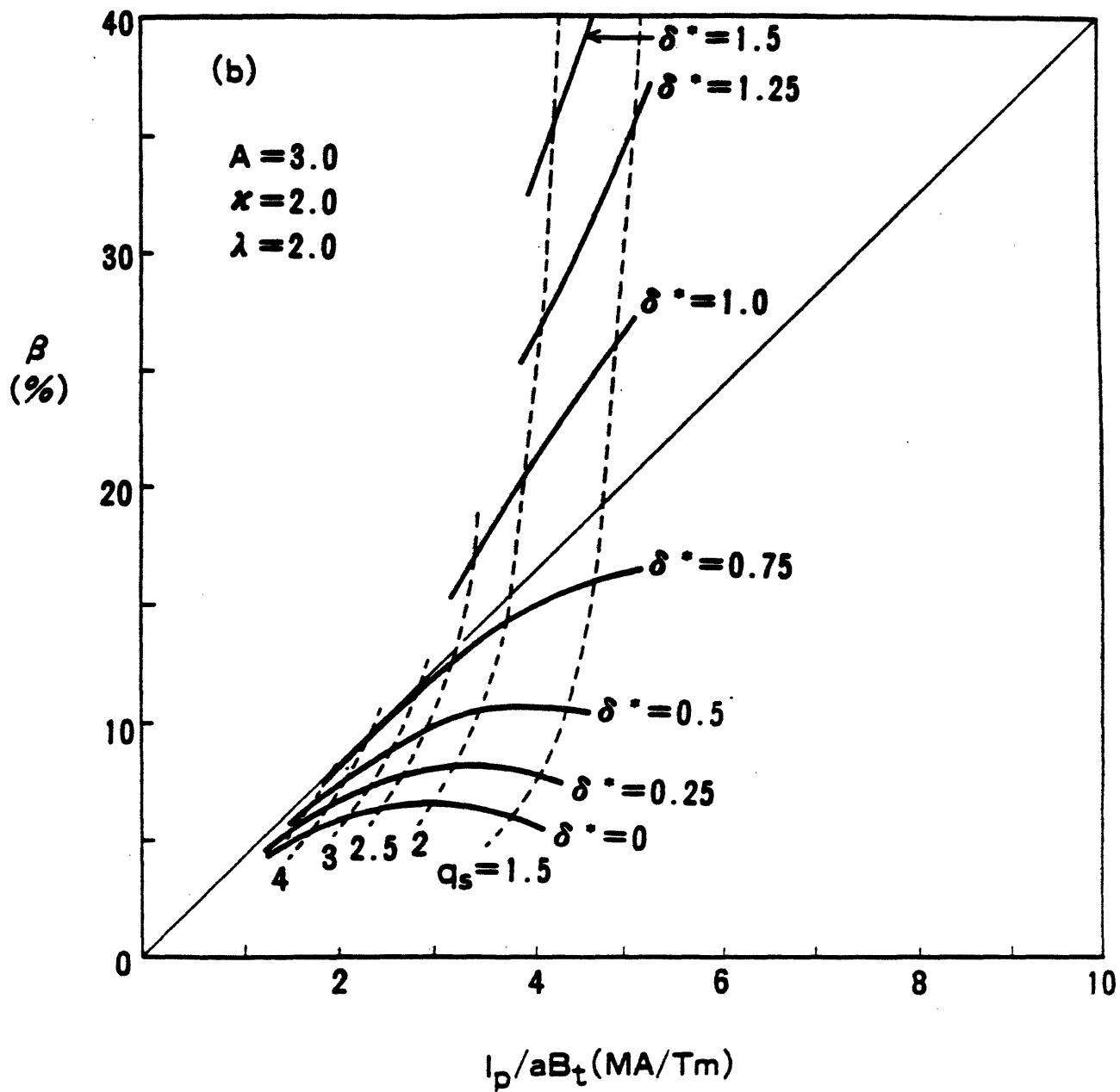
1) dependence of the β -limit on elongation and triangularity. For $\kappa > 1$, the Troyon limit for β_{crit} (against $n = \infty$ ballooning modes) can be exceeded if triangularity δ and (modest) indentation i are provided. See Fig. 4b of Ref. [II-1a]. A corollary is that merely increasing elongation without increasing δ and i is counterproductive, see Fig. 5a of Ref. [II-1c]. $\kappa \approx 2$ with $\delta \lesssim 1$ (for $A = 3$, $q_0 = 1$ and $q_s = 2$) is optimal, allowing $\beta_{\text{crit}} = .25$ at $I/aB_t = 4$ (MA/T_m), $\delta^* = .94$, $\delta^* = 1$, $i \equiv d/2a = .11$, (see Fig. 1 of Ref. [II-1c], for the definition of δ , δ^*

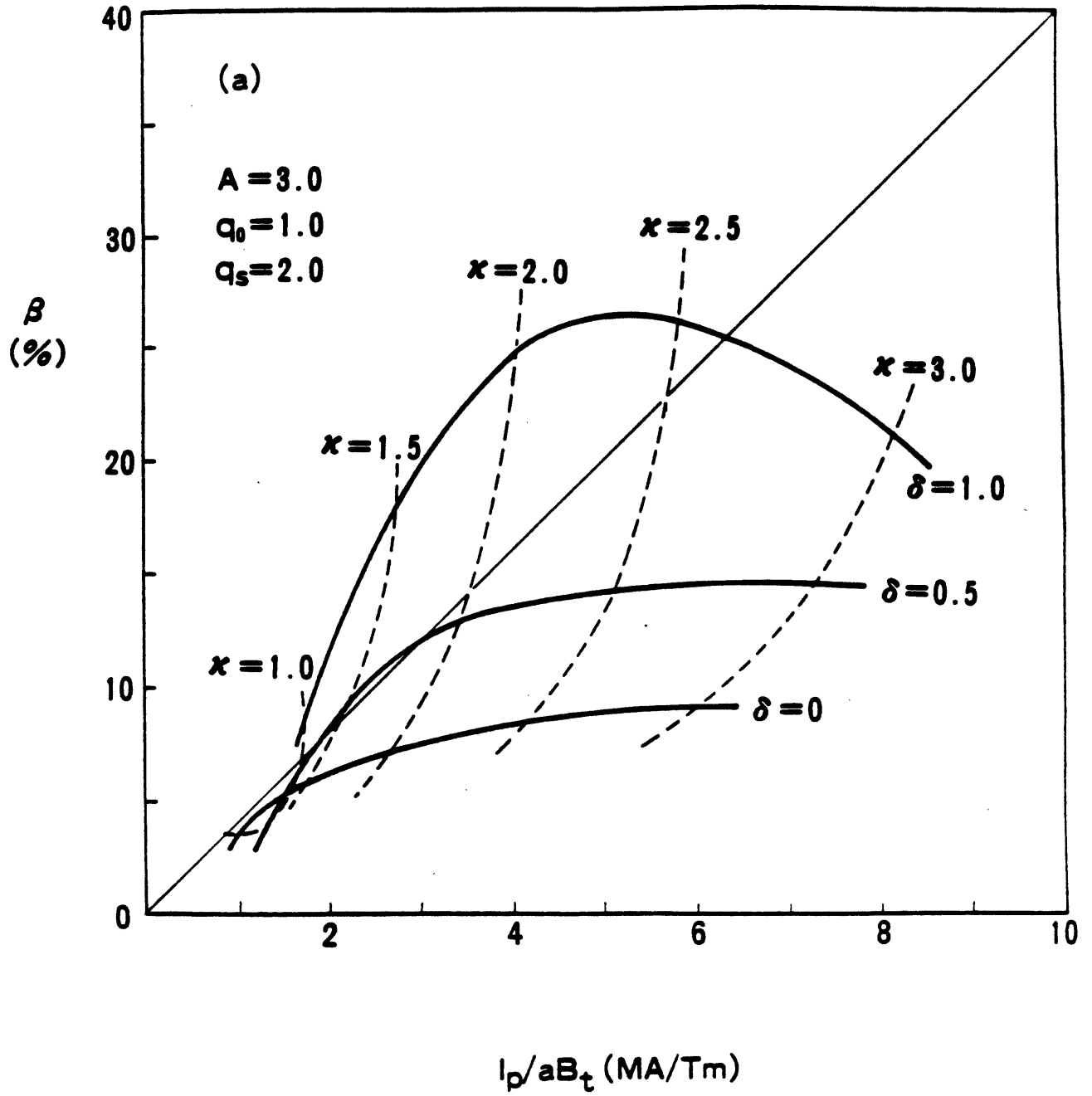
and i.) Fig. 2a, also taken from Ref. [II-1c], shows the flux surfaces which are mildly indented and show relatively sharp tips, i.e. nearby x-points, convenient for an expanded boundary divertor. The current density is rather strongly peaked on the outboard side. If it relaxes somewhat the computations of Ref. [II-1c] indicate mainly a drop of β by a factor of 2, i.e. to 12.5%, still a high value. The poloidal beta is around $\beta_j = .6$ which reflects a fundamental feature of advanced shaping, i.e. $\beta_j < 1$ for very large values of β .

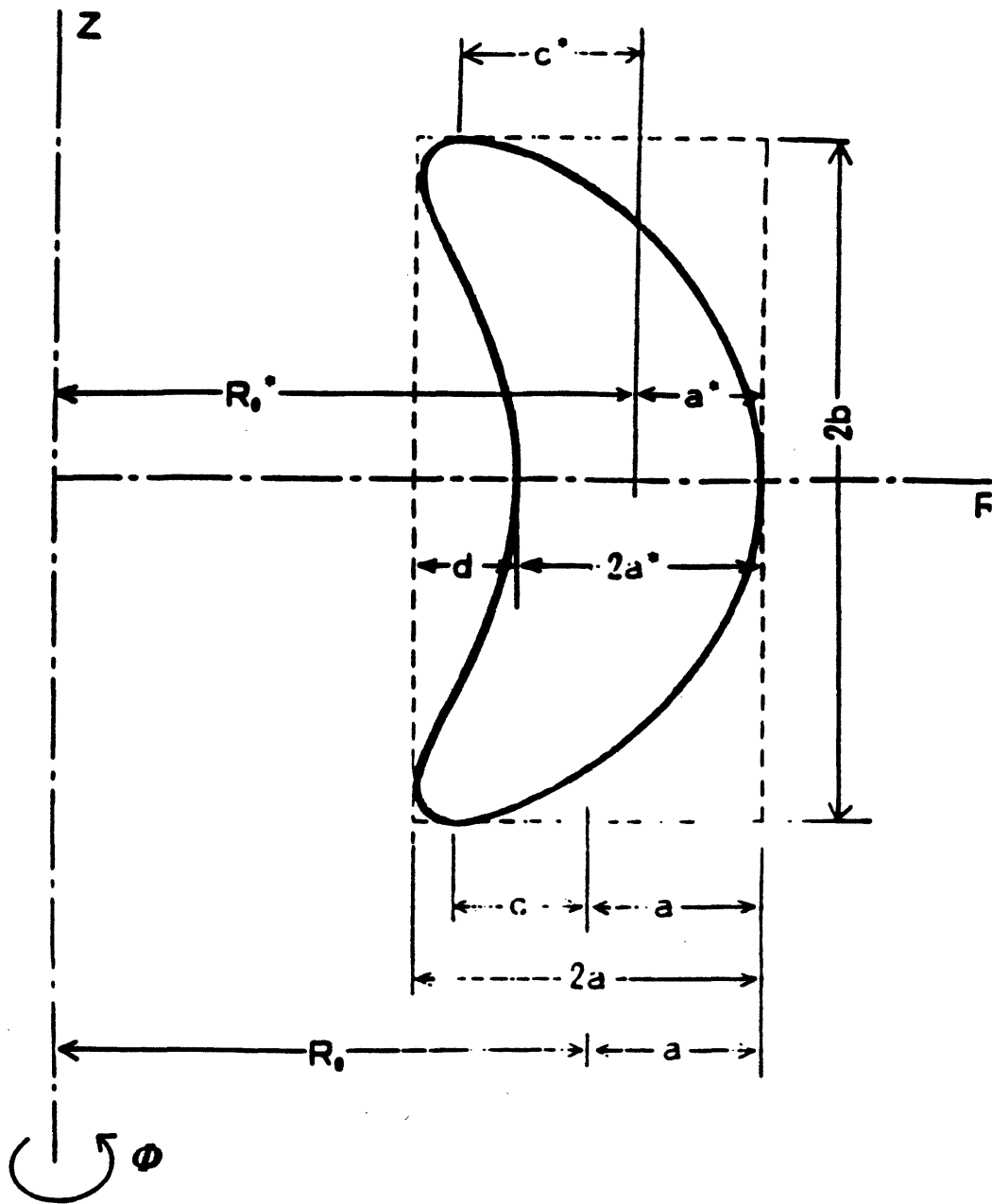
ii) The dependence of the β -limit on aspect ratio A for a fixed Troyon parameter I/aB_t favors going to $A \leq 3$ (see Fig. 6a of Ref. [II-1c]). A desirable data point at $A = 2$ and triangularity $\delta^* = 1$ is missing from Ref. [II-1c] but can be estimated from the rest of the figure.

iii) For indented plasmas the dependence of the β -limit on the shape of the q-profile favors more rapidly rising functions $q(\psi)$ than is typical for sawtooth discharges with the $q = 1$ surface shifted out from the magnetic axis, see Figs 8a and 8b of Ref. [II-1c]. C-MOD with its strong ICRF-heating should be able to shape the q-profile somewhat.

Overall, these results indicate strongly that a thorough study of the effects of shaping the flux geometry and the $p(\psi)$ and $q(\psi)$ - profiles (via variable auxiliary heating) contains the key to reaching the high performance regimes needed for ignition. C-MOD, being a flexible and compact physics oriented prototype, is capable of doing this shaping.







$$\delta = c/a$$

$$\delta^* = c^*/a^*$$

$$i = d/2a$$

$$\kappa = b/a$$

Ref. [II-1] FIG. 1

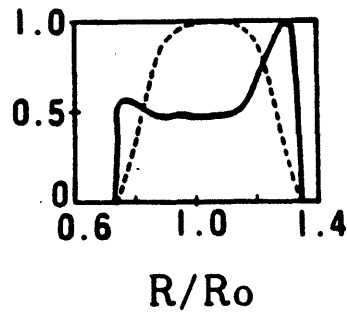
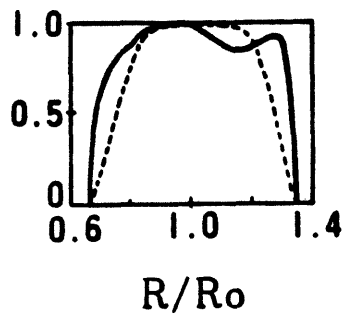
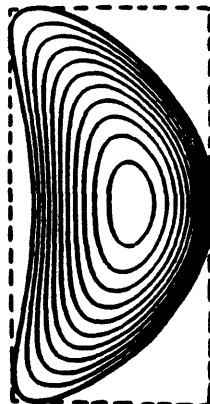
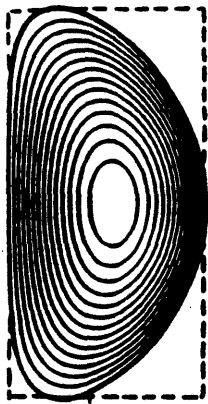
B = 13%

B = 25%

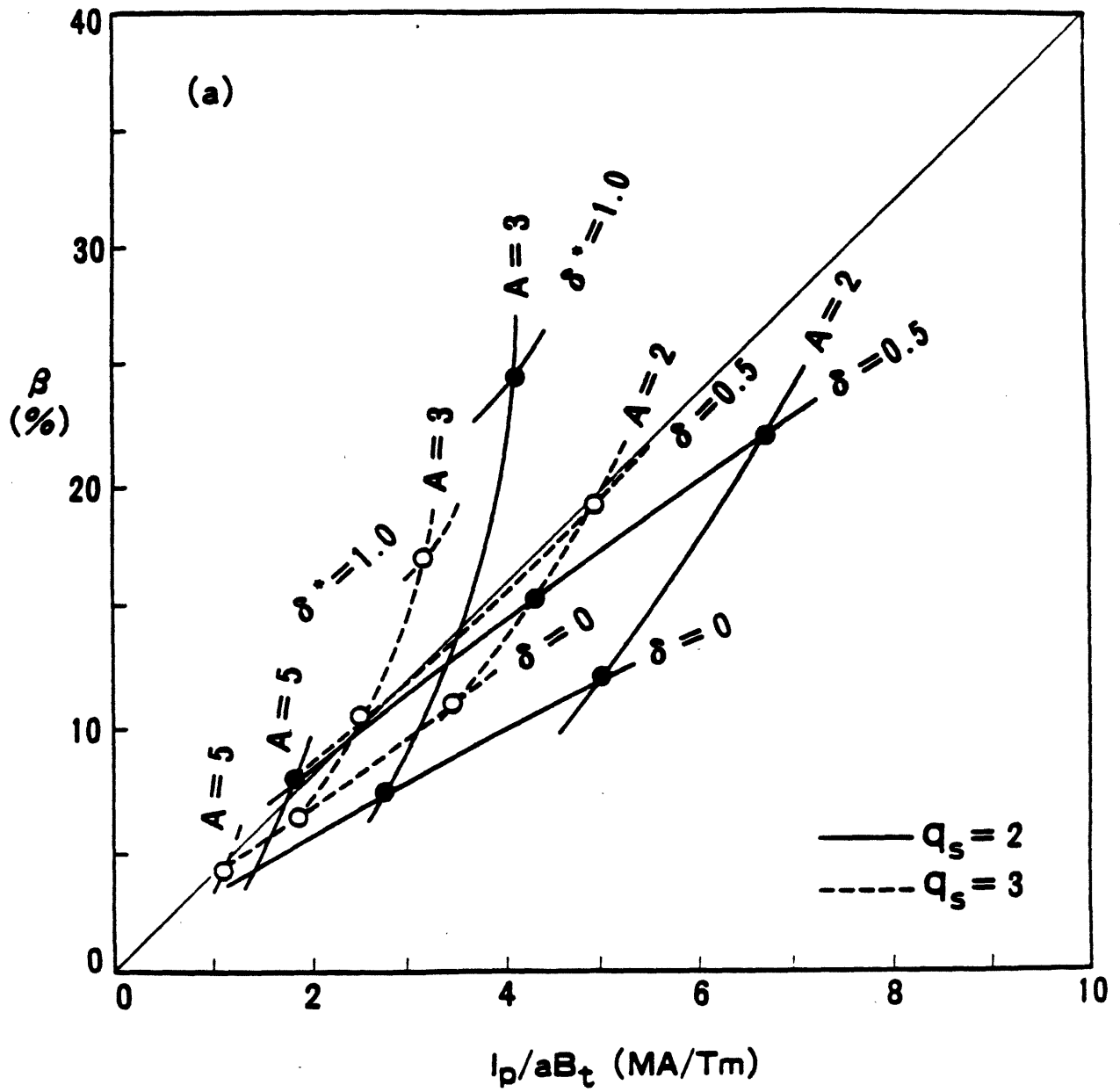
 $\kappa = 2 \quad \delta^* = .5$ $\kappa = 2 \quad \delta^* = 1.$

(a-3)

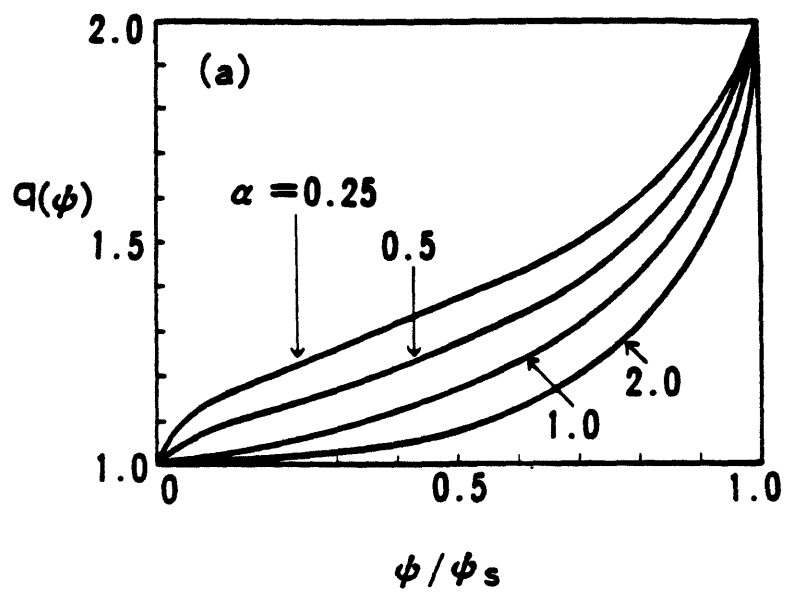
(a-4)

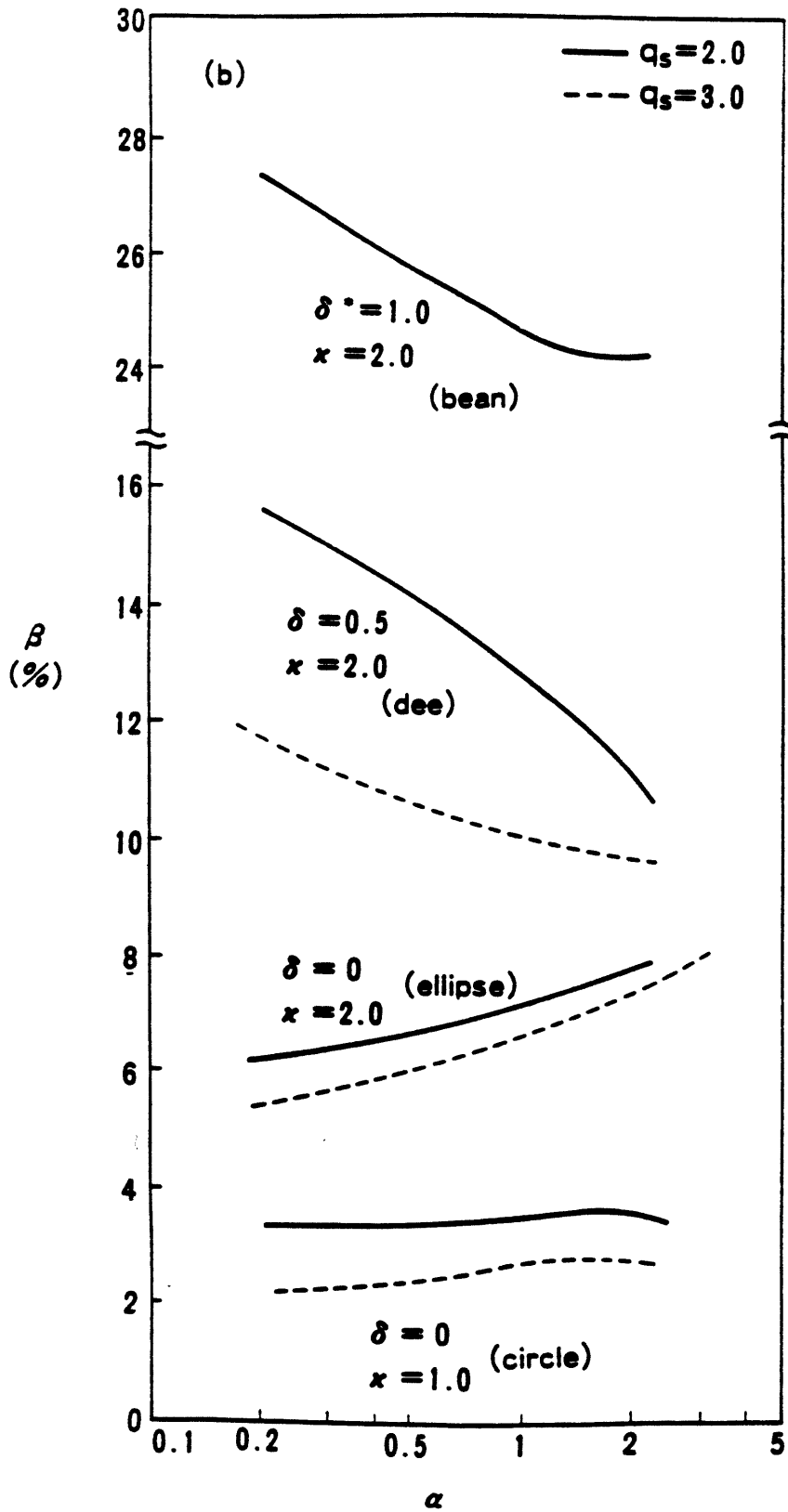


— j/j_{max}
 - - - p/p_{max}



Ref. [II-1] FIG. 6a





Ref. [II-1] FIG. 8b

II.2 Confinement Improvement

Compensating for the Deterioration of τ_E

Combining the Kaye-Goldston scaling law

$$\tau_E \sim P_{aux}^{-.6} I^{1.24} n^{.26} \kappa^{.28} a^{-.5} R^{1.65} \quad (6)$$

with Eq. (2) for the current shows that τ_E will increase with elongation as $\kappa^{.28} \hat{F}^{1.24}$ where \hat{F} is defined in Eq. (4). Thus, one can imagine a sequence of experiments with constant a , R_0 , B_t and q_ψ but increasing the current through κ simultaneously with P_{aux} , in order to keep τ_E constant. One finds an increase of κ from $\sqrt{2}$ to $\sqrt{6}$ compensates for a 19 fold increase in P_{aux} .

Increasing the current density

The strong scaling of the total current I with shaping parameters apparent in Eqs (3) and (4) also implies a favorable scaling for the current density j_ϕ . From

$$I = \iint d\ell_\psi d\ell_\theta j_\phi = (1/2\pi) \int_0^V dV \langle j_\phi/R \rangle = (V/2\pi) \langle \overline{j_\phi/R} \rangle ,$$

where the brackets denote a flux average and the over bar a volume average, it follows that the average of j_ϕ increases as I/V . Since $V \propto a^2 \pi \kappa$ and I increases as $\approx \kappa^2$ (cf. Eq. (3)) this yields approximately $\langle \overline{j_\phi} \rangle \sim \kappa$ at const. R . Indentation will increase this effect. This increase in $\langle \overline{j_\phi} \rangle$ obviously implies more Ohmic power but also a higher Murakami limit, see below.

Improving $nT\tau$

The overall plasma performance as measured by the parameter $nT\tau$ exhibits a strong favorable scaling with elongation. Noting that in the auxiliary heating regime

$$\frac{3nTV}{\tau} = P_a$$

where $V = 2\pi^2 R a^2 \kappa$ is the plasma volume, a simple calculation using Alcator C-MOD parameters then gives

$$nT\tau = 22.5 \frac{P_a \tau^2}{\kappa}$$

For Mirnov ($\tau = .27 I a \kappa^{1/2}$) and Kaye-Goldston scaling this reduces to

$$\text{Mirnov:} \quad nT\tau = .51 P_a \kappa^2 = 5.1 \kappa^2$$

$$\text{Kaye-Goldston} \quad nT\tau = .51 \frac{n^{.52} \kappa^{2.04}}{P_a^{.16}} = .81 \kappa^{2.04}$$

The performance parameters for Mirnov and Kaye-Goldston scaling are:

	$(n_{20T_{keV}\tau})_{\text{Mirnov}}$	$(n_{20T_{keV}\tau})_{\text{Kaye-Goldston}}$
$\kappa = 1$	5.1	.81
$\kappa = 1.8$	16.5	2.7
$\kappa = 3$	45.9	7.6

Observe the strong relative gains due to elongation as well as the large differences between the Mirnov and Kaye-Goldston scaling.

Extending the Murakami Limit

While the details are still unclear, the precondition for the major disruption appears to be that the total ohmic power ηj^2 is expended on ionization and line radiation in the gas-puff. Thus $n_{\text{crit}} \sim j(0) = I/ab\pi \approx (B_t/Rq_\phi)F(\epsilon, \kappa)/\kappa$ where F is given in Eq. (3). F/κ increases approximately linearly with κ . The shaping options in C-MOD should thus lead to an increase in the density limit over the standard value of (B_t/Rq_ϕ) .

II.3 New Regimes of Other Parameters

Collisionality Parameter in Strongly Shaped Plasmas

From the definition $\nu_* \equiv \nu / \left(\frac{\Delta B}{B} \omega_b \right)$ and $\frac{\Delta B}{B} = 2\epsilon$ and, for an ellipse,

$$\omega_b = \sqrt{(\epsilon/2)} \frac{v_l}{Rq} \kappa \quad \text{the result is } \nu_* \sim A^{3/2} \kappa n Rq/T^2 \quad (9)$$

Thus, elongation increases the collisionality linearly with κ but smaller aspect ratio reduces it. E.g., going from $A = 3$ to $A = \sqrt{3}$ reduces ν_* by a factor of .44. With strong ICRF heating T^{-2} can decrease by an order of magnitude. The question of interest is to generate plasmas with $\nu_* < 10^{-2}$ at finite beta, which are the theoretical conditions for anomalous ion heat transport due to trapped ion mode turbulence. These conditions are likely to be met in a reactor plasma and thus of great interest to simulate in C-MOD where these conditions can be varied substantially.

Ion Heat Conduction

When the mod-B contours align themselves with the flux surfaces the magnetic drifts $\propto \vec{B} \times \nabla B$ lie in the flux surface and thus the ion banana width vanishes, thereby eliminating neo-classical transport. [E.g. this alignment has been demonstrated earlier by J. Rome, ORNL, for high β -equilibria ($\beta > 7\%$).] This effect should be substantial for the equilibria of Ref. [II-1] discussed above. This "omnigeneity" property is rigorously impossible in a tokamak equilibrium but is approached locally to some degree in very low aspect ratio tokamaks and, obviously, on the outboard side of a very elongated tokamak such as C-MOD. A reduction of χ_i (neo-classical) is most valuable for obtaining ignition.

III. Advanced Impurity Control

The standard impurity control via pump limiter and expanded boundary divertor is part of the C-MOD base configuration and is described further above, in this proposal. In this section an outlook is given at certain recent advanced techniques, most of them still in an early state of experimental and theoretical development. Since they don't require major design modification or major cost additions they can be implemented in C-MOD when or after it commences plasma operation.

III.1 The different effect of co-vs counter injection of neutral beams on impurity transport is by now well established experimentally. [III-1] The theoretical explanation based on neo-classical theory including the gyroviscous stress tensor [III-2] offers a self consistent explanation which successfully explains impurity transport differences and the concomitant effects on toroidal momentum confinement of several major experi-

ments. [III-4] Obviously, such a classical theory cannot explain the additional, sometimes dominant, effects of internal disruption (sawteeth) on impurity expulsion. (In reactor grade plasmas the sawtooth period may be longer than the energy confinement time, however.) Overall, the work of Ref. [III-2] suggests to provide a radially outward pointing ambipolar electric field to keep the plasma clean. This has been corroborated by electric field measurements using the R.P.I. heavy ion beam probe. [III-4]

In light of this work, R. Taylor's experiments on Macrotor using probes to control the radial electric field and particle confinement [III-6] become theoretically transparent and corroborate the N.B.I. driven impurity control effects.

III.2 In a high performance, high field tokamak such as C-MOD neither neutral beam injection nor probes inside the plasma are practical. There remain the possibilities of controlling the particle confinement time τ_p via electron runaway losses (as a nonambipolar mechanism) with LH current drive in addition to the main inductive current, as has recently been shown by S. Luckhardt, et al., [III-6] or in principle, the application of ECRH power selectively in the edge region. A different idea involving ions rather than electrons is stimulated by the observation in PDX [III-7] and Alcator C [III-8] that pellet fueling can lead to a marked change in impurity confinement. To the extent that continuous pellet fueling can produce a sustained poloidal asymmetry in the flux surface of particle density and temperature the longstanding theoretical work of Ohkawa and Burrell [III-9] for impurity control using asymmetric sources may come back as a viable technique, although it will require different pellet injection geometry. By now there exists a wide body of literature on the

subject of the effects of poloidal density modulation on impurity transport. [III-11, III-2]

In an ICRF heated high field, high density device such as C-MOD the interaction of pellet fueling and RF needs extensive study, since ICRF by itself is known experimentally to generate impurity problems and theoretically, to have an inherent tendency to drive impurities inwards. [III-10]

Since impurity control of intensely ICRF heated plasmas may well become a central issue of ignition physics a C-MOD effort in the area of exploring and developing these advanced impurity techniques may equally well result in major contributions to concept improvements.

References

- [II-1a] M. Okabayashi et al., "The PBX Tokamak Experiment - MHD Aspects of Bean Shaped Tokamaks", Invited Lecture at Course and Workshop on Processes of Toroidal Fusion Plasmas, Varenna 1985.
- [II-1b] D. Spong, D. J. Sigmar, W. A. Cooper, D. Hastings, T. Tsang, Phys. Fl. 28 (August 1985) 2494.
- [II-1c] K. Yamazaki, T. Amano, H. Naitou, Y. Hanada, M. Azumi, "Balloon-ing Beta Limits of D-and Bean Shaped Tokamaks", IPPJ-T13, Feb. 1985.
- [III-1] R. Isler et al., Nucl. Fusion 25, (1985) 386 and references therein.
- [III-2] W. M. Stacey and D. J. Sigmar, Nucl. Fusion 25, (1985) 463 and references therein.

- [III-3] W. M. Stacey and D. J. Sigmar, paper 119 in 12th European Conference on Controlled Fusion and Plasma Physics, Budapest, September 1985.
- [III-4] G. Hallock et al., "Space Potential Distribution in the ISX-B Tokamak", submitted to Phys. Rev. Lett., 1985.
- [III-5] R. J. Taylor et al., Phys. Rev. Lett. 42, (1979) 446; R. J. Taylor, Proc. 9th IAEA Int. Conf. Baltimore 1982, Vol 3, 251.
- [III-6] S. C. Luckhardt et al., Report PFC/JA-84-42, December 1984.
- [III-7] D. Johnson et al., Proc. 9th IAEA Int. Conf. Baltimore 1982, Vol 1, 9.
- [III-8] J. Terry et al., Observations on Alcator C, private communication 1985.
- [III-9] K. H. Burrell, Phys. Fl. 19, (1976) 401.
- [III-10] V. S. Chan et al., Nucl. Fusion 25, (1985) 697.
- [III-11] C. S. Chang et al., Nucl. Fusion 25, (1985) 1397.

IV. Lower Hybrid Current Drive and MHD Stabilization Experiments

IV.1 Current Drive Experiments

Lower hybrid current drive experiments on Alcator C have been highly successful in demonstrating (a) slow wave current drive without inductively driven currents; (b) current ramp-up experiments; (c) transformer recharging; (d) sawteeth stabilization during combined OH-RF current drive experiments; (e) significant electron heating during RF current drive. Due to the high frequencies ($f = 4.6$ GHz) Alcator C has been able to operate in the electron heating/current drive regime at densities $1.0 \times 10^{13} \lesssim \bar{n}_e \lesssim 1.7 \times 10^{14} \text{ cm}^{-3}$ and magnetic fields $5.5 < B(\text{Tesla}) < 11.0$ with powers $P_{\text{RF}} \lesssim 1.4 \text{ MW}$.

At higher densities a substantial reduction in the intensity of electron tail production, and a shift to ion tail production was found, probably due to parametric interactions (and/or the appearance of the mode conversion layer in hydrogen plasmas). This is the so-called density limit which prevented operation with slow waves at higher densities. While these experiments (and others around the world) have verified the fundamental theoretical concepts of RF current drive, it became clear that the efficiency in the present experiments is low, and that substantial improvements will have to be achieved in the future for reactor applications. The causes of the relatively low efficiency may be traced back to the upshift of the N_{\parallel} Brambilla spectrum, which causes the current to be carried by relatively low energy electrons ($E \sim 30 \text{ keV}$) in present day experiments. The efficiency can be improved by performing current drive experiments at higher temperature than those present today. In particular, a survey of existing experiments demonstrated that $\eta_{\text{I}} \propto T_e$ where

$\eta_I \propto \bar{n}_e IR/P_{RF}$, with R being the major machine radius. [IV-1] Therefore, slow wave current drive experiments performed in a high electron temperature plasma ($T_{e0} \gtrsim 5$ keV) are of great interest. Such experiments may be carried out in Alcator C-MOD in conjunction with ICRF heating at densities $\bar{n}_e \lesssim 2 \times 10^{14} \text{ cm}^{-3}$. The maximum current drive efficiency we may expect to achieve is $\eta_I \lesssim 0.6 (10^{20} \text{ m}^{-3} \times A_{\text{m}}/W)$, (as opposed to typical present day values of $\eta_I \lesssim 0.1$).

Using the slow waves, higher efficiencies are difficult to achieve in plasmas with $\omega_{pe}^2/\omega_{ce}^2 \gtrsim 0.5$ because of considerations of accessibility and strong Landau damping. A viable alternative is to use the fast wave (lower hybrid or ICRF). Because of the waveguide launching geometry, demonstration of the effectiveness of fast lower hybrid wave current drive is of great practical importance as a reactor improvement concept. However, at present very little is known experimentally about the coupling, accessibility and absorption of fast lower-hybrid waves (FLHW) in tokamak plasmas. Alcator C-MOD, and the existing 4.0 MW, 4.6 GHz lower hybrid RF system would make a suitable vehicle to test such a fast wave current drive scenario. Calculations indicate that fast lower hybrid waves with parameters $f = 4.6$ GHz, $B = 7.0$ T, using H^+ ions are accessible for $N_{\parallel} \gtrsim 1.8$, and such waves interact with electrons of energy $E \approx 100$ keV. Thus, if such waves were absorbed, it can be shown that the equivalent current drive efficiency in a $T_e \approx 5$ keV plasma is $\eta_I \sim 0.6$, which is a significant improvement over the presently achieved values. (Absorption may be achieved in the presence of a pre-formed electron tail produced by, for example, slow waves.) To further increase the efficiency, we would need to increase the magnetic field (or lower the frequency, but that is not practical in the present case). Assuming

a B = 10 T operation, accessibility in hydrogen at $n_e = 3 \times 10^{14} \text{ cm}^{-3}$ is achieved for $N_{\parallel} \gtrsim 1.3$, and interaction with $E \sim 300 \text{ keV}$ electrons becomes feasible. Of course, in the relatively low temperature plasma ($T_e \sim 5 \text{ keV}$) absorption of such high phase velocity fast waves cannot be achieved unless a pre-formed electron tail is present. Such a tail could be produced by the simultaneous injection of slow lower hybrid waves, and thus by combining slow and fast waves the fast wave current drive concept could be tested. Note that absorption of high parallel phase velocity fast waves in the absence of a pre-formed electron tail is feasible only in a high electron temperature plasma ($T_e \gtrsim 20 \text{ keV}$) such as may be achieved under reactor-like plasma conditions.

Regarding the launching of such waves, we may consider dielectric loaded waveguides using Al_2O_3 , BeO , or TiO_2 , depending on the N_{\parallel} spectrum desired. Alternative launching schemes, such as slotted waveguides will also be considered. Design considerations indicate that the 15 cm wide port is sufficiently wide to install a suitable array of dielectric loaded waveguides with an N_{\parallel} spectrum peaking in the accessible regime. In particular, such a waveguide array is under development for testing of wave-plasma coupling in the Versator II tokamak.

IV.2 MHD Stabilization Experiments

Stabilization of MHD modes has been observed recently in a number of current drive experiments [Petula-B, [IV-2] PLT [IV-3], and Alcator C [IV-4]]. Thus, it has been shown that sawteeth may be stabilized by applying lower hybrid power in the current drive mode of operation. The exact mechanism of stabilization has not been clarified as yet. Initial ideas on current profile broadening by the RF current, being generated

off-axis (and hence raising the effective q on axis) may not be the responsible mechanism. Hence, the exciting possibility exists that some other stabilization mechanisms, which may be favorable toward maintaining higher beta values, have been operative in these experiments. Experiments where the current profiles may be modified by RF injection need to be explored, especially in shaped plasmas, such as Alcator C-MOD. For example, in Alcator C stabilization of sawteeth was observed at $B = 6.1$ T, $\bar{n}_e \approx 1.7 \times 10^{14} \text{ cm}^{-3}$, a relatively high density. While we do not expect stabilization with slow waves at $\bar{n}_e \sim (4-6) \times 10^{14} \text{ cm}^{-3}$ (due to the density limit) fast wave current drive may be less susceptible to the density limit (something to be explored). Therefore, MHD stabilization with fast waves may be effective to higher densities than with slow waves. In any case, even at densities $\bar{n}_e \lesssim 2 \times 10^{14} \text{ cm}^{-3}$, sawtooth stabilization experiments would be of direct relevance to the conventional reactor regime.

Additional experiments may include stabilization of the $m = 2$ modes either by local heating (as in ECRH experiments on T-10) [IV-5] or direct current profile (?) modification on Petula-B, or by feedback techniques proposed by Ignat, Rutherford and Hsuan [IV-6]. These techniques are clearly of great importance in preventing disruptions in tokamaks which may lead to increasing the density limit of tokamak operation above the Murakami limit. Using the 4.6 GHz RF systems, these aspects of tokamak operation could be explored on Alcator C-MOD. Finally, the question of confinement scaling in the presence of current drive and direct electron heating may also be explored at densities $\bar{n}_e \lesssim 2 \times 10^{14} \text{ cm}^{-3}$ in Alcator C-MOD.

References

- [IV-1] M. Porkolab, IEEE Transactions on Plasma Science, PS-12, 107 (1984).
- [IV-2] C. Gormezano et al., Radiofrequency Plasma Heating, 6th Topical Conference (Callaway Gardens, GA, 1985) p. 111, 1985.
- [IV-3] T. K. Chu, et al., *ibid*, p. 131.
- [IV-4] M. Porkolab et al., APS DPP Meeting, San Diego, November, 1985.
- [IV-5] V. V. Alikaev and K. A. Razumova, presented at the "Course and Workshop on Applications of RF Waves to Tokamak Plasma," Varenna, Italy, September 1985.
- [IV-6] P. H. Rutherford, et al., presented at the "Course and Workshop on Applications of RF Waves to Tokamak Plasmas," Varenna, Italy, September 1985.